Eigenstate Structure and Quantum Chaos in the Bose-Hubbard Hamiltonian

Dissertation zur Erlangung des Doktorgrades der
Fakultät für Mathematik und Physik der
Albert-Ludwigs-Universität Freiburg

vorgelegt von
Lukas Pausch

Betreuer:	Prof. Dr. Andreas Buchleitner
In Zusammenarbeit mit:	Dr. Alberto Rodríguez
	Dr. Edoardo Carnio

Freiburg, 26. März 2022

Dekan: Prof. Dr. Michael Thoss

Gutachter: Prof. Dr. Andreas Buchleitner
Prof. Dr. Joachim Dzubiella

Tag der mündlichen Prüfung: 08. Juni 2022

Prüfer: Prof. Dr. Tanja Schilling
Prof. Dr. Tobias Schätz
Prof. Dr. Andreas Buchleitner

Zusammenfassung

Die Dynamik von klassischen Systemen wie von Quantensystemen kann im Wesentlichen in zwei Klassen eingeteilt werden: regulär und chaotisch. In klassischen Systemen zeichnet sich Chaos dadurch aus, dass infinitesimal kleine Störungen der Anfangsbedingungen große Auswirkungen zu späteren Zeiten haben. Für Quantensysteme, deren klassischer Grenzfall nach dieser Definition chaotisch ist, ist bekannt, dass die Differenzen der Eigenenergien derselben statistischen Verteilung folgen wie die Abstände zwischen Eigenwerten Gaußscher Zufallsmatrizen. Quantenchaos, im Sinne von "Chaos in Quantensystemen", kann daher mittels der Statistik der Energie-Eigenwerte definiert werden. Da allerdings das Spektrum allein nicht ausreicht, um ein Quantensystem vollständig zu charakterisieren, ist zu erwarten, dass die Eigenzustände über die spektralen Eigenschaften hinaus weitere Charakteristika von Quantenchaos enthüllen.

In der vorliegenden Arbeit untersuchen wir detailliert, wie sich Quantenchaos in der Struktur der Eigenzustände, charakterisiert durch deren fraktale Dimensionen in bestimmten natürlichen Basissätzen des Systems, äußert. Als Modell dient hierbei der Bose-Hubbard-Hamiltonian, welcher Bosonen auf einem Gitter beschreibt, die zwischen benachbarten Gitterplätzen tunneln können und lokal miteinander wechselwirken. Bei den Energien, Tunnelstärken und Wechselwirkungsstärken, für welche dieses System gemäß der Statistik des Spektrums quantenchaotisch ist, sind die Eigenzustände im Grenzfall großer Systeme (d.h. viele Teilchen und Gitterplätze) delokalisiert in beiden natürlichen Basissätzen. Gleichzeitig nehmen die Fluktuationen der fraktalen Dimensionen zwischen Eigenzuständen ähnlicher Energie drastisch ab und weisen qualitativ basisunabhängige Eigenschaften auf. Zudem zeigen sich die Grenzen der quantenchaotischen Region in den Eigenzuständen durch sehr asymmetrische Verteilungen der faktalen Dimensionen.

Innerhalb der quantenchaotischen Region vergleichen wir die Lokalisierungseigenschaften der Eigenzustände mit den entsprechenden Vorhersagen für Gaußsche Zufallsmatrizen und für Zufallsmatrizen der sogenannten Eingebetteten Ensembles, die im Gegensatz zu den Gaußschen Zufallsmatrizen die Zweiteilchen-Natur des Bose-Hubbard-Hamiltonian abbilden. Der Mittelwert und die Varianz der fraktalen Dimensionen werden sehr gut durch diese beiden Ensembles beschrieben. Dennoch wird die vollständige Wahrscheinlichkeitsverteilung der fraktalen Dimensionen der Eigenzustände des Bose-Hubbard-Hamiltonians mit zunehmender Systemgröße immer besser unterscheidbar von jener der Zufallsmatrizen, womit systemspezifische Merkmale des Bose-Hubbard-Modells auch für unendliche Systemgrößen zugänglich bleiben.

Zuletzt untersuchen wir, wie sich die Ununterscheidbarkeit der Teilchen auf das Auftreten von Quantenchaos auswirkt und stellen fest, dass dieses umso schwächer wird, je besser die Bosonen voneinander unterscheidbar sind.

Abstract

The dynamics of classical and quantum systems can basically be divided into two classes, regular and chaotic. Chaos in classical systems is characterized by the fact that infinitesimally small perturbations of the initial conditions have large effects at later times. For quantum systems whose classical limit is chaotic according to this definition it is known that the eigenenergy differences follow the same statistical distribution as the eigenvalue distances of Gaussian random matrices. Quantum chaos, in the sense of "chaos in quantum systems", can hence be defined via the statistics of energy eigenvalues. However, since the spectrum on its own is not sufficient to fully determine a quantum system, one can expect the eigenstates to reveal further characteristics of quantum chaos, beyond spectral properties.

In the present thesis, we investigate in detail how quantum chaos manifests itself in the eigenstate structure, characterized by the eigenstates' fractal dimensions in certain natural basis sets of the system. As a model, we use the Bose-Hubbard Hamiltonian, which describes bosons on a lattice that can tunnel between neighbouring lattice sites and interact locally with each other. At the energies, tunneling strengths, and interaction strengths for which the system is quantum-chaotic according to spectral statistics, the eigenstates delocalize among the states of both natural basis sets, in the limit of large system size (i.e., large numbers of particles and sites). Simultaneously, the fluctuations of the fractal dimensions among close-in-energy eigenstates decrease drastically and show qualitatively basis-independent properties. Furthermore, the boundaries of the quantum-chaotic region are reflected in the eigenstates by strongly asymmetric distributions of the fractal dimensions.

In the quantum-chaotic region, we compare the localization properties of the eigenstates with the corresponding predictions for Gaussian random matrices and for so-called embedded random-matrix ensembles, which, in contrast to the Gaussian random matrices, reproduce the two-body nature of the Bose-Hubbard model. The mean and the variance of the fractal dimensions are excellently well described by these two ensembles. Nevertheless, as system size grows, the full probability distributions of the eigenstate fractal dimensions of the Bose-Hubbard Hamiltonian becomes ever more distinguishable from that of random matrices, such that distinctive features of the Bose-Hubbard model remain accessible even for infinite system sizes.

Finally, we examine how particle indistinguishability affects the emergence of quantum chaos, and observe that the latter is weaker the more distinguishable the bosons are from each other.

Publications

The following publications are based on parts of this work:

- L. Pausch, E. G. Carnio, A. Rodríguez, and A. Buchleitner, “Chaos and Ergodicity across the Energy Spectrum of Interacting Bosons, Phys. Rev. Lett. **126**, 150601 (2021).
- L. Pausch, E. G. Carnio, A. Buchleitner, and A. Rodríguez, “Chaos in the Bose-Hubbard model and random Two-Body Hamiltonians”, New J. Phys **23**, 123036 (2021).

The author acknowledges support by the state of Baden-Württemberg through bwHPC and by the German Research Foundation (DFG).

Acknowledgements

Even though in the end it will be only me who gets a PhD title for my work, many more people actually contributed in one way or another to the successful completion of this project. First of all, I would like to thank my PhD supervisor Andreas Buchleitner. The German word for PhD supervisor, Doktorvater, literally translates to “doctoral father”, which in my opinion gives a very good description of Andreas’s way of supervising my thesis. Not only did I profit a lot from our scientific discussions, he also got me in contact with researchers from all over the world, by sending me to conferences directly from the beginning of my PhD project, as well as by inviting various guests to the group seminars. And once, when I wrongfully mistrusted the scientific value of my results, he helped me regain confidence.

The most direct impact on my project certainly needs to be attributed to my supervisors Alberto Rodríguez and Edoardo Carnio. Our weekly meetings and discussions helped me a lot to gain a deeper understanding of the research topics and constantly provided new ideas. Even though I sometimes reacted with a certain annoyance to their strong striving for a complete understanding even of smaller questions, I am now very thankful, since this clearly improved the content of my thesis and also my work as a scientist. Thank you both also for carefully proofreading this thesis several times and for your very helpful suggestions to improve it!

Specifically for the research on the interplay of chaos and particle distinguishability, I am very grateful for many fruitful discussions with Eric Brunner, Gabriel Dufour, Kabir Njoya and Christoph Dittel. In particular, I benefited a lot from Eric’s and Gabriel’s expertise on (partially) distinguishable particles.

I would furthermore like to thank Gislinde Bühler and Susanne Trauth for helping me with any administrative issues, and the IT group of the physics institute—Gerald Endres, Matthew Wyneken, Patrick Hacker and Khalil Rehmani—for their support with software and hardware problems. Moreover, I thank the group as a whole. It was really a pleasure to work with you and to enjoy the friendly atmosphere on the ninth floor.

Of course, to perform good scientific work one also needs some time to recreate. I am very grateful to my current and former flatmates, my hiking and running friends, my fellow choir singers, the KHG people in Freiburg and Konstanz, my “coffee group” of fellow students from my undergraduate studies, my longest friends Winni/Merlin/Simon/Flo and every other friends of mine. A special thanks goes to my parents and my sister who were always willing to listen to my problems and support me in every possible way.

Errata

As of 19th July 2022, the author became aware of the following errors and typos in the submitted version of the present thesis:

- page 15, line 11: replace “Conditions” by “For $\mathcal{N} = 2$, conditions”
- page 15, line 13: after “up to an energy scale v that can be set to $v = 1$” add “and up to a constant shift in energy which is here neglected”
- page 32, caption of Figure 2.6: before “for $N = L = 5$” add “, on the full Hilbert space”
- page 34, line 16: after “governing the classical Hamiltonian” add “at fixed scaled energy”
- page 40, line 5: replace “Appendix A.2.1” by “Appendix A.2.3”
- page 41, line 21: replace “as above” by “as on the facing page”
- page 48, line 16: add a comma after “edges and”
- page 56, line 20: add a comma after “populate the same site and”
- page 140: Reference [169] is now published as C. Berke, E. Varvelis, S. Trebst, A. Altland, and D. P. DiVincenzo, “Transmon platform for quantum computing challenged by chaotic fluctuations”, Nat. Commun. **13**, 2495 (2022).

Contents

Chapter 1.

Introduction

1.1. Classical and Quantum Chaos

In classical mechanics, research on chaos dates back at least to the works on celestial mechanics by Henri Poincaré around the year 1900 [1], who theoretically showed the existence of complicated orbits that are very easily distorted by perturbations. Since then, chaos has been intensely studied in classical [2–8] and later also in quantum systems [5, 6, 8–14]. In classical and quantum mechanics, chaos is a phenomenon of single-particle as well as of many-particle systems and is found, for instance, in heavy atomic nuclei [15–18], multi-electron atoms [19], the hydrogen atom in a strong magnetic field [20, 21] and billiards of certain shapes [7, 12, 13, 22]. The latter are single-particle systems in which the particle moves along straight lines in a confined two-dimensional domain and bounces elastically whenever it hits the boundary, like a ball on a billiard table. Figures 1.1(a)–(c) show three examples of billiards. While the motion on the rectangular billiard (a) is regular (non-chaotic), the stadium billiard (b) and the Sinai billiard (c) are chaotic as classical [23, 24] and as quantum systems [12, 22, 25, 26]. In the quantum domain, the chaotic nature of the billiards is reflected in a rather involved structure of their quantum eigenstates as compared to the regular case, as shown in Figures 1.1(d) and (e) (the latter: reproduced from Reference [27]).

Classically, chaotic dynamics are characterized by an exponentially strong influence of infinitesimally small changes of the initial conditions [3, 4, 7]. Related to chaos is the concept of ergodicity [3, 6, 7], i.e., the emergence of classical trajectories that uniformly visit all available phase space throughout their time evolution. These two concepts are, however, not equivalent. For instance, the uniform motion of a single particle on a ring is ergodic in the phase-space region defined by a constant momentum, since each trajectory uniformly passes through all positions along the ring, but it is not chaotic, since two trajectories with slightly different initial positions and momenta deviate from each other just linearly in time.

In quantum mechanics, a similar definition of chaos via exponential sensitivity of the dynamics to infinitesimally small perturbations of the initial conditions is intricate, since positions and momenta are well defined only up to the order of $\hbar$, due to Heisenberg's uncertainty principle. Instead, random matrices yield a very powerful characterization of

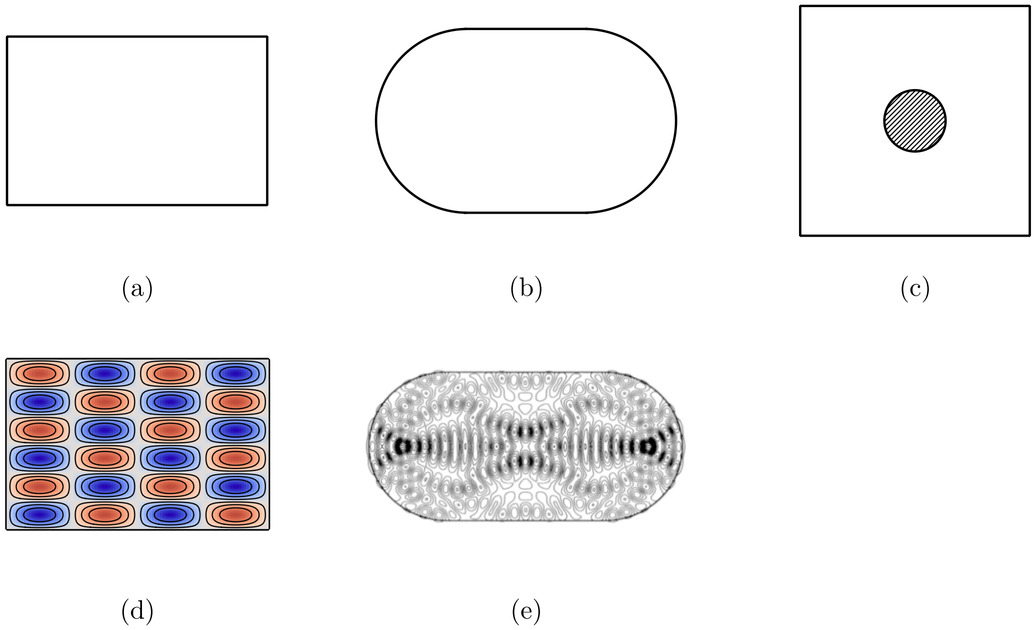

(a) (b) (c)

(d) (e)

Figure 1.1: Examples of regular (non-chaotic) (a) and chaotic (b), (c) billiards, and contour lines of exemplary eigenfunctions of the rectangular (d) and the stadium billiard (e). The shaded area in (c) is not part of the billiard area. Subfigure (e) is reprinted with permission from S. Tomsovic and E. J. Heller, “Semiclassical construction of chaotic eigenstates”, Phys. Rev. Lett. **70**, 1405 (1993), Copyright 1993 by the American Physical Society.

quantum chaos. Random matrices were first introduced in physics by Wigner, to describe the excitation spectra of complex nuclei [15–17]. Apart from nuclear spectra, random-matrix theory has turned out to be of great use also for other fields of mathematics and physics [28, 29], such as number theory [30–32], econophysics [33, 34] or disordered systems [35]. In the field of quantum chaos, it was shown that the spectra of quantum systems with a fully chaotic classical limit (for the symbolic limit “$\hbar \to 0$”, which will be qualified in Section 2.2.1) follow the statistics of Gaussian random-matrix ensembles [36–39], which are a model for random Hamiltonians. In contrast, the spectra of quantum systems with a strictly regular classical limit are, in general, well described by Poisson statistics [40, 41]. These two limiting properties have thus been taken as a definition of quantum chaos and regularity, respectively, even in cases where a well-defined classical limit is not available.

While quantum chaos can thus be identified by spectral properties only, the spectrum does not fully determine the dynamics of a quantum system, but further knowledge of the energy eigenstates is needed [42]. To date, various slightly differing concepts of quantum-chaotic eigenstates are used in the literature. For instance, quantum chaos in the eigenstates has been characterized by their compliance with the eigenstate thermalization hypothesis [43–47]. This hypothesis, introduced to explain the emergence of statistical mechanics from quantum dynamics in closed systems, states that the expectation values of local observables O in the energy eigenstates agree with the microcanonical ensemble average of O at the corresponding energy, up to fluctuations decaying with system size [8, 43, 44]. Alternatively, quantum-chaotic eigenstates have been defined by their agreement with random-matrix predictions, for instance in terms of their entanglement properties [48, 49] or according to their structural features in certain natural bases of the system [11, 14, 50–56].

When investigating the structure of quantum states, the concept of multifractality [57–60] turns out to play an important role. In the limit of infinite Hilbert space dimension, multifractal states participate of a diverging number of basis states, which is nevertheless a vanishing fraction of the full basis. This property has been found to be a generic feature of many-particle ground states [61, 62] and of the eigenstates in many-body localized systems [63–65], i.e., in disordered systems of interacting particles that exhibit an insulating phase in their excitation spectrum [66–71]. Multifractal analysis has been successfully applied to characterize the Anderson transition [72, 73] between localized and delocalized single-particle states in a disordered lattice [73–78], to describe ground-state phase transitions in many-body systems [79–81], and to analyse avoided crossings in a many-particle energy spectrum [82, 83].

Recently, the multifractal properties of the eigenstates of quantum-chaotic spin systems were investigated [84], finding qualitative agreement with the predictions of random-matrix theory as well as quantitative deviations. Such differences could, however, be expected, since the Gaussian random-matrix ensembles are ergodic by construction [85], while classical dynamical systems typically show both chaotic and regular behaviours, depending on the initial conditions (mixed phase space) [86], a feature that is also found to be reflected by the time evolution [87–90] and the eigenstates [88, 91, 92] of the corresponding quantum models.

Specifically for chaotic many-particle quantum systems, where typically only few particles interact collectively with each other, further deviations from the Gaussian random-matrix ensembles would be expected, since the latter do not capture such few-body nature of the interactions. So-called embedded ensembles [93–98] have been introduced to describe many-body quantum chaos more accurately. These ensembles are random, like the Gaussian random-matrix ensembles, and they involve only few-body interactions, like typical many-particle systems.

Besides interactions, also particle indistinguishability has a large impact on many-particle dynamics via interference effects [99–103], which, e.g., influence the time evolution of quantum expectation values for few-particle observables and of their corresponding fluctuations [100, 104–106]. In the context of quantum chaos, spectral statistics in a system of partially distinguishable bosons were reported in Reference [105]. Nevertheless, how particle indistinguishability is related to quantum chaos in many-body systems and whether this relation may set many-particle quantum chaos apart from single-particle quantum chaos remain largely unanswered questions so far.

In recent years, the existence and absence of a quantum-chaotic regime has been intensely investigated, particularly in many-particle systems subject to strong interactions and disorder [66–71]. Typical models are given by spin chains [107–110] and by interacting particles on a lattice [111–113]. These systems are also of high experimental relevance since they can be implemented in a highly controllable manner with ultracold atoms in optical lattices [114–129]. Specifically, on-site interacting bosons in a lattice described by the Bose-Hubbard Hamiltonian provide a paradigmatic model for which traces of quantum chaos have been found theoretically [56, 130–143] and experimentally [116, 117, 124, 127, 129]. These results are presented in more detail in the following section.

1.2. Quantum Chaos in the Bose-Hubbard Hamiltonian

In the Bose-Hubbard model of N bosons on L lattice sites, the bosons can tunnel between nearest-neighbouring sites, with tunneling strength J, and interact with each other on the same lattice site, with interaction strength U. When J and U are of comparable magnitude, signatures of quantum chaos have been found theoretically with respect to various figures of merit: Energy statistics was investigated via the distributions of level spacings s and of level spacing ratios r for one spatial dimension [131, 135, 141] and also for small two-dimensional Bose-Hubbard lattices [142], finding very good agreement with the statistics of the corresponding Gaussian random-matrix ensemble. One of the first examples of these results is shown in Figure 1.2(a) (reproduced from Reference [131]), where the cumulative distribution function $I(s)$ of level spacings is displayed in comparison with the predictions from random-matrix theory and from Poisson statistics. For the scaled tunneling strength $J/UN = 0.292$ shown in this figure, the spectral statistics of a single symmetry-induced subspectrum and of two such subspectra are in good agreement with the corresponding random-matrix predictions, while they clearly deviate from Poisson statistics.

Another example is shown in Figure 1.2(b) (reproduced from Reference [141]), where the numerically calculated distribution $P_{\mathrm{num}}(r)$ of level spacing ratios for the Bose-Hubbard Hamiltonian is compared to the random-matrix prediction $P_{\mathrm{RMT}}(r)$, which is known approximately analytically [144]. Here, the distance of these two distributions is quantified via the L^1 norm of their difference,

$$\|P_{\mathrm{num}} - P_{\mathrm{RMT}}\| = \int_0^1 |P_{\mathrm{num}}(r) - P_{\mathrm{RMT}}(r)| \, \mathrm{d}r. \tag{1.1}$$

This distance becomes minimal for intermediate values $2 \lesssim UN/J \lesssim 20$. For the small two-dimensional lattices also the number variance $\Sigma^2(\ell)$, which is very sensitive to long-range correlations in the spectrum [29], was examined as a function of the energy interval width ℓ, finding good agreement with the random-matrix prediction [142]. Furthermore,

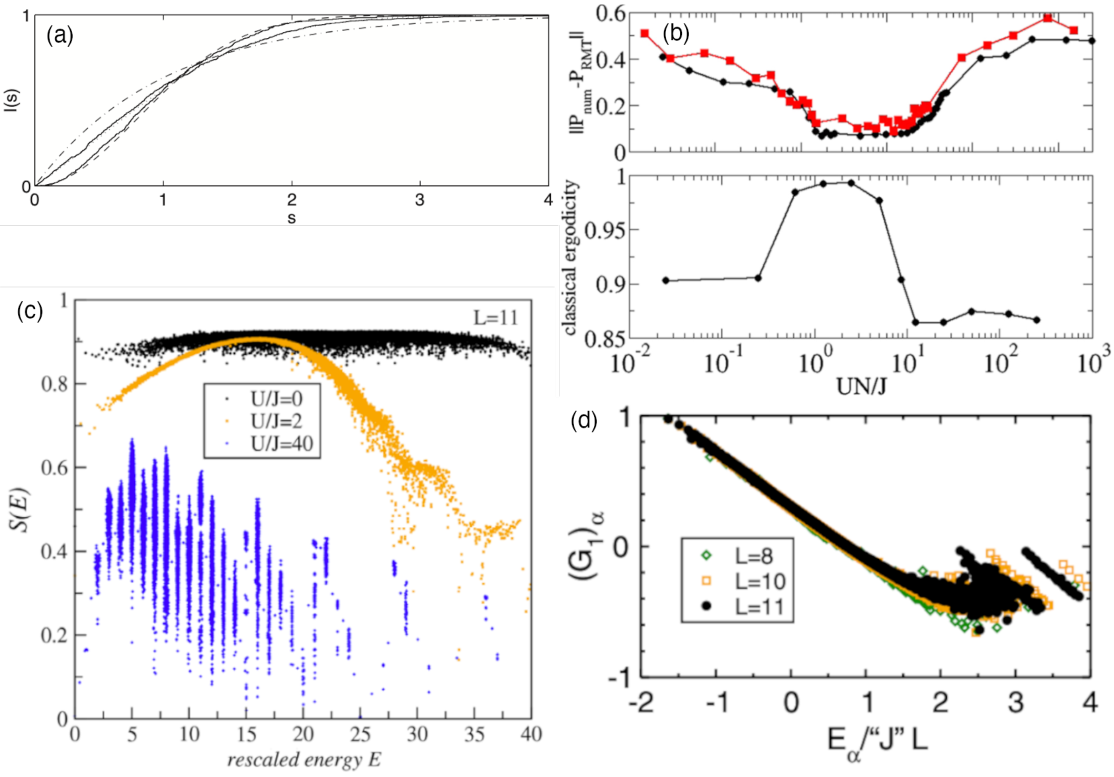

Figure 1.2: Signatures of quantum chaos in the Bose-Hubbard Hamiltonian: (a) cumulative level spacing distribution $I(s)$ for $N = L = 8$, $J/UN = 0.292$, and one and two symmetry-induced subspectra of the Bose-Hubbard model (solid lines) compared to Poisson statistics (dash-dotted), and to random-matrix predictions for one (dashed) and two independent spectra (dotted), (b) distance between the Bose-Hubbard distribution $P_{\mathrm{num}}(r)$ of level spacing ratios r and the random-matrix distribution $P_{\mathrm{RMT}}(r)$ [Equation (1.1)] for $L = 5$, $N = 15$ (red squares) and $L = 5$, $N = 25$ (black circles), and classical ergodicity for $L = 5$, $N = 25$, (c) Shannon entropy S [Equation (1.2)] of eigenstates in the eigenbasis of the interaction term, (d) expectation value G_1 of the tunneling operator [Equation (1.3)] versus eigenenergy E_α.
Copyright information: (a) reproduced from Reference [131], courtesy of A. Buchleitner, (b) reprinted from R. Dubertrand and S. Müller, "Spectral statistics of chaotic many-body systems", New J. Phys. **18**, 033009 (2016) under the terms of the CC BY 3.0 license], (c) © IOP Publishing Ltd and Sissa Medialab, reproduced from C. Kollath et al., "Statistical properties of the spectrum of the extended Bose-Hubbard model", J. Stat. Mech. **2010**, P08011 (2010) by permission of IOP Publishing, all rights reserved, (d) reprinted with permission from G. Biroli et al., "Effect of Rare Fluctuations on the Thermalization of Isolated Quantum Systems", Phys. Rev. Lett. **105**, 250401 (2010), Copyright 2010 by the American Physical Society.

averages of the level spacing ratio r have been computed locally in the spectrum for specific values of the interaction and tunneling strengths, revealing that the spectral statistics differ from those of Gaussian random matrices at the edges of the spectrum [135]. Spectral chaos was even demonstrated to be correlated with the emergence of classical ergodicity [141], as shown in Figure 1.2(b). Here, the degree of classical ergodicity is quantified by comparing the full energy shell, i.e., the set of all phase-space points with the same energy, to the amount of phase space actually visited by the trajectories of the corresponding classical system for $N \gg 1$.

In terms of the eigenstates, Shannon information entropies

$$S = -\sum_{\alpha} |\psi_\alpha|^2 \ln |\psi_\alpha|^2 , \tag{1.2}$$

of eigenstate intensities $|\psi_\alpha|^2$ in a given basis have been calculated as averages over all eigenstates in the eigenbases of the Hamiltonian's tunneling and interaction term [131] as well as for individual eigenstates [131, 135]. Figure 1.2(c) (reproduced from Reference [135]) shows the Shannon entropy of individual eigenstates as a function of energy for several values of U/J. Similarly, participation ratios and entanglement entropies of eigenstates [140], as well as the probability distribution of the eigenstate amplitudes [56] have been considered. All these quantifiers reveal that the eigenstates in the center of the spectrum are on average distributed over a large portion of the basis states once U and J are of similar magnitude.

One- and two-particle observables, such as the tunneling operator [134, 136, 137, 139], the occupation numbers of the lattice sites [137, 139], the occupation numbers of single-particle momentum states [136], and the correlation between on-site occupation numbers [137, 139], have been investigated via their expectation values in energy eigenstates [134, 136], their eigenstate-to-eigenstate fluctuations [137] and via their off-diagonal matrix elements in the energy eigenbasis [139]. These observables have been found to agree with certain consequences of the eigenstate thermalization hypothesis [8, 43, 44] (as introduced on page 3). As an example, Figure 1.2(d) (reproduced from Reference [134]) shows the expectation value

$$G_1 = \frac{1}{L} \sum_{j} \left\langle a_j^\dagger a_{j+1} \right\rangle \tag{1.3}$$

of the scaled tunneling operator with respect to the energy eigenstates, for $U = J$. Here, $a_j^{(\dagger)}$ is a bosonic operator that annihilates (creates) a boson localized at the jth site of the lattice. For energies below $E/JL \lesssim 1.5$, this expectation value becomes an approximately smooth function of the energy accompanied by small fluctuations, in agreement with the eigenstate thermalization hypothesis.[1]

---

[1] Note that the eigenstate thermalization hypothesis entails the even stronger prediction that this smooth function of energy is identical to the microcanonical ensemble average, a statement that goes beyond the results presented in Reference [134] for G_1.

Also from the time evolution after a quench, traces of quantum chaos have been observed in the Bose-Hubbard model [130, 132–134, 136, 138]. Quenching from an interaction-dominated regime to a tunneling-dominated regime, or the other way around, leads to nonequilibrium steady states with memory of the initial state, while quenching to intermediate interactions gives approximately thermal values of correlations [132]. In the latter regime, Bloch oscillations were found to decay irreversibly on short time scales [130]. Also the time-dependent expectation values of observables fluctuate around values that are reasonably well described by the canonical and microcanonical ensemble of statistical mechanics [138]. Furthermore, dynamical signatures of quantum chaos were also found in the survival probability of the initial state [143], even without resolving the symmetries of the system.

Apart from these theoretical results, signatures of quantum chaos in the Bose-Hubbard Hamiltonian have also been found experimentally in cold-atom systems [116, 117, 124, 127, 129]. An initially confined cloud of bosons was shown to expand diffusively for intermediate values of U/J, while ballistic dynamics are observed for dominating interaction or dominating tunneling [116]. The theoretical result of Reference [130] on the irreversible decay of Bloch oscillations has also been confirmed experimentally [117]. Dynamics after a quench show that the Bose-Hubbard system reaches a steady state that locally, i.e., in subsystems of few sites, appears thermal, in agreement with the eigenstate thermalization hypothesis and as measured by the particle number distribution on individual sites, while the system globally remains in a pure, and hence nonthermal, state [124]. In this regime, the entanglement entropy of few-site subsystems with the remaining lattice increases linearly with the number of sites and is in good agreement with the thermal entropy of statistical mechanics [124, 129]. Furthermore, also the correlations between on-site occupation numbers were shown to agree with the predictions for a thermal ensemble [127]

Additionally, the Bose-Hubbard model has been used as a paradigmatic model to study theoretically the impact of particle indistinguishability on many-body dynamics in interacting systems [100, 104–106]. It was shown that the expectation values of on-site occupation numbers and the corresponding variances, as functions of time, fluctuate the strongest for indistinguishable particles [100, 105, 106]. The influence of particle indistinguishability on the dynamics seems to be more prominent for intermediate values of U and J [100, 105], albeit with a strong dependence on the initial configuration. In addition, energy level statistics in the subspaces induced by particle permutation symmetry were investigated for specific values of the interaction and tunneling strengths, finding increasingly better agreement with the predictions from random-matrix theory as the interaction strength is increased from small to intermediate values [105].

Despite the abundant literature, quantum chaos in the Bose-Hubbard Hamiltonian has not been investigated thoroughly as a joint function of energy, interaction, and tunneling strength so far. Furthermore, spectral chaos in the Bose-Hubbard model has not been unambiguously correlated with the eigenvector structure, which in turn has not been connected systematically to Gaussian random-matrix theory and to the more refined embedded ensembles. Moreover, while some results about the influence of particle indistinguishability on the dynamics of observables and on spectral chaos are known, the exact relation between particle indistinguishability and many-body quantum chaos remains unclear. These topics will be addressed in the following chapters.

1.3. Objectives and Outline of the Thesis

In this thesis, we use concepts from multifractal analysis to systematically relate spectral signatures of quantum chaos in the Bose-Hubbard Hamiltonian to the structure of the corresponding many-body eigenstates. In this way, we intend to identify the correct parameter controlling the emergence of quantum chaos, as well as construct an accurate energy-resolved picture of the quantum-chaotic domain. We compare the eigenstates' structure in the quantum-chaotic region to predictions from the standard Gaussian and embedded random-matrix ensembles, and unveil the asymptotic properties of the eigenstates for increasingly larger Hilbert spaces. In particular, we scrutinize whether in the quantum-chaotic regime specific features of the Bose-Hubbard model remain accessible as the thermodynamic limit of infinite system dimension is approached, or whether, on the contrary, only the universal behaviour dictated by random-matrix theory prevails. Additionally, by generalizing the Hamiltonian to include distinguishable bosons, we investigate the interplay of many-body quantum chaos and particle indistinguishability. Parts of the research presented here are already published in References [145, 146].

The remainder of this thesis is organized in the following way: In Chapter 2 the basic concepts and methods applied throughout this thesis to investigate quantum chaos are presented. We also introduce in this chapter the Bose-Hubbard Hamiltonian and discuss its properties in detail. In Chapter 3, we examine markers of quantum chaos in the spectrum and the eigenstates of this model, as functions of the energy and of the interaction and tunneling strengths. These quantum-chaos signatures are linked to Gaussian random matrices and to an appropriate embedded ensemble in Chapter 4, finding system-specific characteristics on top of the universal features predicted by random-matrix theory. Chapter 5, which includes results obtained in cooperation with Eric Brunner and Dr. Gabriel Dufour, addresses the impact of particle indistinguishability on the emergence of quantum chaos. We discuss our results and conclude in Chapter 6.

Chapter 2.

Theoretical Background and Methods

The aim of this chapter is to give an overview of the theoretical foundations and methods developed in the literature and used throughout this thesis. The focus will be laid on the specific aspects relevant for the scope of our work. For topics going beyond those presented here, references to further literature are given at appropriate locations throughout the text.

2.1. Classical Chaos and Integrability

In this section, we briefly discuss some aspects of classical chaos, following mainly References [3, 4, 6, 7, 147], before we turn to the implications of classical chaos on the quantum realm in the next section.

Classically, the state of a mechanical system with n degrees of freedom is described by a point $(\boldsymbol{q}, \boldsymbol{p}) = (q_1, \ldots, q_n, p_1, \ldots, p_n)$ in the $2n$-dimensional phase space of generalized positions q_i and generalized momenta p_i. In the absence of dissipative forces, the dynamics is governed by Hamilton's equations of motion

$$\dot{q}_i = \frac{\partial H}{\partial p_i}, \qquad\qquad \dot{p}_i = -\frac{\partial H}{\partial q_i}, \tag{2.1}$$

where $H = H(\boldsymbol{q}, \boldsymbol{p})$ is the Hamiltonian function and the dot denotes time derivative. With these equations, the (total) time derivative of a function $A(\boldsymbol{q}, \boldsymbol{p})$ is

$$\frac{\mathrm{d}A}{\mathrm{d}t} = \sum_i \dot{q}_i \frac{\partial A}{\partial q_i} + \sum_i \dot{p}_i \frac{\partial A}{\partial p_i} = \{A, H\}\,, \tag{2.2}$$

with the Poisson bracket

$$\{A, B\} := \sum_i \frac{\partial A}{\partial q_i}\frac{\partial B}{\partial p_i} - \sum_i \frac{\partial B}{\partial q_i}\frac{\partial A}{\partial p_i}. \tag{2.3}$$

To precisely describe chaos in such a mechanical system, one defines Lyapunov exponents as

$$\lambda(\boldsymbol{x}) = \lim_{t\to\infty} \lim_{|\delta \boldsymbol{X}_0(\boldsymbol{x})|\to 0} \frac{1}{t} \ln \frac{|\delta \boldsymbol{X}_t(\boldsymbol{x})|}{|\delta \boldsymbol{X}_0(\boldsymbol{x})|}, \tag{2.4}$$

where $\boldsymbol{x} = (\boldsymbol{q}, \boldsymbol{p})$ is a point in phase space, $\delta\boldsymbol{X}_0(\boldsymbol{x}) = \boldsymbol{x}' - \boldsymbol{x}$ is the initial displacement between $\boldsymbol{x}$ and another phase-space point $\boldsymbol{x}'$ and $\delta\boldsymbol{X}_t(\boldsymbol{x})$ is the corresponding difference after evolution for time t according to Equations (2.1). Here, the limit $\lambda(\boldsymbol{x})$ can depend on the initial orientation of $\delta\boldsymbol{X}_0(\boldsymbol{x})$, such that each point in phase space can be characterized by several Lyapunov exponents. Positive Lyapunov exponents roughly correspond to exponential growth $|\delta\boldsymbol{X}_t(\boldsymbol{x})| \,/\, |\delta\boldsymbol{X}_0(\boldsymbol{x})| \sim e^{\lambda(\boldsymbol{x})t}$ as $t \to \infty$, while negative values of $\lambda(\boldsymbol{x})$ signal exponential decay towards 0, and $\lambda(\boldsymbol{x}) = 0$ can correspond to any type of sub-exponential growth or decay.

We consider systems as *chaotic* if their Lyapunov exponents for phase-space points with bounded[1] trajectories are positive for typical initial conditions, i.e., for all phase-space points $\boldsymbol{x}$ and orientations of $\delta\boldsymbol{X}_0(\boldsymbol{x})$ except for a set of measure zero [7]. In other words, two solutions of Equations (2.1) starting from infinitesimally close initial conditions depart from each other exponentially in time in a chaotic system. Note that the infinitesimal nature of the difference of initial conditions is crucial here, since otherwise the boundedness of the trajectories would prevent them from exponentially departing from each other. We understand systems as *regular* if they are not chaotic according to this definition. Typical Hamiltonian systems are neither fully regular nor fully chaotic, but exhibit both types of dynamics for initial conditions in different regions of phase space (“mixed phase space”) [86]. Note that chaos in a dynamical system can be defined using quantifiers other than the Lyapunov exponents, which might, however, yield non-equivalent definitions of chaos. The interested reader may find a discussion of further concepts beyond the scope of this work, such as Kolmogorov-Sinai entropies, C-systems, Bernoulli systems or mixing, for example in References [3, 4, 6–8].

An important property related to classical chaos is *ergodicity*, which, however, does not necessarily imply chaos in the sense of Lyapunov exponents as described above [3, 6–8]. In an ergodic system, the phase-space average of any integrable function f of phase-space points $\boldsymbol{x} = (\boldsymbol{q}, \boldsymbol{p})$ equals the long-time temporal mean of f along a trajectory with typical initial conditions $\boldsymbol{x}(0)$,

$$\int f(\boldsymbol{x})\, \mathrm{d}^{2n}x = \lim_{T\to\infty} \frac{1}{T} \int_0^T f(\boldsymbol{x}(t))\, \mathrm{d}t. \tag{2.5}$$

Here, “typical initial conditions” mean that $\boldsymbol{x}(0)$ may be any point of phase space except for a set of measure zero. In ergodic systems, typical trajectories hence come arbitrarily close to any point in phase space and therefore need to cover a phase-space volume of the same dimension as the full phase space. Note that ergodicity is usually quite difficult to prove exactly [3, 4, 7].

A relevant concept that is closely related to regular systems is *integrability*. We speak of an integrable system, if it has as many independent conserved quantities in invo-

---

[1] I.e., the trajectory starting at $\boldsymbol{x}$ for time $t = 0$ stays within a ball of finite radius R for all times. This property is introduced to rule out trivial cases such as the Hamiltonian $H = pq$ with trajectories $(q(t), p(t)) = (q_0 e^t, p_0 e^{-t})$, which does not show typical features related to chaos such as ergodicity as defined in Equation (2.5), despite having positive Lyapunov exponents for typical initial conditions.

lution (integrals of motion) as degrees of freedom [6, 7, 147], otherwise we speak of a nonintegrable system. Here, we define a quantity $A = A(\boldsymbol{q}, \boldsymbol{p})$ as conserved if it fulfils

$$\frac{\mathrm{d}A}{\mathrm{d}t} = \{A, H\} = 0. \tag{2.6}$$

Independence entails that none of the conserved quantities can be expressed as a function of the others, and involution means that the dynamics generated by the conserved quantity A_k, treating it as a "Hamiltonian", leaves the other conserved quantities A_l unchanged:

$$\{A_l, A_k\} = 0. \tag{2.7}$$

Even if the A_k are independent, this involution property is not necessarily fulfilled. Consider, for instance, the free particle in three dimensions: Here, all three components of the angular momentum are conserved and obviously independent of each other, but involution is not fulfilled, since

$$\{L_x, L_y\} = L_z, \qquad \{L_y, L_z\} = L_x, \qquad \{L_z, L_x\} = L_y.$$

In contrast to chaotic systems, where ergodicity implies that typical trajectories in the $2n$-dimensional phase space fill a volume of dimension $2n$, trajectories in an integrable system are restricted to n-dimensional manifolds given by the conditions

$$A_k = c_k, \qquad k = 1, \dots, n, \tag{2.8}$$

where c_k are constants. The involution condition restricts the shape of these manifolds to n-dimensional (deformed) tori [2, 4]. The time evolution on these tori can be described via action-angle variables $(I_1, \dots, I_n, \theta_1, \dots, \theta_n)$ as

$$I_k(t) = I_k(0), \qquad \theta_k(t) = \omega_k t + \theta_k(0), \tag{2.9}$$

with $\omega_k = \partial H / \partial I_k$, i.e., the trajectories show, in general, a quasiperiodic motion on the torus surface with angular velocities ω_k [2, 4, 7]. According to Equations (2.9), two trajectories in an integrable system depart from each other maximally linearly with time. Consequently, integrable systems are regular.

As an illustrative example, consider the Hamiltonian

$$H(p, \theta, t) = \frac{p^2}{2} + K\cos(\theta) \sum_{n=-\infty}^{\infty} \delta(t - n), \qquad p, \theta \in [0, 2\pi], \tag{2.10}$$

which is known as the *standard map* and which describes a particle on a ring subject to a periodic kicking force of strength K [4, 7, 12, 13]. The corresponding equations of motion are

$$\dot{p} = K\sin(\theta) \sum_{n=-\infty}^{\infty} \delta(t - n), \qquad \dot{\theta} = p, \tag{2.11}$$

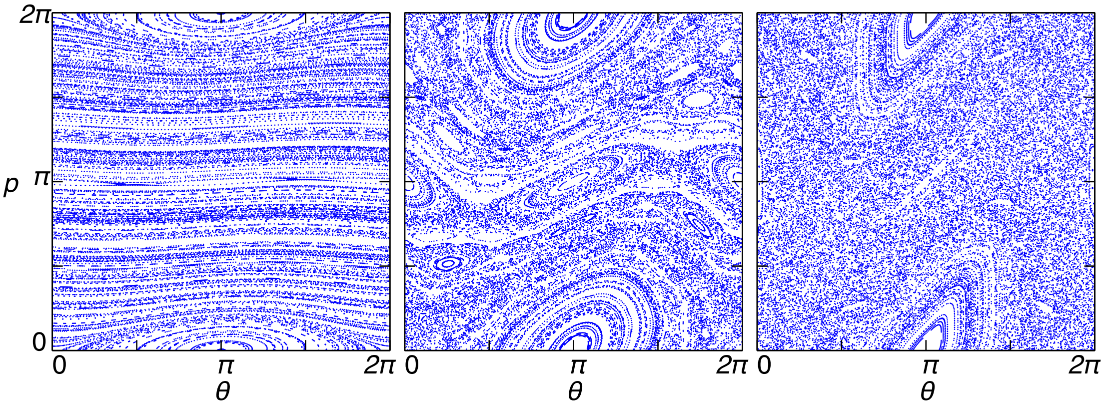

Figure 2.1: Stroboscopic picture of the dynamics of the standard map, Equation (2.10), for 300 randomly chosen initial configurations and 100 time steps for each initial configuration, for $K = 0.1$ (left), $K = 1$ (center) and $K = 2$ (right).

which at integer times $t = n$ yield the following momentum and angle

$$p_n = p_{n-1} + K \sin(\theta_{n-1}) \mod 2\pi, \qquad \theta_n = \theta_{n-1} + p_n \mod 2\pi. \tag{2.12}$$

The parameter K is known to tune between fully regular dynamics for $K = 0$ and increasingly chaotic motion for $K > 0$ [7, 12, 13]. Figure 2.1 shows a visualization of the phase-space dynamics for $K = 0.1$, $K = 1$ and $K = 2$ via the orbits

$$\{(\theta_n, p_n) \,:\, n = 0, 1, \dots, 100\},$$

for 300 randomly chosen initial configurations (θ_0, p_0). In such a stroboscopic picture [4, 7], the orbits of regular integrable motion reproduce the n-dimensional toroidal structure (circles for $n = 1$) of the corresponding trajectory, while the orbits of chaotic motion fill higher-dimensional portions of phase space without resembling any tori. Note that in the representation of phase space as a two-dimensional plane, where $p = 0$ and $\theta = 0$ have to be identified with $p = 2\pi$ and $\theta = 2\pi$, respectively, tori can appear as lines instead of circles. As expected, the picture shows mainly toroidal structures for $K = 0.1$, while increasingly larger granular chaotic regions emerge between the tori with increasing K, until these regions of chaos fill most of the picture for $K = 2$.

2.2. Quantum Chaos and Random Matrix Theory

2.2.1. Fundamental Concepts

When quantum effects come into play, chaotic and regular systems can no longer be distinguished from one another simply via the time evolution of trajectories with infinitesimally close initial conditions, since $\boldsymbol{q}$ and $\boldsymbol{p}$ can only be determined up to a finite phase-space volume $\sim \hbar^n$, according to Heisenberg's uncertainty principle. A very straightforward alternative approach to define chaos in the quantum domain would be to consider the dynamics of the corresponding classical systems. Here, correspondence means that the classical Hamiltonian function H_{class} is the limit of the quantum mechanical Hamilton operator H_{qu} upon formally sending $\hbar$ to 0, which in practice means that the typical actions S of the system fulfil $S/\hbar \to \infty$ [6, 148, 149]. Via this approach, we call a quantum system chaotic (regular), if its corresponding classical analog shows chaotic (regular) dynamics according to our discussion in the preceding section.[2] However, the classical limit might be difficult to obtain or might not even exist, for instance in nuclear systems with many constituents, where the exact forms of the interactions are very complicated. A definition of quantum chaos that is applicable also in these cases will be discussed in the next sections, where we introduce the concept of random matrices.

In contrast to the concept of chaos, the notion of conserved quantities and hence also of integrability directly translates from classical Hamiltonian mechanics to quantum mechanics via the replacement of Poisson brackets $\{\cdot,\cdot\}$ by (scaled) commutators $[\cdot,\cdot]/\mathrm{i}\hbar$: A time-independent observable A is conserved if its commutator with the Hamiltonian operator H vanishes,

$$[A, H] = 0, \tag{2.13}$$

that is, if the underlying Hilbert space of the system has a basis of common eigenstates $|\psi\rangle$ of A and H [42],

$$H\,|\psi\rangle = E\,|\psi\rangle\,, \qquad\qquad A\,|\psi\rangle = a\,|\psi\rangle\,, \tag{2.14}$$

with quantum numbers E, a. We speak of an integrable system if it has as many degrees of freedom n as independent conserved observables A_k that commute with each other, i.e., if n observables are sufficient to define a complete set of commuting observables. Hence, in an integrable system each eigenstate $|\psi\rangle$ of H can be described by a complete set of n “good” quantum numbers a_k such that

$$A_k\,|\psi\rangle = a_k\,|\psi\rangle\,, \tag{2.15}$$

and one can thus write

$$|\psi\rangle = |a_1, \ldots, a_n\rangle\,. \tag{2.16}$$

These quantum numbers a_k are the equivalent of the conserved actions I_k in classical integrable systems.

---

[2] Note, however, that signatures of classical chaos such as ergodicity [Equation (2.5)] emerge on infinite timescales only, such that one has to consider the simultaneous limits $\hbar \to 0$ and $t \to \infty$ to relate quantum and classical dynamics appropriately. Since here we are interested in the classical dynamics only, we may safely skip these details and refer the reader to Reference [148] for a thorough discussion of these two simultaneous limits.

2.2.2. Gaussian Random Matrices

A random matrix is a matrix in which all or at least some entries are random numbers. To describe quantum observables and unitary time evolution with different underlying symmetries, various ensembles of Hermitian and unitary random matrices have been introduced in the literature throughout the years; for an overview, see References [13, 29, 38, 150]. In the following, we discuss only the Gaussian random-matrix ensembles, which have turned out to be very powerful in the context of quantum chaos [13, 37, 38, 98, 150, 151].

The *Gaussian orthogonal, unitary and symplectic ensembles* (GOE, GUE, GSE) are models for random Hamiltonians H, that is, they provide a probability density P_{GxE} (with x = O, U or S) on a subset $\mathcal{M}$ of the set of $\mathcal{N} \times \mathcal{N}$ Hermitian matrices. Their defining properties are the stochastic independence of the individual matrix elements h_{ij} (except for symmetry constraints given by hermiticity and by the definition of $\mathcal{M}$),

$$P_{\mathrm{GxE}}(H) = \prod_{i,j} P_{\mathrm{GxE}}(h_{ij}), \tag{2.17}$$

and their invariance with respect to transformations $H \mapsto AHA^{-1}$ that leave the set $\mathcal{M}$ invariant,

$$P_{\mathrm{GxE}}(H) = P_{\mathrm{GxE}}(AHA^{-1}). \tag{2.18}$$

Particularly for GOE, the Hamiltonian H is drawn from the set of real symmetric matrices and the transformations that leave this set invariant are given by the orthogonal group $O(\mathcal{N})$. Choosing this subset of the full set of Hermitian matrices is motivated by the following: Generically, the time reversal operator T is an antiunitary operator, $\langle T\varphi|T\psi\rangle = \langle\varphi|\psi\rangle^*$, and it fulfils $T^2 = +1$ or $T^2 = -1$ [13, 98]. Now assume $T^2 = +1$ and furthermore that the Hamiltonian H is invariant under the action of T, i.e., $THT^{-1} = H$. Then, for an arbitrary state $|\varphi_1\rangle$ the state $|\psi_1\rangle := |\varphi_1\rangle + T|\varphi_1\rangle$ is an eigenstate[3] of T with eigenvalue 1,

$$T|\psi_1\rangle = T|\varphi_1\rangle + T^2|\varphi_1\rangle = T|\varphi_1\rangle + |\varphi_1\rangle = |\psi_1\rangle. \tag{2.19}$$

Now choose an arbitrary state $|\varphi_2\rangle$ orthogonal to $|\psi_1\rangle$ and define $|\psi_2\rangle = |\varphi_2\rangle + T|\varphi_2\rangle$. Then $T|\psi_2\rangle = |\psi_2\rangle$ and

$$\langle\psi_1|\psi_2\rangle = \langle\psi_1|\varphi_2\rangle + \langle\psi_1|T\varphi_2\rangle = 0 + \langle T\psi_1|T\varphi_2\rangle = \langle\psi_1|\varphi_2\rangle^* = 0. \tag{2.20}$$

Iterating this procedure, one can construct a complete orthogonal basis of the Hilbert space consisting of states $|\psi_i\rangle = T|\psi_i\rangle$. In this basis, the Hamiltonian is a real matrix:

$$\langle\psi_i|H|\psi_j\rangle = \langle T\psi_i|TH|\psi_j\rangle^* = \langle T\psi_i|HT|\psi_j\rangle^* = \langle\psi_i|H|\psi_j\rangle^*. \tag{2.21}$$

---

[3] Note that such eigenstates cannot be found for $T^2 = -1$, since then the states $|\psi\rangle$ and $T|\psi\rangle$ are always orthogonal to each other, $\langle\psi|T\psi\rangle = \langle T\psi|T^2\psi\rangle^* = -\langle T\psi|\psi\rangle^* = -\langle\psi|T\psi\rangle = 0$ [13].

Hence, time-reversal invariant random Hamiltonians with $T^2 = +1$ are generically real symmetric matrices and, consequently, GOE provides a suitable model for such Hamiltonians.

Other symmetry requirements with respect to time reversal and angular momentum lead to GUE, which is defined on the full set of complex Hermitian matrices with the unitary group $U(\mathcal{N})$ as the proper set of transformations, and to GSE, for which $\mathcal{M}$ is the set of so-called quaternion real matrices, which is invariant under the action of the symplectic group $Sp(\mathcal{N})$ [13, 29, 38, 98]. As we will show later, the physical model of interest in this thesis belongs to the symmetry class described by GOE. We will therefore focus only on GOE from now on, even though the properties of GUE and GSE are often very similar.

Conditions (2.17) and (2.18) uniquely define the probability density of GOE [13, 38, 98],

$$P_{\mathrm{GOE}}(H) \sim \exp\left(-\frac{\mathrm{Tr}(H^2)}{4v^2}\right) = \exp\left(-\sum_{i,j}\frac{h_{ij}^2}{4v^2}\right), \tag{2.22}$$

up to an energy scale v that can be set to $v = 1$. Writing this latter exponential as a product of exponentials for the individual matrix elements h_{ij} and using the symmetry constraint $h_{ij} = h_{ji}$,

$$\exp\left(-\sum_{i,j}\frac{h_{ij}^2}{4v^2}\right) = \prod_i \exp\left(-\frac{h_{ii}^2}{4v^2}\right)\prod_{j>i}\exp\left(-2\frac{h_{ij}^2}{4v^2}\right), \tag{2.23}$$

one can see that the numbers h_{ij} are independent Gaussian variables with mean

$$\mu(h_{ij}) = 0 \tag{2.24}$$

and variance

$$\sigma^2(h_{ij}) = (1 + \delta_{ij})v^2. \tag{2.25}$$

According to these properties, GOE random matrices are typically dense matrices with $h_{ij} \neq 0$ for all indices i, j.

A variable transformation from the matrix elements h_{ij} to the eigenenergies E_i and to $\mathcal{N}(\mathcal{N}-1)/2$ additional parameters that specify the eigenstates, followed by an appropriate integration, yields the ensemble-averaged density of states (the probability density of a single energy level) [13, 38, 98],

$$\bar{\rho}_{\mathrm{GOE}}(E) = \begin{cases} \frac{1}{2\pi v^2 \mathcal{N}}(4\mathcal{N}v^2 - E^2)^{1/2}, & |E| \leq 2\sqrt{\mathcal{N}v^2}, \\ 0, & |E| > 2\sqrt{\mathcal{N}v^2}. \end{cases} \tag{2.26}$$

This result, which describes the upper half of an ellipse with semiaxes $2\sqrt{\mathcal{N}v^2}$ and $1/\left(\pi\sqrt{\mathcal{N}v^2}\right)$, is known as the *Wigner semicircle law.*

2.2.3. Spectral Statistics as an Identifier of Quantum Chaos

An important feature of the Gaussian ensembles is given by the statistical properties of their level spacings

$$s_n = E_{n+1} - E_n, \tag{2.27}$$

where E_n is the nth eigenenergy (in ascending order) of the Hamiltonian H. For $\mathcal{N} = 2$, the distribution $P_{\mathrm{GOE}}(s)$ can easily be deduced [13, 98]. In this case, the two eigenvalues $E_\pm$ of H fulfil

$$E_+ + E_- = \operatorname{Tr} H = h_{11} + h_{22}, \qquad E_+ E_- = \det H = h_{11}h_{22} - h_{12}^2. \tag{2.28}$$

Consequently, for $s = E_+ - E_-$ we have

$$s^2 = (E_+ + E_-)^2 - 4E_+E_- = (h_{11} - h_{22})^2 + 4h_{12}^2. \tag{2.29}$$

For GOE, $x_1 := h_{11} - h_{22}$ and $x_2 := 2h_{12}$ are independent Gaussian variables with zero mean and variance $4v^2$, according to Equations (2.24) and (2.25). Since $x_1^2 + x_2^2 = s^2$, they can be parametrized as $x_1 = s\cos\varphi$, $x_2 = s\sin\varphi$. Hence,

$$\begin{aligned} P_{\mathrm{GOE}}(s,\varphi)\,\mathrm{d}s\,\mathrm{d}\varphi &= P_{\mathrm{GOE}}(x_1,x_2)\,\mathrm{d}x_1\,\mathrm{d}x_2 \\ &= \frac{1}{2\pi(4v^2)}\exp\left(-\frac{x_1^2+x_2^2}{8v^2}\right)\mathrm{d}x_1\,\mathrm{d}x_2 \\ &= \frac{1}{2\pi(4v^2)}\exp\left(-\frac{s^2}{8v^2}\right)s\,\mathrm{d}s\,\mathrm{d}\varphi, \end{aligned}$$

which, after integrating over φ, yields

$$P_{\mathrm{GOE}}(s) = \frac{s}{4v^2}e^{-s^2/8v^2}. \tag{2.30}$$

The average spacing $\Delta := \langle s\rangle$ according to this distribution is

$$\Delta = \int_0^\infty sP_{\mathrm{GOE}}(s)\,\mathrm{d}s = \sqrt{2\pi}v, \tag{2.31}$$

and, hence, with $\tilde{s} = s/\Delta$:

$$P_{\mathrm{GOE}}(\tilde{s}) = \frac{\pi\tilde{s}}{2}e^{-\frac{\pi}{4}\tilde{s}^2}. \tag{2.32}$$

This distribution, even though it can be derived exactly only for $\mathcal{N} = 2$, gives a good approximation to the level spacing distribution of GOE also for larger dimensions [13, 38, 98], where, however, Δ needs to be understood as a *local* (in energy) average spacing defined by just few energy levels close to E_n. Note that, according to Equation (2.32), the energy levels of GOE random matrices show level repulsion $P_{\mathrm{GOE}}(\tilde{s} = 0) = 0$, i.e., the probability of finding two energy levels close to each other is strongly suppressed.

It was shown [36–39] that the level spacing distribution of quantum systems with a fully chaotic classical limit (via the procedure sketched in Section 2.2.1) follows closely the predictions of GOE, GUE or GSE, depending on the system's symmetries with respect to angular momentum and time reversal (*Bohigas-Giannoni-Schmit conjecture* [37]). This property provides a definition of quantum chaos even if a classical limit cannot be easily established: Whenever the level spacing distribution of a quantum system follows Equation (2.32) or the corresponding distributions for GUE or GSE, this system can be understood as (quantum) chaotic.

For integrable systems, on the other hand, the energy levels are typically assumed to follow Poisson statistics [13, 38, 40, 152]. In other words, the scaled level spacings $\tilde{s} = s/\Delta$, where Δ is again defined locally in the spectrum, obey the exponential distribution

$$P_{\mathrm{Poisson}}(\tilde{s}) = e^{-\tilde{s}}. \tag{2.33}$$

This result is motivated by the following ideas [13, 40]: Consider a quantum system with a Hamiltonian that depends on a continuous parameter λ that can induce avoided or actual crossings of the energy levels. Furthermore, assume that, for any two energies E_1, E_2, the probability of finding an energy level in the interval $[E_1, E_1 + \mathrm{d}E]$ is independent of whether an energy level is found at E_2 and depends only on the interval length $\mathrm{d}E$. This is a rather strong assumption and obviously not valid if avoided crossings occur as functions of λ, since then two energy levels cannot come arbitrarily close. In integrable systems, on the other hand, the emergence of avoided crossings is strongly reduced, since the eigenstates involved in an avoided crossing mix with each other [42], which contradicts the fact that eigenstates of integrable systems are uniquely specified by the eigenvalues a_k of the conserved quantities A_k. Under these assumptions, the conditional probability density g of finding an energy level in $[E + s, E + s + \mathrm{d}s]$ given a level at E is independent of E and s [13]. The probability density $P(s)$ for the level spacing s is the product of g, i.e., the probability density of finding an energy level at distance s above the level E, and the probability that no other energy level is found between E and $E + s$,

$$P(s) = g\left(1 - \int_0^s P(s')\,\mathrm{d}s'\right). \tag{2.34}$$

Differentiation with respect to s gives the equation

$$\frac{\partial P(s)}{\partial s} = -gP(s), \tag{2.35}$$

which, for the scaled level spacing $\tilde{s}$, is solved by Equation (2.33). Following a similar reasoning, a Poissonian level spacing distribution is also expected if the spectrum is the superposition of many independent subspectra. In this case, an energy level E_1 of one subspectrum does not have an impact on the position of any energy level E_2 belonging to another subspectrum, such that the probability of finding an energy level in $[E + s, E + s + \mathrm{d}s]$ is mostly independent of E and s.

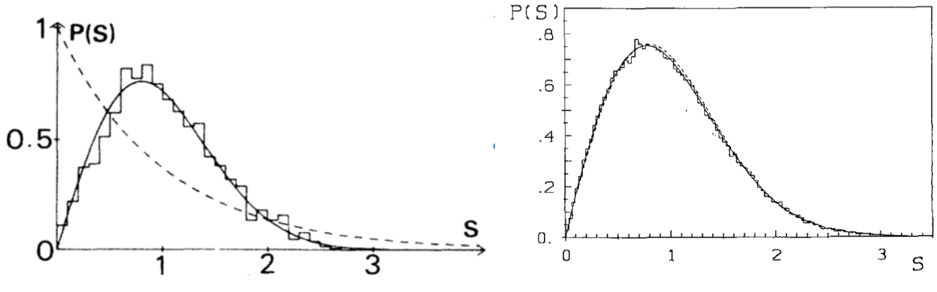

(a) (b)

Figure 2.2: Level spacing distributions $P(s)$ of (a) a hydrogen atom in a strong magnetic field and (b) a periodically kicked quantum spin, the so-called kicked quantum top, compared to $P_{\mathrm{GOE}}(s)$ [Equation (2.32), solid lines] and $P_{\mathrm{Poisson}}(s)$ [Equation (2.33), dashed line in (a)].
Copyright information: (a) reprinted with permission from D. Delande and J. C. Gay, "Quantum Chaos and Statistical Properties of Energy Levels: Numerical Study of the Hydrogen Atom in a Magnetic Field", Phys. Rev. Lett. **57**, 2006 (1986), Copyright 1986 by the American Physical Society, (b) reprinted by permission from Springer Nature Customer Service Centre GmbH: Springer, Z. Physik B, "Level-spacing distributions beyond the Wigner surmise", B. Dietz and K. Życzkowski, Copyright (1991).

There are, however, specific integrable systems, for which the above reasoning fails. For instance, for the harmonic oscillator of frequency ω with energy levels [42]

$$E_n = \hbar\omega\left(n + \frac{1}{2}\right), \tag{2.36}$$

the distribution of the scaled level spacing $\tilde{s}$ is

$$P(\tilde{s}) = \delta(\tilde{s} - 1). \tag{2.37}$$

A more thorough semiclassical derivation of Poissonian statistics for integrable systems and for the superposition of many independent spectra can be found in References [13, 40]. Reference [13] furthermore discusses in more detail integrable systems that do not obey Poissonian level statistics.

Figure 2.2 (reproduced from References [20, 153]) shows the comparison between the level spacing distribution for two examples of quantum systems with a chaotic classical limit, and the GOE and Poisson level spacing distributions. In both cases, the level spacing distributions of these physical systems agree well with the prediction from GOE random-matrix theory, while they deviate from the Poisson distribution predicted for integrable systems. This figure thus confirms that chaotic and integrable quantum systems can clearly be distinguished based on their level spacing distributions, and, hence, the above definition of quantum chaos via the agreement of the level spacing distribution with the predictions from the Gaussian random-matrix ensembles (see pages 16 and 17) is well justified.

However, the calculation of the level spacing distribution requires knowledge of the mean level spacing Δ, which can typically be defined only locally in the spectrum [13, 38, 98, 135], and the required unfolding procedure to scale the level spacings to $\Delta = 1$ throughout the whole spectrum can generate long-range spectral correlations characteristic of chaotic spectra, even for regular systems with originally uncorrelated eigenenergies [154, 155]. Furthermore, the number of levels taken into account for the unfolding can have a serious impact on the result [135, 156]. To avoid these shortcomings of the level spacings s_n, one can instead use the *level spacing ratios* [135, 144, 157]

$$r_n := \min\left\{\frac{s_n}{s_{n+1}}, \frac{s_{n+1}}{s_n}\right\} \tag{2.38}$$

as a measure of (short-range) spectral statistics. As long as the mean level spacing Δ varies only on energy scales larger than Δ itself, r_n is obviously unaffected by any unfolding procedure. However, higher-order level spacing ratios, such as

$$\frac{s_{n+k}}{s_n}, \qquad\qquad \frac{E_{n+k+1} - E_{n+1}}{E_{n+k} - E_n},$$

with $k \gg 1$, might still see an influence of variations in the mean level spacing.

In a similar fashion as for $P_{\mathrm{GOE}}(s)$ with dimension $\mathcal{N} = 2$, an approximate analytical expression of the probability distribution $P_{\mathrm{GOE}}(r)$ has been derived [144] using $\mathcal{N} = 3$,

$$P_{\mathrm{GOE}}(r) = \frac{27}{4}\frac{r + r^2}{(1 + r + r^2)^{5/2}}, \tag{2.39}$$

which yields the mean level spacing ratio

$$\langle r \rangle_{\mathrm{GOE}} = 4 - 2\sqrt{3} \approx 0.5359. \tag{2.40}$$

This result compares well with high-precision numerical results for large $\mathcal{N}$ [144] giving

$$\langle r \rangle_{\mathrm{GOE}} = 0.5307(1). \tag{2.41}$$

For Poissonian level statistics, the probability density $P(r)$ can easily be derived analytically (for details see Appendix A.1) and reads

$$P_{\mathrm{Poisson}}(r) = \frac{2}{(1 + r)^2}, \tag{2.42}$$

yielding the mean level spacing ratio

$$\langle r \rangle_{\mathrm{Poisson}} = 2 \ln 2 - 1 \approx 0.3863. \tag{2.43}$$

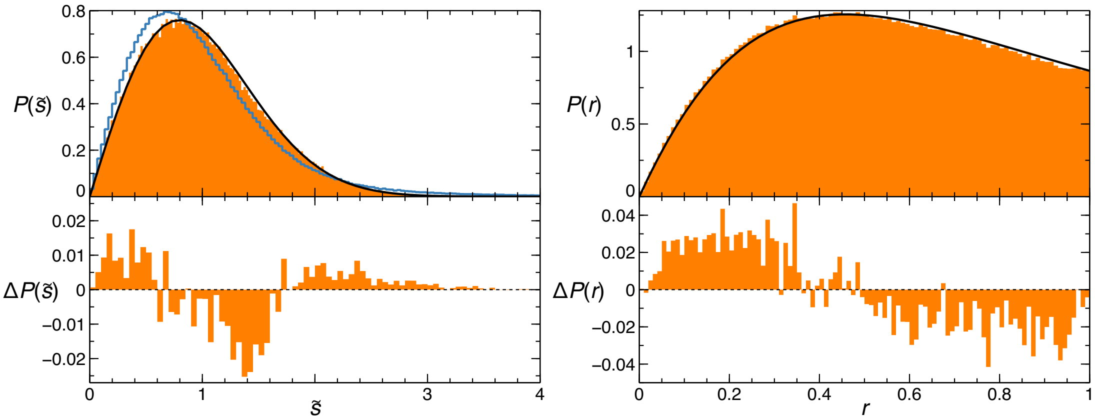

Figure 2.3: Comparison of numerically obtained probability distributions P_{num} of $\tilde{s} = s/\Delta$ (left) and of r (right) for GOE with their analytic approximations P_{ana} according to Equations (2.32) and (2.39), respectively (black lines). In the lower panels, we show $\Delta P(x) = P_{\text{num}}(x) - P_{\text{ana}}(x)$, with $x = \tilde{s}$, r, where P_{ana} is evaluated at the center of each histogram bin. Orange histograms are extracted from the full spectrum for r, and from 200 levels in the center of the spectrum for $\tilde{s}$, for 1000 realizations of a 1000×1000 GOE matrix. The blue curve in the upper left panel shows $P(\tilde{s})$ for the full spectrum.

$P(r)$ has also been derived analytically for block-diagonal matrices of m GOE blocks with identical dimensions [158]. Such matrices are a model for chaotic quantum Hamiltonians with additional symmetries that lead to a separation of the underlying Hilbert space into a direct sum of invariant subspaces. Particularly for $m = 2$, $\langle r \rangle$ evaluates to

$$\langle r \rangle_{2\,\text{GOE}} = 0.423415. \tag{2.44}$$

Figure 2.3 shows the numerically obtained distributions $P(\tilde{s})$ and $P(r)$ for GOE matrices of dimension $\mathcal{N} = 1000$, the corresponding analytical predictions for small $\mathcal{N}$ [Equations (2.32) and (2.39)], and the differences $\Delta P(\tilde{s})$, $\Delta P(r)$ between both. Here, the unfolding from s to $\tilde{s}$ is performed naively by calculating the mean level spacing Δ as a global average over the full range of levels under consideration. Even though there are small deviations between numerical data and analytics, as revealed by ΔP, an overall good agreement is observed for $\tilde{s}$ in the center of the spectrum and for r throughout the full spectrum. The level spacing distribution $P(\tilde{s})$ for the full spectrum deviates clearly from the analytical prediction. This reveals that the mean level spacing Δ may in general not be assumed to be constant throughout the spectrum, and specific care must be taken in the unfolding procedure in order to capture the energy dependence of Δ. The distribution of level spacing ratios, on the other hand, does not show these issues, which confirms that r is just weakly affected by variations of the mean level spacing, even without unfolding, and is hence a more convenient quantifier of short-range spectral statistics than $\tilde{s}$.

2.2.4. Eigenvector Statistics of the Gaussian Orthogonal Ensemble

In addition to spectral properties, let us now discuss features of GOE eigenstates. Assume that

$$\boldsymbol{v} = (v_1, \dots, v_{\mathcal{N}}) \in \mathbb{R}^{\mathcal{N}}$$

is a normalized eigenvector of one realization H of GOE. Since

$$P_{\mathrm{GOE}}(H) = P_{\mathrm{GOE}}(OHO^T),$$

for any orthogonal matrix O, and since the vector $O\boldsymbol{v}$ is an eigenvector of OHO^T, the probability to obtain the rotated vector $O\boldsymbol{v}$ as an eigenvector of a GOE matrix is the same as the probability to obtain $\boldsymbol{v}$. Hence, the probability density $P_{\mathrm{GOE}}(\boldsymbol{v})$ for a single normalized GOE eigenvector needs to be independent of the direction of $\boldsymbol{v}$, which means that $P_{\mathrm{GOE}}(\boldsymbol{v})$ is the uniform distribution on the $\mathcal{N}$-dimensional unit sphere [13, 150],

$$P_{\mathrm{GOE}}(\boldsymbol{v}) = \Gamma\left(\frac{\mathcal{N}}{2}\right) \pi^{-\frac{\mathcal{N}}{2}} \delta\left(\sum_{i=1}^{\mathcal{N}} v_i^2 - 1\right). \tag{2.45}$$

Here, the first two terms are given by the normalization of the distribution and the delta term encodes the normalization of $\boldsymbol{v}$. Numerically, this distribution can be sampled by generating vectors $\widetilde{\boldsymbol{v}}$ of independent Gaussian numbers $\widetilde{v}_i$ with zero mean and unit variance, and subsequent normalization of $\widetilde{\boldsymbol{v}}$ [159]. This procedure is justified by the fact that the joint normal distribution of the vector components $\widetilde{v}_i$,

$$P_{\mathrm{Gauss}}\left(\widetilde{\boldsymbol{v}}\right) \sim \exp\left(\sum_i \widetilde{v}_i^2/2\right),$$

depends only on the (Euclidean) norm of $\widetilde{\boldsymbol{v}}$ and not on its direction, in contrast to, e.g., the joint distribution of $\mathcal{N}$ independent uniformly distributed numbers. Integration of Equation (2.45) over $\mathcal{N} - n$ vector components yields the joint probability density of the remaining n entries [150, 151],

$$P_{\mathrm{GOE}}(v_1, \dots, v_n) = \frac{\Gamma\left(\frac{\mathcal{N}}{2}\right)}{\pi^{\frac{n}{2}}\,\Gamma\left(\frac{\mathcal{N}-n}{2}\right)} \left(1 - \sum_{i=1}^{n} v_i^2\right)^{(\mathcal{N}-n-2)/2}, \quad \text{for } \sum_{i=1}^{n} v_i^2 \leq 1, \tag{2.46}$$

and $P_{\mathrm{GOE}}(v_1, \dots, v_n) = 0$ otherwise. Particularly for $n = 1$ and $n = 2$, this formula gives

$$P_{\mathrm{GOE}}(v_1) = \frac{\Gamma\left(\frac{\mathcal{N}}{2}\right)}{\sqrt{\pi}\,\Gamma\left(\frac{\mathcal{N}-1}{2}\right)} \left(1 - v_1^2\right)^{(\mathcal{N}-3)/2}, \tag{2.47}$$

$$P_{\mathrm{GOE}}(v_1, v_2) = \frac{\mathcal{N} - 2}{2\pi} \left(1 - v_1^2 - v_2^2\right)^{\mathcal{N}/2-2}. \tag{2.48}$$

For $n = 1$, the variable transform $u = \mathcal{N} v_1^2/2$ yields

$$P_{\mathrm{GOE}}(u) = \frac{\sqrt{2}\,\Gamma\left(\frac{\mathcal{N}}{2}\right)}{\sqrt{\mathcal{N}\pi u}\,\Gamma\left(\frac{\mathcal{N}-1}{2}\right)} \left(1 - \frac{2u}{\mathcal{N}}\right)^{(\mathcal{N}-3)/2}, \qquad 0 \le u \le \mathcal{N}/2, \tag{2.49}$$

which in the limit $\mathcal{N} \to \infty$ reduces to the *Porter-Thomas distribution* [13, 150, 151]

$$P_{\mathrm{PT}}(u) = \frac{1}{\sqrt{\pi u}} e^{-u}, \qquad 0 \le u < \infty. \tag{2.50}$$

2.2.5. Embedded Random-Matrix Ensembles

As we have discussed in Section 2.2.3, Gaussian random matrices yield a definition of quantum chaos even when the classical limit is not easily accessible. However, these ensembles fail to reproduce the structure of many-particle Hamiltonians, since the latter typically include only single-particle tunneling processes and few-body interactions, and can hence be expressed as sparse matrices with correlated matrix elements, in contrast to the dense and uncorrelated matrices provided by the Gaussian ensembles. To obtain random-matrix ensembles that describe the structure of many-body systems more faithfully, so-called *embedded ensembles* have been introduced [93–98], which consist of Hamiltonians of the form

$$H = H_1 + H_2 + \dots H_n, \tag{2.51}$$

where H_k is a k-particle operator.

In the following, assume a system of N identical particles, each having access to L orthogonal single-particle states $|i\rangle$ associated with creation and annihilation operators d_i, $d_i^\dagger$, such that $d_i^\dagger |0\rangle = |i\rangle$ with the vacuum state $|0\rangle$. For simplicity, we focus only on bosons and consider just single- and two-particle operators here. Then, the creation operators $d_i^\dagger$ act on the states $|j\rangle$, $|i\rangle$ as [42]

$$d_i^\dagger |j\rangle = |n_i = 1, n_j = 1\rangle \qquad (j \neq i), \qquad\qquad d_i^\dagger |i\rangle = \sqrt{2}\, |n_i = 2\rangle. \tag{2.52}$$

Here, the states $|n_i, n_j\rangle$ are Fock states with n_i particles in state $|i\rangle$ and n_j particles in state $|j\rangle$. We can now introduce operators $D_{ij}^\dagger$ that create normalized (and correctly symmetrized) two-particle states from the vacuum,

$$D_{ij}^\dagger = D_{ji}^\dagger = \frac{1}{\sqrt{1 + \delta_{ij}}} d_i^\dagger d_j^\dagger. \tag{2.53}$$

Consequently, general single- and two-body Hamiltonians are given in second quantization as

$$H_1 = \sum_{i,j=1}^{L} h_{ij}^{(1)} d_i^\dagger d_j, \qquad H_2 = \sum_{i \ge j, k \ge l}^{L} h_{ij,kl}^{(2)} D_{ij}^\dagger D_{kl}, \tag{2.54}$$

with $D_{kl} = \left(D^{\dagger}_{kl}\right)^{\dagger}$ and $h^{(1)}_{ij} = \left(h^{(1)}_{ji}\right)^{*}$, $h^{(2)}_{ij,kl} = \left(h^{(2)}_{kl,ij}\right)^{*}$. The bosonic two-body embedded GOE ensemble is now defined by Hamiltonians

$$H = H_1 + \lambda H_2, \tag{2.55}$$

where the matrix elements $h^{(1)}_{ij}$, $h^{(2)}_{ij,kl}$ are given by GOE random matrices as defined in Section 2.2.2, i.e., they are independent Gaussian random variables with means

$$\mu\left(h^{(1)}_{ij}\right) = \mu\left(h^{(2)}_{ij,kl}\right) = 0 \tag{2.56}$$

and variances

$$\mathrm{var}(h^{(1)}_{ij}) = 1 + \delta_{ij}, \qquad \mathrm{var}(h^{(2)}_{ij,kl}) = 1 + \delta_{ik}\delta_{jl}. \tag{2.57}$$

The parameter λ sets the strength of the two-particle term and can induce a transition between regular and chaotic spectra [98]. During the remainder of this thesis, whenever we refer to “the” embedded ensemble, we always mean the bosonic two-body embedded GOE ensemble defined in Equation (2.55).

By definition, matrix elements of embedded-ensemble Hamiltonians [Equation (2.55)] may be nonzero only for those transitions between quantum states that are mediated by at most two-particle processes, in contrast to GOE, which may yield nonzero matrix elements between any two states. Consequently, every matrix element that is deterministically zero for the embedded ensemble vanishes also for any other two-body Hamiltonian, in any Fock basis. In addition to the enhanced sparsity as compared to GOE, also the nonzero matrix elements are more strongly correlated in the embedded ensemble due to the two-body character of the Hamiltonian. For example, consider the basis of Fock states $|\boldsymbol{n}\rangle = |n_1, \ldots, n_L\rangle$ associated with the creation and annihilation operators $d^{(\dagger)}_i$, such that

$$\begin{aligned} d_i |\boldsymbol{n}\rangle &= \sqrt{n_i}\, |n_1, \ldots, n_i - 1, \ldots, n_L\rangle, \\ d^{\dagger}_i |\boldsymbol{n}\rangle &= \sqrt{n_i + 1}\, |n_1, \ldots, n_i + 1, \ldots, n_L\rangle. \end{aligned} \tag{2.58}$$

In this basis for N bosons and L single-particle states there are

$$\mathcal{N} = \binom{N + L - 1}{N}$$

diagonal entries

$$\langle \boldsymbol{n}| H |\boldsymbol{n}\rangle = \sum_{i=1}^{L} h^{(1)}_{ii} n_i + \lambda \sum_{i \geq j}^{L} h^{(2)}_{ij,ij} \frac{n_i(n_j - \delta_{ij})}{1 + \delta_{ij}},$$

which are, however, defined only by $L + L(L+1)/2$ independent numbers $h^{(1)}_{ii}$ and $h^{(2)}_{ij,ij}$. For GOE, on the contrary, all these diagonal entries would be independent random variables.

We note that the definition of H_1 may vary slightly in the literature. For instance, in References [98, 160] H_1 is defined as a diagonal Hamiltonian in terms of the single-particle states $|i\rangle$,

$$H_1 = \sum_{i=1}^{L} E_i d_i^\dagger d_i, \tag{2.59}$$

where the energies E_i might be given by the semicircle law of GOE, Equation (2.26), or by any other distribution. However, we choose the form given in Equation (2.54) in order to treat single- and two-particle terms on an equal footing.

To account for symmetries that a specific many-body Hamiltonian may have, one may put additional constraints on the matrix elements of the embedded-ensemble Hamiltonians. For instance, let the single-particle states correspond to L sites on a linear lattice labelled from 1 to L. Then, reflection symmetry about the center of the chain would require

$$h_{ij}^{(1)} = h_{(L+1-i)(L+1-j)}^{(1)}, \qquad h_{ij,kl}^{(2)} = h_{(L+1-i)(L+1-j),(L+1-k)(L+1-l)}^{(2)}. \tag{2.60}$$

If, in contrast, the single-particle modes $|i\rangle$ were to have a well-defined parity $\Pi(i) = \pm 1$ [98], reflection symmetry would imply

$$\Pi(i) \neq \Pi(j) \Rightarrow h_{ij}^{(1)} = 0, \qquad \Pi(i)\Pi(j) \neq \Pi(k)\Pi(l) \Rightarrow h_{ij,kl}^{(2)} = 0. \tag{2.61}$$

2.3. Multifractality of Quantum States

In this section, we introduce and discuss the generalized fractal dimensions [57, 60, 76, 79, 81, 161], which provide a very useful tool to characterize basic structural features of quantum states.

Let us consider a finite-dimensional Hilbert space $\mathcal{H}$ of dimension $\dim \mathcal{H} = \mathcal{N}$ with an orthonormal basis $\{|\alpha\rangle\}$, which we can understand as the eigenbasis of an observable $A = \sum_\alpha \alpha |\alpha\rangle \langle\alpha|$ with eigenvalues α. Given a state

$$|\psi\rangle = \sum_\alpha \psi_\alpha |\alpha\rangle$$

with amplitudes ψ_α on the basis elements $|\alpha\rangle$, i.e., measurement probabilities $|\psi_\alpha|^2$ of the eigenvalue α of A, we define the *q-moments* of $|\psi\rangle$, for $q \geq 0$, as

$$R_q = \sum_\alpha |\psi_\alpha|^{2q}. \tag{2.62}$$

These q-moments are generalizations of the *inverse participation ratio* [162]

$$\mathrm{IPR} := \sum_\alpha |\psi_\alpha|^4 = R_2. \tag{2.63}$$

Of these quantities, R_0 just counts the number of nonzero intensities of $|\psi\rangle$, while $R_1 = 1$ simply reproduces the normalization condition, independently of $|\psi\rangle$.

To investigate the scaling of R_q with system size, we define the *finite-size generalized fractal dimensions* $\tilde{D}_q$ as

$$\tilde{D}_q = -\frac{1}{q-1}\frac{\ln R_q}{\ln \mathcal{N}} = -\frac{1}{q-1}\frac{\ln \sum_\alpha |\psi_\alpha|^{2q}}{\ln \mathcal{N}}, \tag{2.64}$$

whose limits for $\mathcal{N} \to \infty$ yield the *generalized fractal dimensions*

$$D_q = \lim_{\mathcal{N}\to\infty} \tilde{D}_q. \tag{2.65}$$

In this work, instead of investigating the limit D_q for individual states $|\psi\rangle$, we will typically consider averages and variances of $\tilde{D}_q$ over several energy eigenstates close to each other in energy, and we will study the limit $\mathcal{N} \to \infty$ for these averages and variances at a fixed energy.

The values of $\tilde{D}_q$ and of their limits D_q provide information about the localization of the state $|\psi\rangle$ in the chosen basis: As an example, assume that the state $|\psi\rangle$ is equally distributed onto n basis elements $|\alpha_1\rangle, \dots, |\alpha_n\rangle$,

$$|\psi\rangle = \sum_{i=1}^{n} \frac{1}{\sqrt{n}} |\alpha_i\rangle .$$

Assume furthermore that n is related to the Hilbert space dimension as $n = c\mathcal{N}^D$, where c and $0 \leq D \leq 1$ are constants. Then the corresponding q-moments are

$$R_q = \sum_{i=1}^{n} n^{-q} = n^{1-q} \tag{2.66}$$

and the finite-size fractal dimensions read

$$\tilde{D}_q = \frac{\ln n}{\ln \mathcal{N}} = D + \frac{\ln c}{\ln \mathcal{N}} \xrightarrow{\mathcal{N}\to\infty} D \tag{2.67}$$

for all q. In other words, the fractal dimensions encode the scaling dimension of the number of basis elements necessary to describe $|\psi\rangle$. In particular, we distinguish four different cases (see also Figure 2.4):

- If $\tilde{D}_q \to 0$ for all $q \geq 1$, we consider the underlying state as *localized*. The number of basis states populated by such a state, or equivalently the number of eigenvalues α of A with nonvanishing measurement probability, grows slower than any power $\mathcal{N}^D$, $D > 0$. For example, states living on maximally $c < \infty$ basis states, where c is independent of $\mathcal{N}$, are localized in this sense. Note that for exponentially localized states, i.e., the intensities on all but a finite number of basis states decay with system size as $|\psi_\alpha|^2 \sim c^{-\mathcal{N}}$, with $c > 1$ [163], all fractal dimensions converge to $D_q = 0$ for all $q \geq 0$, while states that are not exponentially localized may have $D_q = 0$ for $q \geq 1$ and $D_q > 0$ for certain $q < 1$. An example of such states is discussed in Reference [163].

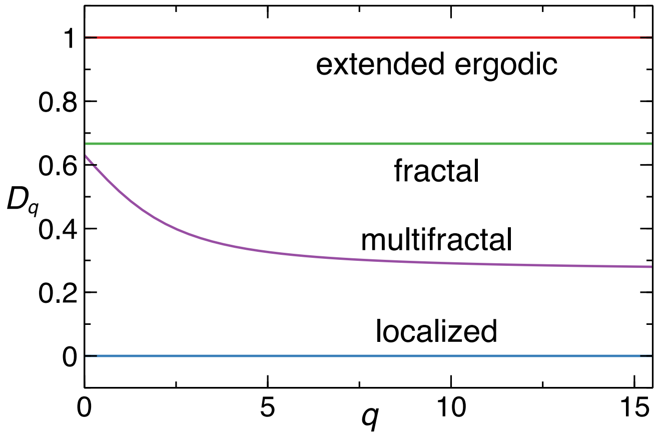

Figure 2.4: Example fractal dimensions of localized, extended ergodic, fractal and multifractal states, versus the index q.

- If $\tilde{D}_q \to 1$ for all q, we call the underlying state *delocalized* or *extended ergodic*. These states live on a number of basis states that increases linearly with Hilbert space dimension $\mathcal{N}$, such that they populate a nonvanishing fraction of the basis even in the limit $\mathcal{N} \to \infty$.
- If $\tilde{D}_q \to D$ for all q and $0 < D < 1$, the underlying state is *fractal*. In the limit $\mathcal{N} \to \infty$, such a state lives on an infinite number of basis states, which nevertheless constitute a vanishing fraction of the full basis.
- If $\tilde{D}_q \to D_q$ and $0 \leq D_q \leq 1$ depends on q, we call the underlying state *multifractal*. Like fractal states, these states populate an infinite number of basis states in the limit $\mathcal{N} \to \infty$, which, however, amount to a vanishing fraction of the full Hilbert space basis.

It can be shown that R_q and $\tilde{D}_q$ are bounded functions of the state $|\psi\rangle$ with

$$1 \leq R_q \leq \mathcal{N}^{-(q-1)} \quad (0 \leq q < 1), \qquad \mathcal{N}^{-(q-1)} \leq R_q \leq 1 \quad (q \geq 1), \tag{2.68}$$

$$0 \leq \tilde{D}_q \leq 1 \qquad (\text{all } q). \tag{2.69}$$

Hence, the four cases discussed above are the only possible limits of $\tilde{D}_q$. A detailed derivation of Equations (2.68) and (2.69) is given in Appendix A.2.1.

Of the uncountably many generalized fractal dimensions $\tilde{D}_q$, we focus mainly on $\tilde{D}_1$, $\tilde{D}_2$ and $\tilde{D}_\infty$. By definition, $\tilde{D}_2$ is the scaling dimension of the inverse participation ratio R_2. As we will see in the following, also $\tilde{D}_1$ and $\tilde{D}_\infty$, which can be defined only via the limits $q \to 1$ and $q \to \infty$ of Equation (2.64), have a simple interpretation in terms of other quantities. For $q = 1$, L'Hôpital's rule yields

$$\tilde{D}_1 = -\frac{1}{\ln \mathcal{N}} \sum_\alpha |\psi_\alpha|^2 \ln |\psi_\alpha|^2. \tag{2.70}$$

For $q \to \infty$, the maximum intensity of $|\psi\rangle$ gives by far the largest contribution to R_q, and consequently (for more details see Appendix A.2.2)

$$\tilde{D}_\infty = -\frac{1}{\ln \mathcal{N}} \ln \max_\alpha |\psi_\alpha|^2. \tag{2.71}$$

These results show that $\tilde{D}_1$ is the Shannon (information) entropy of the system, with a logarithm in base $\mathcal{N}$ instead of the base-2 logarithm widely used in the context of (quantum) information theory. $\tilde{D}_\infty$, in contrast, is the scaling dimension of the maximum intensity of $|\psi\rangle$ in the given basis, and is hence defined by a single basis state only.

Furthermore, note that $\tilde{D}_q$ is a monotonically decreasing function of the index q,

$$\tilde{D}_{q_1} \leq \tilde{D}_{q_2} \quad \text{for } q_1 \geq q_2, \tag{2.72}$$

as we prove in Appendix A.2.3. Hence, for $1 \leq q \leq \infty$, $\tilde{D}_1$ and $\tilde{D}_\infty$ constitute upper and lower bounds to the finite-size generalized fractal dimensions,

$$\tilde{D}_1 \geq \tilde{D}_q \geq \tilde{D}_\infty. \tag{2.73}$$

2.4. The Bose-Hubbard Model

2.4.1. Definition and Fundamental Properties

The *Bose-Hubbard Hamiltonian* [164–167] in one dimension is given as the sum of a tunneling and an interaction Hamiltonian,

$$H = H_{\text{tun}} + H_{\text{int}}, \tag{2.74}$$

with

$$H_{\text{tun}} = -J \sum_{j=1}^{L} \left(a_j^\dagger a_{j+1} + a_{j+1}^\dagger a_j \right), \tag{2.75}$$

$$H_{\text{int}} = \frac{U}{2} \sum_{j=1}^{L} n_j \left(n_j - 1 \right) = \frac{U}{2} \sum_{j=1}^{L} a_j^\dagger a_j^\dagger a_j a_j. \tag{2.76}$$

This model, originally introduced to study the transition between a Mott-insulating and a superfluid phase of interacting bosons [164], is nowadays of high experimental relevance in the context of cold atoms in optical lattices [114–118, 120, 123–125, 127, 129] and is also applied in the theory of superconducting qubits [168, 169]. It describes N bosonic particles on a one-dimensional lattice of L sites, with nearest-neighbour tunneling energy J, and repulsive on-site interaction U (compare the sketch in Figure 2.5). In the above expressions, $a_j^\dagger$ and a_j are bosonic creation and annihilation operators in the basis of site-localized states (Wannier modes) and $n_j = a_j^\dagger a_j$ are the corresponding number operators.

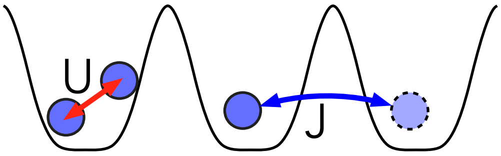

Figure 2.5: Sketch of the Bose-Hubbard model for 3 particles on 3 sites. Each particle can tunnel through the potential barriers, with tunneling strength J, and particles at the same site interact with each other repulsively, with interaction strength U.

We distinguish two types of boundary conditions, periodic boundary conditions (PBCs), where tunneling between the edge sites 1 and L is allowed, and hard-wall boundary conditions (HWBCs), where tunneling between sites 1 and L is forbidden. Depending on the boundary conditions, the creation and annihilation operators $a_{L+1}^{(\dagger)}$ in H_{tun} are defined as

$$a_{L+1}^{(\dagger)} := \begin{cases} a_1^{(\dagger)}, & \text{PBCs,} \\ 0, & \text{HWBCs.} \end{cases} \tag{2.77}$$

The dimension of the underlying Hilbert space, defined by the number of ways to distribute N bosons onto L sites, is

$$\mathcal{N} = \binom{N+L-1}{N} = \binom{N+L-1}{L-1}, \tag{2.78}$$

which scales exponentially with N and L. We treat this model numerically, calculating its eigenenergies and the fractal dimensions of its eigenvectors. Details about the employed numerical methods can be found in Appendix C.

According to Equations (2.75) and (2.76), the matrix elements $\langle \boldsymbol{n}| H |\boldsymbol{m}\rangle$ are real numbers in the basis of Fock states

$$|\boldsymbol{n}\rangle := |n_1, \dots, n_L\rangle\,, \tag{2.79}$$

which are the eigenstates of the on-site number operators with eigenvalues n_j. Hence, according to Section 2.2.2, GOE is the correct random-matrix model to benchmark quantum chaos in the Bose-Hubbard Hamiltonian.

The creation and annihilation operators $a_j^{(\dagger)}$ provide a diagonal representation of H_{int}, according to Equation (2.76). To obtain a diagonal representation of H_{tun} instead, one may perform a basis transformation from $a_j^{(\dagger)}$ to another set of creation and annihilation operators $b_k^{(\dagger)}$, $k = 1, \dots, L$, defined as

$$b_k := \begin{cases} \dfrac{1}{\sqrt{L}} \displaystyle\sum_{j=1}^{L} e^{-2\pi \mathrm{i} kj/L} a_j, & \text{PBCs,} \\ \sqrt{\dfrac{2}{L+1}} \displaystyle\sum_{j=1}^{L} \sin\left(\dfrac{\pi kj}{L+1}\right) a_j, & \text{HWBCs.} \end{cases} \tag{2.80}$$

The action of the operators $b_k^{(\dagger)}$ annihilates (creates) a boson in a plane-wave state with quasimomentum k (PBCs), or in a standing-wave state with $k+1$ nodes (HWBCs). One can easily check that $\left[b_k, b_l^\dagger\right] = \delta_{kl}$, as required for bosonic creation and annihilation operators, and that

$$a_j = \begin{cases} \dfrac{1}{\sqrt{L}} \displaystyle\sum_{k=1}^{L} e^{+2\pi \mathrm{i} kj/L} b_k, & \text{PBCs,} \\ \sqrt{\dfrac{2}{L+1}} \displaystyle\sum_{k=1}^{L} \sin\left(\dfrac{\pi kj}{L+1}\right) b_k, & \text{HWBCs.} \end{cases} \tag{2.81}$$

Inserting Equation (2.81) into H_{tun}, and using that

$$\sum_{j=1}^{L} e^{2\pi \mathrm{i}(k-l)j/L} = L\delta_{kl}, \qquad \sum_{j=1}^{2(L+1)} e^{2\pi \mathrm{i}(k-l)j/(2(L+1))} = 2(L+1)\tilde{\delta}_{kl},$$

with $\delta_{kl} = 1 \Leftrightarrow k = l \mod L$ and $\tilde{\delta}_{kl} = 1 \Leftrightarrow k = l \mod 2(L+1)$, one obtains

$$H_{\text{tun}} = -2J \sum_{k=1}^{L} \cos\varphi(k) b_k^\dagger b_k, \tag{2.82}$$

with

$$\varphi(k) = \begin{cases} \dfrac{2\pi k}{L}, & \text{PBCs,} \\ \dfrac{\pi k}{L+1}, & \text{HWBCs.} \end{cases} \tag{2.83}$$

Via a similar calculation, H_{int} transforms into

$$H_{\text{int}} = \begin{cases} \dfrac{U}{2L} \displaystyle\sum_{k,l,m,n=1}^{L} \delta_{k+l,m+n} b_k^\dagger b_l^\dagger b_m b_n, & \text{PBCs,} \\ \dfrac{U}{4(L+1)} \displaystyle\sum_{k,l,m,n=1}^{L} \left(\sum_{\sigma_{1,2,3}=\pm 1} \sigma_1\sigma_2\sigma_3 \tilde{\delta}_{k+\sigma_1 l, \sigma_2 m + \sigma_3 n} \right) b_k^\dagger b_l^\dagger b_m b_n, & \text{HWBCs.} \end{cases} \tag{2.84}$$

Here, the (k,l,m,n)-dependent prefactor accounts for momentum conservation with $\delta_{kl} = 1 \Leftrightarrow k = l \mod L$ and $\tilde{\delta}_{kl} = 1 \Leftrightarrow k = l \mod 2(L+1)$.

2.4.2. Symmetries, Integrable Limits and Natural Bases

The interaction term H_{int}, Equation (2.76), is obviously invariant under any permutation of the site indices j and hence its symmetry group is the symmetric group $\mathfrak{S}_L$ of L objects. The tunneling term H_{tun}, Equation (2.75), is symmetric with respect to reflection about the center of the chain, which is the specific permutation that maps each site j to the site $L-j+1$:

$$-J\sum_{j=1}^{L}\left(a^\dagger_{L-j+1}a_{L-j}+a^\dagger_{L-j}a_{L-j+1}\right)=-J\sum_{j=L-1}^{0}\left(a^\dagger_{j+1}a_j+a^\dagger_j a_{j+1}\right)=H_{\text{tun}}.$$

Here, we made use of $a_0^{(\dagger)}=a_L^{(\dagger)}$ for PBCs and $a_0^{(\dagger)}=0$ in the case of HWBCs. For PBCs, the tunneling Hamiltonian is also invariant under translations, which are the mappings $j\mapsto j+i \mod L$ for a fixed i. Identifying $a^\dagger_{L+1}a_{L+2}$ with $a^\dagger_1 a_2$, etc., this invariance is immediately clear. Hence, the total Hamiltonian is invariant under reflections about the center and, for PBCs, also under translations. Thus, its symmetry group is the dihedral group D_L (with $2L$ elements) for PBCs and the two-element group $D_1\cong C_2$ for HWBCs.

Representation theory states that eigenstates of H transform under the action of the symmetry operations according to irreducible representations of these groups, which also means that H is block-diagonal with respect to distinct irreducible representations [170, 171]. The two irreducible representations of D_1 are one-dimensional and characterized by the two eigenvalues

$$\Pi=\pm1 \tag{2.85}$$

of the reflection operator (even/odd parity), which consequently characterize also the eigenstates of the Hamiltonian H with HWBCs. For D_L there are two (odd L) or four (even L) one-dimensional irreducible representations [171], characterized by the parities $\Pi=\pm1$ and by the eigenvalues

$$e^{2\pi\mathrm{i}Q/L}=\begin{cases}\pm1, & \text{even } L,\ Q=0,\frac{L}{2},\\ 1, & \text{odd } L,\ Q=0\end{cases} \tag{2.86}$$

of the translation operator. Additionally, D_L has two-dimensional irreducible representations [171], which can be labelled by

$$Q=1,\dots,\frac{L-1}{2}\quad(\text{odd } L),\qquad\qquad Q=1,\dots,\frac{L}{2}-1\quad(\text{even } L). \tag{2.87}$$

For each of these irreducible representations there exists a basis in which the translation operator is diagonal with eigenvalues $e^{2\pi\mathrm{i}Q/L}$, $e^{2\pi\mathrm{i}(L-Q)/L}$, and the reflection operator swaps the two basis states. This means that the eigenstates of H with PBCs can be characterized by their total quasimomentum

$$Q=0,\dots,L-1 \tag{2.88}$$

and in the case of $Q = 0$ or $Q = L/2$ furthermore by their parity

$$\Pi = \pm 1. \tag{2.89}$$

Note that the degenerate eigenstates of H that belong to the two-dimensional irreducible representations can also be combined such that they are eigenstates of the reflection operator. In this case, they are characterized by their parity and by $|Q| := \min\{Q, L - Q\}$ instead of the total quasimomentum. Due to the block-diagonal nature of the Hamiltonian, one can consider independent subspaces of the full Hilbert space, each labelled by Q and/or Π according to the corresponding irreducible representation.

In the limit of vanishing tunneling ($J = 0$), the Hamiltonian (2.74) reduces to H_{int}. As can be seen directly from the form of this operator [Equation (2.76)], its eigenstates are simply the Fock states $|\boldsymbol{n}\rangle$ [Equation (2.79)], i.e., the eigenstates of the on-site number operators. Hence, the eigenstates of H in this limit are uniquely determined by the eigenvalues of L independent commuting observables. Consequently, the system is integrable for $J = 0$, since L is also the number of degrees of freedom: To see the latter, replace the creation and annihilation operators by generalized coordinates and momenta according to

$$q_j = \frac{q_0}{\sqrt{2}} \left(a_j^\dagger + a_j \right), \qquad p_j = \frac{\mathrm{i}\hbar}{\sqrt{2} q_0} \left(a_j^\dagger - a_j \right), \tag{2.90}$$

like for the usual harmonic oscillator [42]. The Bose-Hubbard model then transforms into L coupled (by the tunneling term, for $J \neq 0$) mechanical systems with Hamiltonians

$$H_j = \frac{U}{8} \left(\frac{q_j^2}{q_0^2} + \frac{q_0^2}{\hbar^2} p_j^2 - 1 \right) \left(\frac{q_j^2}{q_0^2} + \frac{q_0^2}{\hbar^2} p_j^2 - 3 \right), \tag{2.91}$$

each contributing one degree of freedom. Here, each H_j describes an anharmonic oscillator positioned on site j.

Similarly, in the non-interacting limit $U = 0$, the system reduces to H_{tun}. According to Equation (2.82), the eigenstates of this Hamiltonian can be written as Fock states

$$|\tilde{\boldsymbol{n}}\rangle := |\tilde{n}_1, \ldots, \tilde{n}_L\rangle, \tag{2.92}$$

defined as the eigenstates of the number operators $\tilde{n}_k = b_k^\dagger b_k$ with eigenvalues $\tilde{n}_k$. Consequently, the system is also integrable in this limit, since the number operators $\tilde{n}_k$ provide L independent commuting observables that uniquely characterize the eigenstates of H for $U = 0$.

Natural bases to describe the Bose-Hubbard Hamiltonian are therefore the *interaction basis* $\{|\boldsymbol{n}\rangle\}$ and the *tunneling basis* $\{|\tilde{\boldsymbol{n}}\rangle\}$, which are the eigenbases of the integrable limits H_{int} and H_{tun}, respectively. To take into account also the symmetries discussed previously in this section, the bare Fock states are projected onto the eigenspaces of the

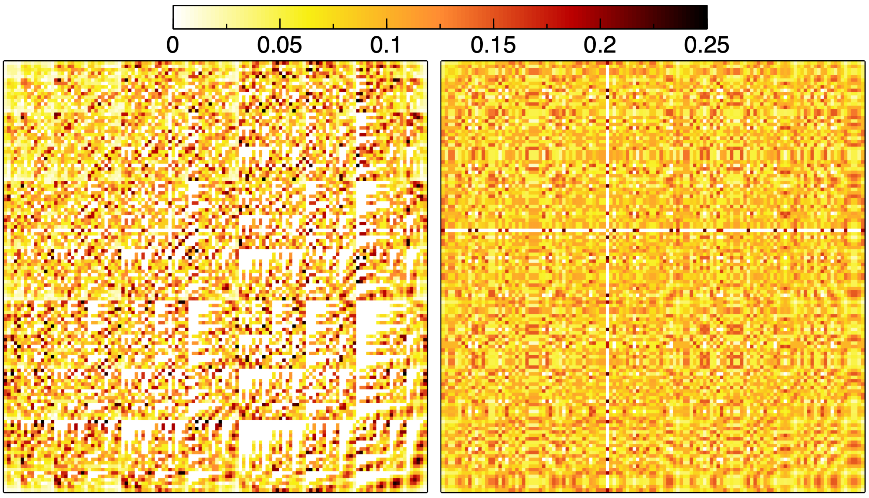

Figure 2.6: Basis transformation matrices from interaction to tunneling basis with HWBCs (left) and PBCs (right) for $N = L = 5$. Each pixel shows the absolute value of the corresponding matrix element according to the color bar, which applies to both panels.

symmetry operations. As an illustrative example consider the Fock state $|1,2,0\rangle$ of 3 bosons on 3 sites. It can be decomposed into

$$|1,2,0\rangle = \frac{|1,2,0\rangle + |0,2,1\rangle}{2} + \frac{|1,2,0\rangle - |0,2,1\rangle}{2},$$

where the first state is symmetric and the second is antisymmetric with respect to reflection symmetry. Projecting onto the symmetric and antisymmetric subspaces and normalizing the resulting states hence gives the two states

$$\frac{|1,2,0\rangle \pm |0,2,1\rangle}{\sqrt{2}}. \tag{2.93}$$

Note that the interaction and tunneling bases are conjugated to each other in the sense that the states of one basis populate a large amount of the basis states in the other basis. For a single particle, this is immediately clear from Equations (2.80) and (2.81). As Figure 2.6 shows, the transformation matrix between the two bases is dense also for $N > 1$, such that the states of one basis are transformed into widely spread states in the other basis.[4]

Figure 2.7 shows the matrix structure of the Bose-Hubbard Hamiltonian in both bases in comparison to the bosonic two-body embedded GOE ensemble introduced in Section 2.2.5. In the interaction basis, only the single-particle term couples different Fock

---

[4] Note that some basis states with enhanced symmetries as compared to the others may still be rather localized in the other basis, for example the fully symmetric state $|1,1,1,1,1\rangle$ in the interaction basis, which is responsible for the "cross" structure visible in the right panel of Figure 2.6.

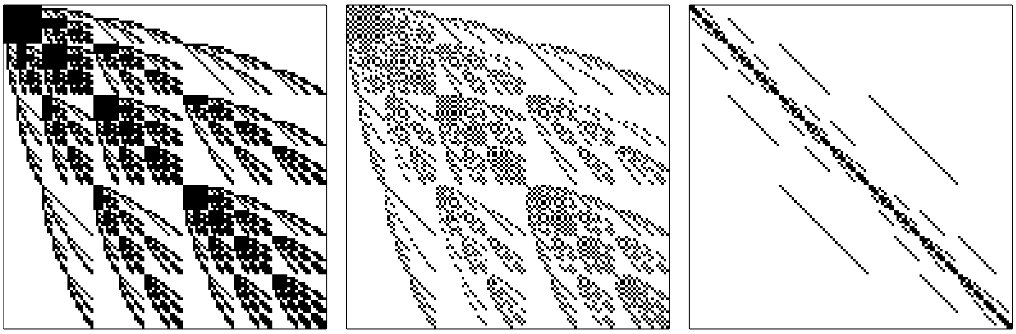

Figure 2.7: Matrix structure of a single realization of the bosonic embedded ensemble introduced in Section 2.2.5 (left), and of the Bose-Hubbard Hamiltonian with HWBCs in the tunneling basis (center), and in the interaction basis (right), for $N = L = 5$ (Hilbert space dimension $\mathcal{N} = 126$). Black pixels indicate nonzero matrix elements.

states via nearest-neighbour tunneling [Equation(2.75)], and, hence, the matrix is much sparser than the more general embedded ensemble. In the tunneling basis, the two-body interaction term [Equation (2.84)] is strongly off-diagonal and the matrix structure is consequently much closer to that of the embedded ensemble, albeit with additional zero elements due to momentum conservation.

2.4.3. Scaled Energy and Scaled Tunneling Strength

When tuning the number of bosons N and the system size L, the energy scales of H change. For instance, the ground state energy in the limit of dominating tunneling scales with N as $E_{\min} \approx -2JN$. Since the width of the spectra of H_{int} and H_{tun} scales differently with N, $E_{\max} - E_{\min} = UN(N-1)/2 \sim N^2$ and $E_{\max} - E_{\min} \approx 4JN \sim N$, respectively, also the relative strength of H_{int} and H_{tun} depends on N and L. Therefore, it does not seem justified to naively compare the properties of Bose-Hubbard Hamiltonians with different system sizes at the same energies, interaction strengths and tunneling strengths. Following References [92, 172, 173], we use the classical limit $\hbar \to 0$ of the Bose-Hubbard Hamiltonian (2.74) to motivate the correct scalings of these three system parameters.

As discussed in Section 2.2.1, the classical limit physically means that the relevant actions S fulfil $S/\hbar \to \infty$. For bosonic many-body systems, the action typically increases with particle number N. This can easily be seen from the definition of the classical action along an orbit Γ with energy E [148, 174],

$$S(\Gamma) = \int_{\Gamma} \boldsymbol{p} \cdot \, \mathrm{d}\boldsymbol{q} - Et. \tag{2.94}$$

Here, the energy typically increases with N, as discussed above for the spectral width of the Bose-Hubbard Hamiltonian, and the same holds true for the (generalized) positions and momenta, since these are linear functions of the creation and annihilation operators [see Equation (2.90) and Reference [42]], which scale with the particle number n_j on the jth site as $a_j^{(\dagger)} \sim \sqrt{n_j}$. Consequently, one way of approaching the limit $S/\hbar \to \infty$ in many-particle systems is given by $N \to \infty$ [148, 175]. By rescaling the creation and annihilation operators as

$$c_j^{(\dagger)} := \frac{1}{\sqrt{N}} a_j^{(\dagger)}, \tag{2.95}$$

the commutator

$$[c_i, c_j^\dagger] = \frac{1}{N}\delta_{ij}$$

vanishes for $N \to \infty$, such that c_j can be replaced by a complex number $c_j = \sqrt{I_j}e^{\mathrm{i}\varphi_j}$ with $c_j^\dagger = c_j^*$. In these new variables, the Hamiltonian reads

$$H = -JN \sum_{j=1}^{L} \left(c_j^\dagger c_{j+1} + c_{j+1}^\dagger c_j \right) + \frac{UN^2}{2} \sum_{j=1}^{L} c_j^\dagger c_j \left(c_j^\dagger c_j - \frac{1}{N} \right). \tag{2.96}$$

Rescaling H by UN^2 and sending N to ∞ yields [92, 172, 173]

$$H_{\text{class}} = \frac{H}{UN^2} = -2\frac{J}{UN} \sum_{j=1}^{L} \sqrt{I_j I_{j+1}} \cos(\varphi_j - \varphi_{j+1}) + \frac{1}{2} \sum_{j=1}^{L} I_j^2. \tag{2.97}$$

Hence, the scaled tunneling strength

$$\eta := \frac{J}{UN} \tag{2.98}$$

is the only parameter governing the classical Hamiltonian. Motivated by this finding, we therefore investigate whether η determines also the properties of the quantum model. As we will see in chapters 3 and 4, this seems to be the case even for moderate particle numbers, although the above calculation is strictly valid only for $N \to \infty$.

Furthermore, we scale the energy E as

$$\varepsilon = \frac{E - E_{\text{min}}}{E_{\text{max}} - E_{\text{min}}}, \tag{2.99}$$

where E_{min} and E_{max} are the energies of the ground state and of the highest excited state of the Bose-Hubbard Hamiltonian, respectively. For $N \to \infty$, the spectral widths of the individual terms H_{int} and H_{tun} are

$$E_{\text{max}} - E_{\text{min}} \approx \begin{cases} \frac{U}{2}N^2, & \text{for } H_{\text{int}}, \\ 4JN = 4\eta UN^2, & \text{for } H_{\text{tun}}, \end{cases} \tag{2.100}$$

and, hence, the spectral width of H behaves as $E_{\text{max}} - E_{\text{min}} \sim UN^2$ for any fixed η. Since ε consequently scales as $1/UN^2$ like H_{class}, this parameter effectively corresponds to the relevant energy scale in the classical limit.

Chapter 3.

Spectrum and Eigenstates of the Bose-Hubbard Hamiltonian

In this chapter we thoroughly investigate the spectrum and the eigenstates of the Bose-Hubbard Hamiltonian. In particular, we use the spectral statistics to determine the region of quantum chaos as a function of energy ε and scaled tunneling strength η, and we relate the emergence of quantum chaos in the spectral statistics to features of the eigenstates as described by their fractal dimensions. If not stated differently, we always consider unit filling factor throughout this chapter, that is, the same number of particles and lattice sites, $N = L$.

3.1. Level Dynamics and Density of States

Before we discuss the features of quantum chaos in the level spacing statistics and the eigenstate fractal dimensions, let us first consider general properties of the spectrum of the Bose-Hubbard Hamiltonian. Figure 3.1 shows the level dynamics of the system, i.e., the evolution of the scaled eigenenergies ε [Equation (2.99)] as functions of the scaled tunneling strength $\eta = J/UN$. Here, we consider $N = 10$ bosons on $L = 10$ sites with PBCs, and the symmetry-induced block with total quasimomentum $Q = 0$ and parity $\Pi = +1$, which gives a Hilbert space of dimension $\mathcal{N} = 4752$.

For small η, i.e., dominating interaction, the energies cluster in distinct manifolds, separated by a certain fundamental spacing or integer multiples thereof. This can easily be explained from the structural features of the Hamiltonian, which in this limit is close to H_{int}. According to Equation (2.76), the eigenenergies of the interaction Hamiltonian are integer multiples of U,

$$E = U \sum_{j=1}^{L} \frac{n_j(n_j - 1)}{2}, \tag{3.1}$$

with on-site occupation numbers $n_1, \dots, n_L$. These energies are typically highly degenerate, since all permutations of the occupation numbers yield the same energy.

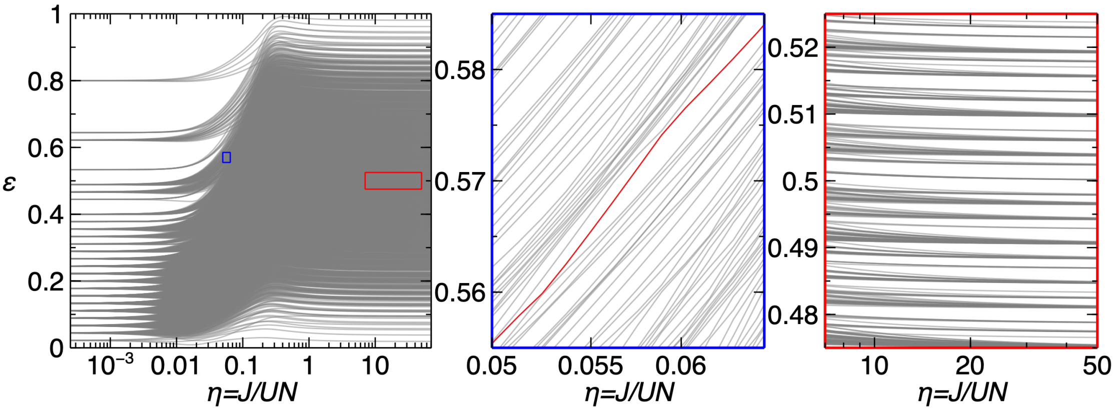

Figure 3.1: Level dynamics of the Bose-Hubbard Hamiltonian (2.74) as a function of the parameter η, for $N = L = 10$, PBCs, total quasimomentum $Q = 0$ and parity $\Pi = +1$ ($\mathcal{N} = 4752$ states). Center and right panels are magnifications of the areas outlined by boxes in the left panel.

Upon increasing η, the degenerate levels fan out and overlap with each other, starting from the low-energy part of the spectrum and subsequently involving also higher energies. For intermediate η, a complex structure emerges, as exemplified by the zoom into the region $\varepsilon \in [0.555, 0.585]$ and $\eta \in [0.05, 0.065]$ (blue panel of Figure 3.1): Energy levels heavily mix via a large number of avoided crossings. For instance, upon a rather small change of η, the level highlighted in red subsequently mixes with the nearest lower and higher levels.

In the regime of dominating tunneling, $\eta \gg 1$, the energies sort again into discrete manifolds, which are much closer together in the center of the spectrum than at its edges. This is illustrated by the magnification of the region $\varepsilon \in [0.475, 0.525]$ and $\eta \in [7, 50]$ (red panel of Figure 3.1). In this limit, the Hamiltonian approaches H_{tun}, whose eigenenergies are the sum of N single-particle contributions

$$E_1(k) = -2J \cos \varphi(k) \tag{3.2}$$

that are distributed symmetrically[1] around the non-scaled energy $E = 0$ [see Equations (2.82) and (2.83)]. Due to this symmetry, the smallest many-particle energy E_{min} is equal to $-E_{\text{max}}$, and, hence, $E = 0$ corresponds to the scaled energy $\varepsilon = 0.5$. Furthermore, various many-particle energies close to $E = 0$ ($\varepsilon = 0.5$) can occur, by combining single-particle energies $E_1(k)$ of different sign and comparable magnitude. These many-particle energies differ slightly from each other depending on the exact combination of single-particle energies. On the other hand, many-particle energies far from $E = 0$ ($\varepsilon = 0.5$) can only be achieved as the addition of single-particle energies with the same

---

[1] Note that for PBCs and odd L, the single-particle spectrum is not exactly symmetric, but deviations from symmetry decay with L. Some implications of these deviations will be discussed in Section 3.2.

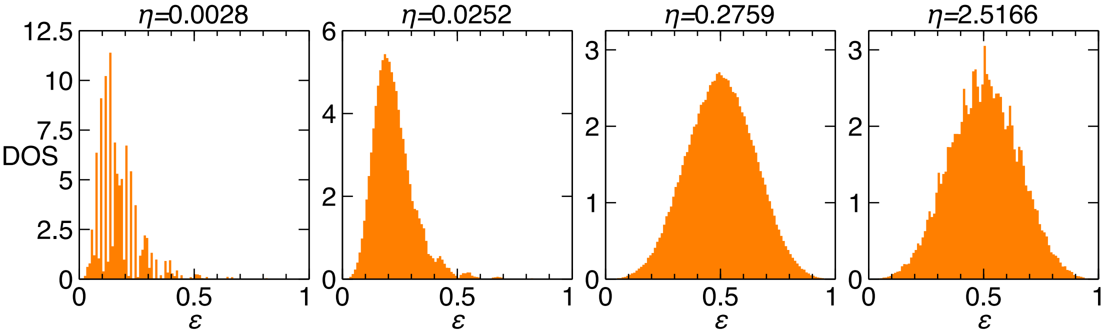

Figure 3.2: Density of states (DOS) for four different η, increasing from left to right, for $N = L = 12$ with PBCs, total quasimomentum $Q = 0$ and parity $\Pi = -1$ (Hilbert space dimension $\mathcal{N} = 55\,898$).

sign and large magnitude, and, consequently, there are fewer energy levels at the edges of the spectrum than around its center.

At $0.01 \lesssim \eta \lesssim 0.03$, the first few excited states (lowest $\varepsilon > 0$) pass through avoided crossings with the ground state [$\varepsilon = 0$ for all η, according to Equation (2.99)]. For the thermodynamic limit $N \to \infty$, $L \to \infty$, $N/L = \text{const}$, it is known that the ground state of the Bose-Hubbard model undergoes a phase transition between a superfluid state at dominating J, in which each particle is spread out over the full lattice, and a Mott-insulating state at dominating U, in which the particles are localized at specific sites [81, 114, 164, 176]. For $N/L = 1$ in one dimension, like for the data shown in Figure 3.1, the critical point of this transition is estimated to be around $J/U \approx 0.3$ [167, 177–180]. If we fix $N = L = 10$, like we do here, this value translates to $\eta \approx 0.03$, which is in good agreement with the positions of the avoided crossings observed here. Further research beyond the scope of this thesis would be needed to unambiguously relate the superfluid-Mott transition of the Bose-Hubbard ground state to these avoided crossings.

In Figure 3.2, the density of states is shown for four exemplary values of η and for $N = 12$ particles on $L = 12$ sites with PBCs, considering the subspace of total quasimomentum $Q = 0$ and parity $\Pi = -1$ (Hilbert space dimension $\mathcal{N} = 55\,898$). At small $\eta = 0.0028$, the density of states consists mainly of discrete peaks, for intermediate $\eta = 0.0252$ and $\eta = 0.2759$ it progressively approaches a seemingly Gaussian shape, and for large $\eta = 2.5166$ several peaks emerge on top of the Gaussian structure. For increasing η, the maximum of the density of states moves from $\varepsilon \approx 0.2$ to $\varepsilon = 0.5$ and the density of states becomes almost symmetric around this maximum.

The peaked structure for small η reflects the discrete energy manifolds of H_{int} emerging for dominating U, and the height of the peaks is associated with the degeneracy of a given manifold's energy levels at $\eta = 0$. This degree of degeneracy is equal to the number of permutations of the on-site occupation numbers n_j and is hence largest, $\sim \mathcal{O}(L!)$, if most n_j are different.[2] In this case, all n_j have to be roughly of order $\mathcal{O}(N/L)$ and each particle interacts only with $n_j - 1 \ll N$ particles, such that the corresponding energy lies in the lower part of the spectrum. Note that the peaks at $\eta = 0.0028$ already cover a finite energy interval and their height is hence slightly reduced as compared to $\eta = 0$.

The highest energy levels, on the other hand, are given by states with $N - n$ particles on a single site and $n \ll N$ particles occupying other sites. Hence, at least $L - n - 1$ sites share the same occupation number $n_j = 0$, and, consequently, the degree of degeneracy of such an energy level (i.e., the number of permutations of occupation numbers) is maximally

$$\frac{L!}{(L-n-1)!}, \tag{3.3}$$

which is a number far smaller than $L!$ for $n \ll L$. The density of states for $\eta \to 0$ is thus strongly reduced in the higher part of the spectrum as compared to the lower part.

In the opposite limit $\eta \to \infty$, H approaches H_{tun}, whose spectrum is the sum of N identical single-particle spectra. According to the central limit theorem, the density of states should then converge to a Gaussian distribution for large N. Deviations from this shape are expected for various reasons: Particle permutation symmetry ensures that many-particle energies emerging from the exact same set of single-particle energies contribute to the density of states just once. Furthermore, the density of states might be enhanced for some many-particle levels if several combinations of single-particle energies sum up to exactly the same value. For instance, single-particle states with quasimomenta k and $L - k$ for PBCs are degenerate, and, consequently, interchanging these two quasimomenta with one another does not change the many-particle energy. Finally, the discrete nature of the single-particle spectrum might still be visible for finite L.

The finding that the maximum of the density of states is at $\varepsilon = 0.5$ for large η can be explained from the separation into single-particle energies, following the same arguments as for the level dynamics in preceding paragraphs of this section: Many energy values around $E = 0$ can be found by combining single-particle terms with different sign and similar magnitude, while just few many-particle energies, given as sums of single-particle energies with the same sign and large magnitude, are available at the edges of the spectrum.

3.2. Fractal Dimensions for Individual Eigenstates

In the following, we will investigate the structure of individual eigenstates, as exposed by their fractal dimensions. Figure 3.3 correlates the scaled eigenenergies ε and the fractal dimensions $\tilde{D}_1$, $\tilde{D}_2$ and $\tilde{D}_\infty$ of all eigenstates of the Bose-Hubbard Hamiltonian in both natural bases, for the same four values of η and the same symmetry-induced subspace

---

[2] Note that for $N = L$, the occupation numbers n_j cannot all be chosen different from one another, such that the degree of degeneracy is typically not exactly $L!$, but slightly smaller.

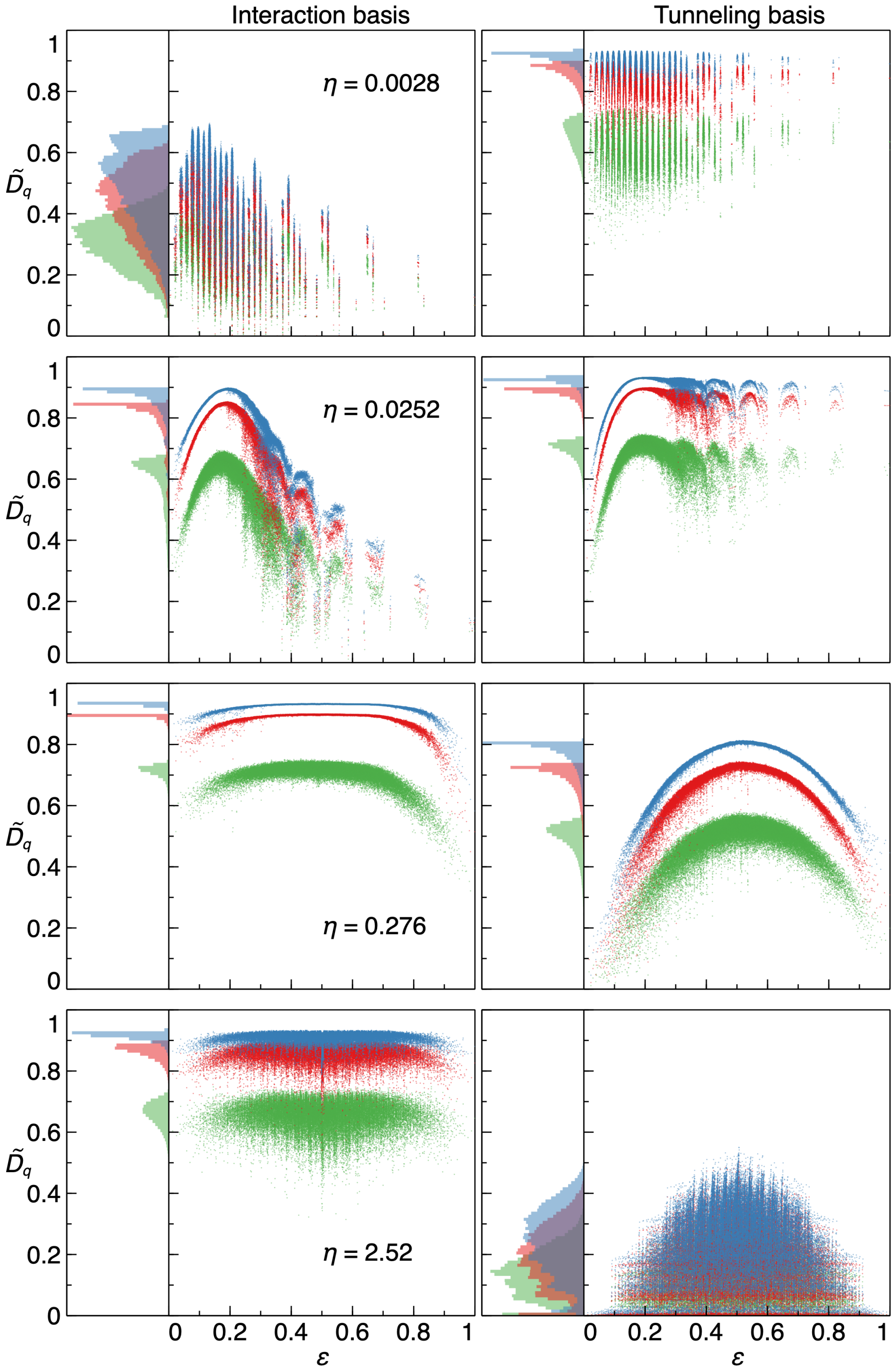

Figure 3.3: Generalized fractal dimensions $\tilde{D}_1$ (blue), $\tilde{D}_2$ (red) and $\tilde{D}_\infty$ (green) as defined in Section 2.3, for the Bose-Hubbard eigenstates, in both natural bases, versus scaled eigenenergy ε, for the same four η values and the same subspace $N = L = 12$, PBCs, $Q = 0$, $\Pi = -1$ ($\mathcal{N} = 55\,898$) as for the density of states in Figure 3.2. The left column of the panels shows the distribution of $\tilde{D}_q$ over all eigenstates.

as for the density of states in Figure 3.2. Furthermore, also the distribution of $\tilde{D}_q$ over all eigenstates is shown.

Quantitatively, $\tilde{D}_1$ is always shifted towards larger values and $\tilde{D}_\infty$ towards smaller values than $\tilde{D}_2$, as expected from the monotonicity of $\tilde{D}_q$ as a function of q [Equation (2.72), proved in Appendix A.2.1]. Qualitatively, though, the three fractal dimensions behave in an analogous manner and depend strongly on η, as well as on the choice of basis:

For small η, i.e., dominating interaction, the fractal dimensions of different eigenstates belonging to the same degenerate manifold for $\eta = 0$ cover a wide range of values. In the interaction basis, the fractal dimensions are much smaller than in the tunneling basis, which is expected, given that the interaction basis is an eigenbasis of H for vanishing tunneling. However, complete localization of the eigenstates in the interaction basis, i.e., $\tilde{D}_q \to 0$, is not found, and must not be expected either: At small η, H_{tun} behaves as a perturbation to H_{int}, and the actual eigenstates for $\eta \to 0$ arise from diagonalizing this perturbation in the degenerate subspaces [42]. Since H_{tun} is off-diagonal in the interaction basis, these eigenstates are typically delocalized over the interaction basis states with the same energy. According to our discussion for the density of states in Section 3.1 (see also Figure 3.2, leftmost panel), the levels at $\varepsilon < 0.5$ are typically more degenerate than the levels close to the upper edge of the spectrum, such that the eigenstates can be delocalized onto a larger portion of the interaction basis and the corresponding fractal dimensions are typically larger. Note that the ground state at unit filling and $U = 0$ is the nondegenerate Fock state $|1, \dots, 1\rangle$ such that the fractal dimensions of this particular state indeed fulfil $\tilde{D}_q \to 0$, see also Reference [81].

Due to the conjugate nature of the two natural bases, as explained in Section 2.4.2, the eigenstates at small η are widely spread in the tunneling basis, and, consequently, their corresponding fractal dimensions are larger than in the interaction basis. However, the fractal dimensions also cover a wide range of values, some of which are clearly distinct from full delocalization in the sense of $\tilde{D}_q \to 1$. To understand the reason for this, consider the interaction basis states $|\boldsymbol{n}\rangle$ in the tunneling basis: According to Equation (2.81), the creation operators $a_j^\dagger$ are superpositions of operators $b_k^\dagger$ with plane-wave (PBCs) or standing-wave (HWBCs) coefficients. Hence, the coefficient $c_{\tilde{\boldsymbol{n}}}$ of the tunneling basis state $|\tilde{\boldsymbol{n}}\rangle$ in the given interaction basis state $|\boldsymbol{n}\rangle$ is essentially a sum of complex exponentials (PBCs) or of trigonometric functions (HWBCs). These summands may add up constructively or destructively, enhancing the amplitude of some tunneling basis states and reducing the amplitude of others. Furthermore, the sum in $c_{\tilde{\boldsymbol{n}}}$ contains more terms for states $|\tilde{\boldsymbol{n}}\rangle$ with many nonzero $\tilde{n}_k$ than for states with just few nonzero $\tilde{n}_k$. Hence, the amplitude of states such as $|\tilde{n}_1 = N, \tilde{n}_{k\neq 1} = 0\rangle$ is further reduced as compared to other tunneling basis states. Consequently, $|\boldsymbol{n}\rangle$ is not uniformly delocalized in the tunneling basis, and $\tilde{D}_q < 1$.

For intermediate η, the distribution of $\tilde{D}_q$ among the eigenstates of similar energies becomes very narrow. For $\eta = 0.0252$, this feature is found only in the lower half of the spectrum, but as η increases to $\eta = 0.276$, almost all regions of the spectrum show this

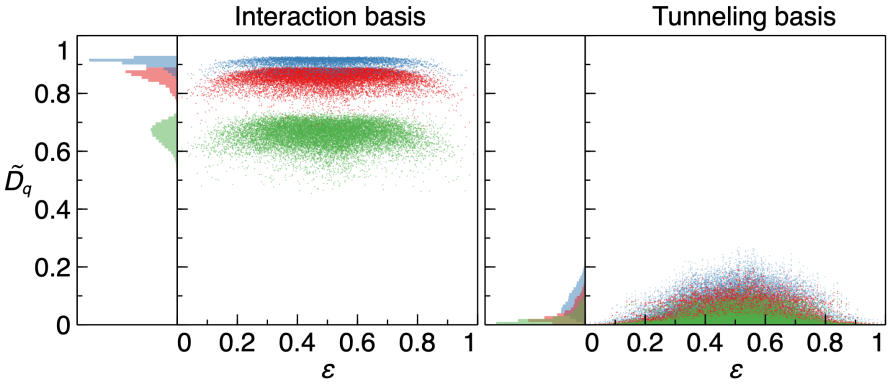

Figure 3.4: Generalized fractal dimensions $\tilde{D}_1$ (blue), $\tilde{D}_2$ (red) and $\tilde{D}_\infty$ (green) as defined in Section 2.3, for the Bose-Hubbard eigenstates, in both natural bases, versus scaled eigenenergy ε, for $\eta = 2.52$ and $N = L = 11$, with PBCs, $Q = 0$ and $\Pi = -1$ ($\mathcal{N} = 15\,907$). The left column of the panels shows the distribution of $\tilde{D}_q$ over all eigenstates.

characteristic. This η dependence correlates with the behaviour of the density of states, in particular with the shift of its maximum from $\varepsilon \approx 0.2$ to $\varepsilon = 0.5$, and can also be related to the level dynamics: The strong mixing of different energy levels is also found predominantly in the lower part of the spectrum for $\eta \lesssim 0.05$, before it starts emerging also for larger energies. Hence we can interpret this “homogenization” of the fractal dimensions among close-in-energy eigenstates as an effect of the strong mixing of these states via avoided crossings.

Specifically in the interaction basis for $\eta = 0.276$, the fractal dimensions of different eigenstates attain large values and become similar throughout a wide portion of the spectrum. This feature is also visible in the distribution of $\tilde{D}_q$ over all eigenstates, which becomes pronouncedly narrow. Such an effect is not seen in the tunneling basis, where the fractal dimensions of eigenstates from different parts of the spectrum are rather distinct and $\tilde{D}_q$ in fact tends to $\tilde{D}_q = 0$ at the edges of the spectrum. Nevertheless, also in this basis the fractal dimensions of close-in-energy eigenstates are very similar, which therefore seems to be a basis-independent feature for intermediate η.

Upon further increasing η towards the limit of dominating tunneling, the distribution of $\tilde{D}_q$ spreads again, in both bases. The fractal dimensions in the interaction basis are still large, but slightly smaller than for intermediate η. For $\eta \to \infty$, H approaches H_{tun} and the eigenbasis is close to the tunneling basis, which is constructed from plane-wave (PBCs) or standing-wave (HWBCs) single-particle states according to Equation (2.80). Following the same arguments as above for the tunneling basis in the opposite limit $\eta \to 0$, the eigenstate coefficients in the interaction basis are larger on some basis states than on others, leading to $\tilde{D}_q < 1$.

As expected, fractal dimensions in the tunneling basis are small in the dominating-tunneling limit $\eta \to \infty$, where the tunneling basis becomes an eigenbasis. Like for the interaction basis in the limit $\eta \to 0$, full localization of all eigenstates in the tunneling basis does not occur, since the eigenstates for $\eta \to \infty$ follow from diagonalizing the perturbation H_{int} on the degenerate energy levels of H_{tun}. However, the fact that not all eigenstates tend towards full localization is a specific feature of PBCs with even L and of HWBCs. For these, the single-particle spectrum is exactly symmetric around the energy $E = 0$, according to

$$\cos\left(\frac{2\pi k}{L}\right) = -\cos\left[\frac{2\pi}{L}\left(\frac{L}{2} - k\right)\right] \qquad \text{(PBCs)}, \tag{3.4}$$

$$\cos\left(\frac{\pi k}{L+1}\right) = -\cos\left[\frac{\pi}{L+1}\left(L + 1 - k\right)\right] \qquad \text{(HWBCs)}. \tag{3.5}$$

Hence, many different combinations of single-particle energies yield exactly the same many-particle energies around $E = 0$ (corresponding to $\varepsilon = 0.5$ for $\eta \to \infty$) and, consequently, the levels around $\varepsilon = 0.5$ are highly degenerate. For PBCs with odd L, where $(L/2) - k$ is not an integer, the single-particle spectrum is not exactly symmetric around $E = 0$, such that the many-particle energies emerging from different sets of single-particle energies are typically distinct and the spectrum is far less degenerate. Figure 3.4 shows a similar scatter plot as the lowest panel of Figure 3.3, for $\eta = 2.52$ with PBCs, quasimomentum $Q = 0$ and parity $\Pi = -1$, using now $N = L = 11$ ($\mathcal{N} = 15\,907$) instead of $N = L = 12$. While the fractal dimensions in the interaction basis are similarly large as for $N = L = 12$, they are much smaller in the tunneling basis, in agreement with the less degenerate spectrum for PBCs with odd L. This is best visible from the distribution of fractal dimensions: For $N = L = 12$, its strongest weight is at small but finite $\tilde{D}_q$ between 0.1 and 0.4 (depending on q), while a strong peak emerges at $\tilde{D}_q = 0$ for $N = L = 11$.

3.3. Energy-Resolved Spectral Statistics and Eigenstate Fractal Dimensions

In the previous two sections, we have discussed various features of the spectrum and of the corresponding eigenstate fractal dimensions, such as a complicated level structure with many avoided crossings for intermediate η (Figure 3.1), accompanied by a delocalization tendency of the eigenstates in both natural bases (Figure 3.3). In the following, we systematically relate the spectral and eigenstate properties to the emergence of quantum chaos as a function of the scaled energy ε and of the scaled tunneling strength η.

3.3.1. Energy Statistics

To determine the chaotic region of the Bose-Hubbard Hamiltonian, we use short-range spectral statistics as described in Section 2.2.3, and in particular the mean level spacing

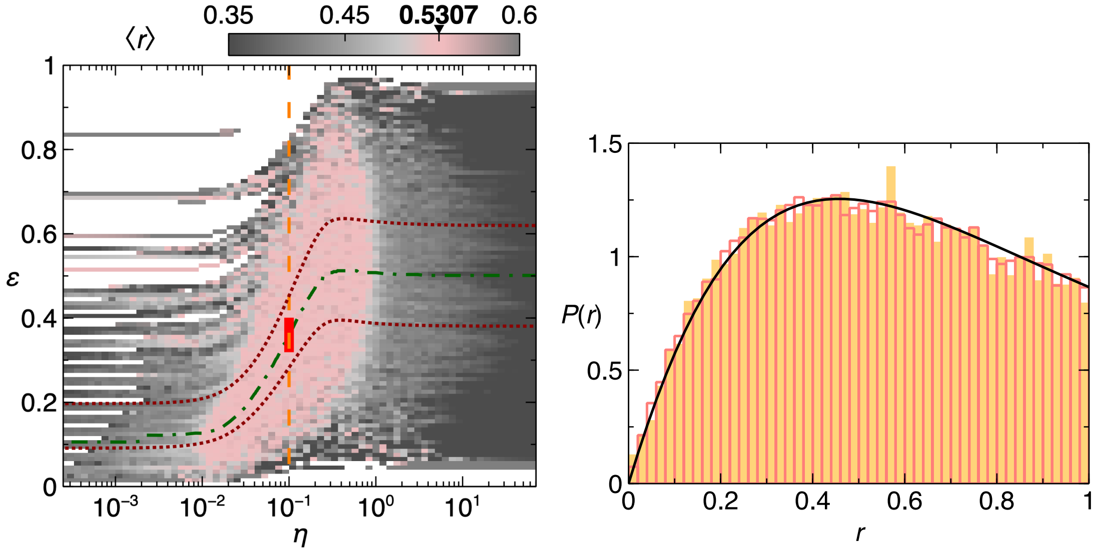

(a)

(b)

Figure 3.5: (a) Mean level spacing ratio $\langle r\rangle$ versus scaled tunneling strength $\eta = J/UN$ and scaled energy ε (Equation (2.99)), and (b) histogram of the level spacing ratio r, for $\eta = 0.100$, $N = L = 12$, with PBCs, total quasimomentum $Q = 0$, and parity $\Pi = +1$ (Hilbert space dimension $\mathcal{N} = 56\,822$). The green dash-dotted line in (a) marks the trajectory of the maximum of the density of states, and the red dotted lines delimit the inner 60 % of the levels, as described in Section 3.4. Empty bars in (b) show $P(r)$ for the full spectrum [orange dashed line in (a)], filled bars give $P(r)$ for $0.33 \leq \varepsilon \leq 0.39$ [thick red line in (a)] and the black line traces $P_{\mathrm{GOE}}(r)$ [Equation (2.39)].

ratio $\langle r\rangle$, Equation (2.38). Figure 3.5(a) shows $\langle r\rangle$ as a function of η and ε, for $N = L = 12$ with PBCs, considering the subspace given by $Q = 0$ and $\Pi = +1$ ($\mathcal{N} = 56\,822$). To obtain this energy-resolved mean, the energy axis is divided into 100 equally spaced bins and the level spacing ratio is calculated for all energies that fall into the same bin. In this figure, white areas denote bins that host less than three levels, which is the minimum number of energies necessary to define the level spacing ratio according to Equation (2.38). These bins are predominantly found at small η, where the discrete spectrum of H_{int} emerges, and at the edges of the spectrum, where the density of states is always small, as shown in Figure 3.2.

For $10^{-2} \lesssim \eta \lesssim 1$ and $0.1 \lesssim \varepsilon \lesssim 0.9$, a slightly bent oval region emerges, in which $\langle r\rangle$ comes close to the value 0.5307 expected numerically for GOE. As discussed in Section 2.2.3, this agreement with $\langle r\rangle_{\mathrm{GOE}}$ is an indication of quantum chaos and we therefore identify this domain as the spectrally chaotic region. In terms of η, this chaotic domain is widest around the center of the spectrum. Upon increasing the energy, the low-η boundary of the chaotic region shifts towards higher η. This shape of the chaotic domain matches well with the region in which the degenerate energy levels fan out and mix with each other, as the comparison of Figure 3.5(a) with the level dynamics in Figure 3.1 shows. Hence, the emergence of chaotic spectral statistics is directly connected to the formation of a bulk of energy levels that interact with each other via a multitude of avoided crossings. We indicate the maximum of the density of states as a function of η by the green dash-dotted line in Figure 3.5(a). Within the chaotic region, this line is always close to the center of the chaotic domain along the ε axis. This shows that the drift of the center of the chaotic region with η is directly connected to the shift of the density of states towards larger ε.

The observed drift of the spectrally chaotic region with the energy and the tunneling strength suggests that a scaling of the form $\varepsilon = \gamma^m \varepsilon_0$ and $\eta = \gamma^n \eta_0$ in terms of a single parameter γ might exist, such that the system properties do not change along curves $(\varepsilon(\gamma), \eta(\gamma))$. Such a scaling would be analogous to the hydrogen atom in a magnetic field [21, 181], where γ corresponds to the strength of the magnetic field.

The mean level spacing ratio, as a single statistical moment, does not fully determine the distribution $P(r)$, which could in principle have the same mean as $P_{\mathrm{GOE}}(r)$ [Equation (2.39)] and still be a rather different distribution. To rule out this possibility, we plot in Figure 3.5(b) the histograms $P(r)$ at $\eta = 0.100$ for the full energy spectrum and for the levels with $0.33 \leq \varepsilon \leq 0.39$, and compare them to $P_{\mathrm{GOE}}(r)$. As the orange and red lines in Figure 3.5(a) show, this value of η is deep in the chaotic domain and $0.33 \leq \varepsilon \leq 0.39$ represents a small energy bin around the maximum of the density of states. This comparison reveals that not just the average $\langle r \rangle$ matches the predictions of GOE, but also the distributions $P(r)$ and $P_{\mathrm{GOE}}(r)$ agree up to fluctuations.[3]

3.3.2. Statistics of Eigenstate Fractal Dimensions

After discussing quantum chaos in terms of spectral statistics, we now go on connecting spectral chaos to eigenstate (de)localization in the two natural bases of the system. For this aim, we study the distribution of fractal dimensions from different eigenstates via its mean $\langle \tilde{D}_q \rangle$, its sample variance $\operatorname{var}(\tilde{D}_q)$ and its skewness parameter $\operatorname{skew}(\tilde{D}_q)$, which for a set of n eigenstates $|\psi_i\rangle$ with fractal dimensions $\tilde{D}_q(|\psi_i\rangle)$ are defined as

$$\langle \tilde{D}_q \rangle = \frac{1}{n} \sum_{i=1}^{n} \tilde{D}_q(|\psi_i\rangle), \tag{3.6}$$

$$\operatorname{var}(\tilde{D}_q) = \frac{1}{n-1} \sum_{i=1}^{n} \left(\tilde{D}_q(|\psi_i\rangle) - \langle \tilde{D}_q \rangle \right)^2, \tag{3.7}$$

$$\operatorname{skew}(\tilde{D}_q) = \frac{\frac{1}{n} \sum_{i=1}^{n} \left(\tilde{D}_q(|\psi_i\rangle) - \langle \tilde{D}_q \rangle \right)^3}{\operatorname{var}(\tilde{D}_q)^{3/2}}. \tag{3.8}$$

---

[3] Note that these fluctuations can be expected, due to the finite number of eigenenergies available for the Bose-Hubbard model and due to the fact that $P_{\mathrm{GOE}}(r)$ as in Equation (2.39) is exact only for $\mathcal{N} = 3$.

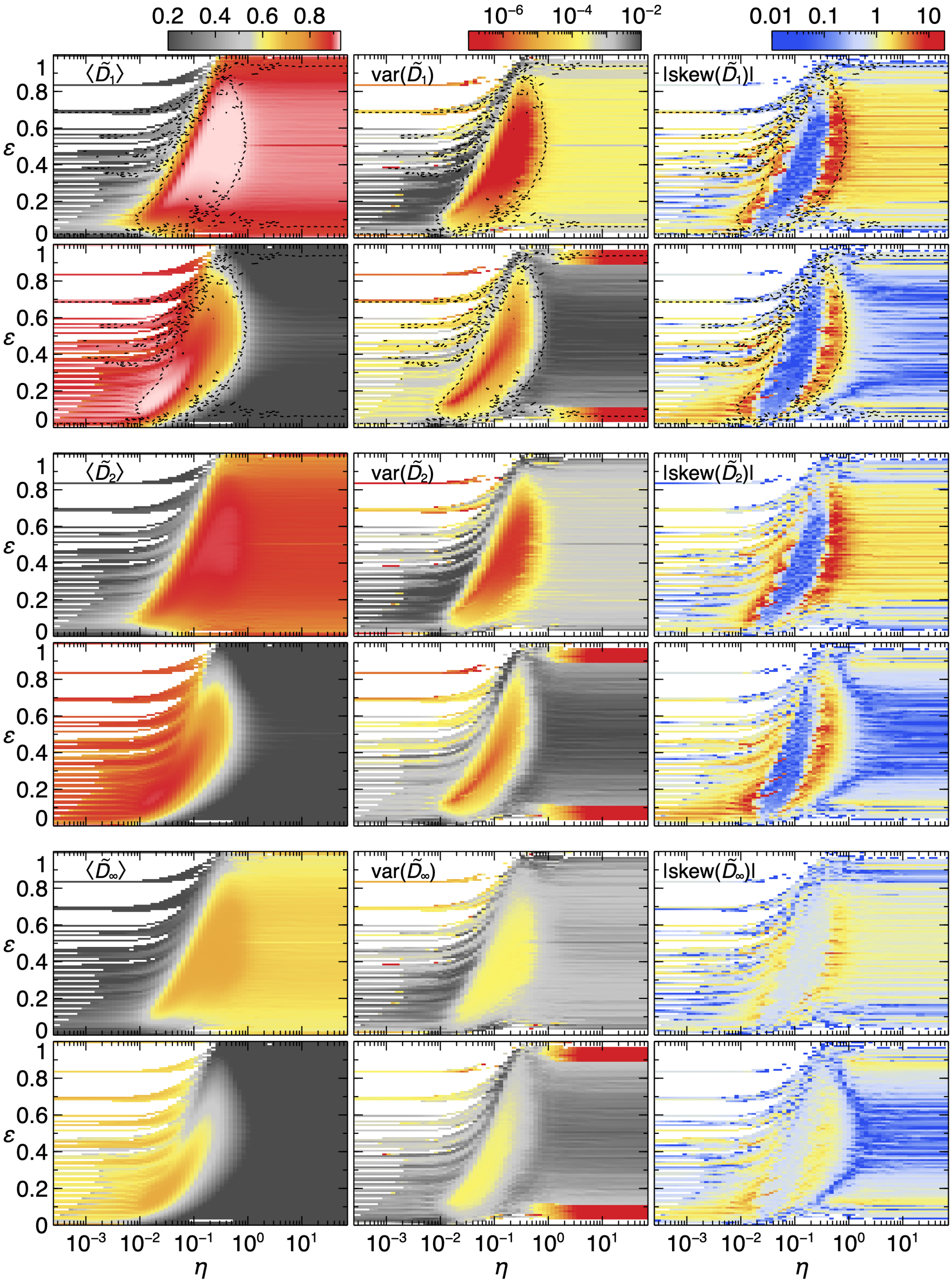

Figure 3.6: Mean (left), variance (center) and absolute skewness (right) for the distributions of $\tilde{D}_1$ (top), $\tilde{D}_2$ (center) and $\tilde{D}_\infty$ (bottom) among different Bose-Hubbard eigenstates [Equations (3.6)–(3.8)], versus η and ε for $N = L = 12$ with PBCs, $Q = 0$ and $\Pi = +1$ ($\mathcal{N} = 56\,822$). Upper (lower) panels of each subplot show the results upon evaluation in the interaction (tunneling) basis. Color bars apply to all panels of the same column. Dashed contour lines in the plots for $\tilde{D}_1$ denote $\langle r \rangle = 0.5$ [see Figure 3.5(a)].

Figure 3.6 shows $\langle \tilde{D}_q \rangle$, $\mathrm{var}\left(\tilde{D}_q\right)$ and the absolute value of $\mathrm{skew}\left(\tilde{D}_q\right)$ for the fractal dimensions $\tilde{D}_1$, $\tilde{D}_2$ and $\tilde{D}_\infty$ as functions of the scaled tunneling strength η and of the scaled energy ε. Here, the energy axis is divided into 100 equally spaced bins and the three statistical quantifiers are calculated for all eigenstates that fall into the same bin at fixed η. The considered subspace is that of quasimomentum $Q = 0$ and parity $\Pi = +1$, for $N = 12$ particles on $L = 12$ sites with PBCs (Hilbert space dimension $\mathcal{N} = 56\,822$), like for $\langle r \rangle$ in Section 3.3.1. Fractal dimensions are calculated in both natural bases.

This figure reveals that the region of quantum chaos as defined by $\langle r \rangle$ (approximately indicated in Figure 3.6 by the contour lines given by $\langle r \rangle = 0.5$) coincides with large average fractal dimensions. These large values are manifestly visible for $\tilde{D}_q$ in the interaction basis, where, e.g., $\langle \tilde{D}_1 \rangle$ rises from $\langle \tilde{D}_1 \rangle \approx 0.5$ to $\langle \tilde{D}_q \rangle \gtrsim 0.9$ in a small ε-dependent range of η that agrees with the low-η boundary of the chaotic region, and falls off again to slightly smaller values around 0.85 on the high-η side of the chaotic domain. In the tunneling basis, the fractal dimensions reach their largest values in the low-energy and low-η range of the chaotic region and fall off already to intermediate values for larger η and ε even deep within the region of quantum chaos. Nevertheless, a further decay from these intermediate values to much smaller $\langle \tilde{D}_q \rangle$ in a small range of η, for instance from $\langle \tilde{D}_1 \rangle \approx 0.7$ to $\langle \tilde{D}_1 \rangle \lesssim 0.3$, unveils clearly the high-η boundary of the chaotic region also in the tunneling basis.

An even stronger correlation with spectral chaos is exhibited by the variance of the fractal dimensions, which is reduced by several orders of magnitude within the region of quantum chaos. This effect is visible on both the high-η and the low-η edge of the chaotic domain, in contrast to the mean fractal dimension, where the difference between the chaotic and the non-chaotic region is significantly more pronounced on one edge. Slight quantitative differences of the variance do occur between different bases, particularly in the high-energy part of the chaotic region, where $\mathrm{var}\left(\tilde{D}_q\right)$ is considerably smaller in the interaction basis than in the tunneling basis. Nevertheless, this pronounced minimum of $\mathrm{var}\left(\tilde{D}_q\right)$ is qualitatively the same for both natural bases and for all fractal dimensions considered. This decay of the variance might therefore serve as a basis-independent quantifier of quantum chaos, in the sense that $\mathrm{var}\left(\tilde{D}_q\right)$ might be strongly reduced in *any* physically relevant basis.

This hypothesis is also supported by the results of Reference [112] for fermions and hard-core bosons. In that work, the Shannon entropy and the inverse participation ratio of the eigenstates were investigated in the tunneling basis and in the eigenbasis of the integrable part of the Hamiltonian, finding that the fluctuations of these quantifiers among close-in-energy eigenstates are smallest exactly in the parameter range of chaotic spectral statistics, for both bases. However, our results presented in Figure 3.6 go beyond the findings of Reference [112], by showing this relation also as a function of the energy.

At this point, we need to elaborate more on the term “physically relevant basis” and stress that it should not be understood as “any arbitrary basis”: At a fixed value of η even deep within the chaotic domain, one can always construct (typically highly nontrivial)

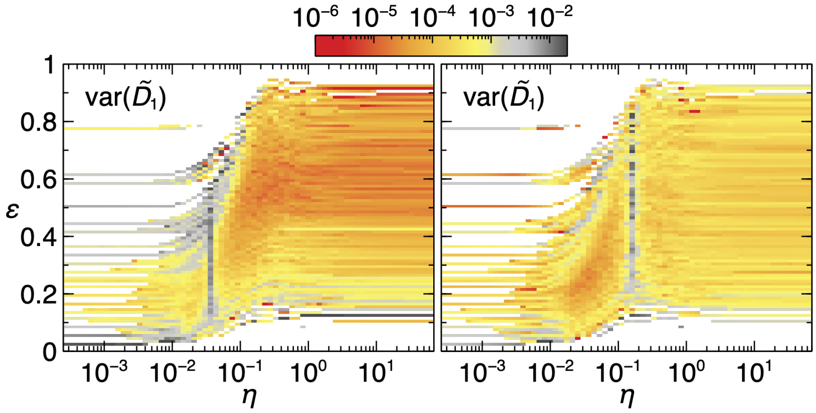

Figure 3.7: Variance var $(\tilde{D}_1)$ in one basis chosen such that var $(\tilde{D}_q)$ is large for $\eta = 0.0485$ (left) and another basis such that var $(\tilde{D}_q)$ is large for $\eta = 0.2117$ (right), for $N = L = 9$ with PBCs, $Q = 0$ and $\Pi = +1$ ($\mathcal{N} = 1387$), both η selected arbitrarily within the chaotic region. See text for details on the construction of these bases.

bases with quite large var $(\tilde{D}_q)$, simply by applying a basis transformation such that the eigenvectors have the exact same coefficients as the eigenvectors in one of the natural bases for an η value far outside the chaotic domain. In a more technical sense, if the eigenstates $|\psi_n(\eta)\rangle$ at a fixed η are given as

$$|\psi_n(\eta)\rangle = \sum_{i=1}^{\mathcal{N}} c_{ni}(\eta)\,|\varphi_i\rangle\,, \tag{3.9}$$

where $\{|\varphi_i\rangle \,:\, i = 1,\ldots,\mathcal{N}\}$ is the tunneling or the interaction basis, then, for two values η_1 and η_2, the eigenstate coefficients in the basis given by

$$|\chi_j\rangle = \sum_{n,i=1}^{\mathcal{N}} c^*_{nj}(\eta_1)c_{ni}(\eta_2)\,|\varphi_i\rangle \tag{3.10}$$

at the scaled tunneling strength η_2 are exactly the same as the eigenstate coefficients at η_1 in the basis $\{|\varphi_i\rangle\}$:

$$|\psi_n(\eta_2)\rangle = \sum_{i=1}^{\mathcal{N}} c_{ni}(\eta_2)\,|\varphi_i\rangle = \sum_{j=1}^{\mathcal{N}} c_{nj}(\eta_1)\,|\chi_j\rangle\,. \tag{3.11}$$

However, due to the large number of avoided crossings in the chaotic region, the eigenstates change strongly even for small variations of η. Hence, even though a deliberate choice of basis may make var $(\tilde{D}_q)$ large for a fixed η in the chaotic region, the variance in that same basis will probably vary drastically under just slight changes of η and might become strongly reduced, similar to the behaviour in the two natural bases. This effect is exemplified in Figure 3.7, where var $(\tilde{D}_1)$ is shown for two bases constructed to have a large variance for a specific value of η chosen arbitrarily deep in the chaotic domain ($\eta = 0.0485$ and $\eta = 0.2117$, respectively). Even for small perturbations of η the variance decreases strongly and stays similarly small throughout the chaotic domain. Hence, even though we cannot expect var $(\tilde{D}_q)$ to be strongly reduced in any basis for all values of η within the chaotic domain, the variance might still be a basis-independent quantifier of quantum chaos in the sense that it is reduced throughout the chaotic region except for a small range of η.

In the tunneling basis, var $(\tilde{D}_q)$ is very small also for large η at the edges of the spectrum, where $\langle \tilde{D}_q \rangle$ in the tunneling basis attains its smallest values. As discussed in Section 3.2, the eigenstates for $\eta \to \infty$ are typically delocalized over the degenerate tunneling basis states. Due to the nonlinear dependence of the single-particle energies on the index k, different sets of single-particle levels will typically not add up to the same many-particle energy and only few states will be degenerate. Consequently, the fractal dimensions in the tunneling basis are equally small for most close-in-energy eigenstates at the spectrum edges and hence, var $(\tilde{D}_q)$ is strongly reduced. Note that the center of the spectrum, with rather large var $(\tilde{D}_q)$ for large η, is an exception to this behaviour, since the symmetry of the spectrum around $E = 0$ adds more degeneracies, as discussed towards the end of Section 3.2.

The skewness, which quantifies the asymmetry of the distribution, also shows a qualitatively basis-independent behaviour like the variance. Particularly at the boundaries of the chaotic region in terms of ε and η, the skewness registers a sharp surge by at least one order of magnitude. Inspection of the data shows that the skewness is actually negative in these ranges of η and ε, which means that a strong tail develops towards smaller values of $\tilde{D}_q$. Hence, not all eigenstates with similar energies acquire large $\tilde{D}_q$ values at exactly the same η, but some states remain at smaller values for a wider range of η, i.e., the delocalization of close-in-energy eigenstates onto the two natural bases starts at slightly different values of η. Deep within the chaotic domain, the skewness is strongly reduced for $q = 1, 2$, yielding values smaller than ≈ 0.1 as compared to values larger than 1 at the boundaries. Hence, the distribution of $\tilde{D}_{1,2}$ in the chaotic region is highly symmetric. For $q = \infty$, the absolute skewness is larger than ≈ 0.4 even deep within the region of quantum chaos, which shows that the distribution remains notably asymmetric. We note that the skewness parameter on its own, even though it captures the boundaries of the chaotic region quite well, does not serve to identify unambiguously the center of the chaotic domain: In the tunneling basis, for instance, the distribution of $\tilde{D}_{1,2}$ for large η and intermediate ε is similarly symmetric as in the center of the chaotic region.

The results for mean and variance of $\tilde{D}_q$ in the chaotic region give a clear connection between spectral chaos and eigenstate localization properties as encoded into the fractal dimensions. Whenever the short-range spectral correlations indicate quantum chaos, the different eigenstates are similarly delocalized, in both natural bases. This can be seen as an analogy to classical ergodicity: As discussed in Section 2.1, ergodic classical trajectories visit the whole phase space uniformly and are therefore widely spread with respect to (generalized) position and momentum coordinates. In a similar way, for the quantum Bose-Hubbard model investigated here, large values of $\tilde{D}_q$ indicate that the eigenstates are widely distributed over the Fock bases given by number operators $n_j = a_j^\dagger a_j$ $(j = 1, \ldots, L)$ and $\tilde{n}_k = b_k^\dagger b_k$ $(k = 1, \ldots, L)$, respectively, and that this distribution is essentially uniform (compare Section 2.3).

Additionally, while the range of momenta and positions visited by trajectories of classically integrable systems differs among individual trajectories, since each of them populates its own invariant torus, trajectories of chaotic systems cover a rather similar amount of phase space as compared to each other. For instance, in the case of strictly ergodic motion, all of them fill the entire phase space. Hence, classical localization properties, understood as the amount of phase space that is visited throughout time evolution, are very similar among different classical chaotic trajectories. This is directly analogous to the comparable delocalization in Fock space of all chaotic quantum eigenstates, as revealed by the sharp decay of $\operatorname{var}\left(\tilde{D}_q\right)$ towards the center of the chaotic region.

The fact that the eigenstates within the chaotic region are widely distributed across the interaction and tunneling basis states can furthermore be related to thermalization, in analogy to classical ergodicity as defined in Equation (2.5): According to this definition, the time average of a phase-space function f along an ergodic trajectory approaches the corresponding phase-space average and hence becomes independent of the specific trajectory at a certain fixed energy. Due to the wide distribution of eigenstates over the basis states, we can expect in a similar way that a Bose-Hubbard system initialized in a Fock state quickly becomes distributed over a large portion of the eigenstates, independently of the specific initial state.

3.4. Spectrally Averaged Spectral Statistics and Eigenstate Structure

In the preceding section, the Bose-Hubbard Hamiltonian was discussed considering statistical moments of the distributions of $\tilde{D}_q$ and r over fixed energy intervals. We now investigate these distributions over the bulk of the spectrum instead. In the following, we fix a certain percentage $p \in [0, 100]$ and define the bulk as the inner $p\%$ of the spectrum, neglecting the highest and the lowest $(100 - p/2)\%$ of the energy levels. In Figure 3.5(a) of the preceding section, the evolution of the bulk defined by the inner $60\,\%$ is indicated by red dotted lines on top of the energy-resolved $\langle r \rangle$. From this figure, it is clear that the energy range occupied by the bulk shifts with η in a similar way as the maximum of the density of states [green dash-dotted line in Figure 3.5(a)]. Hence, this approach offers a different perspective on the emergence of the chaotic region as a function of η.

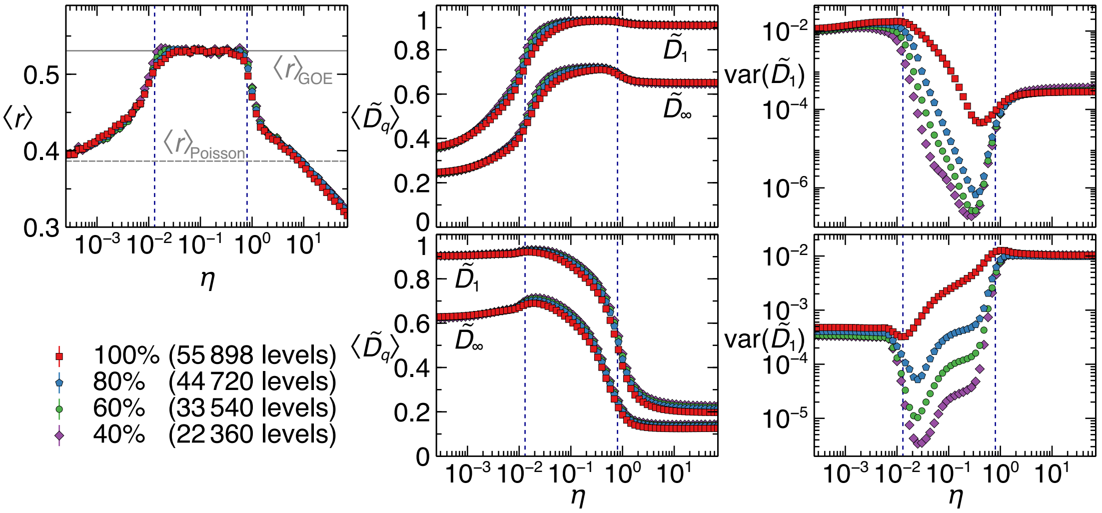

Figure 3.8: Mean level spacing ratio $\langle r \rangle$ (left), mean fractal dimensions $\langle \tilde{D}_{1,\infty} \rangle$ (center), and variance $\operatorname{var}(\tilde{D}_1)$ (right) over the inner $p\%$ of the spectrum ($p \in [40, 100]$) corresponding to n levels as indicated in the legend, for $N = L = 12$ with PBCs, total quasimomentum $Q = 0$ and parity $\Pi = -1$. Top (bottom) panels show results in the interaction (tunneling) basis. Grey lines in the plot of $\langle r \rangle$ mark $\langle r \rangle_{\text{GOE}}$ (solid) and $\langle r \rangle_{\text{Poisson}}$ (dashed), Equations (2.41) and (2.43). Blue dashed lines approximately indicate the η region where $\langle r \rangle \approx \langle r \rangle_{\text{GOE}}$. Error bars are contained within symbol size.

3.4.1. Averages over Different Percentages of the Spectrum

Figure 3.8 shows, as functions of η, the quantifiers $\langle r \rangle$, $\langle \tilde{D}_1 \rangle$, $\langle \tilde{D}_\infty \rangle$ and $\operatorname{var}(\tilde{D}_1)$ in the interaction and tunneling bases calculated from the inner $p\%$ of the states, with p ranging from 40 to 100. Here, we treat the individual level spacing ratios and fractal dimensions as independent data points which sample a continuous probability distribution, such that we can attach error bars to the data points according to standard errors $\delta\mu$ of the mean and δv of the variance. These read for $n \gg 1$ data points $x_1, \ldots, x_n$ [182, 183]

$$\delta\mu^2 = \frac{\operatorname{var}(x_1, \ldots, x_n)}{n}, \qquad \delta v^2 = \frac{1}{n}\left(\mu_4 - \frac{n-3}{n-1}\mu_2^2\right), \tag{3.12}$$

with the usual variance, like in Equation (3.7), and the kth central moments

$$\mu_k = \frac{1}{n}\sum_{i=1}^{n} \left(x_i - \langle x \rangle\right)^k . \tag{3.13}$$

The system under consideration is that of $N = L = 12$ with PBCs, and the subspace defined by quasimomentum $Q = 0$ and parity $\Pi = -1$.

Also in the spectral average, the mean level spacing ratio shows a clear fingerprint of quantum chaos for $1.3 \times 10^{-2} \lesssim \eta \lesssim 0.8$, where $\langle r \rangle \approx \langle r \rangle_{\text{GOE}}$. This holds true even if the average is taken over the full spectrum, $p = 100$. This result confirms that quantum chaos manifests itself not only in a large energy interval, as we discussed in the previous section, but also in a large percentage of the levels. Note that these two statements are not necessarily equivalent to each other, since, in principle, large energy intervals can host just few states, and the majority of states can, in principle, populate a rather small energy interval. The transition between $\langle r \rangle < \langle r \rangle_{\text{GOE}}$ and $\langle r \rangle \approx \langle r \rangle_{\text{GOE}}$ is rather sharp and becomes ever sharper when reducing the percentage of the states that are considered. This sharpening of the quantum-chaos transition is in agreement with the energy dependence of the chaotic region observed in Figure 3.5(a) of the preceding section: As the number of levels considered for the bulk is decreased, also the corresponding energy interval becomes smaller, and hence the range of η values within which the spectral statistics switches to GOE statistics gets narrower.

In the integrable limits, $\langle r \rangle$ changes just minimally with the percentage p. We stress that this does not necessarily imply that the spectral statistics at the edges of the spectrum, $\varepsilon \gtrsim 0$ and $\varepsilon \lesssim 1$, is the same as in the center of the spectrum, $\varepsilon \approx 0.5$: The highest and lowest $(100 - p/2)\%$ of the levels might cover a quite large energy interval and their average level spacing ratio could be dominated by energies clearly different from $\varepsilon = 0$ or $\varepsilon = 1$. For instance at $\eta \approx 10$, the latter is a very likely scenario, since $\langle r \rangle$ is smaller at the edges of the spectrum than around $\varepsilon = 0.5$ [see Figure 3.5(a)], while it barely changes as a function of the percentage of the spectrum.

The limit of $\langle r \rangle$ for $\eta \to \infty$ is clearly distinct from the Poisson prediction, [Equation (2.43)], even though the Hamiltonian is integrable in this limit. On the other hand, $\langle r \rangle$ seems to converge to $\langle r \rangle_{\text{Poisson}}$ in the opposite limit $\eta \to 0$. Note, however, that the exact limit $\eta = 0$ deviates from Poissonian level statistics again: Here, the only possible level spacings are $s = 0$ and $s = nU$, with $n \in \mathbb{N}$, such that the level spacing distribution obeys a peaked structure rather than the exponential decay of Poisson, Equation (2.33). Close inspection shows that our reasoning for Poissonian level statistics, as outlined in Section 2.2.3, is not applicable to the integrable limits $\eta = 0$ and $\eta = \infty$ of the Bose-Hubbard Hamiltonian: For these two points, the Hamiltonian depends on a single parameter only (U or J, respectively), which governs just the global energy scale and does not induce any level crossings, in contrast to the parameter dependence discussed in Section 2.2.3 for the motivation of Poissonian level statistics.

The finding that $\langle r \rangle \approx \langle r \rangle_{\text{Poisson}}$ for $\eta \to 0$ can be understood from the symmetries of H_{int} and H_{tun}. As discussed in Section 2.4.2, H_{int} is symmetric with respect to all permutations of the sites, and its symmetry group is hence the symmetric group $\mathfrak{S}_L$. On the other hand, the full Hamiltonian just fulfils the symmetries of the dihedral group D_L for PBCs and of the two-element group D_1 for HWBCs. At $\eta = 0$, the levels are sorted into subspectra defined by the different irreducible representations of $\mathfrak{S}_L$. Since D_L and D_1 are subgroups of $\mathfrak{S}_L$, each of these irreducible representations is also a (not necessarily irreducible) representation of D_L and D_1 [170, 171]. As the symmetry is reduced towards D_L (D_1), the irreducible representations of $\mathfrak{S}_L$ decompose into irreducible representations of the smaller group D_L (D_1) [170, 171]. Since one irreducible representation of D_L (D_1) can appear in the decompositions of several irreducible representations of $\mathfrak{S}_L$, the energy levels at $\eta = 0$ will typically belong to various subspectra induced by the symmetries of $\mathfrak{S}_L$, even if we consider just the symmetry-induced subspace corresponding to one irreducible representation of D_L (D_1). If the subspectra of different irreducible representations of $\mathfrak{S}_L$ can be treated as independent of each other, levels from different subspectra undergo real crossings and our reasoning for the emergence of Poissonian statistics, as outlined in Section 2.2.3, is applicable. Note that these symmetry arguments are not valid in the limit $\eta \to \infty$, since H_{tun} has exactly the same symmetries as the full Hamiltonian.

Also in terms of the spectral averages, quantum chaos as defined by $\langle r \rangle \approx \langle r \rangle_{\text{GOE}}$ is accompanied by an increase in the average fractal dimensions in both natural bases, as shown in Figure 3.8. Recall that $\tilde{D}_1$ and $\tilde{D}_\infty$ constitute, respectively, upper and lower bounds for the other $\tilde{D}_q$ with $1 \leq q \leq \infty$. Consequently, also the other mean fractal dimensions $\langle \tilde{D}_q \rangle$ become large in the chaotic region. At the boundaries of the chaotic domain, $\langle \tilde{D}_q \rangle$ increases slightly when the influence of the spectral edges is reduced. In the interaction basis, this effect is predominantly visible for the low-η edge of quantum chaos, while in the tunneling basis it is more pronounced in the center of the chaotic region and at its high-η boundary. These are also the ranges of η for which $\tilde{D}_q$ changes the most as a function of η, as the eigenstates switch from being strongly localized in one of the two natural bases to becoming delocalized in both of them. The influence of non-chaotic states with lower $\tilde{D}_q$ is hence most noticeable at the low-η edge for the interaction basis and the high-η edge for the tunneling basis.

As in the energy-resolved picture of Section 3.3, the variance of $\tilde{D}_1$ over a certain percentage of the spectrum reduces by several orders of magnitude within the chaotic region, for both natural bases. In the tunneling basis, $\operatorname{var}(\tilde{D}_1)$ in the chaotic region decreases strongly when the percentage of the states is reduced, while the minimum of $\operatorname{var}(\tilde{D}_1)$ in the interaction basis becomes only slightly more pronounced for the inner 40 % of states as compared to the inner 80 %. This finding is in good agreement with the observation from Figure 3.3 that $\tilde{D}_q$ of different eigenstates in the interaction basis become similar throughout a wide energy range in the chaotic region. Quantitatively, the minimum of $\operatorname{var}(\tilde{D}_1)$ is at least one order of magnitude deeper in the interaction basis than in the tunneling basis, and the minimal values of $\operatorname{var}(\tilde{D}_q)$ are found at larger $0.2 \lesssim \eta \lesssim 0.4$ for the interaction basis as compared to $0.02 \lesssim \eta \lesssim 0.03$ for the tunneling basis. Nevertheless, the η range in which the variance is strongly reduced, $10^{-2} \lesssim \eta \lesssim 1$, is the same for both bases.

3.4.2. Dependence on System Size

In the following, we discuss the dependence of quantum chaos on system size from the perspective of spectral averages, considering always the inner 70 % of the spectrum, i.e., neglecting the highest and lowest 15 % of the levels. A similar investigation from the energy-resolved perspective will follow in Section 4.3. In Figure 3.9, $\langle r \rangle$, $\langle \tilde{D}_1 \rangle$, $\langle \tilde{D}_\infty \rangle$ and

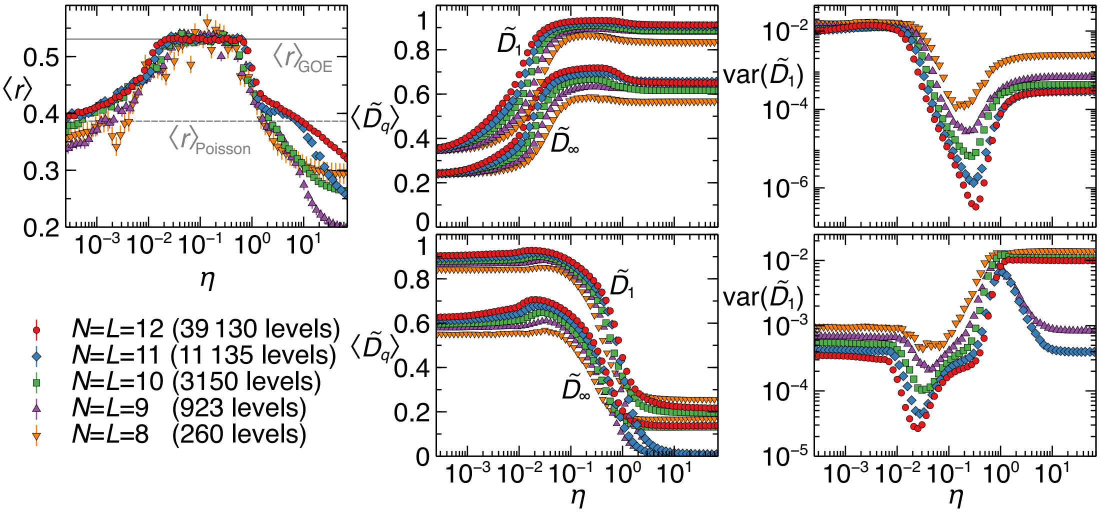

Figure 3.9: Mean level spacing ratio $\langle r\rangle$ (left), mean fractal dimensions $\langle \tilde{D}_{1,\infty}\rangle$ (center), and variance var $(\tilde{D}_1)$ (right) over the inner 70 % of the spectrum (including n levels as indicated in the parentheses in the legend), for the subspace $Q = 0$, $\Pi = -1$ with PBCs, and for $N = L$ from 8 to 12. Top (bottom) panels show results in the interaction (tunneling) basis. Grey lines in the plot of $\langle r\rangle$ mark $\langle r\rangle_{\text{GOE}}$ (solid) and $\langle r\rangle_{\text{Poisson}}$ (dashed), Equations (2.41) and (2.43). When not explicitly shown, error bars [calculated as in Equation (3.12)] are contained within symbol size.

var $(\tilde{D}_1)$ are shown as functions of η, for particle numbers and lattice lengths ranging from $N = L = 8$ to $N = L = 12$. Here, we consider PBCs with quasimomentum $Q = 0$ and parity $\Pi = -1$.

For $10^{-2} \lesssim \eta \lesssim 1$ and for all system sizes considered, $\langle r\rangle$ approximately equals the prediction of GOE, Equation (2.41). This holds true even for the smallest system $N = L = 8$, even though fluctuations around $\langle r\rangle_{\text{GOE}}$ are large, due to the small number of levels available. Upon increasing system size, the region of spectral chaos, $\langle r\rangle \approx \langle r\rangle_{\text{GOE}}$, slightly increases towards smaller and larger η. The mean level spacing ratio for η outside the region $10^{-2} \lesssim \eta \lesssim 1$ is clearly different from $\langle r\rangle_{\text{GOE}}$ for all system sizes considered, which shows that the region of spectral chaos can be identified even for the smallest L investigated here.

Towards the limit $\eta \to \infty$, $\langle r\rangle$ deviates from the prediction of Poissonian level statistics for all system sizes, and the slope of $\langle r\rangle$ as a function of η differs among different system sizes in this limit. There is hence no clear hint that for this range of η, $\langle r\rangle$ attains a well-defined value $\langle r\rangle_\infty$ in the limit $N, L \to \infty$. In contrast, the mean level spacing ratio in the other limit $\eta \to 0$ comes closer to $\langle r\rangle_{\text{Poisson}}$ as L grows, in agreement with the symmetry-based discussion of the previous section.

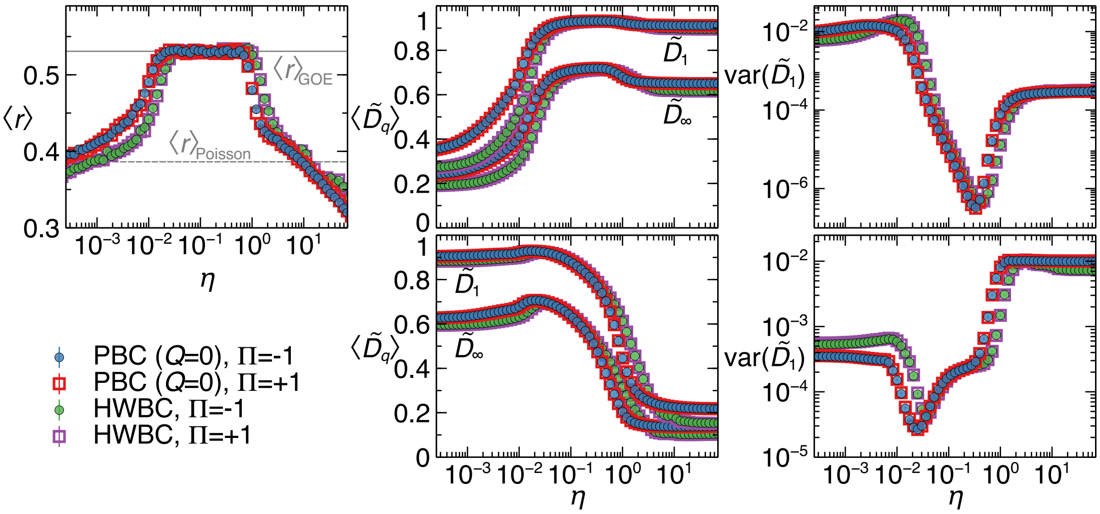

Figure 3.10: Mean level spacing ratio $\langle r \rangle$ (left), mean fractal dimensions $\langle \tilde{D}_{1,\infty} \rangle$ (center), and variance var $(\tilde{D}_1)$ (right) over the inner 70 % of the spectrum, for the boundary conditions and parities indicated in the legend, and $N = L = 12$ for PBCs, $N = L = 10$ for HWBCs. Top (bottom) panels show results in the interaction (tunneling) basis. Grey lines in the plot of $\langle r \rangle$ mark $\langle r \rangle_{\text{GOE}}$ (solid) and $\langle r \rangle_{\text{Poisson}}$ (dashed), Equations (2.41) and (2.43). Error bars are contained within symbol size.

In both bases, the maximum of $\langle \tilde{D}_q \rangle$ in the chaotic region takes larger values and gets more pronounced as the system size increases, which is particularly visible for $\langle \tilde{D}_\infty \rangle$. At the same time, the region of maximal $\langle \tilde{D}_q \rangle$ widens slightly on both ends, in agreement with the increase of the chaotic region as defined by $\langle r \rangle$.

The minimum of var $(\tilde{D}_1)$ is also clearly visible even for the smallest system size considered, in both bases. Hence, the pronounced decrease of var $(\tilde{D}_q)$ can serve as a probe of quantum chaos even for small systems. As N and L grow, the region of very small variance widens on both ends, in unison with $\langle r \rangle$ and $\langle \tilde{D}_q \rangle$.

For the interaction basis in both limits $\eta \to 0$, $\eta \to \infty$ and for the tunneling basis in the limit $\eta \to 0$, $\langle \tilde{D}_{1,\infty} \rangle$ and var $(\tilde{D}_1)$ are of similar magnitude for all system sizes considered, up to small deviations which decay with L. In contrast, $\langle \tilde{D}_{1,\infty} \rangle$ and var $(\tilde{D}_1)$ in the tunneling basis for $\eta \to \infty$ are significantly smaller for odd $N = L$ than for even $N = L$. This reflects the enhanced localization of the eigenstates as $\eta \to \infty$ for PBCs with odd L, as discussed in Section 3.2.

3.4.3. Effect of Parity and Boundary Conditions

We now analyse how the spectral statistics and eigenstate fractal dimensions are affected by boundary conditions and parity. Figure 3.10 shows the quantifiers $\langle r \rangle$, $\langle \tilde{D}_{1,\infty} \rangle$ and

$\operatorname{var}(\tilde{D}_1)$ as functions of η, for both boundary conditions (PBCs and HWBCs) and both parities $\Pi = \pm 1$. Here, we consider the inner 70 % of the spectrum, and for PBCs we choose the quasimomentum $Q = 0$. The particle numbers and lattice lengths ($N = L = 12$ for PBCs and $N = L = 10$ for HWBCs) are chosen to have comparable dimensions of the different symmetry subspaces: $\mathcal{N} = 46\,126$ ($\Pi = -1$) and $\mathcal{N} = 46\,252$ ($\Pi = +1$) for HWBCs, and $\mathcal{N} = 55\,898$ ($\Pi = -1$) and $\mathcal{N} = 56\,822$ ($\Pi = +1$) for PBCs. Note that the even-parity subspace is always larger than the odd-parity subspace, since reflection-symmetric Fock states, such as $|n_1 = 1, \dots, n_L = 1\rangle$, contribute only to the even-parity subspace.

All quantifiers considered in Figure 3.10 have a qualitatively similar shape for both boundary conditions. This shape is, however, shifted to smaller η for PBCs as compared to HWBCs, which affects in particular the onset of quantum chaos as a function of η. The minimum of the variance is marginally smaller for PBCs than for HWBCs, especially in the tunneling basis, which we interpret as an effect of the larger Hilbert space dimension, in a similar fashion as the reduction of $\operatorname{var}(\tilde{D}_q)$ observed for larger $N = L$ in Section 3.4.2. The shift of all quantifiers towards smaller η for PBCs can be understood as a consequence of the different structures of the Hamiltonian for the two boundary conditions: Due to the link between sites 1 and L for PBCs, the effect of tunneling in Fock space is stronger for PBCs than for HWBCs, such that smaller values of the scaled tunneling strength η are sufficient to drive the system into quantum chaos.

For both boundary conditions and all quantifiers shown, positive and negative parity essentially yield the same values and can barely be distinguished from one another. Only for $\langle r\rangle$ at the boundaries of the chaotic region, small differences between $\Pi = +1$ and $\Pi = -1$ are visible. Numerical inspection shows that the relative deviations

$$\frac{|A(\Pi = +1) - A(\Pi = -1)|}{A(\Pi = -1)}, \qquad A = \langle r\rangle\,, \langle \tilde{D}_q\rangle, \operatorname{var}(\tilde{D}_q), \tag{3.14}$$

are typically below 1 % and maximally $\lesssim 1.5\,\%$ for $\langle r\rangle$ and $\langle \tilde{D}_q\rangle$, while they reach slightly larger values for $\operatorname{var}(\tilde{D}_1)$, typically below 5 % and in extreme cases reaching up to $\lesssim 13\,\%$ (HWBCs in the interaction basis at $\eta = 0.575$). This large deviation, which is found close to the minimum of the variance, is probably caused by a slight displacement of this minimum for one parity as compared to the other, which has a large effect onto the relative deviation due to the small values of $\operatorname{var}(\tilde{D}_q)$. Overall, we can confirm that the spectral statistics as captured by $\langle r\rangle$ and the eigenstate localization properties as described by $\langle \tilde{D}_q\rangle$ and $\operatorname{var}(\tilde{D}_q)$ are essentially the same for both parities.

Since the chaotic region emerges essentially in the same η range for both parities, one should be able to detect quantum chaos also without resolving the parity symmetry. This is exemplified in Figure 3.11(a) for HWBCs. Here, we plot the mean level spacing ratio over the inner 70 % of the levels for the full Hilbert space including both parities and compare it to the analytical prediction $\langle r\rangle_{2\text{ GOE}} = 0.423415$, Equation (2.44). The system sizes considered range from $N = L = 7$ ($\mathcal{N} = 1716$) to $N = L = 10$ ($\mathcal{N} = 92\,378$). Spectral chaos in the region $2 \times 10^{-2} \lesssim \eta \lesssim 2$ can clearly be identified by the good

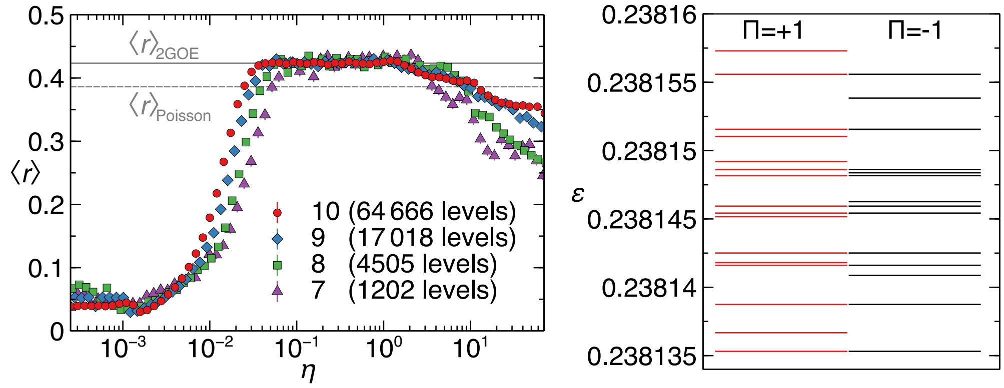

(a) (b)

Figure 3.11: (a) Mean level spacing ratio $\langle r\rangle$ over the inner 70 % of the full spectrum (including n levels as indicated in the legend), for $N = L$ from 7 to 10 with HWBCs. (b) Magnified spectrum at $\eta = 9.01 \times 10^{-4}$ for $N = L = 7$ with HWBCs and both parities. Grey lines in (a) mark $\langle r\rangle_{\mathrm{Poisson}}$ (dashed) and $\langle r\rangle_{2\,\mathrm{GOE}}$ (solid), Equations (2.43) and (2.44). When not explicitly shown, error bars are contained within symbol size.

agreement of $\langle r\rangle$ with $\langle r\rangle_{2\,\mathrm{GOE}}$. Here, the shift of the chaotic region as compared to the range $10^{-2} \lesssim \eta \lesssim 1$ identified in Sections 3.3 to 3.4.2 is just an effect of HWBCs versus PBCs, as discussed in the preceding paragraphs.

It is worth noting that, in the limit $\eta \to 0$, $\langle r\rangle$ does not converge to the Poisson prediction, in contrast to the single-parity subspace discussed in Section 3.4.1. In principle, the symmetry arguments of that section are applicable also to HWBCs with both parities. Hence, if the energies of the different symmetry-induced subspectra were independent of each other, one would expect Poissonian level statistics. Close inspection reveals, however, that the subspectra for different parities are *strongly* correlated in the low-η range: Figure 3.11(b) shows a magnification of the spectrum for $N = L = 7$ and HWBCs at $\eta = 9.01 \times 10^{-4}$. The majority of levels with $\Pi = +1$ is accompanied by a level with essentially the same energy and $\Pi = -1$. Hence, the spacings between these partner levels of different parity are typically much smaller than the spacings between other levels, and the corresponding level spacing ratios take values close to 0. Consequently, also the mean level spacing ratio is strongly reduced.

3.5. Influence of the Filling Factor

In this section, we give a short overview of the emergence of quantum chaos in systems with integer filling factors $N/L > 1$. Figure 3.12 shows the mean level spacing ratio $\langle r\rangle$ and the mean and variance of the distribution of $\tilde{D}_1$ in the interaction basis among close-in-energy eigenstates as functions of the scaled tunneling parameter η and the

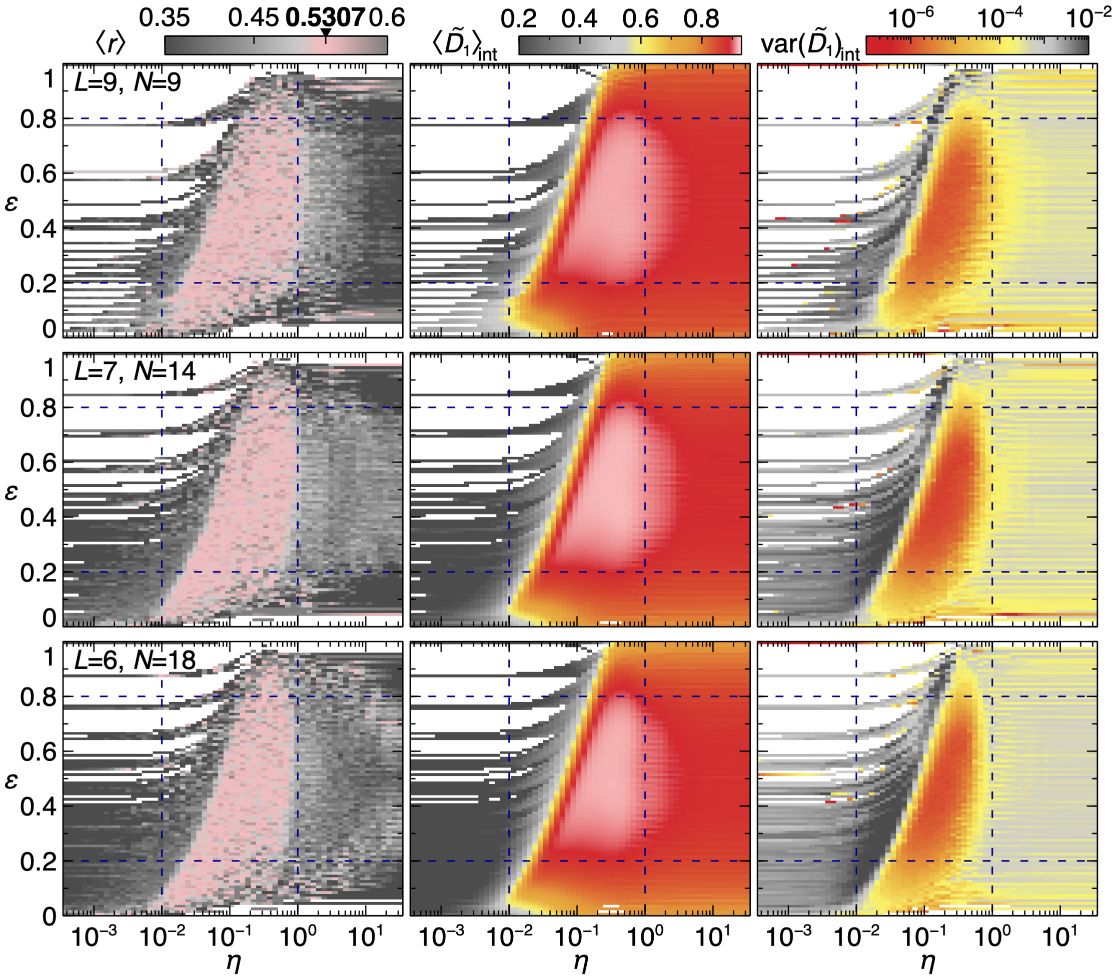

Figure 3.12: Mean level spacing ratio $\langle r \rangle$ (left), mean fractal dimension $\langle \tilde{D}_1 \rangle$ (center) and variance var $(\tilde{D}_1)$ (right), in the interaction basis, among close-in-energy Bose-Hubbard eigenstates, with HWBCs and parity $\Pi = -1$, versus η and ε, for systems with different integer filling factors and comparable Hilbert space dimensions: $N = L = 9$ ($\mathcal{N} = 12\,120$, upper panels), $L = 7$ and $N = 14$ ($\mathcal{N} = 19\,320$, center panels), $L = 6$ and $N = 18$ ($\mathcal{N} = 16\,797$, lower panels). Color bars apply to all panels in the same column. Blue dashed lines at $\varepsilon = 0.2$, $\varepsilon = 0.8$, $\eta = 0.01$ and $\eta = 1$ are guides to the eye.

scaled energy ε, for filling factors $N/L = 1$, 2, 3 and irreducible subspaces of comparable dimension.

The chaotic region emerges in approximately the same ranges of η and ε for all three systems considered, which is demonstrated by the blue dashed lines that indicate specific values of η and ε close to the edges of the chaotic domain. Furthermore, the maximum of $\tilde{D}_1$ and the minimum of var $(\tilde{D}_1)$ are of similar magnitude for the three filling factors, with small deviations in agreement with the different Hilbert space dimensions of the three systems. Hence, the emergence of quantum chaos seems to be largely independent of the integer filling factor as long as the Hilbert space dimension is kept approximately constant. Slight deviations occur in the limit $\eta \to 0$, however, where $\langle \tilde{D}_1 \rangle$ tends to be smaller for larger filling. For given N and L, the number of discrete energy levels in this limit, i.e., the number of sets $\{n_1, \dots, n_L\}$ of site occupation numbers n_j such that $\sum_j n_j = N$, can be calculated as the number of integer partitions of N with length $\leq L$ and is found to increase with the filling factor for comparable Hilbert space dimensions. Hence, the eigenstates at $\eta \to 0$ delocalize over a smaller percentage of the full interaction basis for larger filling factors, and consequently $\langle \tilde{D}_1 \rangle$ is smaller.

In previous works on fermions [113], hard-core bosons [112] and spin systems [108] it was found that quantum chaos sets in at smaller interaction strengths for increasing N. This finding is not necessarily in contradiction with our results, since in those systems particles may not populate the same site and hence, the filling factor cannot be increased beyond unity.

3.6. Summary

In this chapter, we have investigated the spectrum of the Bose-Hubbard model and its eigenstates' fractal dimensions, as functions of the scaled energy ε and of the scaled tunneling strength η. In the energy-resolved picture, as well as in the bulk-averaged perspective, clear fingerprints of quantum chaos are visible for intermediate values of η. Quantum chaos, as defined via short-range spectral statistics captured by the level spacing ratios, is connected to the emergence of complicated level dynamics dominated by avoided crossings. The density of states attains a seemingly Gaussian shape within the region of quantum chaos and the trajectory of its maximum correlates with the position of the center of the chaotic domain in the ε-η parameter space.

Whenever the spectrum signals quantum chaos, the fractal dimensions reveal strong delocalization of the corresponding eigenstates in both the interaction and the tunneling basis. Most remarkably, the region of quantum chaos coincides with a strong reduction of the eigenstate-to-eigenstate fluctuations of the fractal dimensions. This effect is qualitatively the same for both natural bases and hence qualifies as a basis-independent hallmark of quantum chaos in any non-trivial basis. Additionally, the boundaries of the chaotic region are unmistakeably indicated by the pronounced asymmetry of the distribution of fractal dimensions.

While the position of the chaotic domain as a function of the scaled tunneling strength depends slightly on the boundary conditions due to their influence on the connectivity of Fock space, the emergence of quantum chaos is essentially the same for different parity-induced subspaces, and can even be identified if parity symmetry remains unresolved. For systems of similar Hilbert space dimension, quantum chaos was found to be largely independent of the integer filling factor N/L.

In addition to the eigenstate fractal dimensions discussed throughout this chapter, we have investigated the structure of the Bose-Hubbard eigenstates via correlations of their amplitudes and intensities in the interaction basis. These results are presented in Appendix B.

Chapter 4.

Bose-Hubbard Model versus Random Matrix Theory

In Chapter 3, we have seen how spectral chaos in the Bose-Hubbard Hamiltonian is reflected in the eigenstates by an increase of their fractal dimensions and by a strong reduction of the fractal dimensions' eigenstate-to-eigenstate fluctuations. Since spectral chaos is defined via the eigenvalue statistics of Gaussian random matrices (see Section 2.2.3), it is natural to ask whether these random-matrix ensembles would also give a good approximation to eigenvector properties of chaotic many-body quantum systems. As we will see in the following, analytically calculated mean fractal dimensions $\langle \tilde{D}_q \rangle$ and variances $\operatorname{var}(\tilde{D}_q)$ for GOE eigenvectors give a good approximation to the corresponding quantities for the Bose-Hubbard model, while, nevertheless, the full probability distribution of fractal dimensions reveals clear differences. Furthermore, we compare the Bose-Hubbard Hamiltonian in the chaotic domain to the embedded GOE ensemble, which, as discussed in Section 2.2.5, contains only two-body interactions. It will be shown that the embedded ensemble can reproduce certain Bose-Hubbard features more closely than GOE, but deviations in terms of the full probability distributions of the fractal dimensions remain.

4.1. Analytical Results for Fractal Dimensions of GOE eigenstates

In this section we derive analytical expressions of $\langle \tilde{D}_q \rangle$ and $\operatorname{var}(\tilde{D}_q)$, $q = 1, 2, \infty$, for the eigenvectors of GOE random matrices of size $\mathcal{N} \times \mathcal{N}$ and obtain approximations to the full distribution functions of $\tilde{D}_q$.

In the following, let

$$\boldsymbol{v} = (v_1, \dots, v_{\mathcal{N}})$$

be a vector whose components follow the joint distribution of GOE [Equation (2.45) on page 21]. The probability distributions of a single component v_i and a pair of components (v_i, v_j) are consequently given by Equations (2.47) and (2.48), respectively (both on page 21). Then, the ensemble average of $|v_i|^2 \ln |v_i|^2$, that is, the average over different realizations of GOE matrices, reads

$$\left\langle |v_i|^2 \ln |v_i|^2 \right\rangle = \int_{-1}^{1} |v_i|^2 \ln |v_i|^2 \, P_{\mathrm{GOE}}(v_i) \, \mathrm{d}v_i = -\frac{\mathfrak{h}_{\mathcal{N}/2} - 2 + \ln 4}{\mathcal{N}}. \tag{4.1}$$

Here, $\mathfrak{h}_n$ is the harmonic number [184, p. 206],

$$\mathfrak{h}_n = \sum_{k=1}^{n} \frac{1}{k} = \int_0^1 \frac{1 - x^n}{1 - x} \, \mathrm{d}x, \tag{4.2}$$

where the sum is the definition for positive integers n and the integral, which equals the sum for these integers, defines $\mathfrak{h}_n$ also for non-integer values $n \geq 0$. Consequently, the corresponding GOE ensemble average of $\tilde{D}_1$ reads

$$\langle \tilde{D}_1 \rangle_{\mathrm{GOE}} = -\frac{1}{\ln \mathcal{N}} \sum_{i=1}^{\mathcal{N}} \left\langle |v_i|^2 \ln |v_i|^2 \right\rangle = \frac{\mathfrak{h}_{\mathcal{N}/2} - 2 + \ln 4}{\ln \mathcal{N}}. \tag{4.3}$$

In the limit $\mathcal{N} \to \infty$, this expression expands to

$$\left\langle \tilde{D}_1 \right\rangle_{\mathrm{GOE}} = 1 - \frac{1}{\ln \mathcal{N}} \left[2 - \gamma - \ln 2 - \frac{1}{\mathcal{N}} + \frac{1}{3\mathcal{N}^2} + \mathcal{O}\left(\frac{1}{\mathcal{N}^4} \right) \right], \tag{4.4}$$

where γ is the Euler-Mascheroni constant (Equation 5.2.3 of Reference [185]),

$$\gamma = \lim_{n \to \infty} \left(\mathfrak{h}_n - \ln n \right) \approx 0.577\,215\,665. \tag{4.5}$$

In a similar fashion as for $\langle \tilde{D}_1 \rangle_{\mathrm{GOE}}$, we can calculate $\operatorname{var}(\tilde{D}_1)$, using

$$\left\langle D_1^2 \right\rangle_{\mathrm{GOE}} = \frac{1}{\ln^2 \mathcal{N}} \left(\sum_{\substack{i,j=1 \\ i \neq j}}^{\mathcal{N}} \left\langle |v_i|^2 \ln |v_i|^2 \quad |v_j|^2 \ln |v_j|^2 \right\rangle + \sum_{i=1}^{\mathcal{N}} \left\langle \left(|v_i|^2 \ln |v_i|^2 \right)^2 \right\rangle \right),$$

which leads to

$$\begin{aligned} \operatorname{var}(\tilde{D}_1)_{\mathrm{GOE}} &= \left\langle \tilde{D}_1^2 \right\rangle_{\mathrm{GOE}} - \langle \tilde{D}_1 \rangle_{\mathrm{GOE}}^2 \\ &= \frac{(3\pi^2 - 24)(\mathcal{N} + 2) - 8}{2(\mathcal{N} + 2)^2 \ln^2 \mathcal{N}} - \frac{\psi^{(1)}\left(2 + \frac{\mathcal{N}}{2}\right)}{\ln^2 \mathcal{N}}. \end{aligned} \tag{4.6}$$

Here, $\psi^{(1)}$ is the first derivative of the digamma function ψ (Equations 5.2.1 and 5.2.2 of Reference [185]),

$$\psi(z) := \frac{1}{\Gamma(z)} \frac{\mathrm{d}}{\mathrm{d}z} \Gamma(z), \qquad \text{with } \Gamma(z) := \int_0^\infty e^{-x} x^{z-1} \, \mathrm{d}x. \tag{4.7}$$

For $\mathcal{N} \to \infty$, the variance expands to

$$\operatorname{var}\left(\tilde{D}_1\right)_{\mathrm{GOE}} = \frac{1}{\ln^2 \mathcal{N}} \left[\frac{3\pi^2 - 28}{2\mathcal{N}} + \frac{26 - 3\pi^2}{\mathcal{N}^2} + \mathcal{O}\left(\frac{1}{\mathcal{N}^3}\right)\right]. \tag{4.8}$$

We stress that the correlations between different vector components v_i, v_j, as described by their joint probability distribution, Equation (2.48), cannot be neglected in the variance of $\tilde{D}_1$: Without these correlations, $\operatorname{var}\left(\tilde{D}_1\right)_{\mathrm{GOE}}$ would be given just by the single-component variances as

$$\frac{1}{\ln^2 \mathcal{N}} \sum_{i=1}^{\mathcal{N}} \left[\left\langle \left(|v_i|^2 \ln |v_i|^2\right)^2 \right\rangle - \left\langle |v_i|^2 \ln |v_i|^2 \right\rangle^2\right],$$

whose scaling for $\mathcal{N} \to \infty$ is different from that of the full variance, with a leading term $\sim 1/\mathcal{N}$ instead of $\sim 1/\left(\mathcal{N} \ln^2 \mathcal{N}\right)$.

For $\tilde{D}_2$, we approximate the GOE average by a more accessible quantity,

$$\left\langle \tilde{D}_2 \right\rangle_{\mathrm{GOE}} \approx -\frac{\ln \langle R_2 \rangle_{\mathrm{GOE}}}{\ln \mathcal{N}} = -\frac{1}{\ln \mathcal{N}} \ln \sum_{i=1}^{\mathcal{N}} \left\langle |v_i|^4 \right\rangle. \tag{4.9}$$

This expression is in fact always a lower bound for $\left\langle \tilde{D}_2 \right\rangle_{\mathrm{GOE}}$ [84], a statement that follows directly from Jensen's inequality (Equation 1.7.10 of Reference [185]) using that the negative logarithm is a convex function. To find an approximation to the variance of $\tilde{D}_2$, we use propagation of uncertainty [186], which leads to

$$\operatorname{var}\left(\tilde{D}_2\right)_{\mathrm{GOE}} \approx \left[\left(\frac{\partial \tilde{D}_2}{\partial R_2}\right)_{R_2 = \langle R_2 \rangle_{\mathrm{GOE}}}\right]^2 \operatorname{var}(R_2)_{\mathrm{GOE}} = \frac{\operatorname{var}(R_2)_{\mathrm{GOE}}}{\langle R_2 \rangle_{\mathrm{GOE}}^2 \ln^2 \mathcal{N}}. \tag{4.10}$$

This approach yields

$$\left\langle \tilde{D}_2 \right\rangle_{\mathrm{GOE}} \approx \frac{\ln(\mathcal{N}+2) - \ln 3}{\ln \mathcal{N}}, \tag{4.11}$$

$$\operatorname{var}\left(\tilde{D}_2\right)_{\mathrm{GOE}} \approx \frac{8(\mathcal{N}-1)}{3(\mathcal{N}+4)(\mathcal{N}+6)\ln^2(\mathcal{N})}, \tag{4.12}$$

which for $\mathcal{N} \to \infty$ expand to

$$\left\langle \tilde{D}_2 \right\rangle_{\mathrm{GOE}} \approx 1 - \frac{1}{\ln \mathcal{N}} \left[\ln 3 - \frac{2}{\mathcal{N}} + \frac{2}{\mathcal{N}^2} + \mathcal{O}\left(\frac{1}{\mathcal{N}^3}\right)\right], \tag{4.13}$$

$$\operatorname{var}\left(\tilde{D}_2\right)_{\mathrm{GOE}} \approx \frac{1}{\ln^2 \mathcal{N}} \left[\frac{8}{3\mathcal{N}} - \frac{88}{3\mathcal{N}^2} + \mathcal{O}\left(\frac{1}{\mathcal{N}^3}\right)\right]. \tag{4.14}$$

Hence, the first few orders of the large-$\mathcal{N}$ expansions have the same functional form for $q = 1$ and $q = 2$.

For $\tilde{D}_\infty$, we neglect the correlations induced by normalization of $\boldsymbol{v}$, assuming that the different vector components are independent of one another, and we choose $\mathcal{N}$ large enough, such that the single-amplitude distribution, Equation (2.47), can be approximated by the Porter-Thomas distribution $P_{\mathrm{PT}}(u_i)$ of the scaled intensity $u_i := \mathcal{N} v_i^2/2$, Equation (2.50) on page 22. Then, the cumulative distribution function $F(t)$ of the maximum intensity $t := \max_i v_i^2$, i.e., the probability that all intensities are bounded from above by t, is just the product of the probabilities that the individual intensities v_i^2 are smaller than or equal to t. Hence,

$$F(t) = \prod_{i=1}^{\mathcal{N}} \left(\int_0^{\mathcal{N}t/2} \mathrm{d}u_i \; P_{\mathrm{PT}}(u_i) \right) = \left[\mathrm{Erf}\left(\sqrt{\frac{\mathcal{N}t}{2}} \right) \right]^{\mathcal{N}}, \tag{4.15}$$

where $\mathrm{Erf}(x)$ is the error function (Equation 7.2.1 of Reference [185]),

$$\mathrm{Erf}(x) = \frac{2}{\sqrt{\pi}} \int_0^x e^{-y^2} \, \mathrm{d}y. \tag{4.16}$$

Here, the normalization of $\boldsymbol{v}$ restricts t to the range $1/\mathcal{N} \leq t \leq 1$. From the cumulative distribution function, the probability density is obtained as

$$P_{\mathrm{GOE}}(t) = \frac{\mathrm{d}}{\mathrm{d}t} F(t) = \frac{\mathcal{N}^{3/2} e^{-\mathcal{N}t/2}}{\sqrt{2\pi t}} \left[\mathrm{Erf}\left(\sqrt{\frac{\mathcal{N}t}{2}} \right) \right]^{\mathcal{N}-1}, \tag{4.17}$$

which, after partial integration and the variable substitution $x = \sqrt{\mathcal{N}t/2}$, gives the kth moment of the random variable $\tilde{D}_\infty = -\ln t / \ln \mathcal{N}$ as

$$\begin{aligned} \left\langle \tilde{D}_\infty^k \right\rangle_{\mathrm{GOE}} &= \int_{1/\mathcal{N}}^1 \left(-\frac{\ln t}{\ln \mathcal{N}} \right)^k P_{\mathrm{GOE}}(t) \, \mathrm{d}t \\ &= \frac{2k(-1)^{k-1}}{\ln^k \mathcal{N}} \int_{1/\sqrt{2}}^{\sqrt{\mathcal{N}/2}} \frac{\mathrm{Erf}(x)^{\mathcal{N}}}{x} \left[\ln\left(\frac{2x^2}{\mathcal{N}} \right) \right]^{k-1} \mathrm{d}x - \mathrm{Erf}\left(\frac{1}{\sqrt{2}} \right)^{\mathcal{N}}. \end{aligned} \tag{4.18}$$

Since the last term of Equation (4.18) decays exponentially with $\mathcal{N}$, it can be neglected for large $\mathcal{N}$. Note that, in contrast to the approximate treatment of GOE discussed here, expressions for $F(t)$ and $P_{\mathrm{GUE}}(t)$ for the Gaussian *unitary* ensemble are known exactly [187].

In contrast to $\tilde{D}_1$ and $\tilde{D}_2$, obtaining the expansion of $\langle \tilde{D}_\infty \rangle_{\mathrm{GOE}}$ and $\mathrm{var}\,(\tilde{D}_\infty)_{\mathrm{GOE}}$ for $\mathcal{N} \to \infty$ is rather involved and requires a suitable approximation of the error function in the integrals. We therefore leave the details for Appendix A.3 and quote just the final results:

$$\langle \tilde{D}_\infty \rangle_{\mathrm{GOE}} = 1 - \frac{\ln(\ln \mathcal{N}) + \ln 2}{\ln \mathcal{N}} + \frac{\ln(\ln \mathcal{N})}{\ln^2 \mathcal{N}} + \mathcal{O}\left(\frac{1}{\ln^2 \mathcal{N}} \right), \tag{4.19}$$

$$\mathrm{var}\,(\tilde{D}_\infty)_{\mathrm{GOE}} = \frac{c_1}{\ln^4 \mathcal{N}} + \frac{c_2 \ln(\ln \mathcal{N})}{\ln^5 \mathcal{N}} + \mathcal{O}\left(\frac{1}{\ln^5 \mathcal{N}} \right). \tag{4.20}$$

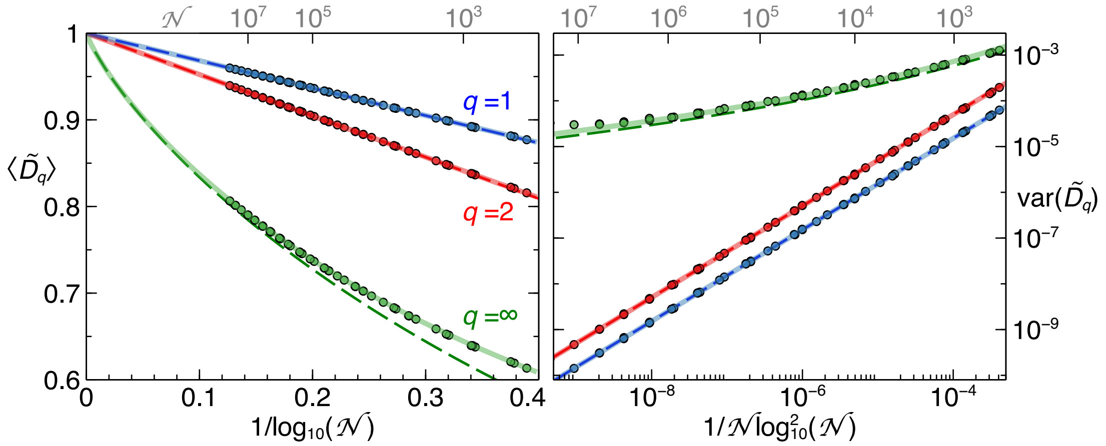

Figure 4.1: Numerical data [dots], analytical predictions [solid lines, Equations (4.3), (4.6), (4.11), (4.12), (4.18)] and large-$\mathcal{N}$ expansions of the analytical predictions [dashed lines, Equations (4.4), (4.8), (4.13), (4.14), (4.19), (4.20)] for $\langle \tilde{D}_q \rangle_{\mathrm{GOE}}$ (left) and $\mathrm{var}\left(\tilde{D}_q\right)_{\mathrm{GOE}}$ (right), $q = 1, 2, \infty$. For the large-$\mathcal{N}$ expansions, only the leading finite-size corrections are taken into account (for $\langle \tilde{D}_\infty \rangle$, only the first two corrections). The coefficient c_1 for $\mathrm{var}\left(\tilde{D}_\infty\right)$ is chosen as $c_1 = 2/\left(3\ln^2 2\right)$ [compare Equation (A.34) in Appendix A.3].

Here, the exact values of the coefficients $c_{1,2}$ depend on the precise approximation to the error function, but the functional form of the finite-size corrections can be predicted reliably.

In Figure 4.1, we compare the analytical formulas for $\langle \tilde{D}_q \rangle_{\mathrm{GOE}}$ and $\mathrm{var}\left(\tilde{D}_q\right)_{\mathrm{GOE}}$, Equations (4.3), (4.6), (4.11), (4.12) and (4.18), to the means and variances of $\tilde{D}_q$ obtained numerically by sampling the uniform distribution on the unit sphere, as described in Section 2.2.4 on page 21. We also show the leading terms of the expansions for $\mathcal{N} \to \infty$, Equations (4.4), (4.8), (4.13), (4.14), (4.19) and (4.20) (for $\langle \tilde{D}_\infty \rangle$ including also the first subleading correction). For all three values of q, the numerical data is well described by the analytical predictions, and for $q = 1, 2$, the large-$\mathcal{N}$ expansion to leading order agrees exceptionally well with the exact analytical formula already for small $\mathcal{N}$. For $q = \infty$, the analytical expression for the mean and the corresponding expansion for $\mathcal{N} \to \infty$ to second order agree only for dimensions larger than those investigated numerically. Hence, finite-size effects play a more significant role for $\langle \tilde{D}_\infty \rangle_{\mathrm{GOE}}$. The first-order expansion for $\mathrm{var}\left(\tilde{D}_\infty\right)_{\mathrm{GOE}}$ at $\mathcal{N} \to \infty$ and the corresponding analytical formula show the same qualitative behaviour as functions of $\mathcal{N}$, but they appear slightly shifted. Hence, our large-$\mathcal{N}$ expansion describes the functional form of the leading order correctly, while the coefficient is probably not predicted exactly.

In addition to the mean and variance of $\tilde{D}_q$, we now construct analytical approximations to the full probability densities $P_{\mathrm{GOE}}(\tilde{D}_q)$. For $\tilde{D}_\infty$, this function can directly

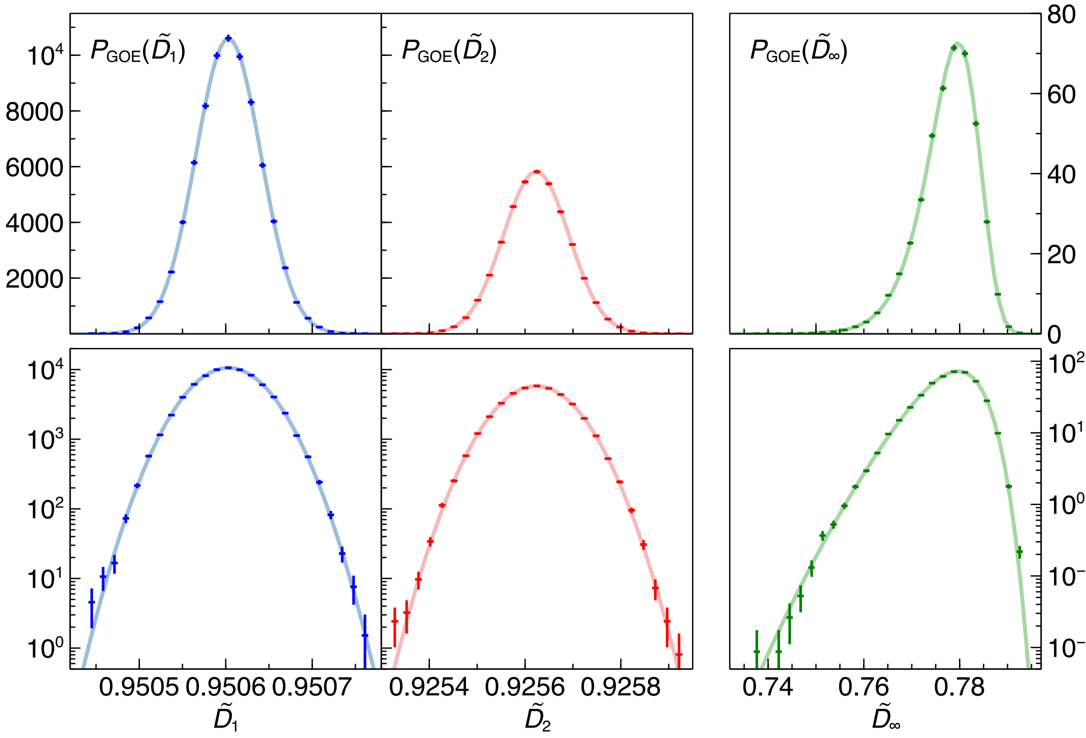

Figure 4.2: Numerically calculated histograms of $\tilde{D}_q$ for vectors of dimension $\mathcal{N} = 2\,599\,688$ distributed according to GOE [Equation (2.45)], compared to Gaussian distributions [Equation (4.22)] for $q = 1, 2$ and to the distribution function of Equation (4.21) for $q = \infty$. Upper (lower) panels show the distributions in linear (logarithmic) scale.

be obtained from the probability density in terms of the maximum intensity t [Equation (4.17)], according to

$$P_{\mathrm{GOE}}(\tilde{D}_\infty)\,\mathrm{d}\tilde{D}_\infty = P_{\mathrm{GOE}}(t)\,\mathrm{d}t.$$

This procedure yields

$$P_{\mathrm{GOE}}(\tilde{D}_\infty) = P_{\mathrm{GOE}}\left(t = \mathcal{N}^{-\tilde{D}_\infty}\right)\mathcal{N}^{-\tilde{D}_\infty}\ln\mathcal{N}. \tag{4.21}$$

Since $\tilde{D}_1$ is the sum of identically distributed terms, the central limit theorem would, for $\mathcal{N} \to \infty$, yield the Gaussian distribution

$$P_{\mathrm{GOE}}(\tilde{D}_1) = \frac{1}{\sqrt{2\pi\,\mathrm{var}\left(\tilde{D}_1\right)_{\mathrm{GOE}}}}\exp\left[-\frac{\left(\tilde{D}_1 - \langle\tilde{D}_1\rangle_{\mathrm{GOE}}\right)^2}{2\,\mathrm{var}\left(\tilde{D}_1\right)_{\mathrm{GOE}}}\right], \tag{4.22}$$

if the different summands of $\tilde{D}_1$ were independent. Numerical inspection reveals that $P_{\mathrm{GOE}}(\tilde{D}_1)$ and also $P_{\mathrm{GOE}}(\tilde{D}_2)$ are very well approximated by a Gaussian distribution for sufficiently large $\mathcal{N}$, even though the different vector components are correlated via the normalization of $\boldsymbol{v}$. This is demonstrated in Figure 4.2, where numerically obtained histograms of $\tilde{D}_q$ for GOE are compared against Gaussian distributions with means and variances according to Equations (4.3), (4.6), (4.11) and (4.12) for $q = 1, 2$ and against Equation (4.21) for $q = \infty$. Here, the (linear) matrix dimension is $\mathcal{N} = 2\,599\,688$, which is the same dimensionality as the subspace of parity $\Pi = -1$ with $N = L = 13$ and HWBCs for the Bose-Hubbard Hamiltonian.

4.2. Properties of the Bosonic Embedded Ensemble

In contrast to GOE, where spectral and eigenvector properties such as the distributions of level spacing ratios r and of fractal dimensions $\tilde{D}_q$ can be accessed (approximately) analytically, the corresponding quantities for the bosonic embedded GOE ensemble defined in Section 2.2.5 are typically known only from numerical calculations [98]. In the following, we briefly discuss their main features as functions of the parameter λ and of the scaled energy ε, comparing the energy dependence also to the Bose-Hubbard model.

We apply reflection symmetry to the embedded ensemble, as discussed at the end of Section 2.2.5, and consider only the corresponding symmetric or antisymmetric subspace with respect to that symmetry. If not stated differently, the reflection symmetry is implemented according to Equation (2.60) on page 24. The resulting Hilbert space dimensions are the same as for the symmetry-induced subspaces of the Bose-Hubbard Hamiltonian with HWBCs.

4.2.1. Parameter Dependence

As discussed in Section 2.2.5, the parameter λ of the embedded ensemble tunes the strength of the two-body Hamiltonian in relation to the single-particle Hamiltonian [see Equation (2.55) on page 23]. We now investigate how this parameter influences spectral chaos, as described by the mean level spacing ratio $\langle r \rangle$, and the eigenstate structure, as captured by the mean and the variance of $\tilde{D}_1$.

Figure 4.3 shows the mean level spacing ratio $\langle r \rangle$ as a function of λ for the embedded ensemble with $N = 10$ particles in $L = 10$ single-particle modes and parity $\Pi = -1$ ($\mathcal{N} = 46\,126$), averaged over 100 realizations of the ensemble. Here, $\langle r \rangle$ is calculated from the full spectrum of each individual realization and subsequently averaged over realizations (ensemble average). A good agreement with $\langle r \rangle_{\mathrm{GOE}}$, and hence a clear signal of spectral chaos, appears already for small values $\lambda \gtrsim 0.04$. This is in accord with the results of Reference [160], where the level spacing distribution of a bosonic embedded ensemble with $N \in [7, 16]$, $L \in \{4, 5\}$ and single-particle energies $E_i = i + 1/i$ [diagonal single-particle Hamiltonian H_1 as in Equation (2.59) on page 24] was compared to GOE and Poisson. There, the critical λ for GOE spectral statistics was found to be between 0.0148 and 0.02975, depending on N and L. The fact that the critical value of λ is rather

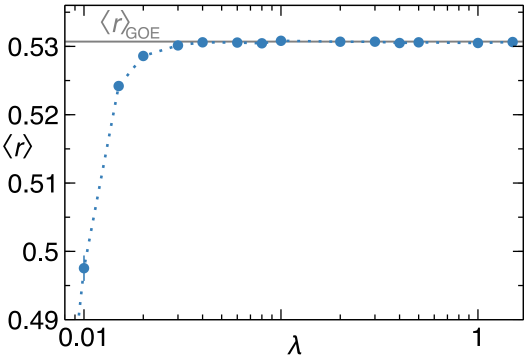

Figure 4.3: Mean level spacing ratio $\langle r \rangle$ versus λ, for the full spectrum of the embedded ensemble [Equation (2.55) with $N = L = 10$ and $\Pi = -1$ ($\mathcal{N} = 46\,126$), averaged over 100 ensemble realizations. The solid line indicates $\langle r \rangle_{\mathrm{GOE}}$, Equation (2.41) on page 19. Error bars are defined solely from the average over realizations.

small raises the question whether in the limit of infinite Hilbert space dimension already an infinitesimally small two-body contribution is sufficient to break the integrability at $\lambda = 0$.[1] However, note that we find a slightly larger critical λ than the values reported in Reference [160], even though we consider a much larger Hilbert space dimension here.

To see how the emergence of quantum chaos in the spectrum is reflected by the eigenvector properties, we investigate in Figure 4.4 the mean and variance of $\tilde{D}_1$ over close-in-energy eigenstates as functions of λ, for different values of the energy. Here, we consider the same N, L, and parity ($N = L = 10$, $\Pi = -1$) as for the level spacing ratios in Figure 4.3. Mean and variance are obtained from the 100 eigenstates closest to the scaled target energy $\varepsilon \in \{0.0, 0.2, 0.4, 0.6, 0.8, 1.0\}$ for each individual realization, and are subsequently averaged over realizations. The scaled energy ε is defined according to Equation (2.99) on page 34, as for the Bose-Hubbard model, where the minimum and maximum energies $E_{\min}$, $E_{\max}$ for the embedded ensemble are calculated per realization.

As a function of ε, $\langle \tilde{D}_1 \rangle$ gets larger and $\mathrm{var}\,(\tilde{D}_1)$ gets smaller towards the center of the spectrum, $\varepsilon = 0.5$. For the Bose-Hubbard Hamiltonian, we have found that large fractal dimensions accompanied by a strong suppression of their eigenstate-to-eigenstate fluctuations are characteristic of the chaotic regime. If we apply the same reasoning here, quantum chaos for the embedded ensemble manifests itself more strongly in the center of the spectrum than at its edges. This is clearly different from GOE, where $\langle \tilde{D}_q \rangle$ and $\mathrm{var}\,(\tilde{D}_q)$, as discussed in Section 4.1, are independent of the energy. Furthermore, the behaviour of the mean and the variance for the embedded ensemble is very similar for scaled energies ε and $1 - \varepsilon$. This symmetry is immediately clear from the definition

---

[1] Integrability at $\lambda = 0$ can easily be seen from the fact that the occupation numbers of the L eigenmodes of the single-particle Hamiltonian with matrix elements $h_{ij}^{(1)}$ [compare Equation (2.54)] define a complete set of L commuting observables.

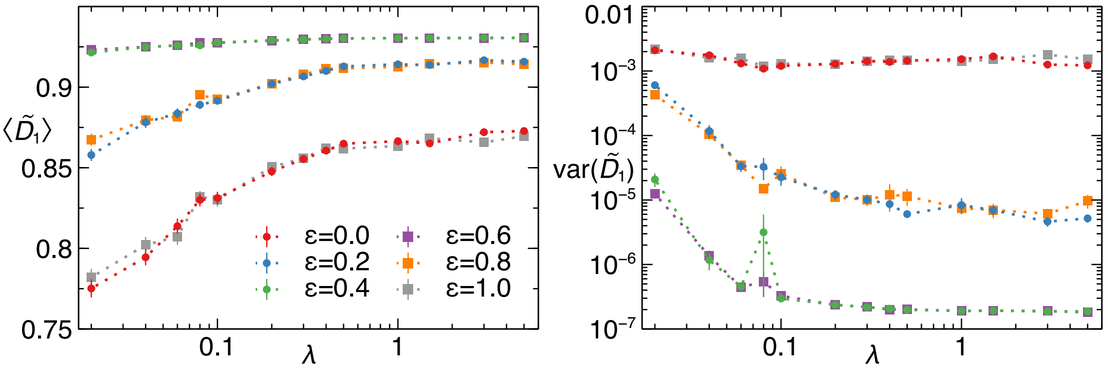

Figure 4.4: Mean $\langle\tilde{D}_1\rangle$ (left) and variance var $(\tilde{D}_1)$ (right) for 100 states around specific scaled energies ε as indicated, versus λ, for the embedded ensemble with $N = L = 10$ and $\Pi = -1$ ($\mathcal{N} = 46\,126$), averaged over 100 ensemble realizations. Error bars are defined solely from the average over realizations.

of the embedded ensemble, Equations (2.54)–(2.57): Since the matrix elements of the single- and two-body Hamiltonians $H_{1,2}$ are distributed symmetrically around 0, the probability densities for the Hamiltonians H and $-H$ are the same. Consequently, after ensemble average all spectral and eigenvector properties of the embedded ensemble are symmetric around the non-scaled energy $E = 0$, which hence corresponds to $\varepsilon = 0.5$.

For $\lambda \leq 0.1$, $\langle\tilde{D}_1\rangle$ increases and var $(\tilde{D}_1)$ strongly decreases as a function of λ, even though the mean level spacing ratio is already in good agreement with $\langle r\rangle_{\mathrm{GOE}}$ for these values of λ. Only for $\lambda \geq 0.5$ do $\langle\tilde{D}_1\rangle$ and var $(\tilde{D}_1)$ reach an essentially constant value. By choosing $\lambda = 1$, as we do from now on, we can therefore ensure that the features of quantum chaos in the eigenstates, as described by the latter two quantities, are well developed for any value of the energy.

4.2.2. Spectral Properties in Comparison with Bose-Hubbard

In the left panels of Figure 4.5, the density of states and the mean level spacing ratio $\langle r\rangle$ are shown for the embedded ensemble (with $\lambda = 1$), as functions of the scaled energy ε, for $N = L = 10$ and parity $\Pi = -1$ ($\mathcal{N} = 46\,126$). Here, the energy axis is divided into 100 equally spaced bins, and $\langle r\rangle$ is calculated for the levels that fall into the same bin, before being averaged over 100 ensemble realizations.

The right panels of Figure 4.5 show the density of states and the mean level spacing ratio for the Bose-Hubbard model with HWBCs, $N = L = 10$, and parity $\Pi = -1$. Here, error bars are obtained as standard errors of the mean, for each of the 50 equally spaced bins into which the energy axis is discretized. The value $\eta = 0.1905$ of the scaled tunneling strength is chosen deep within the chaotic domain, as can be seen for instance in Figures 3.5(a) and 3.6 on pages 43 and 45. To ease the comparison with the embedded ensemble, whose properties are symmetric around $\varepsilon = 0.5$ on average, η is furthermore

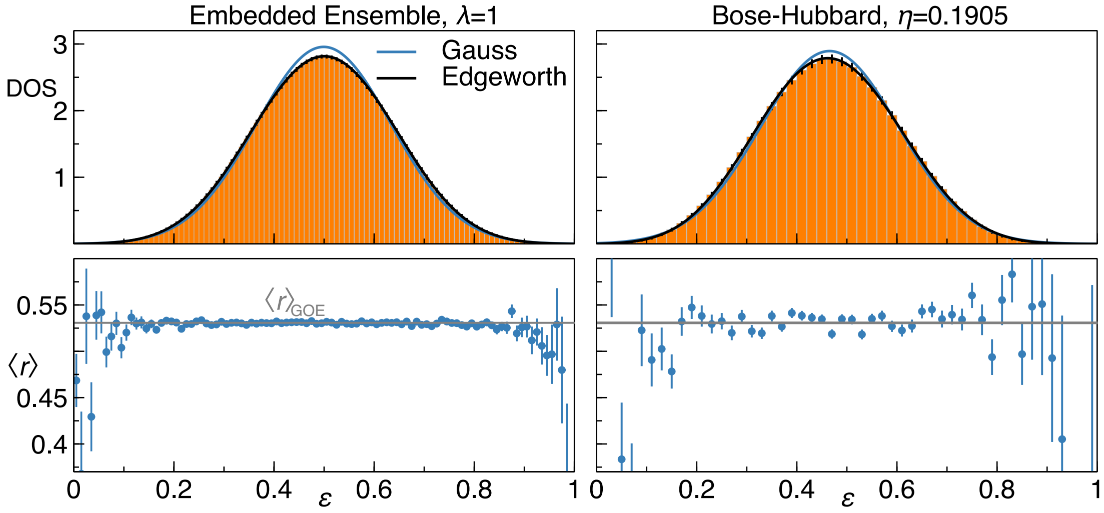

Figure 4.5: Density of states and mean level spacing ratio $\langle r\rangle$ versus scaled energy ε, for the embedded ensemble and the Bose-Hubbard Hamiltonian with HWBCs and $\eta = 0.1905$, for $N = L = 10$ and $\Pi = -1$ ($\mathcal{N} = 46\,126$). $\langle r\rangle$ is calculated separately for each of the 100 (50) bins into which the energy axis is discretized for the embedded ensemble (for the Bose-Hubbard model), and further averaged over 100 realizations for the embedded ensemble (error bars defined only from this second average). Solid lines in the upper panels show fits by a Gaussian distribution and by a second-order Edgeworth expansion, Equation (4.23). The grey lines in the lower panels indicate $\langle r\rangle_{\mathrm{GOE}}$, Equation (2.41) on page 19.

chosen large enough, such that the density of states for the Bose-Hubbard Hamiltonian is sufficiently symmetric around $\varepsilon = 0.5$.

The shape of the density of states for the embedded ensemble is clearly similar to a Gaussian distribution, in stark contrast to GOE, where the density of states follows the semicircle law [Equation (2.26) on page 15], but in very good agreement with the behaviour of the density of states for the Bose-Hubbard Hamiltonian within the chaotic regime, as discussed in Section 3.1 and as shown in the upper right panel of Figure 4.5. However, close inspection shows deviations from Gaussianity for both the Bose-Hubbard model and the embedded ensemble, as visible from the Gaussian fits (blue lines) in Figure 4.5. To account for these deviations, we consider a correction in the form of an Edgeworth expansion to second order [98, 188], which was previously found to give a good description of the density of states for fermionic embedded ensembles [98]. For a distribution with zero mean and unit variance, this expansion reads

$$P_{\mathrm{Edgeworth}}(x) = P_{\mathrm{Gauss}}(x)\left(1 + \frac{k_3}{3!}\,\mathrm{He}_3(x) + \frac{k_4}{4!}\,\mathrm{He}_4(x) + \frac{k_3^2}{2!\,(3!)^2}\,\mathrm{He}_6(x)\right). \quad (4.23)$$

Here, P_{Gauss} is the probability density of a standard Gaussian random variable, k_j are the scaled cumulants of the distribution to be approximated,

$$k_j = \frac{K_j}{\sigma^j}, \tag{4.24}$$

with the cumulants K_j [182] and the standard deviation σ, and He_n are the Hermite polynomials defined as

$$\mathrm{He}_n(x) = (-1)^n e^{x^2/2} \frac{\mathrm{d}^n}{\mathrm{d}x^n} e^{-x^2/2}, \tag{4.25}$$

which yields

$$\mathrm{He}_3(x) = x^3 - 3x, \quad \mathrm{He}_4(x) = x^4 - 6x^2 + 3, \quad \mathrm{He}_6(x) = x^6 - 15x^4 + 45x^2 - 15. \tag{4.26}$$

Details on the derivation of this expansion can be found in References [98, 188]. For the embedded ensemble as well as for the Bose-Hubbard Hamiltonian, the Edgeworth expansion gives a much better description of the density of states. Hence, the embedded ensemble qualitatively describes the deviations of the Bose-Hubbard density of states from Gaussianity.

For both models, $\langle r \rangle$ agrees well with the GOE prediction and hence signals spectral chaos for $0.2 \lesssim \varepsilon \lesssim 0.8$, while it fluctuates strongly and clearly deviates from $\langle r \rangle_{\text{GOE}}$ towards the edges of the spectrum, where the density of states is very small for both models. (Note that the additional average over ensemble realizations leads to a smoother behaviour of $\langle r \rangle$ for the embedded ensemble than for the Bose-Hubbard model.) Hence, the embedded ensemble qualitatively describes the absence of quantum chaos and the reduced density of states exhibited by the Bose-Hubbard model at the edges of the spectrum, in contrast to GOE, whose short-range spectral statistics do not show any energy dependence (compare Section 2.2.3). This result demonstrates that the sparsity of the many-body Hamiltonian, or in other words the fact that Fock states are connected via single- and two-body processes only, can be associated with non-chaotic behaviour at the spectral edges, accompanied by a very small density of states.

4.2.3. Fractal Dimensions in Comparison with Bose-Hubbard

After investigating the spectrum, we now discuss the eigenstate fractal dimensions in terms of their mean, variance and skewness as functions of the scaled energy ε. Here, we note that for the embedded ensemble, the distribution of eigenstate fractal dimensions can be defined in several ways. After discretizing the energy axis like in Section 4.2.2, the energy-resolved mean, variance and skewness could be calculated incorporating all eigenstates that belong to the same energy bin for all different realizations of the ensemble. However, this procedure does not distinguish the uncorrelated eigenstates of different ensemble realizations from the eigenstates of the same realization that are therefore correlated with each other. Alternatively, $\langle \tilde{D}_q \rangle$, $\operatorname{var}(\tilde{D}_q)$ and $\operatorname{skew}(\tilde{D}_q)$ could be calculated

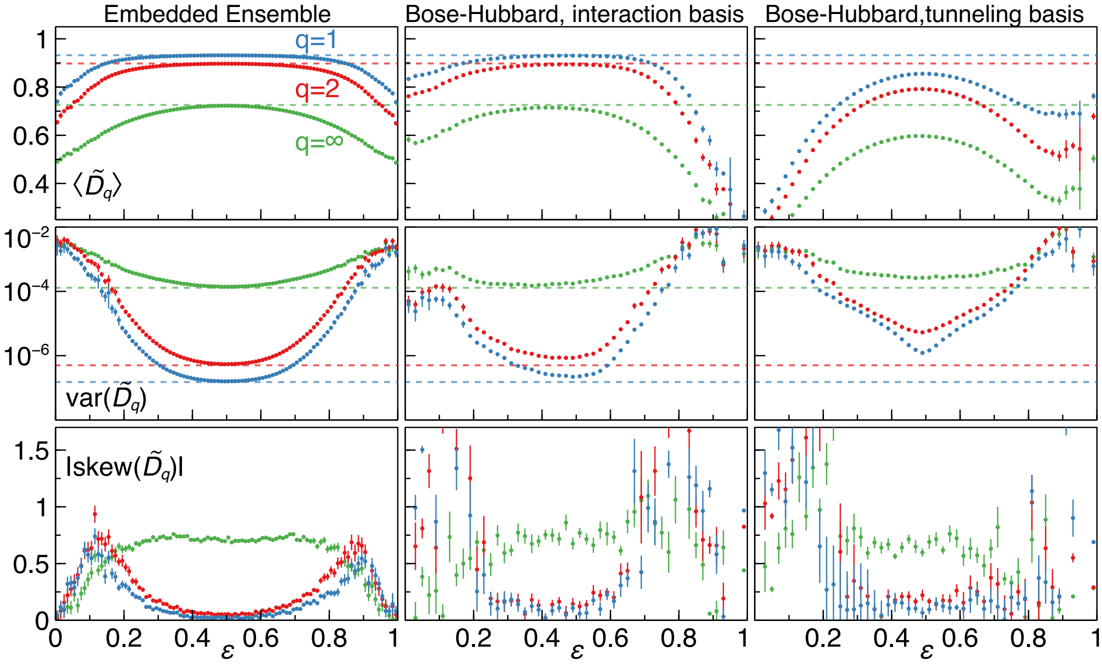

Figure 4.6: Mean $\langle \tilde{D}_q \rangle$, variance $\operatorname{var}(\tilde{D}_q)$ and absolute skewness $\left|\operatorname{skew}(\tilde{D}_q)\right|$, $q = 1, 2, \infty$, as functions of the scaled energy ε for the embedded ensemble and the Bose-Hubbard model with HWBCs and $\eta = 0.1905$, for $N = L = 10$ and $\Pi = -1$ ($\mathcal{N} = 46\,126$). Each quantity is calculated individually for the 100 (50) equally spaced bins, into which the energy axis is discretized for the embedded ensemble (for the Bose-Hubbard model), and in the case of the embedded ensemble further averaged over 100 realizations, with error bars defined only from this second average. Dashed lines indicate the corresponding GOE expectation, Equations (4.3), (4.6), (4.11), (4.12) and (4.18).

individually for each realization and for the eigenstates that belong to the same energy bin, like for the Bose-Hubbard Hamiltonian in Section 3.3, subsequently averaging these quantities over different realizations. This approach treats correlated eigenstates from the same realization and uncorrelated eigenstates from distinct realizations on a different footing. We will therefore use this type of averaging for the embedded ensemble, where $\langle \tilde{D}_q \rangle$, $\operatorname{var}(\tilde{D}_q)$ and $\operatorname{skew}(\tilde{D}_q)$ are hence quantifiers of the distribution over close-in-energy eigenstates of the *same* Hamiltonian, i.e. the same realization, and do not describe the distribution over different ensemble realizations.

Figure 4.6 shows the mean, the variance and the absolute value of the skewness of the distribution of fractal dimensions among different eigenstates versus scaled energy ε, for the embedded ensemble and the Bose-Hubbard model in both natural bases. Here, we use the same system parameters and energy discretization procedure as for Figure 4.5. The mean fractal dimension for all three models rises to its maximum around the center

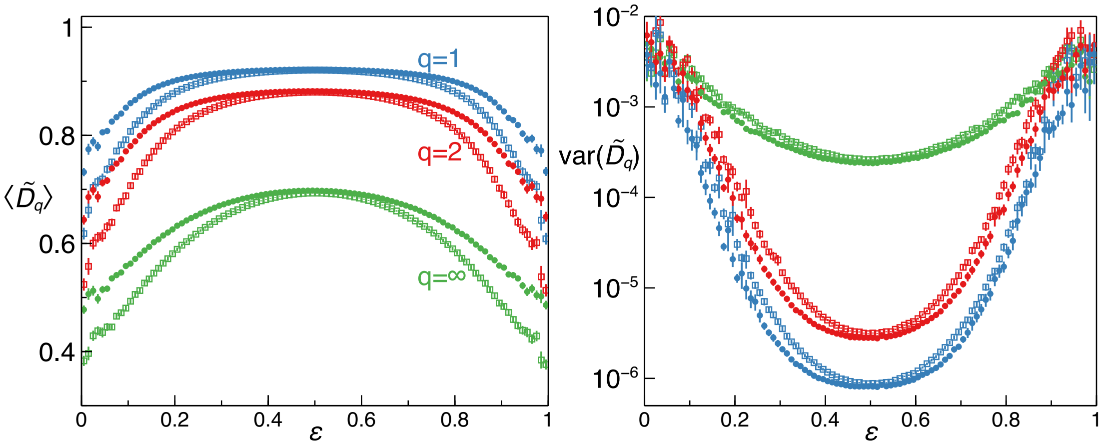

Figure 4.7: Comparison of $\langle\tilde{D}_q\rangle$ and var $(\tilde{D}_q)$ as functions of ε for the two possible implementations of reflection symmetry into the embedded ensemble, the "site approach" [filled circles, Equation (2.60)] and the "parity approach" [empty squares, Equation (2.61)] as described in the main text, for $N = L = 9$ and $\Pi = -1$ ($\mathcal{N} = 12\,190$).

of the spectrum, $\varepsilon = 0.5$, where the variance decays by several orders of magnitude towards its minimum. For the embedded ensemble and the Bose-Hubbard model in the interaction basis, $\langle\tilde{D}_q\rangle$ and var $(\tilde{D}_q)$ become almost constant around the maximum or minimum, respectively, exhibiting a good quantitative agreement for these two models. Note, however, that the Bose-Hubbard Hamiltonian shares the symmetry of the embedded ensemble around $\varepsilon = 0.5$ only in the limit $\eta \to \infty$. As revealed by the dashed horizontal lines, which indicate the corresponding $\langle\tilde{D}_q\rangle_{\text{GOE}}$ and var $(\tilde{D}_q)_{\text{GOE}}$, the maximum of $\langle\tilde{D}_q\rangle$ and the minimum of var $(\tilde{D}_q)$ for these two models are furthermore well described by GOE.

While the basic features, namely the much larger mean and much smaller variance in the center than at the boundaries of the spectrum, are qualitatively the same also for the Bose-Hubbard model in the tunneling basis, the embedded ensemble reproduces the shape of $\langle\tilde{D}_q\rangle$ and var $(\tilde{D}_q)$ as functions of ε only for the Bose-Hubbard Hamiltonian in the interaction basis. This qualitative disagreement of $\langle\tilde{D}_q\rangle$ and var $(\tilde{D}_q)$ between the embedded ensemble and the Bose-Hubbard model in the tunneling basis is surprising, given the strong resemblance of their matrix structure (see Figure 2.7 on page 33 and the discussion towards the end of Section 2.4.2). At first glance, one might conjecture that this deviation is caused by the way the reflection symmetry is applied to the embedded ensemble. In Figure 4.6, reflection symmetry is implemented treating the L single-particle modes as spatially localized Wannier states ["site approach", Equation (2.60) on page 24], like for the Bose-Hubbard Hamiltonian in the interaction basis. Alternatively, reflection symmetry could also be applied assuming that each single-particle mode has a well-defined parity ["parity approach", Equation (2.61) on page 24], as is the case for the Bose-Hubbard Hamiltonian in the tunneling basis with HWBCs, where the single-particle basis states are standing waves. In Figure 4.7, $\langle \tilde{D}_q \rangle$ and $\operatorname{var}(\tilde{D}_q)$ as functions of the scaled energy ε are compared for these two approaches, using $N = L = 9$ and parity $\Pi = -1$ ($\mathcal{N} = 12\,120$). While the plateau of constant values for $\langle \tilde{D}_q \rangle$ and $\operatorname{var}(\tilde{D}_q)$ around $\varepsilon = 0.5$ is slightly less pronounced for the "parity approach" and the values of $\langle \tilde{D}_q \rangle$ and $\operatorname{var}(\tilde{D}_q)$ towards the edges of the spectrum differ between the two approaches, the qualitative shape of mean and variance is comparable between both implementations of reflection symmetry and also the maximum of $\langle \tilde{D}_q \rangle$ and the minimum of $\operatorname{var}(\tilde{D}_q)$ are very similar. Hence, the much better agreement between the embedded ensemble and the Bose-Hubbard Hamiltonian in the interaction basis cannot solely be explained by the implementation of the reflection symmetry.

In contrast to the Bose-Hubbard Hamiltonian, whose matrix elements depend on just two parameters J and U and are therefore highly correlated, the matrix elements of the embedded ensemble are determined by

$$\frac{1}{2}L(L+1) + \frac{1}{2}\frac{L(L+1)}{2}\left(\frac{L(L+1)}{2} + 1\right)$$

independent numbers—namely the $d(d+1)/2$ independent elements of the $d \times d$ dimensional symmetric matrices H_1 and H_2 [Equation (2.54) on page 22], with $d = L$ and $d = L(L+1)/2$, respectively—and are therefore much less correlated. The mismatch between the embedded ensemble and the Bose-Hubbard Hamiltonian in the tunneling basis must therefore be related to the different correlations in the matrix elements.

The skewness of $\tilde{D}_q$, as discussed for the Bose-Hubbard Hamiltonian in Section 3.3.2, is particularly pronounced at the boundaries of the chaotic region. The lower panels of Figure 4.6 show that this statement is true also for the embedded ensemble for $q = 1, 2$. In this model, as well as in the Bose-Hubbard model for both natural bases, the absolute value of the skewness is strongly reduced in the center of the chaotic domain, while it becomes maximal at the boundaries of that region, where the errors of the skewness are largest. For $q = \infty$, the skewness in the center of the spectrum clearly differs from 0, $\left|\operatorname{skew}(\tilde{D}_\infty)\right| \approx 0.7$, which indicates that the distribution of $\tilde{D}_\infty$ stays asymmetric within the chaotic domain. These observations are in qualitative agreement with the behaviour exhibited by the GOE distributions of $\tilde{D}_q$ discussed in Section 4.1 and shown in Figure 4.2. There, it was found that the distributions of $\tilde{D}_{1,2}$ are well approximated by a Gaussian, which is symmetric by definition, while $\tilde{D}_\infty$ has a notably asymmetric distribution.

4.3. Comparison of the Models around Specific Target Energies

In this section, we analyse the fractal dimensions of the eigenstates closest to certain target energies ε as functions of η, investigating the agreement between the random-matrix predictions discussed in the preceding sections and the Bose-Hubbard Hamiltonian in the chaotic domain.

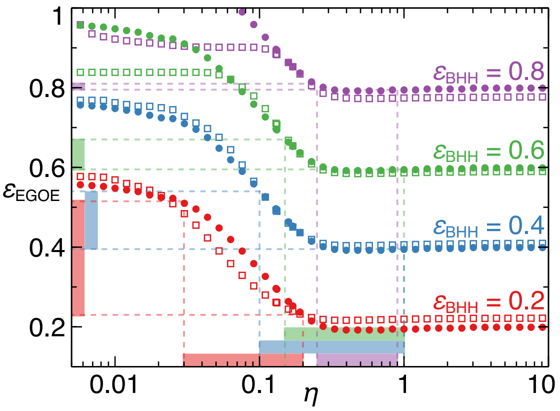

Figure 4.8: Energies $\varepsilon_{\mathrm{EGOE}}$ for the embedded ensemble with $N = L = 10$ and parity $\Pi = -1$ (Hilbert space dimension $\mathcal{N} = 46\,126$), as a function of η, for four values of $\varepsilon_{\mathrm{BHH}}$, as defined by the maximum of the density of states [Equation (4.27), filled circles] and by the condition that the same number of levels lies between the energy target and $\varepsilon = 0$ for both models (open squares). Dashed lines and thick shades on the axes indicate the η ranges identified as the chaotic regions in Figures 4.9 and 4.10 and the corresponding intervals of $\varepsilon_{\mathrm{EGOE}}$.

As discussed in Section 4.2.1, the spectral and eigenvector properties of the embedded ensemble are symmetric around $\varepsilon = 0.5$ after ensemble average, whereas the Bose-Hubbard model obeys such a symmetry only for $\eta \to \infty$. Consequently, the hallmarks of quantum chaos in $\langle r \rangle$ and $\tilde{D}_q$ for the embedded ensemble are always strongest around $\varepsilon = 0.5$, while the energy at which quantum chaos is maximally developed for the Bose-Hubbard model depends on η. Therefore, one cannot directly compare the chaotic properties of both models around the same energy value ε. Since the maximum of the density of states lies deep in the center of the chaotic region for both models, as shown in Figure 3.5(a) (page 43) for the Bose-Hubbard model and in Figure 4.5 for the embedded ensemble, one may define comparable target energies, $\varepsilon_{\mathrm{BHH}}$ for the Bose-Hubbard Hamiltonian and $\varepsilon_{\mathrm{EGOE}}$ for the embedded ensemble, as those energies that lie at the same distance from the corresponding maximum of the density of states, $\varepsilon^{*}_{\mathrm{BHH}}(\eta)$ and $\varepsilon^{*}_{\mathrm{EGOE}} = 0.5$, that is,

$$\varepsilon_{\mathrm{EGOE}}(\varepsilon_{\mathrm{BHH}}, \eta) = \varepsilon_{\mathrm{BHH}} - \varepsilon^{*}_{\mathrm{BHH}}(\eta) + 0.5. \tag{4.27}$$

Alternatively, $\varepsilon_{\mathrm{BHH}}$ and $\varepsilon_{\mathrm{EGOE}}$ could be defined as those energies that bound from above the same number of energy levels.

In Figure 4.8, the target energies $\varepsilon_{\mathrm{EGOE}}$ are shown as functions of η for both definitions and for four different values of $\varepsilon_{\mathrm{BHH}}$. The system under consideration is that of $N = L = 10$ particles and sites with parity $\Pi = -1$, for the Bose-Hubbard model furthermore with HWBCs ($\mathcal{N} = 46\,126$). While the two definitions do yield different results for

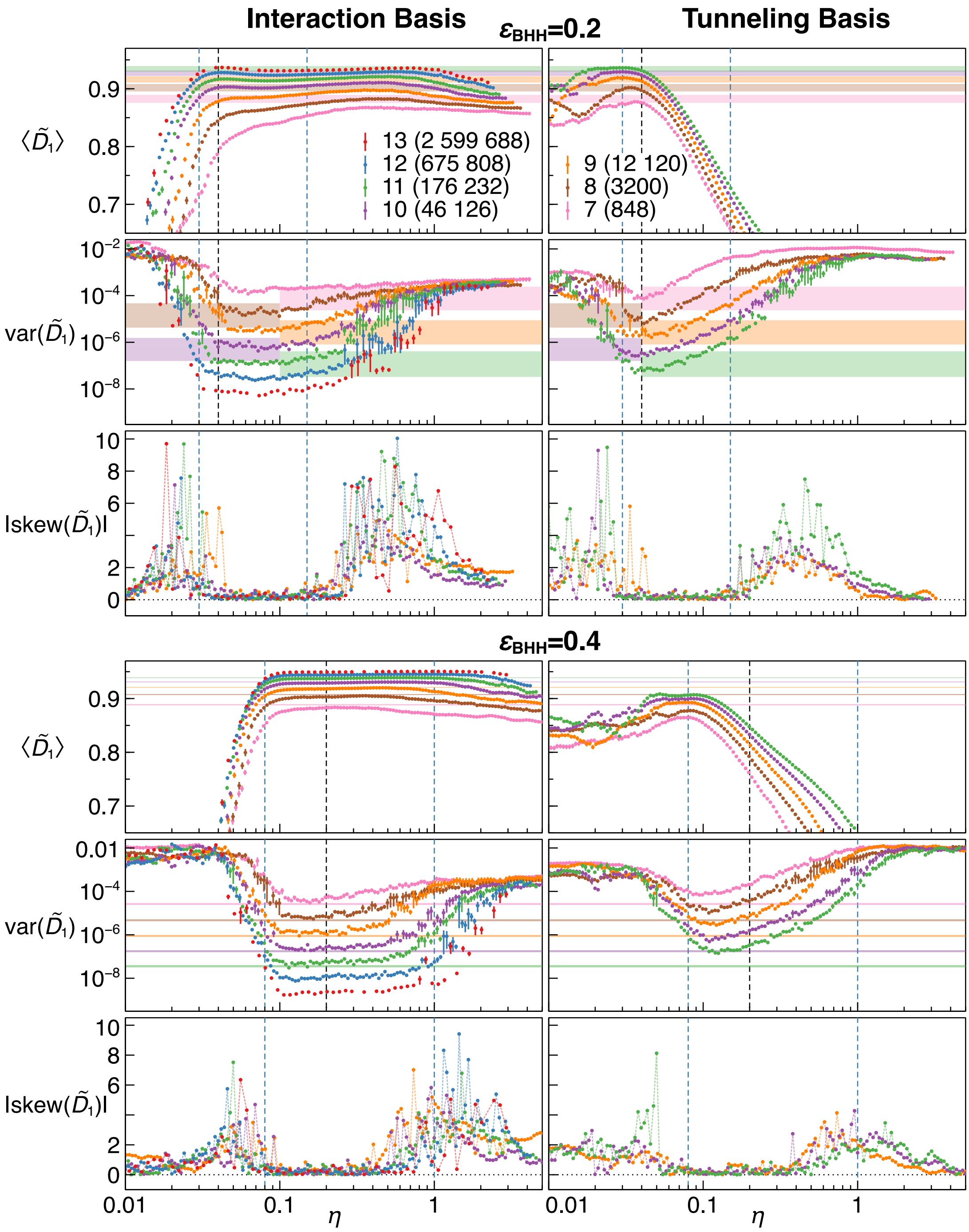

Figure 4.9: Mean, variance and absolute skewness of $\tilde{D}_1$, in both natural bases, versus $\eta = J/UN$, for the 100 Bose-Hubbard eigenstates closest to $\varepsilon_{\mathrm{BHH}} = 0.2$ and $\varepsilon_{\mathrm{BHH}} = 0.4$, with HWBCs, $\Pi = -1$, $N = L \in [7, 13]$ ($\mathcal{N} \in [848, 2\,599\,688]$). Shaded regions highlight corresponding results for the embedded ensemble as described in the main text. Dashed vertical lines indicate the η range of the chaotic domain [blue, Equation (4.28)] and the η values investigated in Figures 4.12 and 4.13 (black). When not shown, error bars are contained within symbol size (not included for the skewness to ease visualization).

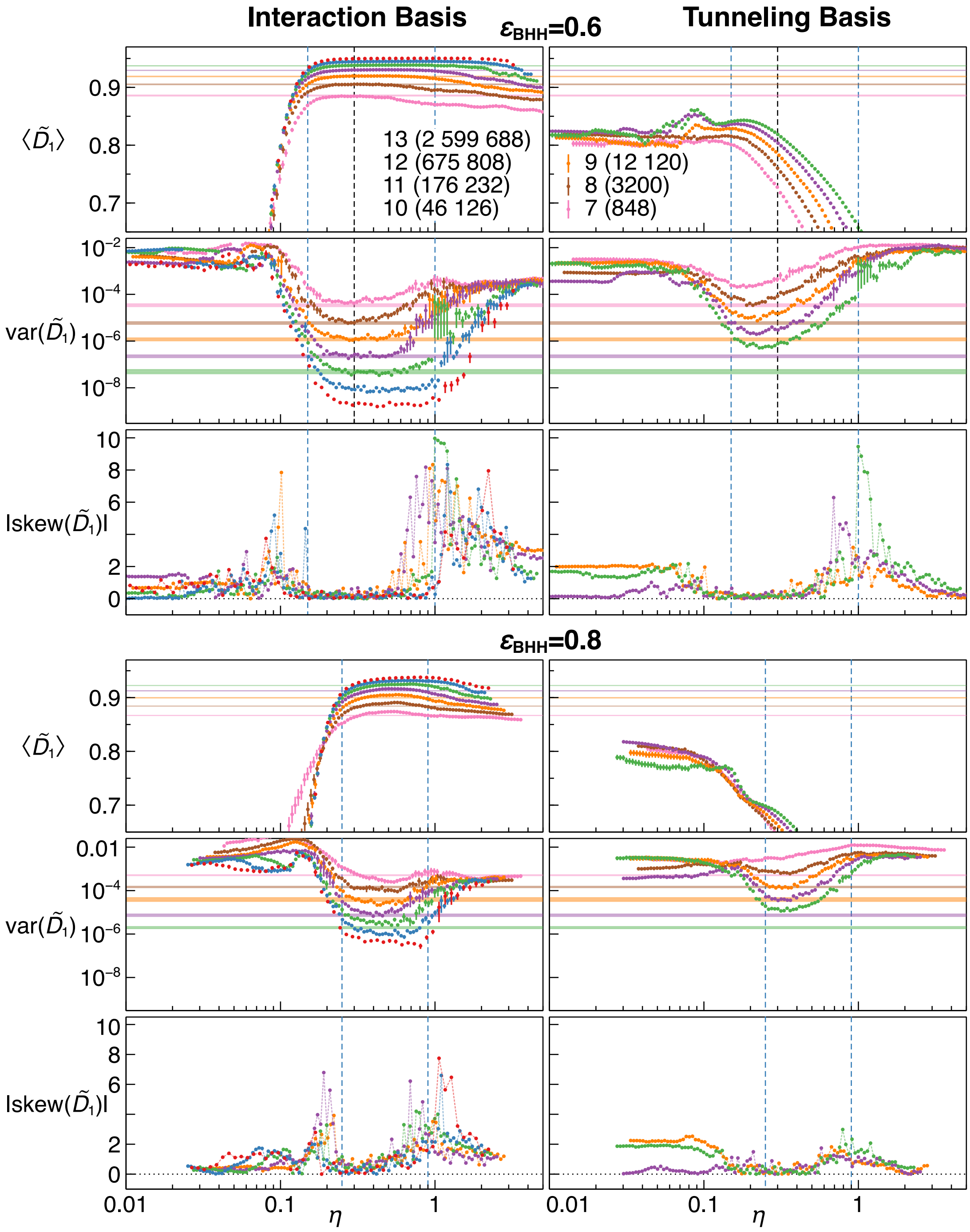

Figure 4.10: Same as Figure 4.9, for $\varepsilon_{\mathrm{BHH}} = 0.6$ and $\varepsilon_{\mathrm{BHH}} = 0.8$.

$\varepsilon_{\mathrm{EGOE}}$ at small η,[2] the values are essentially equivalent in the relevant chaotic domains for η. Note that, at large η, the energies $\varepsilon_{\mathrm{EGOE}}$ according to Equation (4.27) become equal to the energies $\varepsilon_{\mathrm{BHH}}$, since the density of states becomes symmetric around $\varepsilon = 0.5$ for the Bose-Hubbard Hamiltonian.

Figures 4.9 and 4.10 (pages 76 and 77) show the evolution of the mean $\langle \tilde{D}_1 \rangle$, the variance $\operatorname{var}(\tilde{D}_1)$ and the absolute value of the skewness $\left|\operatorname{skew}(\tilde{D}_1)\right|$ over the 100 Bose-Hubbard eigenstates closest to the target energies $\varepsilon_{\mathrm{BHH}} = 0.2$, 0.4, 0.6 and 0.8, for HWBCs, parity $\Pi = -1$, and system sizes from $N = L = 7$ ($\mathcal{N} = 848$) to $N = L = 13$ ($\mathcal{N} = 2\,599\,688$). For each $\varepsilon_{\mathrm{BHH}}$, we identify the range of η values defining the chaotic domain, making sure that it covers the variance minimum in both natural bases. These η intervals are

$$\begin{aligned} &\varepsilon_{\mathrm{BHH}} = 0.2 \mapsto \eta \in [0.03, 0.15], && \varepsilon_{\mathrm{BHH}} = 0.4 \mapsto \eta \in [0.08, 1.0], \\ &\varepsilon_{\mathrm{BHH}} = 0.6 \mapsto \eta \in [0.15, 1.0], && \varepsilon_{\mathrm{BHH}} = 0.8 \mapsto \eta \in [0.25, 0.9]. \end{aligned} \tag{4.28}$$

Then the corresponding $\varepsilon_{\mathrm{EGOE}}$ intervals are read off from Figure 4.8, according to Equation (4.27):

$$\begin{aligned} &\varepsilon_{\mathrm{BHH}} = 0.2 \mapsto \varepsilon_{\mathrm{EGOE}} \in [0.23, 0.515], && \varepsilon_{\mathrm{BHH}} = 0.4 \mapsto \varepsilon_{\mathrm{EGOE}} \in [0.395, 0.54], \\ &\varepsilon_{\mathrm{BHH}} = 0.6 \mapsto \varepsilon_{\mathrm{EGOE}} \in [0.595, 0.67], && \varepsilon_{\mathrm{BHH}} = 0.8 \mapsto \varepsilon_{\mathrm{EGOE}} \in [0.795, 0.81], \end{aligned} \tag{4.29}$$

as highlighted by the dashed lines and the thick shades in Figure 4.8. For each of the intervals, we consider the values of $\varepsilon_{\mathrm{EGOE}}$ closest to and furthest from $\varepsilon = 0.5$, since these yield the extremal values of $\langle \tilde{D}_q \rangle$ and $\operatorname{var}(\tilde{D}_q)$, according to Figure 4.6. Around these target energies, we then calculate $\langle \tilde{D}_1 \rangle$ and $\operatorname{var}(\tilde{D}_1)$ for 100 eigenstates of the embedded ensemble, averaging the results over 100 ensemble realizations, and show in Figures 4.9 and 4.10 the corresponding ranges of $\langle \tilde{D}_1 \rangle$ and $\operatorname{var}(\tilde{D}_1)$. Note that system sizes $N \geq 12$ are out of numerical reach for the embedded ensemble.

For all $\varepsilon_{\mathrm{BHH}}$ and all system sizes considered, the mean fractal dimension in the interaction basis registers a sharp increase as a function of η towards an almost constant plateau around its largest values, which is accompanied by a sharp decrease of the variance by several orders of magnitude into an equally constant plateau of minimal values. Furthermore, the skewness increases at the boundaries of the plateau region and is strongly reduced around the center of that domain. As discussed in Sections 3.3 and 3.4, these three features, particularly the sharp minimum of the variance, indicate quantum chaos in terms of the fractal dimensions.

The extension of the plateau depends on the energy, in agreement with our preceding discussion of $\tilde{D}_q$ versus $\varepsilon_{\mathrm{BHH}}$ and η in Section 3.3: For increasing $\varepsilon_{\mathrm{BHH}}$, the onset of the plateau is shifted to larger η, and the plateau width is maximal for intermediate energies $\varepsilon_{\mathrm{BHH}} = 0.4$ and $\varepsilon_{\mathrm{BHH}} = 0.6$. Within the plateau, the values of $\langle \tilde{D}_1 \rangle$ for $\varepsilon_{\mathrm{BHH}} \geq 0.4$ and of $\operatorname{var}(\tilde{D}_1)$ for all $\varepsilon_{\mathrm{BHH}}$ are in good agreement with the corresponding embedded-ensemble data. Hence, when the correspondence between $\varepsilon_{\mathrm{BHH}}$ and $\varepsilon_{\mathrm{EGOE}}$ is correctly

---

[2] Note that for $\varepsilon_{\mathrm{BHH}} = 0.8$, Equation (4.27) leads to unphysical values $\varepsilon_{\mathrm{EGOE}} > 1$ for small η and is hence not applicable here.

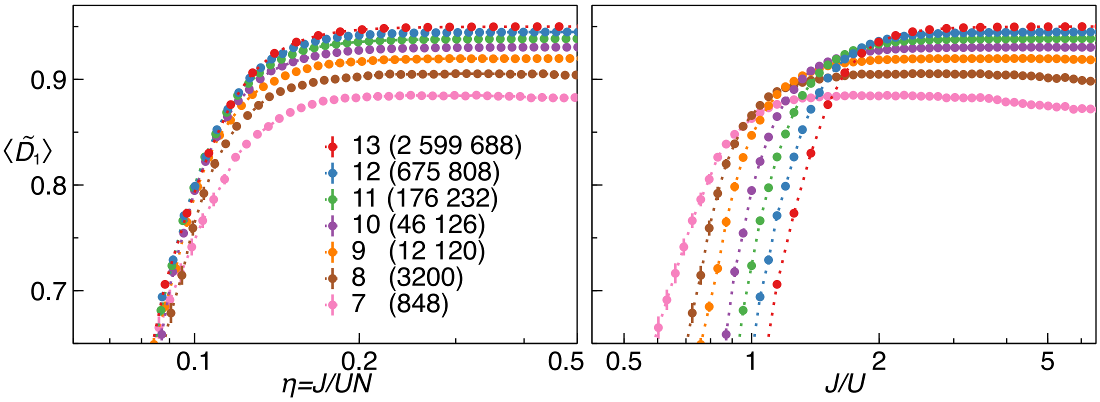

Figure 4.11: $\langle \tilde{D}_1 \rangle$ versus $\eta = J/UN$ (left) and J/U (right), for the 100 Bose-Hubbard eigenstates closest to $\varepsilon_{\mathrm{BHH}} = 0.6$, with HWBCs, $\Pi = -1$, and $N = L \in [7, 13]$ ($\mathcal{N} \in [848, 2\,599\,688]$). When not shown explicitly, error bars are contained within symbol size.

established, the embedded ensemble captures also the energy dependence of the chaotic domain in the Bose-Hubbard model.

The emergence of the plateaux in terms of $\langle \tilde{D}_1 \rangle$ and var $(\tilde{D}_1)$ is strongest for $\varepsilon_{\mathrm{BHH}} \leq 0.6$. These energies belong to the bulk of the spectrum for an η interval within the chaotic range: In that η range, they come close to the maximum of the density of states and they belong to the inner 60 % of the states, as shown in Figure 3.5(a). But even for $\varepsilon_{\mathrm{BHH}} = 0.8$, which is far from the maximum of the density of states for all η and can hence be considered as the edge of the spectrum, a clear fingerprint of quantum chaos can be seen in the strong reduction of var $(\tilde{D}_1)$.

In the tunneling basis, $\langle \tilde{D}_1 \rangle$ reaches a maximum and var $(\tilde{D}_1)$ decays by several orders of magnitude within similar ranges of η as for the interaction basis. However, a plateau is emerging only for $\langle \tilde{D}_1 \rangle$ at energies $\varepsilon_{\mathrm{BHH}} \leq 0.4$ and in a rather limited η interval. The embedded ensemble describes the Bose-Hubbard data in the tunneling basis well only for $\varepsilon_{\mathrm{BHH}} = 0.2$, where, however, the agreement is even better than with the Bose-Hubbard model in the interaction basis. This result shows the strong basis dependence of the emergence of quantum chaos in terms of the mean fractal dimensions. Nevertheless, the behaviours of var $(\tilde{D}_1)$ and skew $(\tilde{D}_1)$ are qualitatively the same for both bases, which confirms their importance as qualitatively basis-independent markers of quantum chaos.

For energies $\varepsilon_{\mathrm{BHH}} \geq 0.4$, the low-$\eta$ boundary of the plateau region for $\langle \tilde{D}_1 \rangle$ and var $(\tilde{D}_1)$ in the interaction basis clearly attains a system-size independent value for increasing L, a behaviour which the available data strongly suggests also for $\varepsilon_{\mathrm{BHH}} = 0.2$ and L currently out of numerical reach. This shows that $\eta = J/UN$ is indeed the correct parameter to describe the transition to quantum chaos at fixed energies $\varepsilon_{\mathrm{BHH}}$. In contrast, the high-$\eta$ boundary of the plateau keeps increasing with L, which indicates that the chaotic region might extend to arbitrarily large η in the thermodynamic limit $\mathcal{N} \to \infty$ at fixed density N/L, and the integrable point $\eta = \infty$ might thus become a discontinuity. This finding is in agreement with previous results for fermions [113], hard-core bosons [112] and spin systems [108], where it was found that the critical strength of an integrability-breaking perturbation decays with linear system size L, and hence quantum chaos sets in for arbitrarily small perturbation strengths at $L \to \infty$.

To further strengthen the claim that the semiclassically inspired parameter $\eta = J/UN$ correctly describes the onset of quantum chaos in the Bose-Hubbard Hamiltonian at fixed values of ε, we compare in Figure 4.11 (page 79) the behaviour of the mean $\langle \tilde{D}_1 \rangle$ as a function of η and of J/U around $\varepsilon_{\mathrm{BHH}} = 0.6$ for increasing $N = L$. While the onset of the plateau for $\langle \tilde{D}_q \rangle$ is found at approximately the same η for all system sizes, the position of this surge keeps drifting to larger J/U upon increasing system size. Hence, our results show that in the limit $N = L \to \infty$ the chaotic region will disappear for any finite value of J/U, but not for finite values of η. This finding can also be understood intuitively: For fixed J/U, the different scalings of $\langle H_{\mathrm{tun}} \rangle$ and $\langle H_{\mathrm{int}} \rangle$, linear versus quadratic in N (compare Section 2.4.3 on page 33), effectively make the system flow towards the integrable limit of infinite interactions upon increasing the number of particles.

4.4. Scaling of Fractal Dimensions with Hilbert Space Dimension in the Chaotic Region

We have seen in the preceding section that the maximum of the mean $\langle \tilde{D}_q \rangle$ and the minimum of the variance $\mathrm{var}\left(\tilde{D}_q\right)$ of Bose-Hubbard eigenstates in the tunneling basis at $\varepsilon_{\mathrm{BHH}} = 0.2$ and in the interaction basis at $\varepsilon_{\mathrm{BHH}} = 0.4$ and $\varepsilon_{\mathrm{BHH}} = 0.6$ agree very well with the embedded ensemble for $\varepsilon_{\mathrm{EGOE}}$ in the center of the spectrum[3] and, consequently, also with GOE (for the latter, see Figure 4.6). Therefore, one might ask whether the eigenstates of the Bose-Hubbard model in the chaotic domain become ergodic in the sense of $\tilde{D}_q \to 1$ for $\mathcal{N} \to \infty$, just like the corresponding eigenstates of GOE random matrices (see the finite-size scalings discussed in Section 4.1). To answer this question, we compare in this section the fractal dimensions as functions of Hilbert space dimension $\mathcal{N}$ for the three models (Bose-Hubbard, embedded ensemble and GOE), investigating specifically the mean $\langle \tilde{D}_q \rangle$, the variance $\mathrm{var}\left(\tilde{D}_q\right)$ and the full distributions of $\tilde{D}_q$.

4.4.1. Mean and Variance

In the following, we fix three different pairs of values $(\varepsilon_{\mathrm{BHH}}, \eta) = (0.2, 0.04)$, $(0.4, 0.2)$, $(0.6, 0.3)$ (highlighted by black dashed lines in Figures 4.9 and 4.10) within the chaotic domain of the Bose-Hubbard model. We investigate $\langle \tilde{D}_q \rangle$ and $\mathrm{var}\left(\tilde{D}_q\right)$ for the 100 eigen-

---

[3] Note that for $\varepsilon_{\mathrm{BHH}} = 0.2$, the interval $\varepsilon_{\mathrm{EGOE}} \in [0.23, 0.515]$ shown in Figure 4.9 is quite broad, but the maximum of $\left\langle \tilde{D}_q \right\rangle$ and the minimum of $\mathrm{var}\left(\tilde{D}_q\right)$ in the tunneling basis for the largest L agree best with the upper limit of that energy range, i.e., $\varepsilon_{\mathrm{EGOE}} \approx 0.5$.

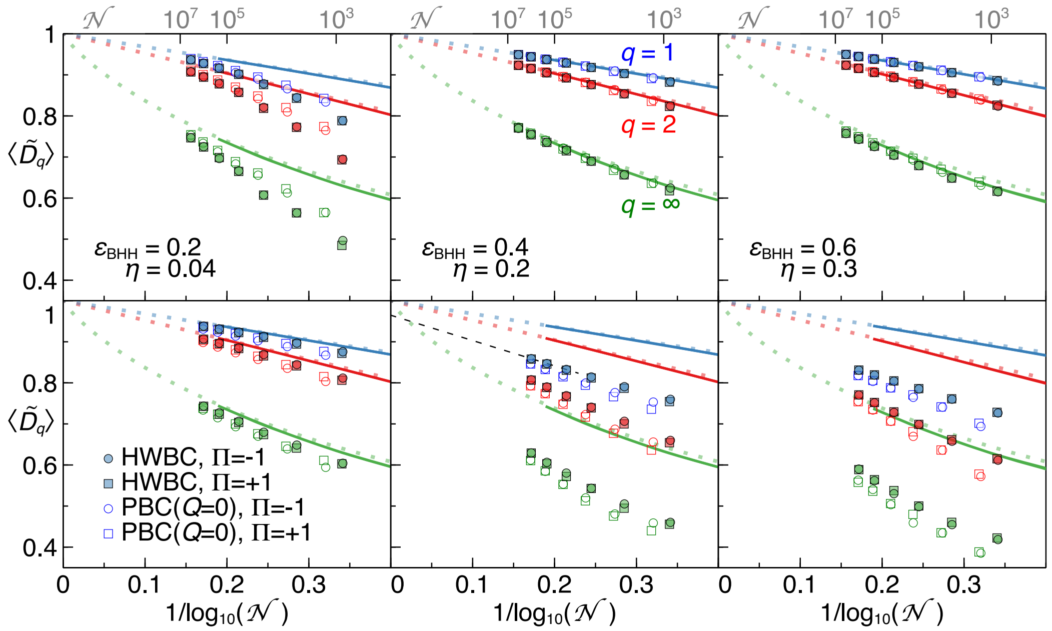

Figure 4.12: Dependence of $\langle \tilde{D}_q \rangle$, $q = 1, 2, \infty$, in the interaction basis (upper panels) and in the tunneling basis (lower panels) on the Hilbert space dimension $\mathcal{N}$, for three values of $(\varepsilon_{\mathrm{BHH}}, \eta)$, and for boundary conditions and parities/quasimomenta as indicated in the legend. Bose-Hubbard data points are calculated from the 100 eigenstates closest to the given $\varepsilon_{\mathrm{BHH}}$ at the given η. Dotted lines indicate $\langle \tilde{D}_q \rangle_{\mathrm{GOE}}$, Equations (4.3), (4.11), (4.18), and solid lines show numerically calculated embedded-ensemble data for energies $\varepsilon_{\mathrm{EGOE}}$ obtained from $(\varepsilon_{\mathrm{BHH}}, \eta)$ according to Equation (4.27) and given in Equation (4.30). The black dashed line in the lower central panel is a fit of $f(\mathcal{N}) = a + b/\ln \mathcal{N}$ to the last three $\langle \tilde{D}_1 \rangle$ data points, for HWBCs, $\Pi = -1$, yielding $a \approx 0.9647$, $b \approx -0.6165$. Error bars are contained within symbol size.

states closest to the given $\varepsilon_{\mathrm{BHH}}$ at the given η for all available system sizes, considering the subspaces of HWBCs and parity $\Pi = \pm 1$ as well as the subspaces given by quasimomentum $Q = 0$ and parity $\Pi = \pm 1$ for PBCs. Figure 4.12 shows the mean of $\tilde{D}_q$, with $q = 1, 2, \infty$, for the Bose-Hubbard model in both natural bases, for the embedded ensemble and for GOE, as functions of $1/\log \mathcal{N}$, which is the functional form of the leading-order finite-size correction to $\langle \tilde{D}_{1,2} \rangle_{\mathrm{GOE}}$ [Equations (4.4) and (4.13)]. Similarly, Figure 4.13 shows the variance of $\tilde{D}_q$, with $q = 1, 2, \infty$, for these three models, as functions of $1/\mathcal{N} \log^2 \mathcal{N}$, i.e., the leading-order finite-size correction to $\operatorname{var}(\tilde{D}_{1,2})_{\mathrm{GOE}}$ [Equations (4.8) and (4.14)]. Here, the GOE curves are calculated according to the analytical predictions, Equations (4.3), (4.6), (4.11), (4.12) and (4.18). Data for the embedded ensemble is calculated numerically from the 100 eigenstates closest to the

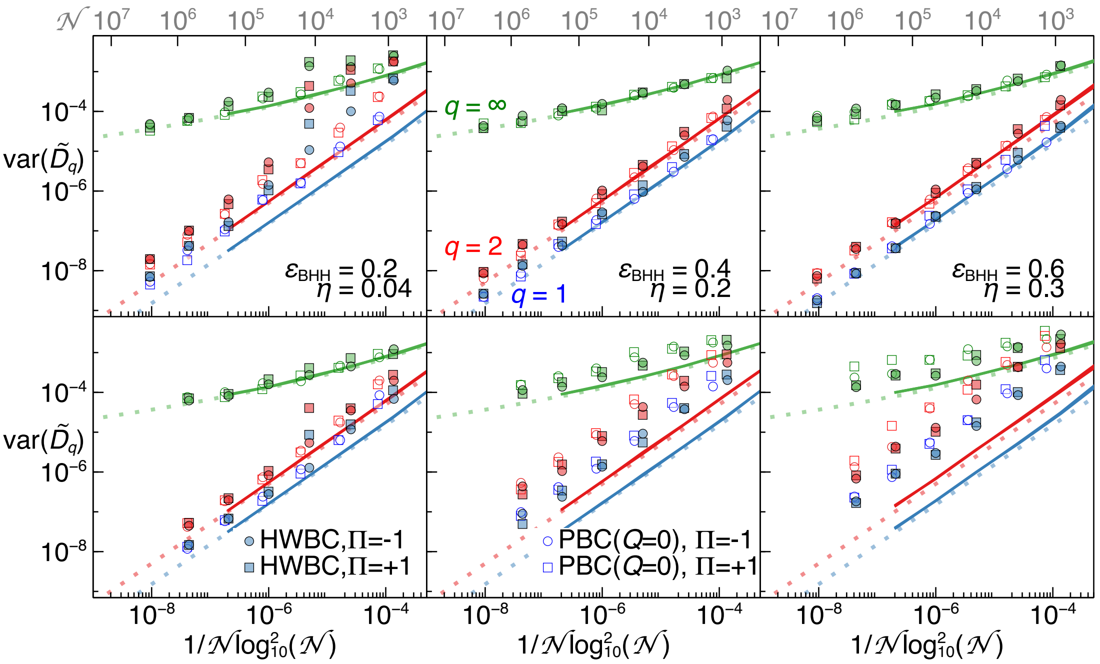

Figure 4.13: Dependence of $\mathrm{var}\,(\tilde{D}_q)$, $q = 1, 2, \infty$, in the interaction basis (upper panels) and in the tunneling basis (lower panels) on the Hilbert space dimension $\mathcal{N}$, for three different values of $(\varepsilon_{\rm BHH}, \eta)$, and for boundary conditions and parities/quasimomenta as indicated in the legend. Bose-Hubbard data points are calculated from the 100 eigenstates closest to the given $\varepsilon_{\rm BHH}$ at the given η. Dotted lines indicate $\mathrm{var}\,(\tilde{D}_q)_{\rm GOE}$, Equations (4.6), (4.12), (4.18), and solid lines show numerically calculated embedded-ensemble data for energies $\varepsilon_{\rm EGOE}$ obtained from $(\varepsilon_{\rm BHH}, \eta)$ according to Equation (4.27) and given in Equation (4.30). Error bars are contained within symbol size.

energy target $\varepsilon_{\rm EGOE}$, for $N = L \in [7, 11]$, averaging each data point over 100 ensemble realizations and subsequently joining the data points of different $\mathcal{N}$ by straight lines. Two embedded-ensemble curves are shown for the two parities $\Pi = \pm 1$, which are, however, barely distinguishable from one another. Like in the preceding section, $\varepsilon_{\rm EGOE}$ is calculated from η and $\varepsilon_{\rm BHH}$ according to Equation (4.27), and can be read off from Figure 4.8:

$$\begin{aligned}(\varepsilon_{\rm BHH} = 0.2, \eta = 0.04) &\mapsto \varepsilon_{\rm EGOE} = 0.5,\\ (\varepsilon_{\rm BHH} = 0.4, \eta = 0.2) &\mapsto \varepsilon_{\rm EGOE} = 0.45,\\ (\varepsilon_{\rm BHH} = 0.6, \eta = 0.3) &\mapsto \varepsilon_{\rm EGOE} = 0.6.\end{aligned} \tag{4.30}$$

For these three values of $\varepsilon_{\rm EGOE}$, which are well in the center of the spectrum of the embedded ensemble, $\langle \tilde{D}_q \rangle$ and $\mathrm{var}\,(\tilde{D}_q)$ for the two random ensembles are very close to each other and can barely be distinguished for the largest numerically accessible system sizes. Hence, the large-$\mathcal{N}$ behaviour coincides for these two models, and, in particular, the dominant finite-size corrections for the embedded ensemble follow the same functional forms as for GOE, Equations (4.4), (4.8), (4.13), (4.14), (4.19), (4.20).

Whether the Bose-Hubbard data is in agreement with the two random-matrix models depends strongly on $\varepsilon_{\mathrm{BHH}}$ and on the basis considered: In the tunneling basis at $\varepsilon_{\mathrm{BHH}} = 0.2$, and in the interaction basis at $\varepsilon_{\mathrm{BHH}} = 0.4$ and $\varepsilon_{\mathrm{BHH}} = 0.6$, the mean and the variance of $\tilde{D}_q$ quickly converge towards the random-matrix data. At the largest system sizes accessible for the tunneling basis at $\varepsilon_{\mathrm{BHH}} = 0.2$, the deviation between $\langle \tilde{D}_{1,2} \rangle$ and $\langle \tilde{D}_{1,2} \rangle_{\mathrm{GOE}}$ is already below $\langle \tilde{D}_{1,2} \rangle_{\mathrm{GOE}} - \langle \tilde{D}_{1,2} \rangle \lesssim 10^{-2}$. In the interaction basis at $\varepsilon_{\mathrm{BHH}} = 0.4$ and $\varepsilon_{\mathrm{BHH}} = 0.6$, where larger system sizes are numerically accessible, an even smaller difference $\langle \tilde{D}_{1,2} \rangle_{\mathrm{GOE}} - \langle \tilde{D}_{1,2} \rangle \lesssim 2 \times 10^{-3}$ is reached. A convergence to the random-matrix predictions is also observed in the interaction basis at $\varepsilon_{\mathrm{BHH}} = 0.2$, where, however, finite-size effects are stronger. Given this good agreement with GOE and with the embedded ensemble already for finite system sizes, we can expect that the leading-order finite-size corrections to the mean and the variance of $\tilde{D}_q$ for the Bose-Hubbard model follow the same functional form as for GOE, and that $\langle \tilde{D}_q \rangle$ and $\mathrm{var}\,(\tilde{D}_q)$ converge to the same values as the two random-matrix models in the limit $\mathcal{N} \to \infty$, that is,

$$\langle \tilde{D}_q \rangle \to 1, \qquad \mathrm{var}\,(\tilde{D}_q) \to 0. \tag{4.31}$$

In other words, the eigenstates of the Bose-Hubbard Hamiltonian become extended ergodic (as defined in Section 2.3) for $\mathcal{N} \to \infty$ in both bases at $(\varepsilon_{\mathrm{BHH}}, \eta) = (0.2, 0.04)$ and in the interaction basis at $(\varepsilon_{\mathrm{BHH}}, \eta) = (0.4, 0.2)$ and $(\varepsilon_{\mathrm{BHH}}, \eta) = (0.6, 0.3)$.

On the other hand, for the tunneling basis at $\varepsilon_{\mathrm{BHH}} = 0.4$ and $\varepsilon_{\mathrm{BHH}} = 0.6$, differences between the Bose-Hubbard model and the random-matrix models remain clearly visible for all available system sizes. Nevertheless, the overall qualitative tendency of $\langle \tilde{D}_q \rangle$ and $\mathrm{var}\,(\tilde{D}_q)$ with $\mathcal{N}$ is the same for the three models, and, hence, the Bose-Hubbard eigenstates might become extended ergodic for $\mathcal{N} \to \infty$ also in the tunneling basis at $\varepsilon_{\mathrm{BHH}} = 0.4$ and $\varepsilon_{\mathrm{BHH}} = 0.6$. However, the available data indicates that the leading-order corrections to $\langle \tilde{D}_q \rangle$ cannot follow the same functional form as for GOE, if $\langle \tilde{D}_q \rangle \to 1$. This is exemplified by the black dashed line in the lower central panel of Figure 4.12, which is a linear fit of the function

$$f(\mathcal{N}) = a + \frac{b}{\mathcal{N}}, \tag{4.32}$$

with parameters a, b, to $\langle \tilde{D}_1 \rangle$ with HWBCs and parity $\Pi = -1$, for the three largest system sizes. If $\langle \tilde{D}_1 \rangle$ converges to 1 in the limit $\mathcal{N} \to \infty$ with the same functional form of the leading-order correction as for GOE, one would expect $a = 1$, which is not true here: Instead, one obtains $a \approx 0.9647$ and $b \approx -0.6165$.

This result reveals that the Bose-Hubbard Hamiltonian does not follow the “weakly ergodic” regime introduced and discussed in Reference [84]. This regime is characterized by convergence of the eigenstates to ergodicity in the limit $\mathcal{N} \to \infty$, following the

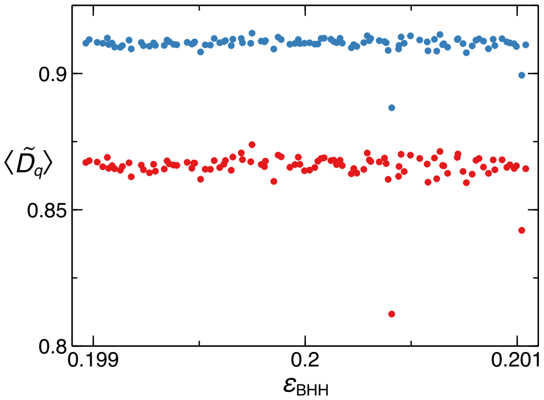

Figure 4.14: Eigenstate fractal dimensions $\tilde{D}_1$ (red) and $\tilde{D}_2$ (blue) in the tunneling basis versus scaled eigenenergies $\varepsilon_{\mathrm{BHH}}$, for the 100 eigenstates closest to $\varepsilon_{\mathrm{BHH}} = 0.2$ at $\eta = 0.04$, for $N = L = 9$ with HWBCs and $\Pi = +1$ ($\mathcal{N} = 12\,190$).

functional form of the leading-order finite-size corrections predicted by GOE, but with a different coefficient. In that work, it was concluded from investigating $\langle \tilde{D}_q \rangle$ for the quantized standard map and for spin systems that chaotic many-body Hamiltonians generically follow this weakly ergodic behaviour. As we have shown here, this is not true for the Bose-Hubbard Hamiltonian in the tunneling basis, which reveals that this weakly ergodic regime cannot be as universal as claimed in Reference [84].

The behaviour of $\mathrm{var}\left(\tilde{D}_q\right)$ for $\varepsilon_{\mathrm{BHH}} = 0.2$ in both natural bases shows some features that deserve further discussion. For the interaction basis and HWBCs, the variance as a function of $\mathcal{N}$ first decreases much slower than the GOE prediction, then drops by several orders of magnitude and subsequently decays qualitatively similar to the GOE variance. This behaviour is in agreement with the shift of the chaotic region with $N = L$ at $\varepsilon_{\mathrm{BHH}} = 0.2$, as observed in Figure 4.9: For the smallest system sizes, $\eta = 0.04$ does not yet belong to the plateau of $\mathrm{var}\left(\tilde{D}_q\right)$ in the interaction basis, which explains the larger variances for small $\mathcal{N}$. As soon as the onset of the plateau shifts to $\eta < 0.04$, $\mathrm{var}\left(\tilde{D}_q\right)$ decreases by several orders of magnitude and then matches well with the functional form given by GOE.

For the tunneling basis, HWBCs and parity $\Pi = +1$, $\mathrm{var}\left(\tilde{D}_q\right)$ is strongly enhanced for $N = L = 9$ ($\mathcal{N} = 12\,190$) as compared to the tendency of the other system sizes. In Figure 4.14, the fractal dimensions $\tilde{D}_1$ and $\tilde{D}_2$ of all the eigenstates entering this variance for $N = L = 9$ are shown as functions of the corresponding scaled eigenenergies. This figure reveals that the anomalously large variance is caused by just two states with significantly smaller fractal dimensions. This shows that, for $N = 9$, quantum chaos has not fully developed yet for all eigenstates at these values of $\varepsilon_{\mathrm{BHH}}$ and η.

4.4.2. Comparison of Full Distributions

As revealed by the results of the preceding section, the distribution of fractal dimensions from different Bose-Hubbard eigenstates deep in the chaotic regime shows clear agreement with the universal predictions of random-matrix theory in terms of its first two moments $\langle \tilde{D}_q \rangle$ and $\operatorname{var}(\tilde{D}_q)$. We will see in the following that, despite this emergence of universal features, the full $\tilde{D}_q$ distributions of the Bose-Hubbard model become ever more distinguishable from those of GOE and of the embedded ensemble as system size increases. For this analysis, we consider the Bose-Hubbard eigenvectors in the interaction basis at $\varepsilon_{\mathrm{BHH}} = 0.5$, which is between the energies $\varepsilon_{\mathrm{BHH}} = 0.4$ and $\varepsilon_{\mathrm{BHH}} = 0.6$, for which $\langle \tilde{D}_q \rangle$ and $\operatorname{var}(\tilde{D}_q)$ in the chaotic domain are closest to GOE and the embedded ensemble.

In Figure 4.15 on the next page, the probability density functions of $\tilde{D}_q$ are shown for the three models, for HWBCs with $\Pi = -1$, and system dimensions ranging up to $N = L = 13$ ($\mathcal{N} = 2\,599\,688$). For the embedded ensemble, which is numerically more challenging than the Bose-Hubbard model, due to a larger number of nonzero matrix elements, the largest system size shown is $N = L = 11$ ($\mathcal{N} = 176\,232$). Here, the Bose-Hubbard distributions are calculated from a total of 500 values of $\tilde{D}_q$ deep in the chaotic domain, which are obtained from five values of η in $[0.25, 0.38]$ and, for each η, from 100 eigenstates around $\varepsilon_{\mathrm{BHH}} = 0.5$. Data for the embedded ensemble is obtained numerically from 100 realizations and, per realization, from 100 eigenstates around $\varepsilon_{\mathrm{EGOE}} = 0.5$ [obtained from $\varepsilon_{\mathrm{BHH}}$ and η according to Equation (4.27), as described in Section 4.3].

As system size increases, instead of converging towards each other, the distributions of the three models become ever more distinguishable from one another. At the two largest system sizes $N = L = 12$ and $N = L = 13$, for $q = 1, 2$, the distributions for the Bose-Hubbard model and for GOE do not even overlap. The distribution for the embedded ensemble is always between the Bose-Hubbard and GOE distributions, and, for $q = 1, 2$, it departs from both of them. This observation shows that the distance between the Bose-Hubbard and GOE distributions is partially explained by the two-body nature of the former Hamiltonian, which is also a feature of the embedded ensemble, but not of GOE. Nevertheless, the two-body nature of the embedded ensemble is not enough to describe the distribution $P(\tilde{D}_q)$ of the Bose-Hubbard model in the chaotic domain completely: Instead, the more specific nearest-neighbour character of the tunneling and the on-site nature of the interactions in the Bose-Hubbard Hamiltonian, as well as the enhanced correlations between its matrix elements due to their dependence on J and U alone, need to play a major role.

We quantify the distance between two probability distributions $P_1(\tilde{D}_q)$, $P_2(\tilde{D}_q)$ via the relative separation of their means,

$$d_q(P_1, P_2) = \frac{\left| \langle \tilde{D}_q \rangle_1 - \langle \tilde{D}_q \rangle_2 \right|}{\sqrt{\operatorname{var}(\tilde{D}_q)_1}}, \tag{4.33}$$

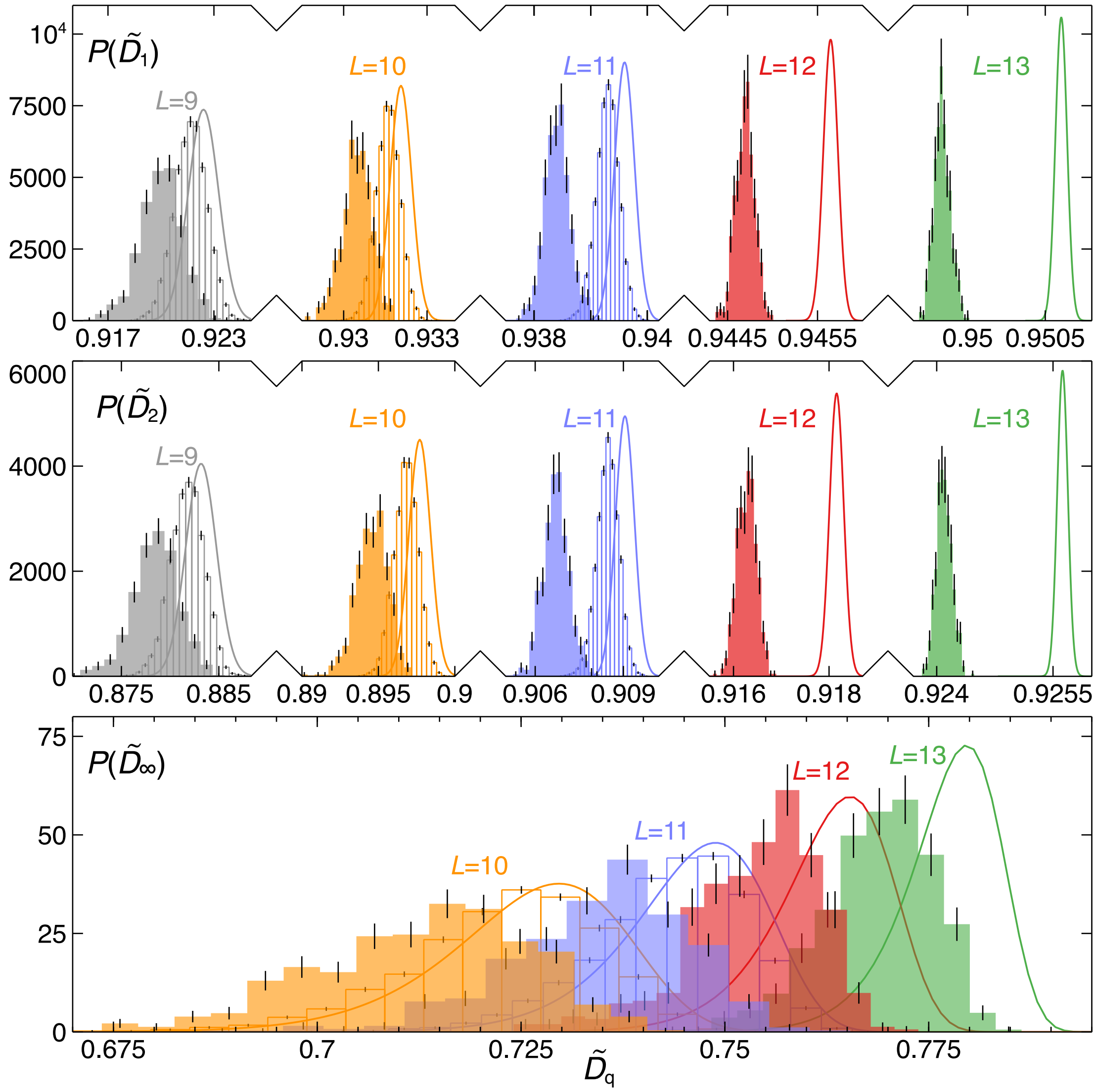

Figure 4.15: Probability density functions $P(\tilde{D}_q)$ for the Bose-Hubbard model in the interaction basis [filled histograms], for the embedded ensemble [outlined histograms] and for GOE [solid lines, Equations (4.21) and (4.22)], for HWBCs with $\Pi = -1$, and system sizes from $N = L = 9$ ($\mathcal{N} = 12\,120$), to $N = L = 13$ ($\mathcal{N} = 2\,599\,688$). To enhance visibility, $P(\tilde{D}_{1,2})$ is multiplied by a factor of 2 ($L = 12$), 4 ($L = 11$), 8 ($L = 10$) and 16 ($L = 9$), respectively. Bose-Hubbard distributions are calculated from five η values in $[0.25, 0.38]$ and, for each η, from 100 eigenstates closest to $\varepsilon_{\mathrm{BHH}} = 0.5$. Embedded-ensemble data is obtained from 100 realizations and, per realization, from 100 eigenstates around $\varepsilon_{\mathrm{EGOE}} = 0.5$.

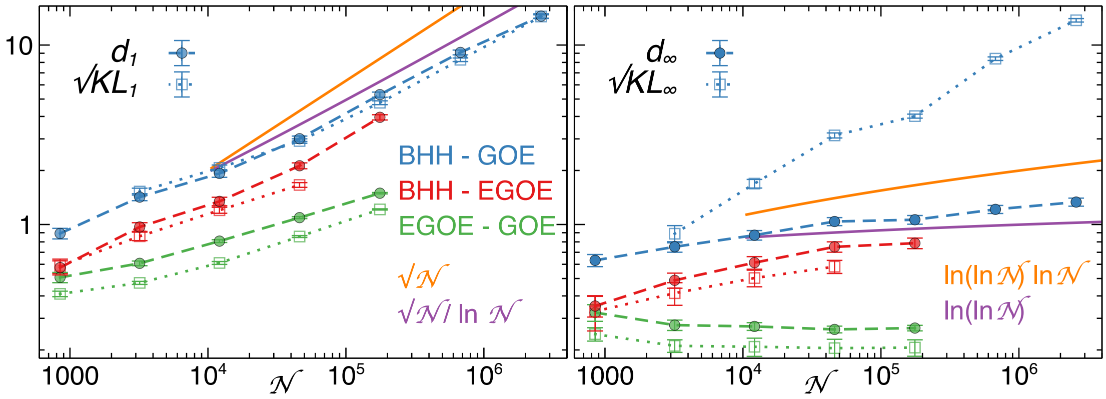

Figure 4.16: Distance measures d_q [Equation (4.33)] and $\sqrt{KL_q}$ [Equation (4.34)] between the probability distributions of $\tilde{D}_1$ (left) and of $\tilde{D}_\infty$ (right) shown in Figure 4.15, for the Bose-Hubbard model (BHH), the embedded ensemble (EGOE), and GOE, versus Hilbert space dimension $\mathcal{N}$, for HWBCs with $\Pi = -1$. Solid lines denote the scalings of d_q (as indicated in the legend) that would emerge if the finite-size correction coefficients in leading order were to be different for the three models (orange) and if $P(\tilde{D}_q)$ followed the same functional form for the three models, with different effective dimensions $\tilde{\mathcal{N}}$ (purple).

and via the Kullback-Leibler divergence (information entropy) [189, 190],

$$KL_q(P_1, P_2) = \int_0^1 P_1(\tilde{D}_q) \ln \frac{P_1(\tilde{D}_q)}{P_2(\tilde{D}_q)} \, \mathrm{d}\tilde{D}_q. \tag{4.34}$$

Here, we always choose P_1 as the Bose-Hubbard distribution and P_2 as GOE or the embedded ensemble, depending on the comparison. Note that an accurate calculation of KL_q requires detailed knowledge of $P_2(\tilde{D}_q)$ in the range where $P_1(\tilde{D}_q)$ is large, since this is the region which contributes the most to KL_q. Hence, for the numerically obtained distributions of the Bose-Hubbard Hamiltonian and of the embedded ensemble, the Kullback-Leibler divergence for the largest accessible system size $N = L = 11$ cannot be calculated reliably, due to the small overlap of the distributions.

For two Gaussian distributions of $\tilde{D}_q$ with identical variances $\mathrm{var}\,(\tilde{D}_q)_1 = \mathrm{var}\,(\tilde{D}_q)_2$, the Kullback-Leibler divergence can be calculated exactly and reads

$$\sqrt{KL_q}(P_1, P_2) = \frac{1}{\sqrt{2}} d_q(P_1, P_2). \tag{4.35}$$

Hence, the comparison between $\sqrt{KL_q}$ and d_q also provides insight into the Gaussian shape of the distributions and deviations from Gaussianity.

As shown in Figure 4.16 for the distributions displayed in Figure 4.15, both distance measures increase with system size for $q = 1$ and all three models, which confirms and quantifies the departure of the underlying probability distributions. For the largest system size considered ($N = L = 13$), the means of $\tilde{D}_1$ for the Bose-Hubbard Hamiltonian and for GOE already differ by more than ten standard deviations, and extrapolation suggests that the distance between the embedded ensemble and the Bose-Hubbard model will be of similar magnitude for this system size.

While the distance measures d_∞ and KL_∞ between the Bose-Hubbard Hamiltonian and any of the random-matrix models increase with system size, they decrease for GOE and the embedded ensemble, suggesting that the distributions $P(\tilde{D}_\infty)$ of these two models approach each other for increasing $\mathcal{N}$. Hence, the two random-matrix models cannot be distinguished solely from the statistics of the largest eigenvector intensity (which fully defines $\tilde{D}_\infty$), but this single intensity is sufficient to distinguish the Bose-Hubbard Hamiltonian in the chaotic domain from the two random-matrix models.

The measures d_1 and KL_1 show a very good qualitative agreement with each other. Given that the variances converge to one another and that the shape of the distributions looks Gaussian, this behaviour is expected from Equation (4.35). On the other hand, d_∞ and KL_∞ for the Bose-Hubbard Hamiltonian versus GOE clearly deviate from one another, in agreement with the obviously non-Gaussian shape of $P(\tilde{D}_\infty)$ observed in Figure 4.15.

The behaviour of d_q as a function of $\mathcal{N}$ provides insight into the source of the deviations between the distributions. The good agreement of $\langle \tilde{D}_q \rangle$ and $\mathrm{var}\,(\tilde{D}_q)$ among the three models already for rather small $\mathcal{N}$, as discussed in Section 4.4.1, indicates that their leading-order finite-size corrections have the same functional form. With the known finite-size expansions of GOE, Equations (4.4), (4.8), (4.13), (4.14), (4.19) and (4.20), this means that

$$1 - \langle \tilde{D}_{1,2} \rangle \sim \frac{1}{\ln \mathcal{N}}, \qquad 1 - \langle \tilde{D}_\infty \rangle \sim \frac{\ln(\ln \mathcal{N})}{\ln \mathcal{N}}, \tag{4.36}$$

$$\mathrm{var}\,(\tilde{D}_{1,2}) \sim \frac{1}{\mathcal{N} \ln^2 \mathcal{N}}, \qquad \mathrm{var}\,(\tilde{D}_\infty) \sim \frac{1}{\ln^4 \mathcal{N}}, \tag{4.37}$$

in leading order for the embedded ensemble and the Bose-Hubbard Hamiltonian in the interaction basis around $\varepsilon = 0.5$. Regarding the scaling of $\langle \tilde{D}_q \rangle$, three scenarios are possible:

1. The models share the same functional form of the leading-order correction, but the coefficient is different. This means that the distance between the means of any two of the models scales as

   $$\left| \langle \tilde{D}_{1,2} \rangle_1 - \langle \tilde{D}_{1,2} \rangle_2 \right| \sim \frac{1}{\ln \mathcal{N}}, \qquad \left| \langle \tilde{D}_\infty \rangle_1 - \langle \tilde{D}_\infty \rangle_2 \right| \sim \frac{\ln(\ln \mathcal{N})}{\ln \mathcal{N}},$$

   and hence d_q scales as

   $$d_{1,2} \sim \sqrt{\mathcal{N}}, \qquad d_\infty \sim \ln(\ln \mathcal{N}) \ln \mathcal{N}. \tag{4.38}$$

   These scalings are shown in Figure 4.16 as orange solid lines.

2. The coefficient of the leading-order correction is the same for the models, and the first subleading correction that is different decays slower than $\sqrt{\mathrm{var}\,(\tilde{D}_q)}$. In this case, d_q increases with $\mathcal{N}$, but slower than the scalings given in Equation (4.38).
3. The finite-size corrections of the means agree up to an order that decays faster than $\sqrt{\mathrm{var}\,(\tilde{D}_q)}$. The distance d_q would then decrease with $\mathcal{N}$.

The increase of d_1 with $\mathcal{N}$ clearly rules out the third case for $q = 1$ and all three models. Particularly between the Bose-Hubbard model and GOE, D_1 grows slower with $\mathcal{N}$ than the scaling suggested in Equation (4.38) (orange solid line in Figure 4.16), which indicates that the second case holds. Note that d_q between the Bose-Hubbard model and the embedded ensemble is bounded from above by d_q between the Bose-Hubbard Hamiltonian and GOE, since $\langle \tilde{D}_q \rangle_{\mathrm{GOE}}$ is always larger than $\langle \tilde{D}_q \rangle$ for the embedded ensemble in the accessible range of $\mathcal{N}$, and the departure of the distributions indicates that this holds true also for larger $\mathcal{N}$. Hence, the second scenario needs to apply also for d_1 between the Bose-Hubbard Hamiltonian and the embedded ensemble. The three models thus share exactly the same leading-order correction, but differ in higher orders. Note that, according to Equation (4.4), the second finite-size correction to $\langle \tilde{D}_1 \rangle_{\mathrm{GOE}}$ is already of order $1/\mathcal{N} \ln \mathcal{N}$ and, hence, decays faster than the square root of $\mathrm{var}\,(\tilde{D}_1)$. Consequently, the second finite-size correction of the Bose-Hubbard model and of the embedded ensemble cannot have the same functional form as for GOE, since then one would see a decay of d_1. Note that d_2, which is not shown in Figure 4.16, is very similar to d_1, also quantitatively, such that the findings discussed here hold also for d_2.

The distance d_∞ between the Bose-Hubbard model and any of the two random-matrix ensembles increases, and, hence, the third scenario discussed above does not hold here either. In this case, however, a definite conclusion about whether the scaling of Equation (4.38) holds cannot be drawn, due to the slow logarithmic increase of d_∞ and since the leading-order correction is not sufficient to capture the finite-size behaviour of $\langle \tilde{D}_\infty \rangle_{\mathrm{GOE}}$ for the accessible system sizes (see Figure 4.1). Note that the first three finite-size corrections to $\langle \tilde{D}_\infty \rangle_{\mathrm{GOE}}$, Equation (4.19), decay slower than $1/\ln^2 \mathcal{N}$, which is the scaling of the square root of $\mathrm{var}\,(\tilde{D}_\infty)$, and, hence, an increasing behaviour of d_∞ is compatible with the three models sharing the first three finite-size corrections. On the other hand, the decrease and the convergence to a non-zero value of d_∞ between the embedded ensemble and GOE reveals that the first term of the finite-size expansion of $\langle \tilde{D}_\infty \rangle$ for which the two random-matrix models differ scales as $1/\ln^2 \mathcal{N}$, like the square root of the variance.

From the scaling of d_q with $\mathcal{N}$, we can furthermore check the hypothesis that the $\tilde{D}_q$ distributions of the Bose-Hubbard model in its chaotic domain and of the embedded ensemble comply with GOE, but with an effective dimension $\tilde{\mathcal{N}} = \mathcal{N} - n$. This possibility is suggested by the fact that the Bose-Hubbard and embedded-ensemble distributions shown in Figure 4.15 seem compatible with shifted GOE distributions. Additionally, due to the orthogonalization requirement, the absence of quantum chaos at the edges of the spectrum (see, e.g., Figures 3.3 and 4.6 on pages 39 and 72), which manifests itself in higher localization of the corresponding eigenstates in Fock space, effectively reduces the available basis on which the chaotic eigenstates can delocalize. For instance, in the extreme case of an eigenstate that is fully localized on a single basis state $|\alpha\rangle$, every other eigenstate has vanishing amplitude on $|\alpha\rangle$, due to orthogonality.

With this assumption about the $\tilde{D}_q$ distributions and with the GOE results of Equations (4.3) and (4.11), we obtain for $q = 1, 2$ to leading order

$$\langle\tilde{D}_{1,2}\rangle_{\mathrm{GOE}}(\mathcal{N}) \;-\; \langle\tilde{D}_{1,2}\rangle_{\mathrm{GOE}}(\mathcal{N}-n) \sim \frac{n}{\mathcal{N}\ln^2\mathcal{N}}, \tag{4.39}$$

which is the leading order of $\operatorname{var}(\tilde{D}_q)$ multiplied by n. For $q = \infty$, inserting $\tilde{\mathcal{N}} = \mathcal{N} - n$ into the first few finite-size corrections to $\langle\tilde{D}_\infty\rangle_{\mathrm{GOE}}$ [Equation (4.19)] and expanding the result for $\mathcal{N} \to \infty$ yields

$$\langle\tilde{D}_\infty\rangle_{\mathrm{GOE}}(\mathcal{N}) \;-\; \langle\tilde{D}_\infty\rangle_{\mathrm{GOE}}(\mathcal{N}-n) \sim \frac{n\ln(\ln\mathcal{N})}{\mathcal{N}\ln^2\mathcal{N}}. \tag{4.40}$$

Hence, the assumption that the $\tilde{D}_q$ distributions for the three models are the same function with different effective dimensions $\tilde{\mathcal{N}}$ is compatible with an increase of $d_{1,2}$ (of d_∞) only if n grows faster than $\sqrt{\mathcal{N}}\ln\mathcal{N}$ (than $\mathcal{N}/\ln(\ln\mathcal{N})$). Specifically, if the effective dimension scales linearly with $\mathcal{N}$, $\tilde{\mathcal{N}} = c\mathcal{N}$, the same reasoning as above yields, to leading order,

$$d_{1,2} \sim \frac{\sqrt{\mathcal{N}}}{\ln\mathcal{N}}, \qquad\qquad d_\infty \sim \ln(\ln\mathcal{N}). \tag{4.41}$$

As the solid purple line in the left panel of Figure 4.16 shows, the scaling of Equation (4.41) is in good agreement with the slope of d_1 for large $\mathcal{N}$. Hence, one may interpret the deviations between the $\tilde{D}_1$ probability distribution of the Bose-Hubbard model and the Gaussian orthogonal ensemble as an effect of the enhanced localization of the eigenstates at the edges of the spectrum, which, due to orthogonality, prevents the chaotic eigenstates from delocalizing on the full interaction basis. On the other hand, the scaling of Equation (4.41) for d_∞ increases similarly slowly as the scaling of Equation (4.38) and as the data, and a definite conclusion can hence not be drawn here.

4.5. Summary

In the current chapter, we have compared the Bose-Hubbard Hamiltonian to GOE and to the embedded ensemble, in terms of their short-range spectral statistics, as described by the level spacing ratios, and in terms of their eigenstate localization properties, as captured by the fractal dimensions. We have found that the embedded ensemble qualitatively reproduces the energy dependence of the chaotic domain in the Bose-Hubbard model and in particular the absence of quantum chaos at the edges of the spectrum, in contrast to GOE, whose properties are independent of the energy. This latter feature can be attributed to the few-body nature of the Bose-Hubbard and embedded-ensemble Hamiltonians. The finding that the agreement of the embedded ensemble with the Bose-Hubbard model in the tunneling basis is limited, despite the very similar matrix structure of these two models, reveals furthermore the importance of the additional correlations between the Bose-Hubbard matrix elements due to their dependence on just two parameters, J and U.

Deep in the chaotic region, the mean fractal dimensions over different eigenstates and the corresponding variances imply that the eigenstates of the Bose-Hubbard Hamiltonian become ergodic in the limit $\mathcal{N} \to \infty$. Their finite-size behaviour differs between the two natural bases and also depends on the energy: While $\langle \tilde{D}_q \rangle$ and $\operatorname{var}(\tilde{D}_q)$ for the Bose-Hubbard Hamiltonian in the tunneling basis, in the center of the spectrum, deviate clearly from the two random-matrix models, very good agreement between the three models is achieved for the tunneling basis in the low-energy part of the chaotic region and for the interaction basis in the center of the spectrum. The latter suggests that the functional forms of the dominant finite-$\mathcal{N}$ corrections are the same for all three models in these bases and energy regions.

Even though, in the chaotic region, the first two moments of the probability distributions $P(\tilde{D}_q)$ for the Bose-Hubbard Hamiltonian in the interaction basis around the center of the spectrum agree exceptionally well with the universal predictions of GOE and with the embedded ensemble, the full probability densities $P(\tilde{D}_q)$ deviate from each other and become ever more distinguishable from one another as system size increases. The relative deviation of the mean fractal dimensions shows that this departure is a consequence of different subleading corrections in the finite-$\mathcal{N}$ expansion of $\langle \tilde{D}_q \rangle$. Hence, specific features of the Bose-Hubbard Hamiltonian in its chaotic phase remain accessible even in the limit $\mathcal{N} \to \infty$, enabling an unambiguous distinction from the universal GOE model and also from random two-body Hamiltonians provided by the embedded ensemble.

Chapter 5.

Chaos and Distinguishability

The results of this chapter were obtained in a joint project with Eric Brunner and Dr. Gabriel Dufour.

As we have seen in the previous chapters, the interplay of tunneling and interactions in the Bose-Hubbard Hamiltonian leads to complex spectral and eigenvector properties and induces chaos. In the following, we study particle indistinguishability as a second source of complexity in quantum many-body systems and analyse its influence on the emergence of chaos in the Bose-Hubbard model.

The impact of particle indistinguishability on many-particle dynamics was first demonstrated experimentally in 1987 by Hong, Ou and Mandel [99]. In their experiment [see the sketch in Figure 5.1(a)], two photons from a coherent light source are sent through a symmetric beam splitter from two different sides (in the sketch: from above and from below) and are subsequently detected. By manipulating the time delay between the two photons, the temporal overlap of the underlying wave functions and hence the distinguishability of the two photons is tuned. When the particles are maximally indistinguishable, the coincidence probability of jointly detecting one photon on each side of the beam splitter is strongly reduced.

This observation can be explained as follows: Initially, one photon enters the beam splitter from above, and the other one from below, which we can encode into states $|a\rangle$ and $|b\rangle$. These two states are orthogonal to each other, since they correspond to classically distinct paths. Furthermore, each photon carries a distinguishability label, which is here given by the temporal overlap of the two photonic wave functions and which we can model by a state $|\sigma_{a,b}\rangle$. The full state of each photon is hence the product state

$$|d\rangle\,|\sigma_d\rangle\,, \tag{5.1}$$

with $d = a$ or $d = b$. Since the two photons are identical bosons, the state of the full system is given by the symmetrization of the two-particle product state [42],

$$|\Phi\rangle = \frac{|a\rangle\,|b\rangle\,|\sigma_a\rangle\,|\sigma_b\rangle + |b\rangle\,|a\rangle\,|\sigma_b\rangle\,|\sigma_a\rangle}{\sqrt{2}}. \tag{5.2}$$

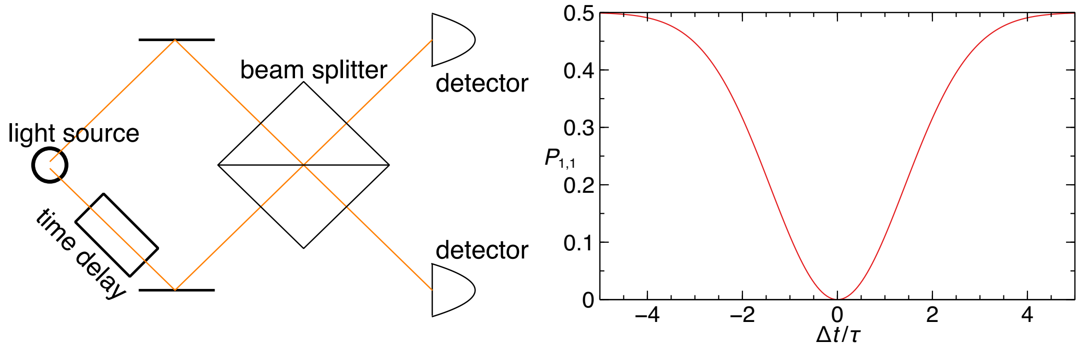

(a) (b)

Figure 5.1: (a) Sketch of the Hong-Ou-Mandel experiment. Orange lines correspond to the photon paths from the light source to the detectors. (b) Theoretically expected coincidence probability $P_{1,1}$ in a Hong-Ou-Mandel experiment, as a function of the scaled time delay $\Delta t/\tau$, Equation (5.6).

For later convenience, we have here sorted the distinguishability labels to the right of the product states. The beam splitter acts on the "above" and "below" states as the unitary matrix[1]

$$U = \frac{1}{\sqrt{2}}\begin{pmatrix} 1 & 1 \\ 1 & -1 \end{pmatrix}, \tag{5.3}$$

while it leaves the distinguishability labels unchanged. Here, the prefactor $1/\sqrt{2}$ encodes the fairness of the beam splitter, and the unitarity of U makes sure that the state after the action of the beam splitter is still a properly normalized quantum state. The action of U on $|\Phi\rangle$ yields the state

$$\begin{aligned} U|\Phi\rangle = \frac{1}{\sqrt{2}}\Bigg[&\left(\frac{|a\rangle|a\rangle - |b\rangle|b\rangle}{\sqrt{2}}\right)\left(\frac{|\sigma_a\rangle|\sigma_b\rangle + |\sigma_b\rangle|\sigma_a\rangle}{\sqrt{2}}\right) \\ &+\left(\frac{|b\rangle|a\rangle - |a\rangle|b\rangle}{\sqrt{2}}\right)\left(\frac{|\sigma_a\rangle|\sigma_b\rangle - |\sigma_b\rangle|\sigma_a\rangle}{\sqrt{2}}\right)\Bigg]. \end{aligned} \tag{5.4}$$

The coincidence probability $P_{1,1}$, i.e., the probability to detect one photon in each detector, is then given by the intensity of the projection onto the state $(|b\rangle|a\rangle - |a\rangle|b\rangle)/\sqrt{2}$,

$$P_{1,1} = \frac{1}{2}\left|\left(\frac{|\sigma_a\rangle|\sigma_b\rangle - |\sigma_b\rangle|\sigma_a\rangle}{\sqrt{2}}\right)\right|^2 = \frac{1}{2}\left(1 - |\langle\sigma_a|\sigma_b\rangle|^2\right). \tag{5.5}$$

---

[1] Note that some phase factors are neglected here, since they do not alter the final result. For a detailed discussion of beam splitters, see, e.g., Chapter 8 of Reference [191].

If the overlap of $|\sigma_a\rangle$ and $|\sigma_b\rangle$ is given specifically by a time delay Δt between Gaussian wave packets of identical temporal variance τ^2, this probability is

$$P_{1,1} = \frac{1}{2}\left[1 - \exp\left(-\frac{\Delta t^2}{4\tau^2}\right)\right]. \tag{5.6}$$

Figure 5.1(b) shows this probability as a function of the time delay. While for large time delays, the coincidence probability approaches 1/2 like for classical particles, coincidence events are strongly suppressed as the time delay vanishes and the two photons become mutually indistinguishable. This result can be interpreted as an interference effect: Each photon may be reflected at the beam splitter or transmitted through it, leading to four different two-photon paths, two of which yield one photon per detector. When the photons are indistinguishable, these two paths, i.e., the path in which both photons are reflected and the path in which both are transmitted, interfere destructively with each other, leading to the suppression of the coincidence events.

5.1. Theoretical Framework

In this section, we introduce the general methods used throughout the rest of the chapter to describe (partially) distinguishable particles. Assume that the Hilbert space $\mathcal{H}_1$ of a single particle can be decomposed into a tensor product

$$\mathcal{H}_1 = \mathcal{H}_{\text{ext}} \otimes \mathcal{H}_{\text{int}} \tag{5.7}$$

of an "external" Hilbert space $\mathcal{H}_{\text{ext}}$ spanned by L orthogonal modes $|m\rangle$ and an "internal" Hilbert space $\mathcal{H}_{\text{int}}$ of S orthogonal species states $|\sigma\rangle$ [100, 105, 106, 192–194]. The L modes could, for instance, be photonic modes like $|a\rangle$ and $|b\rangle$ in the Hong-Ou-Mandel experiment discussed above or spatial modes like in the Bose-Hubbard model. The S species, which describe the distinguishability of the particles, might for example be given by photon polarizations or by spin degrees of freedom. The N-particle Hilbert space is then the tensor product [192, 193]

$$\mathcal{H} = \mathcal{H}_1^{\otimes N} \cong \mathcal{H}_{\text{ext}}^{\otimes N} \otimes \mathcal{H}_{\text{int}}^{\otimes N}. \tag{5.8}$$

States of this Hilbert space are hence linear combinations of the product states

$$|m_1\rangle \otimes \ldots \otimes |m_N\rangle \otimes |\sigma_1\rangle \otimes \ldots \otimes |\sigma_N\rangle =: |m_1, \ldots, m_N\rangle \otimes |\sigma_1, \ldots, \sigma_N\rangle \tag{5.9}$$

of external modes and internal species states. For identical bosons, only the subspace $\mathcal{SH}$ of fully symmetrized states is physically relevant. A projector onto this subspace is given by the symmetrization operator [193, 194]

$$\mathcal{S} = \frac{1}{\sqrt{N!}} \sum_{\pi \in \mathfrak{S}_N} \pi \otimes \pi, \tag{5.10}$$

where $\mathfrak{S}_N$ is the symmetric group of N objects [170, 171] and where $\pi \otimes \pi$ acts on the internal and external states by permuting the particles. For instance, product states

$$|\Psi\rangle = |m_1, \dots, m_N\rangle \otimes |\sigma_1, \dots, \sigma_N\rangle$$

are symmetrized to

$$\mathcal{S}\,|\Psi\rangle = \frac{1}{\sqrt{N!}} \sum_{\pi \in \mathfrak{S}_N} \Big| m_{\pi^{-1}(1)}, \dots, m_{\pi^{-1}(N)} \Big\rangle \otimes \Big| \sigma_{\pi^{-1}(1)}, \dots, \sigma_{\pi^{-1}(N)} \Big\rangle . \tag{5.11}$$

The Hamiltonian of the system is assumed to act only on the external degrees of freedom,

$$H = H_{\text{ext}} \otimes \mathbb{1}_{\text{int}}, \tag{5.12}$$

such that the system dynamics leave the internal configurations unchanged. In fact, this property of the Hamiltonian is what sets apart internal from external degrees of freedom. The internal states nevertheless influence the dynamics, since they are responsible for the particle distinguishability and hence for the emergence of many-particle interference. In particular, the species-blind Bose-Hubbard Hamiltonian reads [106]

$$H = -J \sum_{j=1}^{L} \sum_{\sigma=1}^{S} \left(a^{\dagger}_{j,\sigma} a_{j+1,\sigma} + a^{\dagger}_{j+1,\sigma} a_{j,\sigma} \right) + \frac{U}{2} \sum_{j=1}^{L} \sum_{\sigma,\mu=1}^{S} n_{j,\sigma} \left(n_{j,\mu} - \delta_{\sigma\mu} \right) . \tag{5.13}$$

Here, $a^{\dagger}_{j,\sigma}$, $a_{j,\sigma}$ are creation and annihilation operators of a boson at the jth lattice site in the internal state $|\sigma\rangle$, with

$$a^{(\dagger)}_{L+1,\sigma} := \begin{cases} a^{(\dagger)}_{1,\sigma}, & \text{PBCs,} \\ 0, & \text{HWBCs} \end{cases} \tag{5.14}$$

(compare Section 2.4).

Since the Hamiltonian does not affect the internal states, H commutes with all permutations

$$\pi_{\text{int}} := \mathbb{1}_{\text{ext}} \otimes \pi, \qquad \pi \in \mathfrak{S}_N, \tag{5.15}$$

of the species labels,

$$[H, \pi_{\text{int}}] = 0. \tag{5.16}$$

According to representation theory, the Hamiltonian can thus be made block diagonal, where each block corresponds to an irreducible representation of $\mathfrak{S}_N$ [106, 170, 171]. The eigenvalues of different blocks corresponding to the same irreducible representation are identical, and hence these blocks of H are equal up to a basis transformation. Note that, due to the symmetrization of the full state, π_{int} is equivalent to the permutation

$$\pi_{\text{ext}} = \pi^{-1} \otimes \mathbb{1}_{\text{int}}, \tag{5.17}$$

which acts only on the external degrees of freedom.

We now discuss how to obtain this block-diagonal form of the Hamiltonian. The irreducible representations of $\mathfrak{S}_N$ are labelled by the integer partitions $\boldsymbol{\lambda}$ of N [170, 171], that is, by the tuples

$$\boldsymbol{\lambda} = (\lambda_1, \ldots, \lambda_n), \qquad \lambda_i \in \mathbb{N}, \quad \lambda_1 \geq \ldots \geq \lambda_n > 0, \tag{5.18}$$

such that

$$\sum_{i=1}^{n} \lambda_i = N. \tag{5.19}$$

Each such partition is associated to a *Young diagram* [170], which consists of N boxes in n rows, with λ_i boxes in the ith row. For instance, the partition $\boldsymbol{\lambda} = (2, 2, 1)$ of $N = 5$ corresponds to the Young diagram

$$\boldsymbol{\lambda} = \begin{array}{|c|c|} \hline & \\ \hline & \\ \hline \multicolumn{1}{|c|}{} & \multicolumn{1}{c}{} \\ \cline{1-1} \end{array}. \tag{5.20}$$

From a given Young diagram, we obtain a *Young tableau* by filling the diagram with numbers $1, \ldots, N$, such that each number appears once [170]. For example, a possible numbering of the Young diagram shown above is

$$\begin{array}{|c|c|} \hline 1 & 2 \\ \hline 3 & 4 \\ \hline \multicolumn{1}{|c|}{5} & \multicolumn{1}{c}{} \\ \cline{1-1} \end{array}. \tag{5.21}$$

Each Young tableau defines two subgroups of the symmetric group [170],

$$\begin{aligned} R_{\boldsymbol{\lambda}} &= \{\pi \in \mathfrak{S}_N \ : \ \pi \text{ preserves the rows of the tableau}\}, \\ C_{\boldsymbol{\lambda}} &= \{\pi \in \mathfrak{S}_N \ : \ \pi \text{ preserves the columns of the tableau}\}. \end{aligned} \tag{5.22}$$

The Young tableau of Equation (5.21), for instance, yields the two subgroups

$$\begin{aligned} R_{\boldsymbol{\lambda}} &= \mathfrak{S}_{\{1,2\}} \times \mathfrak{S}_{\{3,4\}}, \\ C_{\boldsymbol{\lambda}} &= \mathfrak{S}_{\{1,3,5\}} \times \mathfrak{S}_{\{2,4\}}. \end{aligned} \tag{5.23}$$

Here, $\mathfrak{S}_{\{i_1,\ldots,i_n\}}$ is the symmetric group of all permutations of the set $\{i_1, \ldots, i_n\}$ and the cross denotes the (internal) direct product of two subgroups of $\mathfrak{S}_N$, that is, the group

$$G_1 \times G_2 := \{g_1 g_2 \ : \ g_1 \in G_1, g_2 \in G_2\}, \tag{5.24}$$

where the subgroups $G_1, G_2 \subseteq \mathfrak{S}_N$ fulfil $g_1 g_2 = g_2 g_1$ for all $g_1 \in G_1$ and $g_2 \in G_2$. The subgroups $R_{\boldsymbol{\lambda}}$ and $C_{\boldsymbol{\lambda}}$ define, respectively, the *row symmetrizer* $s_{\boldsymbol{\lambda}}$ and the *column antisymmetrizer* $a_{\boldsymbol{\lambda}}$ as [170]

$$s_{\boldsymbol{\lambda}} = \mathbb{1}_{\text{ext}} \otimes \sum_{\pi \in R_{\boldsymbol{\lambda}}} \pi, \qquad a_{\boldsymbol{\lambda}} = \mathbb{1}_{\text{ext}} \otimes \sum_{\pi \in C_{\boldsymbol{\lambda}}} \operatorname{sgn}(\pi)\pi. \tag{5.25}$$

Here, sgn denotes the signature of the group element π [171]: Each $\pi \in \mathfrak{S}_N$ can be written as a product of transpositions (permutations of just two elements). If ν is the number of transpositions in such a product, the signature is defined as $\operatorname{sgn}(\pi) = (-1)^\nu$ and is uniquely determined by π. The action of $s_{\boldsymbol{\lambda}}$ on a state $|\Psi\rangle$ yields a state that transforms symmetrically under the action of any $\pi \in R_{\boldsymbol{\lambda}}$, whereas $a_{\boldsymbol{\lambda}}$ results in states that are antisymmetric with respect to $\pi \in C_{\boldsymbol{\lambda}}$. The product of $s_{\boldsymbol{\lambda}}$ and $a_{\boldsymbol{\lambda}}$ defines the *Young symmetrizer* $y_{\boldsymbol{\lambda}}$ associated with the Young tableau [170],

$$y_{\boldsymbol{\lambda}} = s_{\boldsymbol{\lambda}} a_{\boldsymbol{\lambda}}. \tag{5.26}$$

A classic result of representation theory [170] states that $y_{\boldsymbol{\lambda}}$ is a projector, up to a normalization factor, and that the action of $y_{\boldsymbol{\lambda}}$ (by multiplication from the right) on the group algebra $\mathbb{C}\mathfrak{S}_N$ yields one realization of the irreducible representation labelled by $\boldsymbol{\lambda}$. The group algebra is the vector space

$$\mathbb{C}\mathfrak{S}_N = \left\{ \sum_{\pi \in \mathfrak{S}_N} c_\pi e_\pi \ : \ c_\pi \in \mathbb{C} \right\}, \tag{5.27}$$

in which every basis element e_π is associated with a group element π, and multiplication by elements $\pi' \in \mathfrak{S}_N$ from the right is defined as $e_\pi \pi' = e_{\pi\pi'}$. This result essentially means that the subspace

$$\{ y_{\boldsymbol{\lambda}} |\Psi\rangle \ : \ |\Psi\rangle \in \mathcal{H} \} \tag{5.28}$$

onto which $y_{\boldsymbol{\lambda}}$ projects yields one block of the Hamiltonian corresponding to the irreducible representation labelled by $\boldsymbol{\lambda}$. Natural bases for the Bose-Hubbard model with distinguishable particles are therefore obtained from the interaction and tunneling basis states, respectively, by acting on them with $y_{\boldsymbol{\lambda}}$ and orthogonalizing the resulting set of states. Note that, since the projection by $y_{\boldsymbol{\lambda}}$ does not change the occupation numbers n_m of the external modes $|m\rangle$, the orthogonalization can be performed independently on the subspaces with a fixed set of n_m, which is numerically much more efficient than orthogonalizing the full set of states at once.

Let us now discuss in further detail the characteristics of these subspaces and how they are related to particle indistinguishability. For the partitions $\boldsymbol{\lambda} = (N)$ and $\boldsymbol{\lambda} = (1, \ldots, 1)$, which correspond to Young diagrams consisting of a single row and a single column, respectively, one can easily check that the Young symmetrizer is

$$y_{(N)} = \mathbb{1}_{\text{ext}} \otimes \sum_{\pi \in \mathfrak{S}_N} \pi, \qquad y_{(1,\ldots,1)} = \mathbb{1}_{\text{ext}} \otimes \sum_{\pi \in \mathfrak{S}_N} \operatorname{sgn}(\pi)\pi. \tag{5.29}$$

Hence, $y_{(N)}$ ($y_{(1,\ldots,1)}$) fully symmetrizes (antisymmetrizes) the species labels, and the Hamiltonian on this block is identical to that of indistinguishable bosons (fermions). For other $\boldsymbol{\lambda}$, the subspaces induced by $y_{\boldsymbol{\lambda}}$ correspond to mixed symmetries, which become more symmetric (antisymmetric) the more elements are contained in $R_{\boldsymbol{\lambda}}$ ($C_{\boldsymbol{\lambda}}$), i.e., the longer the rows (columns) of the Young diagram are.

To understand the connection of the $\boldsymbol{\lambda}$ subspaces to the number of species S, it is convenient to use *semistandard Young tableaux* [106, 170]. These are obtained from a Young diagram by filling it with numbers $1, \ldots, N$ such that they do not decrease (from left to right) within one row and they strictly increase (from top to bottom) within one column. For example, a semistandard Young tableau to the Young diagram of Equation (5.20) is given by

$$\begin{array}{|c|c|}\hline 1 & 1 \\ \hline 2 & 3 \\ \hline 3 & \multicolumn{1}{c}{} \\ \cline{1-1}\end{array}\,. \tag{5.30}$$

Now consider a state $|\Psi\rangle$ with a well-defined number of particles in each internal state $|\sigma\rangle$, $\sigma = 1, \ldots, S$. Then, under the action of the Young symmetrizer $y_{\boldsymbol{\lambda}}$, $|\Psi\rangle$ is projected to zero if the list of internal states $(\sigma_1, \ldots, \sigma_N)$ cannot fill the Young diagram $\boldsymbol{\lambda}$ to form a semistandard Young tableau. Furthermore, it can be shown that the number of possible fillings for a given species configuration defines the number of blocks in H associated with the same $\boldsymbol{\lambda}$ [106]. As an example, consider the partition $\boldsymbol{\lambda} = (2, 1)$ for $N = 3$ particles. For a single species, $S = 1$, and hence fully indistinguishable bosons, no semistandard Young tableau is possible for this $\boldsymbol{\lambda}$, while for $S = 2$ and $S = 3$, with species configurations $(1, 1, 2)$ and $(1, 2, 3)$, respectively, the following fillings are allowed:

$$S = 2 : \begin{array}{|c|c|}\hline 1 & 1 \\ \hline 2 & \multicolumn{1}{c}{} \\ \cline{1-1}\end{array}\,, \qquad S = 3 : \begin{array}{|c|c|}\hline 1 & 2 \\ \hline 3 & \multicolumn{1}{c}{} \\ \cline{1-1}\end{array}\,, \quad \begin{array}{|c|c|}\hline 1 & 3 \\ \hline 2 & \multicolumn{1}{c}{} \\ \cline{1-1}\end{array}\,. \tag{5.31}$$

A possible column antisymmetrizer for $\boldsymbol{\lambda} = (2, 1)$ is

$$a_{\boldsymbol{\lambda}} = \mathbb{1} - (\sigma_1 \mapsto \sigma_3, \sigma_3 \mapsto \sigma_1), \tag{5.32}$$

which is defined by the Young tableau

$$\begin{array}{|c|c|}\hline 1 & 2 \\ \hline 3 & \multicolumn{1}{c}{} \\ \cline{1-1}\end{array}\,. \tag{5.33}$$

While the state

$$|\Psi_1\rangle = |\sigma_1 = 1, \sigma_2 = 1, \sigma_3 = 1\rangle \tag{5.34}$$

of three indistinguishable bosons (mode occupations neglected here for simplicity) is projected to zero by this antisymmetrizer, the states

$$|\Psi_2\rangle = |\sigma_1 = 1, \sigma_2 = 1, \sigma_3 = 2\rangle\,, \qquad |\Psi_3\rangle = |\sigma_1 = 1, \sigma_2 = 2, \sigma_3 = 3\rangle \tag{5.35}$$

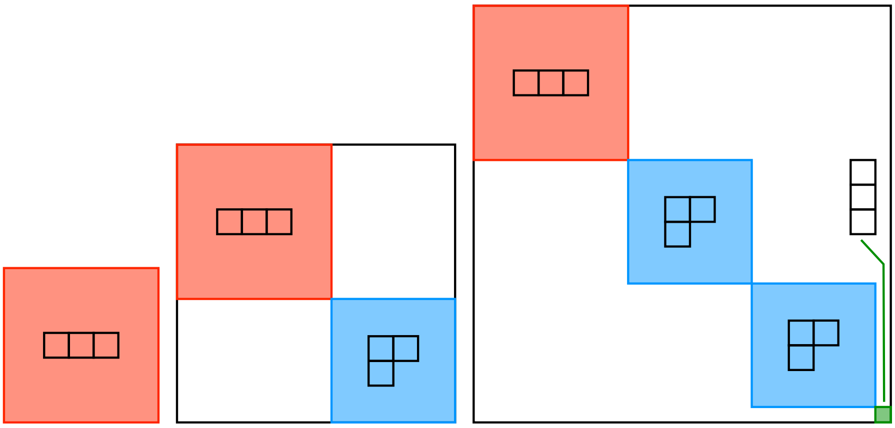

Figure 5.2: Sketch of the block structure of the Bose-Hubbard Hamiltonian for $N = L = 3$ and $S = 1$ (left), $S = 2$ (center) and $S = 3$ (right) particle species, compare Reference [106]. The coloured areas correspond to the irreducible representations labelled by $\boldsymbol{\lambda} = (3)$ (red), $\boldsymbol{\lambda} = (2, 1)$ (blue) and $\boldsymbol{\lambda} = (1, 1, 1)$ (green), and their size indicates the dimension of each block.

of (partially) distinguishable particles are not. Consequently, the species configuration defines which particle permutation symmetries can be realized, i.e., which irreducible representations of $\mathfrak{S}_N$, labelled by $\boldsymbol{\lambda}$, appear in the block-diagonal decomposition of H. In particular, for $S = N$, i.e., fully distinguishable particles, each Young diagram can be filled to form a semistandard Young tableau, and, hence, each mixed symmetry given by $\boldsymbol{\lambda}$ is accessible, while the only allowed block of H for fully indistinguishable bosons, $S = 1$, is the fully symmetric one, $\boldsymbol{\lambda} = (N)$. An example of the block structure of the Hamiltonian for $N = 3$ particles in $L = 3$ modes and up to $S = 3$ species is sketched in Figure 5.2.

By virtue of the equivalence between π_{int} and π_{ext}, the same statements as for states with a well-defined number of particles per species hold also for states with a well-defined number of particles per mode $|m\rangle$. Hence, states with more than λ_1 particles in a single mode, or, more generally, more than $\lambda_1 + \ldots + \lambda_i$ particles in i modes, are forbidden in the subspace labelled by $\boldsymbol{\lambda}$.

5.2. Spectral Statistics and Eigenstate Structure as Functions of Permutation Symmetry

In the following, we investigate the Bose-Hubbard Hamiltonian of (partially) distinguishable bosons, using the spectral averages that were discussed for fully indistinguishable particles in Section 3.4. Figure 5.3 shows, as functions of the scaled tunneling strength $\eta = J/UN$, the mean level spacing ratio $\langle r \rangle$, as well as the mean and the variance of the eigenstate fractal dimension $\tilde{D}_1$ in the interaction basis, over the inner 70 % of the

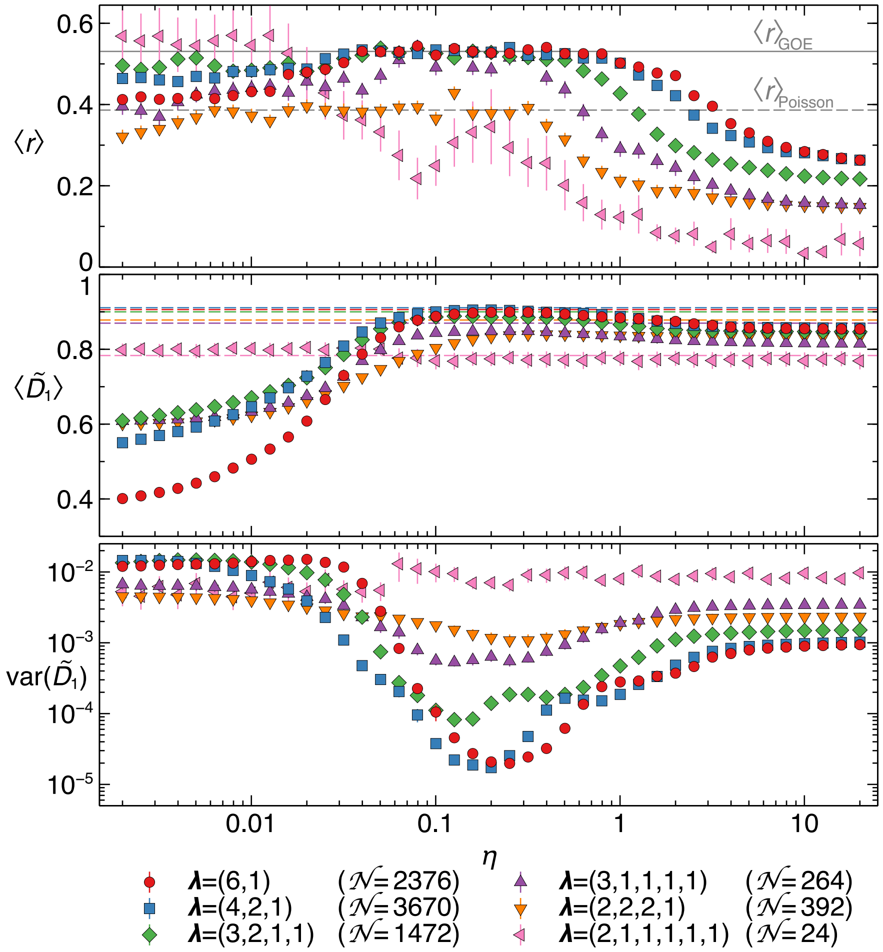

Figure 5.3: Mean level spacing ratio $\langle r \rangle$ (upper panel), mean fractal dimension $\langle \tilde{D}_1 \rangle$ (center panel) and variance $\mathrm{var}\,(\tilde{D}_1)$ (lower panel) in the interaction basis over the inner 70 % of the spectrum for different symmetry-induced subspaces labelled by partitions $\boldsymbol{\lambda}$ as indicated in the legend, for $N = L = S = 7$, with HWBCs and parity $\Pi = -1$. Grey lines in the plot of $\langle r \rangle$ mark $\langle r \rangle_{\mathrm{GOE}}$ [solid, Equation (2.41) on page 19] and $\langle r \rangle_{\mathrm{Poisson}}$ [dashed, Equation (2.43) on page 19]. Dashed lines in the center panel indicate $\langle \tilde{D}_1 \rangle_{\mathrm{GOE}}$ [Equation (4.3) on page 62] for the same Hilbert space dimensions $\mathcal{N}$ as the symmetry-induced subspaces. When not shown, error bars are contained within symbol size. Note that the seemingly good agreement of $\langle \tilde{D}_1 \rangle$ with GOE for $\boldsymbol{\lambda} = (2,1,1,1,1,1)$ is merely a coincidence, see the discussion on page 102.

energy levels. Various symmetry-induced subspaces are shown for $N = 7$ fully distinguishable particles on $L = 7$ sites, with HWBCs and parity $\Pi = -1$. Note that, while all irreducible representations of $\mathfrak{S}_7$ are accessible for fully distinguishable particles, as discussed in Section 5.1, only a selection is shown to ease visualization.

For partitions $\boldsymbol{\lambda}$ of short length, such as $\boldsymbol{\lambda} = (6, 1)$ or $\boldsymbol{\lambda} = (4, 2, 1)$, chaos can clearly be identified for $0.03 \lesssim \eta \lesssim 1$: The mean level spacing ratio $\langle r \rangle$ approaches the GOE prediction $\langle r \rangle_{\mathrm{GOE}}$, the mean fractal dimension $\langle \tilde{D}_1 \rangle$ reaches a maximum and the variance $\mathrm{var}\,(\tilde{D}_1)$ decreases by several orders of magnitude. At its maximum, the mean fractal dimension for $\boldsymbol{\lambda} = (6, 1)$ and $\boldsymbol{\lambda} = (4, 2, 1)$ agrees well with the predictions from GOE (indicated by dashed lines). As we have discussed in Section 5.1, the short-length $\boldsymbol{\lambda}$ correspond to more symmetric subspaces with respect to species permutations, since the rows of the corresponding Young diagram are longer than its columns.

As the symmetry-induced subspace becomes more antisymmetric, i.e., the partitions $\boldsymbol{\lambda}$ become longer, signatures of chaos are reduced in $\langle r \rangle$, $\langle \tilde{D}_1 \rangle$ and $\mathrm{var}\,(\tilde{D}_1)$. The spectral statistics is no longer in agreement with GOE, the maximum of $\langle \tilde{D}_1 \rangle$ is smaller and differs from GOE (except for $\boldsymbol{\lambda} = (2, 1, 1, 1, 1, 1)$, see next paragraph), and the minimum of $\mathrm{var}\,(\tilde{D}_1)$ is less sharp. Note that also the subspace dimension $\mathcal{N}$ tends to be smaller for the more antisymmetric subspaces, and as we have seen previously for indistinguishable bosons (see, for instance, Figures 3.9, 4.9, and 4.10 on pages 53, 76, and 77, respectively), the maximum of $\langle \tilde{D}_q \rangle$ and the minimum of $\mathrm{var}\,(\tilde{D}_q)$ are less pronounced for smaller $\mathcal{N}$. For $\boldsymbol{\lambda} = (3, 1, 1, 1, 1)$, however, the maximum of $\langle \tilde{D}_1 \rangle$ is larger and the minimum of $\mathrm{var}\,(\tilde{D}_1)$ is deeper than for $\boldsymbol{\lambda} = (2, 2, 2, 1)$, even though the corresponding dimensions suggest the opposite behaviour. This result is a clear sign that the species permutation symmetry impacts the signatures of chaos in the fractal dimensions.

Note that for the most antisymmetric subspace shown, $\boldsymbol{\lambda} = (2, 1, 1, 1, 1, 1)$, the mean fractal dimension is in very good agreement with GOE for all values of η. However, this is a coincidence caused by the very small Hilbert space dimension and cannot be interpreted as a signature of chaos: The variance shows no minimum as a function of η and the spectral statistics clearly deviate from GOE in a wide range of η values.

The finding that chaos is weaker in the more antisymmetric subspaces is directly connected to the structure of the Hamiltonian on the different symmetry-induced subspaces. As discussed towards the end of Section 5.1, states with more than $\lambda_1 + \ldots + \lambda_i$ particles in i modes (here: spatial modes) are forbidden in the symmetry subspace given by $\boldsymbol{\lambda}$, thus reducing the influence of the on-site interaction for the more antisymmetric subspaces. Consequently, the emergence of chaos, as an effect of the interplay of interaction and tunneling, is suppressed. Note that the effect discussed here is similar to defining a maximum occupation number per site, but not exactly the same: For $\boldsymbol{\lambda} = (2, 2, 2, 1)$ and $\boldsymbol{\lambda} = (2, 1, 1, 1, 1, 1)$ maximally two particles per spatial mode are allowed due to symmetry, but the chaos signatures, for instance the minimum of $\mathrm{var}\,(\tilde{D}_1)$, are much weaker in $\boldsymbol{\lambda} = (2, 1, 1, 1, 1, 1)$ since states with two particles in more than one spatial mode are forbidden in this subspace.

As we have discussed in Section 5.1, the species configuration directly influences which $\boldsymbol{\lambda}$ subblocks contribute to the Hamiltonian. Hence, the results of the current section show that the emergence of chaos in the Bose-Hubbard Hamiltonian depends on particle indistinguishability. This finding has implications for dynamical studies, as typically performed in experiments [124, 127, 195]: If, on the one hand, the system is initialized in a Fock state of fully indistinguishable particles, this initial state lives only on the fully symmetric subspace $\boldsymbol{\lambda} = (N)$ and hence the system should thermalize for long times (as defined, for instance, by the expectation value of single-particle observables) in the η ranges of the chaotic domain. On the other hand, an initial Fock state of distinguishable particles overlaps with several symmetry-induced subspaces with different degrees of chaos, which should give rise to different signatures in the equilibrium dynamics as compared to the fully indistinguishable case [196].

Chapter 6.

Conclusions and Outlook

In this thesis, we have thoroughly investigated the quantum-chaotic and regular phases of the Bose-Hubbard Hamiltonian, as functions of the scaled energy and of the scaled tunneling strength, via short-range spectral statistics and via the eigenstate localization properties encoded into the eigenstates' fractal dimensions. Spectral chaos reflects the complicated level dynamics, which is dominated by a multitude of avoided crossings in the chaotic region, and is furthermore correlated with eigenstate delocalization and with strongly reduced eigenstate-to-eigenstate fluctuations of the fractal dimensions, in both natural bases of the Hamiltonian (the eigenbases of the interaction term and of the tunneling term). In particular, these fluctuations behave qualitatively similarly in the two natural bases, and hence appear as a qualitatively basis-independent quantifier of the emergence of quantum chaos. Additionally, as signalled by the skewness parameter, the distribution of the eigenstate fractal dimensions becomes strongly asymmetric at the boundaries of the chaotic domain, indicating that the onset of delocalization for close-in-energy eigenstates occurs at slightly different values of the scaled tunneling strength.

Since spectral chaos is defined via the agreement of the spectral statistics with that of GOE random matrices, we have compared the eigenstate fractal dimensions of the Bose-Hubbard model with the corresponding GOE predictions and furthermore with the bosonic two-body embedded GOE ensemble, which captures the two-body nature of the Bose-Hubbard Hamiltonian. The chaotic region in the embedded ensemble depends on the energy in qualitatively the same way as in the Bose-Hubbard model. In particular, the disappearance of quantum chaos at the edges of the spectrum, accompanied by a strongly reduced density of states, is well described by the embedded ensemble, in contrast to GOE, which indicates that this feature of the chaotic region is rooted in the few-body character of the Hamiltonians and hence in their sparsity as matrices in Fock space. Even though the sparsity of the embedded-ensemble matrices is close to the Bose-Hubbard Hamiltonian in the eigenbasis of the tunneling term, the eigenstates' structural features (described by the fractal dimensions) agree much better between the embedded ensemble and the Bose-Hubbard Hamiltonian in the eigenbasis of the interaction term. Hence, besides the two-body character of the Hamiltonian, additional correlations between Bose-Hubbard matrix elements, all of which depend on the same two parameters (interaction and tunneling strength), need to play an important role in the formation of the chaotic domain.

The scaling of the averaged fractal dimensions and of their eigenstate-to-eigenstate variance with Hilbert space dimension $\mathcal{N}$ reveals that the eigenstates in the chaotic domain become ergodic for $\mathcal{N} \to \infty$ in both natural bases of the Bose-Hubbard Hamiltonian, albeit with a strong basis dependence of the convergence to ergodicity. Specifically for the eigenbasis of the interaction term in the center of the spectrum and for the eigenbasis of the tunneling term at small energies, the mean fractal dimensions of close-in-energy eigenstates and the corresponding variances agree exceptionally well between the Bose-Hubbard Hamiltonian in its quantum-chaotic phase, the embedded ensemble and GOE for the numerically reachable system sizes.

Despite this agreement of the three models in terms of low-order statistical moments, their full fractal-dimension distributions become ever more distinguishable from one another with increasing Hilbert space dimension. Since the Bose-Hubbard model departs from GOE as well as from the embedded ensemble, the difference between the Bose-Hubbard model and GOE cannot solely be explained by the two-body nature of the Bose-Hubbard Hamiltonian, but one needs to take into account also the more specific on-site and nearest-neighbour structure of the interaction and tunneling terms, respectively. These results show that distinctive features of the Bose-Hubbard Hamiltonian remain accessible in the chaotic domain for $\mathcal{N} \to \infty$, on top of the universal random-matrix predictions, which hints towards a statistical way to differentiate among distinct many-body Hamiltonians in the chaotic regime. Our findings are thus related to the certification problem of system-specific properties in complex quantum systems for analytically and numerically intractable Hamiltonians [103, 197–200].

As a second source of complexity in quantum many-body systems besides interactions, we also investigated the influence of particle distinguishability on the spectral statistics and the eigenstate fractal dimensions of the Bose-Hubbard model, finding a clear impact on the emergence of quantum chaos. In particular, the signatures of quantum chaos vanish in the more antisymmetric subspaces induced by particle permutation symmetry. This result is directly related to the specific structure of the Bose-Hubbard Hamiltonian, since states with many particles per site are forbidden in the more antisymmetric subspaces, and hence the interaction term is strongly suppressed due to its on-site nature. Further investigations with models that include longer-range interaction terms would be needed to understand on a deeper level how particle distinguishability affects quantum chaos. Additionally, relating quantum chaos, as discussed in this thesis, to the dynamics of (partially) distinguishable bosons would shed light on the interplay between many-particle interference, whose presence or absence is a dynamical signature of the particles' (in)distinguishability [99–101, 103, 105, 106, 192], and the emergence of chaos.

Another interesting topic for further investigation is the question of how exactly the additional correlations in the Bose-Hubbard Hamiltonian affect the eigenstates and lead to the observed departure of this Hamiltonian in its chaotic domain from GOE and the embedded ensemble. One clear difference between the matrix structures of the Bose-Hubbard Hamiltonian and of the two random-matrix models is that the former changes under basis transformations between Fock bases. Hence, one could investigate which

Fock basis yields the strongest or the weakest signature of quantum chaos in terms of eigenstate delocalization. The structure of these “preferred” bases and of the underlying single-particle modes might reveal in more detail how correlations in the matrix elements influence the eigenstate structure.

In this work we have investigated the emergence of quantum chaos for integer filling factors only. It is known that some properties of the Bose-Hubbard Hamiltonian change for non-integer filling, e.g., the Mott insulating phase of the ground state (for dominating interactions) is absent in this case [80, 164]. Hence, one may ask whether the filling factor impacts also the formation of the chaotic region. Furthermore, the limit $\mathcal{N} \to \infty$ could be approached for a fixed number of lattice sites and increasing particle number, instead of keeping the filling factor fixed as investigated in this thesis. Whether or not the distinctiveness of the Bose-Hubbard Hamiltonian in its chaotic phase versus random-matrix universality is equally observable in this alternative limit remains to be confirmed.

Appendix A.

Additional Calculations

A.1. Level Spacing Ratios for the Poisson Distribution

In the following, we derive the probability distribution $P(r)$ and the corresponding mean $\langle r\rangle$ of the level spacing ratio for Poissonian level statistics [Equations (2.42) and (2.43) in the main text, page 19]. We start with the probability $\mathbb{P}(\tilde{r}_n \leq \alpha)$ that the number

$$\tilde{r}_n := \frac{s_n}{s_{n+1}} \geq 0 \tag{A.1}$$

is smaller than a certain $\alpha > 0$, where the level spacings $s_n = E_{n+1} - E_n$ and $s_{n+1} = E_{n+2} - E_{n+1}$ are independently distributed according to Poisson statistics [Equation (2.33) on page 17]:

$$\begin{aligned}\mathbb{P}(\tilde{r}_n \leq \alpha) &= \mathbb{P}(s_n \leq \alpha s_{n+1}) \\ &= \int_0^\infty e^{-s_{n+1}} \int_0^{\alpha s_{n+1}} e^{-s_n}\,\mathrm{d}s_n\,\mathrm{d}s_{n+1} \\ &= \frac{\alpha}{1+\alpha}.\end{aligned} \tag{A.2}$$

Now we can calculate the cumulative distribution function for $r_n = \min\{\tilde{r}_n, 1/\tilde{r}_n\}$ based on the fact that $r_n \leq \alpha$ for $0 \leq \alpha \leq 1$ is equivalent to $\tilde{r}_n = r_n \leq \alpha$ or $\tilde{r}_n = 1/r_n \geq 1/\alpha$:

$$\begin{aligned}\mathbb{P}(r_n \leq \alpha) &= \mathbb{P}(\tilde{r}_n \leq \alpha) + \mathbb{P}\left(\tilde{r}_n \geq \frac{1}{\alpha}\right) \\ &= \frac{\alpha}{1+\alpha} + \left(1 - \frac{\frac{1}{\alpha}}{1+\frac{1}{\alpha}}\right) \\ &= \frac{2\alpha}{1+\alpha}.\end{aligned} \tag{A.3}$$

The probability density of r is hence the derivative

$$P_{\text{Poisson}}(r) = \left(\frac{\mathrm{d}}{\mathrm{d}\alpha}\frac{2\alpha}{1+\alpha}\right)_{\alpha=r} = \frac{2}{(1+r)^2}. \tag{A.4}$$

In particular the mean level spacing ratio evaluates to

$$\langle r\rangle_{\text{Poisson}} = \int_0^1 \frac{2}{(1+r)^2} r\,\mathrm{d}r = 2\ln 2 - 1. \tag{A.5}$$

A.2. Limits of Fractal Dimensions and q-Moments

In this section we give detailed proofs of some properties of fractal dimensions and q-moments discussed in Section 2.3. In particular, we will deduce maxima and minima of the fractal dimensions and q-moments as functions of the state $|\psi\rangle$, we will determine the limit of $\tilde{D}_q$ for $q \to \infty$, and we will show that R_q and $\tilde{D}_q$ are monotonic functions of the parameter q. In the following, let

$$|\psi\rangle = \sum_\alpha \psi_\alpha \, |\alpha\rangle \tag{A.6}$$

be an arbitrary normalized state belonging to the Hilbert space $\mathcal{H}$ spanned by the basis $\{|\alpha\rangle\}$, $\dim \mathcal{H} = \mathcal{N}$.

A.2.1. Dependence on the State

Let $q \geq 0$ be fixed. For a single index α and $q \geq 1$, the term

$$|\psi_\alpha|^2 \, (1 - |\psi_\alpha|^{2(q-1)}) \tag{A.7}$$

is always greater than or equal to 0, since $|\psi_\alpha|^2 \geq 0$ and $|\psi_\alpha|^{2(q-1)} \leq 1^{q-1} = 1$. For $q < 1$, the same arguments yield

$$|\psi_\alpha|^2 \, (1 - |\psi_\alpha|^{2(q-1)}) \leq 0. \tag{A.8}$$

In both cases, equality holds if and only if one of the factors vanishes, that is, if $|\psi_\alpha|^2 \in \{0, 1\}$. Summation yields

$$\sum_\alpha |\psi_\alpha|^2 \left(1 - |\psi_\alpha|^{2(q-1)}\right) \begin{cases} \geq 0, & q \geq 1, \\ \leq 0, & q < 1, \end{cases} \tag{A.9}$$

where the equality holds if and only if all $|\psi_\alpha|^2 \in \{0, 1\}$, i.e. if and only if $|\psi\rangle$ is localized on a single basis state $|\alpha\rangle$. This inequality translates into

$$R_q = \sum_\alpha |\psi_\alpha|^{2q} \leq \sum_\alpha |\psi_\alpha|^2 = 1 \tag{A.10}$$

for $q \geq 1$ and, similarly, $R_q \geq 1$ for $q < 1$, where the equality holds exactly for $|\psi\rangle = |\alpha\rangle$, with a single basis state $|\alpha\rangle$.

On the other hand, to determine the minimum of R_q for $q \geq 1$ (maximum for $q < 1$), consider the gradient of R_q with respect to $|\psi_\alpha|^2$, whose α component, with $\alpha = 1, \ldots, \mathcal{N}$, reads

$$\left(\nabla R_q\right)_\alpha = q |\psi_\alpha|^{2(q-1)}. \tag{A.11}$$

Additionally, the normalization condition $\sum_\alpha |\psi_\alpha|^2 = 1$ needs to be fulfilled, which means that, by the method of Lagrange multipliers, we have to subtract

$$\left[\nabla\lambda\left(\sum_\alpha |\psi_\alpha|^2 - 1\right)\right]_\alpha = \lambda \tag{A.12}$$

from the α component of the gradient in order to find an extremum. For all α, this ansatz leads to

$$q|\psi_\alpha|^{2(q-1)} - \lambda = 0 \qquad \Rightarrow \qquad |\psi_\alpha|^{2(q-1)} = \frac{\lambda}{q}. \tag{A.13}$$

Consequently, all vector intensities are the same, i.e., the state $|\psi\rangle$ is equally distributed over all basis elements $|\alpha\rangle$. This condition, together with normalization, yields $|\psi_\alpha|^2 = 1/\mathcal{N}$ and hence

$$R_q = \mathcal{N}^{-(q-1)}. \tag{A.14}$$

This point is a minimum for $q > 1$ (maximum for $q < 1$), as can be checked from the Hessian matrix of R_q as a function of the vector intensities $|\psi_\alpha|^2$.

Since the logarithm and the exponential are monotonically increasing functions, the minima (maxima) of R_q are also minima (maxima) of $\ln R_q$ and vice versa. However, the extremum $\tilde{D}_q = 1$ for $R_q = \mathcal{N}^{-(q-1)}$, i.e., fully delocalized states, is always a maximum, since the factor $-(q-1)^{-1}$ in the definition of $\tilde{D}_q$ [Equation (2.64) on page 25] flips the sign and hence interchanges maxima and minima for $q > 1$, while the sign is preserved for $q < 1$. $\tilde{D}_q = 0$ for $R_q = 1$, i.e., fully localized states, is always a minimum for the same reasons. By deducing these bounds we have shown that it is exactly the fully delocalized (fully localized) states with respect to the given basis that obey $\tilde{D}_q = 1$ ($\tilde{D}_q = 0$), and no other states with larger $\tilde{D}_q > 1$ (smaller $\tilde{D}_q < 0$) exist.

A.2.2. The Fractal Dimension $\tilde{D}_\infty$

To determine the limit $q \to \infty$ of the generalized fractal dimensions $\tilde{D}_q$, define $\mathcal{A}_{\max}$ as the set of indices α for which $|\psi_\alpha|^2 = \max_\beta |\psi_\beta|^2$. Let c be the number of elements in $\mathcal{A}_{\max}$. Now consider

$$\begin{aligned}\lim_{q\to\infty}\left(\ln\frac{\sum_\alpha |\psi_\alpha|^{2q}}{c\max_\alpha |\psi_\alpha|^{2q}}\right) &= \lim_{q\to\infty}\ln\left(\sum_{\alpha\in\mathcal{A}_{\max}}\frac{1}{c} + \sum_{\alpha\notin\mathcal{A}_{\max}}\frac{|\psi_\alpha|^{2q}}{c\,(\max_\alpha |\psi_\alpha|^2)^q}\right)\\ &= \ln\lim_{q\to\infty}\left(1 + \sum_{\alpha\notin\mathcal{A}_{\max}}\frac{|\psi_\alpha|^{2q}}{c\,(\max_\alpha |\psi_\alpha|^2)^q}\right)\\ &= \ln 1 = 0.\end{aligned}$$

In the second step of this calculation we have used that the logarithm is continuous and hence one can interchange it with the limit. With this result we can write

$$\ln \sum_\alpha |\psi_\alpha|^{2q} = \ln \max_\alpha |\psi_\alpha|^{2q} + \ln c + \epsilon(q) \tag{A.15}$$

with $\lim_{q\to\infty} \epsilon(q) = 0$, and hence

$$\tilde{D}_\infty = -\frac{1}{\ln \mathcal{N}} \lim_{q\to\infty} \frac{q \ln \max_\alpha |\psi_\alpha|^2 + \ln c + \epsilon(q)}{q-1} = -\frac{1}{\ln \mathcal{N}} \ln \max_\alpha |\psi_\alpha|^2, \tag{A.16}$$

as stated in Equation (2.71) of the main text (page 27).

A.2.3. Monotonicity as Functions of the Index q

In the following, we keep the state $|\psi\rangle$ fixed. Since $0 \le |\psi_\alpha|^2 \le 1$, it is clear that $|\psi_\alpha|^{2q}$ and, in consequence, also R_q are monotonically decreasing functions of q. To obtain the monotonicity of $\tilde{D}_q$, we calculate its derivative with respect to q,

$$\begin{aligned}\ln \mathcal{N} \frac{\mathrm{d}\tilde{D}_q}{\mathrm{d}q} &= -\frac{(q-1)\sum_\alpha |\psi_\alpha|^{2q} \ln(|\psi_\alpha|^2)/\sum_\beta |\psi_\beta|^{2q} - \ln \sum_\alpha |\psi_\alpha|^{2q}}{(q-1)^2} \\ &= -\frac{1}{(q-1)^2} \sum_\alpha \ln \left[|\psi_\alpha|^{2q}/(|\psi_\alpha|^2 \sum_\beta |\psi_\beta|^{2q}) \right] |\psi_\alpha|^{2q}/\sum_\beta |\psi_\beta|^{2q} \\ &= -\frac{1}{(q-1)^2} \sum_\alpha z_\alpha \ln(z_\alpha/|\psi_\alpha|^2), \end{aligned} \tag{A.17}$$

where $z_\alpha := |\psi_\alpha|^{2q}/\sum_\beta |\psi_\beta|^{2q}$. Since the logarithm is a strictly concave function, Jensen's inequality (Equation 1.7.10 of Reference [185]) holds, that is, for $p_\alpha \ge 0$ and $\sum_\alpha p_\alpha = 1$, we have

$$\sum_\alpha p_\alpha \ln(x_\alpha) \le \ln \left(\sum_\alpha p_\alpha x_\alpha \right). \tag{A.18}$$

In our case, $\sum_\alpha z_\alpha = 1$ and $z_\alpha \ge 0$ are fulfilled by definition; therefore

$$\begin{aligned}\sum_\alpha -z_\alpha \ln(z_\alpha/|\psi_\alpha|^2) &= \sum_\alpha z_\alpha \ln(|\psi_\alpha|^2/z_\alpha) \\ &\le \ln \left(\sum_\alpha z_\alpha (|\psi_\alpha|^2/z_\alpha) \right) \\ &= \ln \sum_\alpha |\psi_\alpha|^2 \\ &= \ln 1 = 0. \end{aligned} \tag{A.19}$$

Inserting this result into the derivative of $\tilde{D}_q$ yields $\frac{\mathrm{d}\tilde{D}_q}{\mathrm{d}q} \le 0$, and, hence, $\tilde{D}_q$ is a monotonically decreasing function of q.

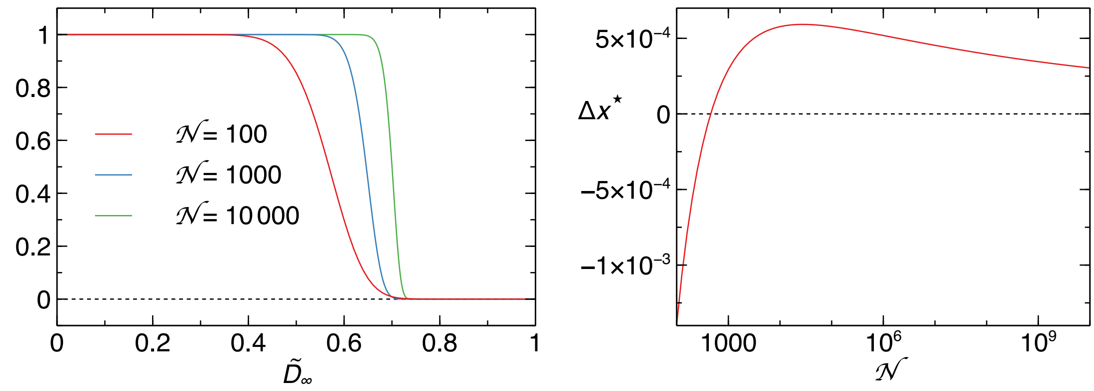

(a) (b)

Figure A.1: (a) $[\mathrm{Erf}\,(x)]^{\mathcal{N}}$, with $x = \mathcal{N}^{(1-\tilde{D}_\infty)/2}/\sqrt{2}$, versus $\tilde{D}_\infty$ for $\mathcal{N} = 100,\ 1000,\ 10\,000$, (b) relative deviation $\Delta x^\star$ [Equation (A.32)] of $x^\star$, according to Equation (A.31), from the numerical solution $x^\star_{\mathrm{num}}$ of Equation (A.23), as a function of dimension $\mathcal{N}$.

A.3. Scaling of the Fractal Dimension $\tilde{D}_\infty$ for the Gaussian Orthogonal Ensemble

This section provides details on the scaling of $\langle \tilde{D}_\infty \rangle_{\mathrm{GOE}}$ and $\mathrm{var}\,(\tilde{D}_\infty)_{\mathrm{GOE}}$ with Hilbert space dimension $\mathcal{N}$ in the limit $\mathcal{N} \to \infty$ [see Equations (4.19) and (4.20) on page 64]. As a first step, we approximate the integrand in Equation (4.18) appropriately. This works best using an alternative representation of $\left\langle \tilde{D}^k_\infty \right\rangle$ substituting the integration variable x by

$$\tilde{D}_\infty = 1 - \frac{\ln 2x^2}{\ln \mathcal{N}} \tag{A.20}$$

and neglecting the exponentially decaying term:

$$\left\langle \tilde{D}^k_\infty \right\rangle_{\mathrm{GOE}} = k \int_0^1 \left[\mathrm{Erf} \left(\frac{\mathcal{N}^{(1-\tilde{D}_\infty)/2}}{\sqrt{2}} \right) \right]^{\mathcal{N}} \tilde{D}^{k-1}_\infty \, \mathrm{d}\tilde{D}_\infty . \tag{A.21}$$

As can be seen in Figure A.1(a), the error function term in this integral becomes essentially a step function for large Hilbert space dimensions $\mathcal{N}$, which changes between 1 and 0 in a small range of $\tilde{D}_q$. In order to capture also this finite interval of the decay from 1 to 0, we approximate the error function term as a piecewise function,

$$\left[\mathrm{Erf} \left(\frac{\mathcal{N}^{(1-\tilde{D}_\infty)/2}}{\sqrt{2}} \right) \right]^{\mathcal{N}} \approx \begin{cases} 1, & 0 \le \tilde{D}_\infty \le \mathcal{D}^{(1)}, \\ 1 - a_1 \left(\tilde{D}_\infty - \mathcal{D}^{(1)} \right)^2, & \mathcal{D}^{(1)} < \tilde{D}_\infty \le \mathcal{D}^\star, \\ a_2 \left(\tilde{D}_\infty - \mathcal{D}^{(2)} \right)^2, & \mathcal{D}^\star < \tilde{D}_\infty \le \mathcal{D}^{(2)}, \\ 0, & \mathcal{D}^{(2)} < \tilde{D}_\infty \le 1. \end{cases} \tag{A.22}$$

Here, $\mathcal{D}^\star$ is the solution of

$$\left[\mathrm{Erf}\left(\frac{\mathcal{N}^{(1-\mathcal{D}^\star)/2}}{\sqrt{2}}\right)\right]^{\mathcal{N}} = \frac{1}{2}, \tag{A.23}$$

and $\mathcal{D}^{(1)}$, $\mathcal{D}^{(2)}$, a_1, a_2 are determined such that the piecewise function is continuously differentiable at $\mathcal{D}^\star$ and its derivative at $\mathcal{D}^\star$ is equal to

$$\alpha := \left(\frac{\mathrm{d}}{\mathrm{d}\tilde{D}_\infty}\left[\mathrm{Erf}\left(\frac{\mathcal{N}^{(1-\tilde{D}_\infty)/2}}{\sqrt{2}}\right)\right]^{\mathcal{N}}\right)_{\tilde{D}_\infty=\mathcal{D}^\star} = -\frac{2^{1/\mathcal{N}}\mathcal{N}\frac{\mathcal{N}^{(1-\mathcal{D}^\star)/2}}{\sqrt{2}}e^{-\frac{\mathcal{N}^{1-\mathcal{D}^\star}}{2}}\ln\mathcal{N}}{2\sqrt{\pi}}. \tag{A.24}$$

These conditions yield

$$\mathcal{D}^\star - \mathcal{D}^{(1)} = -\left(\mathcal{D}^\star - \mathcal{D}^{(2)}\right) = -\frac{1}{\alpha}, \qquad a_1 = a_2 = \frac{\alpha^2}{2}. \tag{A.25}$$

By this construction, the piecewise function is continuously differentiable for all $\tilde{D}_\infty$. Mean and variance of $\tilde{D}_\infty$ within this approximation read

$$\langle\tilde{D}_\infty\rangle_{\mathrm{GOE}} = \mathcal{D}^\star, \qquad \mathrm{var}\left(\tilde{D}_\infty\right)_{\mathrm{GOE}} = \frac{1}{6\alpha^2}. \tag{A.26}$$

Note that a simpler approximation of the error function term by a Heaviside step function, assuming an immediate change from 1 to 0, would give the same mean, but the variance, and also any other central moment, would vanish exactly. Hence, we need a more sophisticated approximation than the step function, such as the piecewise function provided here.

To solve Equation (A.23) approximately for

$$x^\star = \frac{\mathcal{N}^{(1-\mathcal{D}^\star)/2}}{\sqrt{2}}, \tag{A.27}$$

we expand $2^{-1/\mathcal{N}}$ for large $\mathcal{N}$,

$$2^{-\frac{1}{\mathcal{N}}} = 1 - \frac{\ln 2}{\mathcal{N}} + \mathcal{O}\left(\frac{1}{\mathcal{N}^2}\right), \tag{A.28}$$

and we use an expansion of the error function for large arguments, Equation 7.12.1 of Reference [185],

$$\mathrm{Erf}(x) = 1 - \frac{e^{-x^2}}{\sqrt{\pi}}\left[\frac{1}{x} + \mathcal{O}\left(\frac{1}{x^2}\right)\right]. \tag{A.29}$$

Doing such an expansion for the error function is justified for large enough $\mathcal{N}$, since $2^{-1/\mathcal{N}}$ converges to 1 in the limit $\mathcal{N} \to \infty$, and $\mathrm{Erf}(x)$ is close to 1 only for $x \to \infty$. With these two expansions, we obtain the approximate equation

$$(x^\star)^2 = \ln\mathcal{N} - \frac{1}{2}\ln\pi - \ln(\ln 2) - \ln x^\star, \tag{A.30}$$

which can be solved iteratively by replacing $x^\star$ in $\ln x^\star$ by the right-hand side of this equation, and which yields after one iteration the approximate solution

$$(x^\star)^2 = \ln\mathcal{N} - \frac{1}{2}\ln\pi - \ln(\ln 2) - \frac{1}{2}\ln\left(\ln\mathcal{N} - \frac{1}{2}\ln\pi - \ln(\ln 2)\right). \tag{A.31}$$

As shown in Figure A.1(b), the relative difference

$$\Delta x^\star = \frac{x^\star_{\mathrm{num}} - x^\star}{x^\star_{\mathrm{num}}} \tag{A.32}$$

between Equation (A.31) and a direct numerical solution $x^\star_{\mathrm{num}}$ of Equation (A.23) is maximally of order 10^{-3} for large enough $\mathcal{N}$, which confirms the quality of the approximation. Inserting Equation (A.31) into Equations (A.24) and (A.26) and doing an expansion for $\mathcal{N} \to \infty$ finally yields the expressions presented in Equations (4.19) and (4.20) of the main text,

$$\langle\tilde{D}_\infty\rangle_{\mathrm{GOE}} = 1 - \frac{\ln(\ln\mathcal{N}) + \ln 2}{\ln\mathcal{N}} + \frac{\ln(\ln\mathcal{N})}{\ln^2\mathcal{N}} + \mathcal{O}\left(\frac{1}{\ln^2\mathcal{N}}\right), \tag{A.33}$$

$$\mathrm{var}\left(\tilde{D}_\infty\right)_{\mathrm{GOE}} = \frac{2}{3\ln^2 2\ln^4\mathcal{N}} + \frac{\ln(\ln\mathcal{N})}{3\ln^2 2\ln^5\mathcal{N}} + \mathcal{O}\left(\frac{1}{\ln^5\mathcal{N}}\right). \tag{A.34}$$

An alternative approach, approximating the decay of the error function term by its tangent at $\mathcal{D}^\star$,

$$\left[\mathrm{Erf}\left(\frac{\mathcal{N}^{(1-\tilde{D}_\infty)/2}}{\sqrt{2}}\right)\right]^{\mathcal{N}} \approx \begin{cases} 1, & 0 \le \tilde{D}_\infty \le \mathcal{D}^{(1)}, \\ \alpha\left(\tilde{D}_\infty - \mathcal{D}^{(2)}\right), & \mathcal{D}^{(1)} < \tilde{D}_\infty \le \mathcal{D}^{(2)}, \\ 0, & \mathcal{D}^{(2)} < \tilde{D}_\infty \le 1, \end{cases} \tag{A.35}$$

where $\mathcal{D}^{(1)}$ is chosen such that the piecewise function is continuous, would lead to the same mean, but to a different prefactor of the variance. Therefore, the coefficients of the scaling of $\mathrm{var}\left(\tilde{D}_\infty\right)_{\mathrm{GOE}}$ depend on the precise treatment of the error function term and are difficult to obtain exactly, but, as is also revealed in Figure 4.1 of the main text (page 65), the functional form of the leading terms in $\mathcal{N}$ is correctly captured by this method.

Appendix B.

Correlations of Eigenvector Coefficients

In this appendix we give an overview of our study of the correlations

$$\psi_\alpha \psi_\beta, \qquad\qquad |\psi_\alpha|^2 \, |\psi_\beta|^2 \tag{B.1}$$

between eigenvector coefficients $\psi_\alpha = \langle \alpha | \psi \rangle$, $\psi_\beta = \langle \beta | \psi \rangle$ in the chaotic domain.

B.1. Spatial Correlations for Chaotic Wave Functions and at the Anderson Transition

Let us first discuss several known results about correlations of eigenstate coefficients for single-particle wave functions. In a semiclassical setting, Berry [201, 202] studied the autocorrelation functions

$$C(\boldsymbol{x}, \boldsymbol{r}) = \overline{\psi\left(\boldsymbol{r} + \frac{1}{2}\boldsymbol{x}\right) \psi^*\left(\boldsymbol{r} - \frac{1}{2}\boldsymbol{x}\right)} / \overline{|\psi(\boldsymbol{r})|^2} \tag{B.2}$$

of energy eigenfunctions $\psi(\boldsymbol{r})$ for chaotic and regular systems with a $2n$-dimensional phase space spanned by n (generalized) positions and n (generalized) momenta (compare Section 2.1). Here, $\boldsymbol{x}$ and $\boldsymbol{r}$ are positions in real space and the bar denotes a local average over the coordinates $\boldsymbol{r}$ in a small phase-space volume. Approximating the Wigner function

$$\Psi(\boldsymbol{r}, \boldsymbol{p}) = \frac{1}{(2\pi\hbar)^n} \int \mathrm{d}^n x \;\; \mathrm{e}^{-\mathrm{i}\boldsymbol{p}\cdot\boldsymbol{x}/\hbar} \, \psi\left(\boldsymbol{r} - \frac{1}{2}\boldsymbol{x}\right) \psi^*\left(\boldsymbol{r} + \frac{1}{2}\boldsymbol{x}\right) \tag{B.3}$$

of positions $\boldsymbol{r}$ and momenta $\boldsymbol{p}$ by the classical phase-space density given by the corresponding classical trajectory (for integrable motion, equidistribution on a torus; for chaotic motion in the absence of any traces of mixed phase space [7], equidistribution on all available phase space at fixed energy), and using the relation

$$C(\boldsymbol{x}, \boldsymbol{r}) = \int \mathrm{d}^n p \;\; \mathrm{e}^{\mathrm{i}\boldsymbol{p}\cdot\boldsymbol{x}/\hbar} \, \overline{\Psi(\boldsymbol{r}, \boldsymbol{p})} / \overline{|\psi(\boldsymbol{r})|^2}, \tag{B.4}$$

he showed that in the chaotic regime the autocorrelation function behaves as [201, 203]

$$C(\boldsymbol{x}, \boldsymbol{r}) = \Gamma\left(\frac{n}{2}\right) \frac{J_{n/2-1}\left(|\boldsymbol{x}|\sqrt{2m(E - V(\boldsymbol{r}))}/\hbar\right)}{\left(|\boldsymbol{x}|\sqrt{2m(E - V(\boldsymbol{r}))}/(2\hbar)\right)^{n/2-1}}, \tag{B.5}$$

if the Hamiltonian is of the form

$$H(\boldsymbol{r}, \boldsymbol{p}) = \frac{\boldsymbol{p}^2}{2m} + V(\boldsymbol{r}). \tag{B.6}$$

Here, J_k is the Bessel function of index k (Equation 10.2.2 of Reference [185]), E is the energy of the eigenfunction $\psi(\boldsymbol{r})$, and $\Gamma(n/2)$ accounts for normalization. This Bessel-function shape of the autocorrelation is known as *Berry's conjecture*.

Another relevant result on wave function correlations in real space was given in the context of Anderson localization. Anderson localization describes the disorder-induced transition between extended and localized single-particle wave functions $\psi(\boldsymbol{r})$ on a d-dimensional lattice of length L [72], where the wave functions at the critical point of the transition are multifractal according to our definition in Section 2.3 of the main text [73–75]. One now defines the anomalous dimensions Δ_q as [73]

$$\Delta_q = -d(1 - D_q)(q - 1). \tag{B.7}$$

In particular the anomalous dimension Δ_2 was found to determine the scaling with distance and system size of spatial correlations between intensities of a multifractal wave function [73],

$$L^{2d} \left\langle |\psi(\boldsymbol{r})|^2 \, |\psi(\boldsymbol{r} + \boldsymbol{x})|^2 \right\rangle \sim \left(\frac{|\boldsymbol{x}|}{L}\right)^{\Delta_2}, \tag{B.8}$$

where $\langle \cdot \rangle$ is an average over disorder realizations. Higher-order correlations of the intensities are known to depend on Δ_q in a similar way [73], e.g.,

$$L^{d(q_1+q_2)} \left\langle |\psi(\boldsymbol{r})|^{2q_1} \, |\psi(\boldsymbol{r} + \boldsymbol{x})|^{2q_2} \right\rangle \sim L^{-q_1-q_2} \left(\frac{|\boldsymbol{x}|}{L}\right)^{\Delta_{q_1+q_2} - \Delta_{q_1} - \Delta_{q_2}}. \tag{B.9}$$

Motivated by these results, we investigate the correlations of eigenstate amplitudes and intensities in the Bose-Hubbard model. In contrast to the wave functions discussed above, which are defined in real space, we will consider many-body eigenstates in the interaction basis, i.e., the Fock basis built on single-particle states localized in real space. The first task is therefore to come up with an adequate definition of distances in Fock space.

B.2. Distances in Fock Space

For the following discussion, let

$$|\boldsymbol{n}\rangle = |n_1, \dots, n_L\rangle, \qquad |\boldsymbol{m}\rangle = |m_1, \dots, m_L\rangle \tag{B.10}$$

be two Fock states of N particles in L single-particle modes.

One possible distance between Fock states is the Hamming distance d_h [204]. For mode occupation numbers n_i, $m_i \in \{0, 1\}$, this distance is defined as the number of pairs (n_i, m_i) such that $n_i \neq m_i$. It can be generalized to higher occupation numbers in two ways, either by defining d_h, again, as the number of occupation numbers $n_i \neq m_i$, or by summing up the differences between the occupation numbers, i.e.,

$$d_h(|\boldsymbol{n}\rangle, |\boldsymbol{m}\rangle) = \sum_{i=1}^{L} |n_i - m_i|. \tag{B.11}$$

Since the latter takes into account how many particles need to be moved from one single-particle mode to another in order to transform $|\boldsymbol{n}\rangle$ into $|\boldsymbol{m}\rangle$, this second generalization seems more appropriate for bosonic Fock states. Note that the distance defined in Equation (B.11) is also known as the 1-distance, the taxicab distance, or the Manhattan distance of the two vectors $\boldsymbol{n}$ and $\boldsymbol{m}$.

Another possible distance is the tunneling distance d_t. It is defined as the minimum number of tunneling processes that connect the two Fock states. For instance, the states

$$|\boldsymbol{n}\rangle = |1, 0, 2\rangle, \qquad |\boldsymbol{m}\rangle = |2, 0, 1\rangle \tag{B.12}$$

have distance $d_t = 1$ for nearest-neighbour tunneling with PBCs and $d_t = 2$ for nearest-neighbour tunneling with HWBCs. In contrast to the Hamming distance, the tunneling distance depends on the connectivity of the single-particle modes provided by a tunneling Hamiltonian. Note that for all-to-all connectivity of the single-particle modes the tunneling distance agrees with the Hamming distance up to a constant factor, $d_h = 2d_t$.

When reflection and, for PBCs, translation symmetries are taken into account, the interaction basis states are typically linear combinations of few Fock states. In this case, we define the distance d_k, $k = h$, t, of two basis states

$$|\varphi\rangle = \sum_i \alpha_i |\boldsymbol{n}_i\rangle, \qquad |\psi\rangle = \sum_i \beta_j |\boldsymbol{m}_j\rangle \tag{B.13}$$

that belong to the same symmetry-induced subspace as the minimum of the distances between the Fock states $|\boldsymbol{n}_i\rangle$, $|\boldsymbol{m}_j\rangle$ contributing to the basis states,

$$d_k(|\varphi\rangle, |\psi\rangle) = \min_{i,j} d_k(|\boldsymbol{n}_i\rangle, |\boldsymbol{m}_j\rangle). \tag{B.14}$$

Note that, by construction, each Fock state contributes to maximally one interaction basis state per symmetry-induced subspace and hence $d_k(|\varphi\rangle, |\psi\rangle) > 0$ for $|\varphi\rangle \neq |\psi\rangle$. The distance between two basis states belonging to different symmetry-induced subspaces can be set to infinity, since the dynamics respect the symmetry and hence do not couple the different symmetry-induced subspaces.

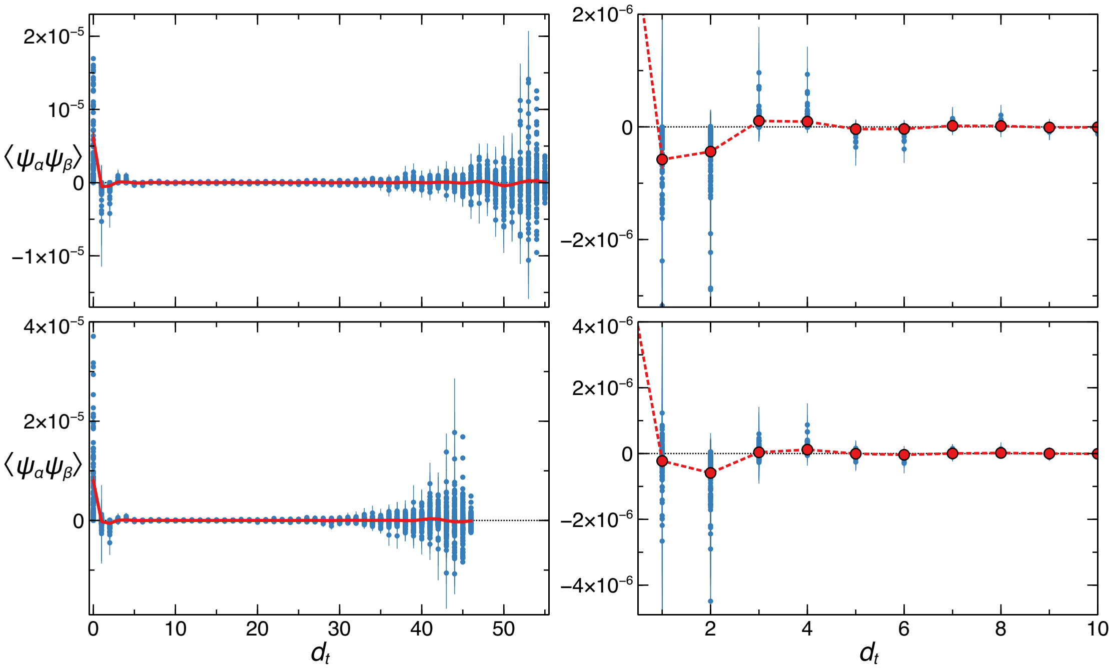

Figure B.1: Correlations $\langle\psi_\alpha\psi_\beta\rangle$ [Equation (B.15)] of eigenstate amplitudes in the interaction basis, versus tunneling distance d_t as defined in Section B.2, for 100 eigenstates around $\varepsilon = 0.5$ at $\eta = 0.3760$, $N = L = 11$, HWBCs, and $\Pi = +1$ ($\mathcal{N} = 176\,484$). Each blue point corresponds to one eigenstate after averaging over all basis states $|\beta\rangle$ at the same distance from a reference basis state $|\alpha\rangle$. Red lines (all panels) and red circles (right panels) denote the additional average over all eigenstates. The chosen reference state in the upper (lower) panels is $|\alpha\rangle = |1, \ldots, 1\rangle$ (the symmetrized version of $|\alpha\rangle = |3, 1, 0, 1, 0, 2, 0, 2, 1, 0, 1\rangle$). The right panels are magnifications for $1 \leq d_t \leq 10$.

B.3. Correlations in the Bose-Hubbard Model

In the following, we present results about correlations of the eigenstate amplitudes $\psi_\alpha = \langle\alpha|\psi\rangle$ and of the corresponding intensities for the Bose-Hubbard model, where the set $\{|\alpha\rangle\}$ is the interaction basis. Figure B.1 shows the amplitude correlations

$$\langle\psi_\alpha\psi_\beta\rangle\,(d) := \frac{1}{\#\mathcal{B}(d)} \sum_{|\beta\rangle\in\mathcal{B}(d)} \psi_\alpha\psi_\beta \tag{B.15}$$

as functions of the tunneling distance d_t, where $\mathcal{B}(d) := \{|\beta\rangle \;:\; d_t(|\alpha\rangle\,, |\beta\rangle) = d\}$ is the set of basis states with tunneling distance d from $|\alpha\rangle$, and $\#\mathcal{B}(d)$ is the number of elements in $\mathcal{B}(d)$. In other words, we fix a reference state $|\alpha\rangle$ and average $\psi_\alpha\psi_\beta$ over all basis states $|\beta\rangle$ with the same tunneling distance from $|\alpha\rangle$. Here, we consider the 100 eigenstates closest to $\varepsilon = 0.5$ at $\eta = 0.3760$, and we choose $N = L = 11$ with HWBCs

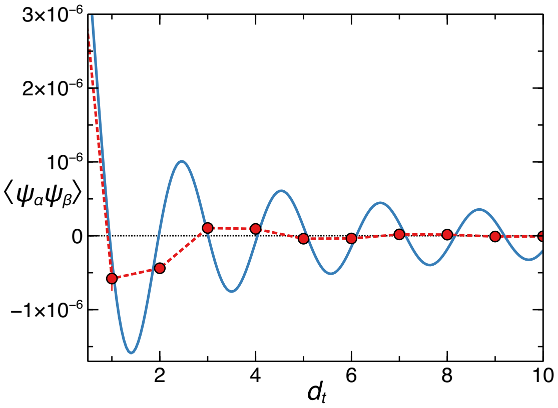

Figure B.2: Correlations of eigenstate amplitudes [Equation (B.15)] on the interaction basis versus tunneling distance, averaged over all interaction basis states $|\beta\rangle$ at the same distance from $|\alpha\rangle = |1,\ldots,1\rangle$ and, furthermore, over 100 eigenstates around $\varepsilon = 0.5$ at $\eta = 0.3760$ (red, compare Figure B.1, upper panels), for $N = L = 11$, HWBCs and $\Pi = +1$ ($\mathcal{N} = 176\,484$). To benchmark the behaviour of $\langle\psi_\alpha\psi_\beta\rangle$ against Berry's conjecture [Equation (B.5)], the blue curve represents a fit of the parametrized version $f(d_t)$ [Equation (B.16)] of Equation (B.5) to the correlation function $\langle\psi_\alpha\psi_\beta\rangle$, for the first six data points, $0 \leq d_t \leq 5$.

and parity $\Pi = +1$ (Hilbert space dimension $\mathcal{N} = 176\,484$). As reference states, we consider the fully symmetric state $|\alpha\rangle = |1,\ldots,1\rangle$, which is in the center of the lattice defined by the Fock states as vertices and their tunneling connections as edges, and the symmetrized version of $|\alpha\rangle = |3,1,0,1,0,2,0,2,1,0,1\rangle$, which was picked randomly. For both states $|\alpha\rangle$ considered here, the amplitude correlations quickly decay to 0 as a function of d_t. For large distances, the correlations attain large absolute values and fluctuate strongly among different eigenstates. The latter is likely a finite-size effect when approaching the boundary of the lattice defined by the Fock states.

At small positive distances, the correlations show an oscillating pattern. When d_t is increased by 2, the correlations change sign. This holds true on average over different eigenstates as well as for individual eigenstates and is most clearly visible in the right panels of Figure B.1. Note that this pattern is found for both reference states $|\alpha\rangle$ and is hence not an effect of the specific symmetries of the one reference state or the other. Such an oscillatory behaviour is qualitatively in agreement with Berry's conjecture, Equation (B.5). However, naively fitting the function

$$f(d_t) = a\frac{J_{n/2-1}\left(kd_t\right)}{\left(kd_t\right)^{n/2-1}}, \tag{B.16}$$

with parameters a, k, n, to the data does not seem to yield a reliable result. This is exemplified in Figure B.2 by fitting to the first six data points of the correlation $\langle\psi_\alpha\psi_\beta\rangle$,

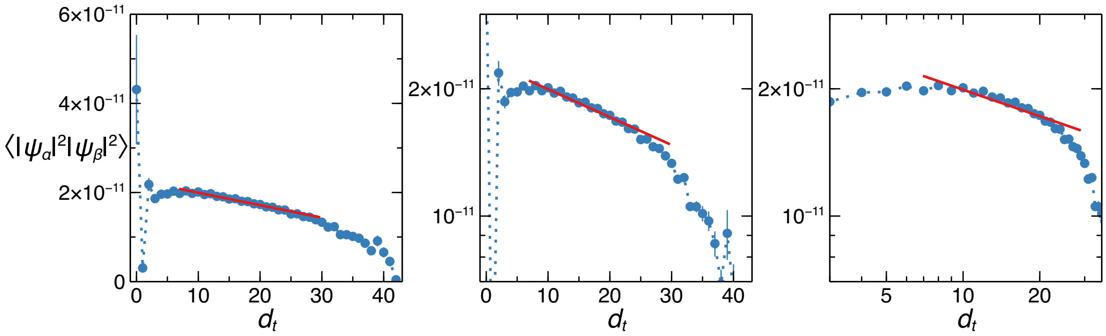

Figure B.3: Linear (left), semi-logarithmic (center) and log-log graph (right) of the correlations of eigenstate intensities [Equation (B.17)] in the interaction basis, versus tunneling distance d_t as defined in Section B.2, averaged over all interaction basis states $|\beta\rangle$ at the same distance from $|\alpha\rangle = |1,\dots,1\rangle$ and over 100 eigenstates around $\varepsilon = 0.5$ at $\eta = 0.3181$, for $N = L = 13$, PBCs, $Q = 0$ and $\Pi = +1$ ($\mathcal{N} = 200\,474$). Red lines are fits with $f(d_t) = a(1 - b\,d_t)$ (left), $g(d_t) = a\,e^{-b\,d_t}$ (center), $h(d_t) = a\,d_t^{-b}$ (right), for $7 \le d_t \le 30$.

with $|\alpha\rangle = |1,\dots,1\rangle$. The fit $f(d_t)$ reproduces the values of the correlation at the given discrete distances d_t, but, nevertheless, its oscillation pattern shows some deviations from the one suggested by the correlation data: Consider, e.g., the minimum of $f(d_t)$ between $d_t = 3$ and $d_t = 4$, where the numerical data suggests a maximum of $\langle\psi_\alpha\psi_\beta\rangle$. Further analysis would be needed to understand whether and how the oscillation of $\langle\psi_\alpha\psi_\beta\rangle$ with the tunneling distance is related to Berry's conjecture.

To check whether the decay of the intensity correlations is connected to the fractal dimension D_2 like for the single-particle Anderson problem, we plot in Figures B.3 and B.4 the averaged correlations

$$\left\langle |\psi_\alpha|^2\,|\psi_\beta|^2 \right\rangle(d) := \frac{1}{100}\sum_{i=1}^{100}\frac{1}{\#\mathcal{B}(d)}\sum_{|\beta\rangle\in\mathcal{B}(d)}\left|\psi_\alpha^{(i)}\right|^2\left|\psi_\beta^{(i)}\right|^2, \tag{B.17}$$

as functions of the tunneling distance (Figure B.3) and of the Hamming distance (Figure B.4). Here, for $d_k = d_t$ or $d_k = d_h$, respectively, the set $\mathcal{B}(d) := \{|\beta\rangle \,:\, d_k(|\alpha\rangle, |\beta\rangle) = d\}$ contains exactly the basis states with distance $d_k = d$ from the reference state $|\alpha\rangle$, $\#\mathcal{B}(d)$ is the number of such basis states contained in $\mathcal{B}(d)$, and the index i labels the 100 eigenstates closest to a target energy ε at a fixed value of η, i.e., Equation (B.17) describes a joint average over basis states $|\beta\rangle$ with the same distance from $|\alpha\rangle$ and over eigenstates. Specifically, we consider the reference state $|\alpha\rangle = |1,\dots,1\rangle$, and we fix $\varepsilon = 0.5$ and $\eta = 0.3181$. The system under consideration is that of $N = L = 13$ with PBCs, quasimomentum $Q = 0$, and parity $\Pi = +1$ (dimension $\mathcal{N} = 200\,474$).

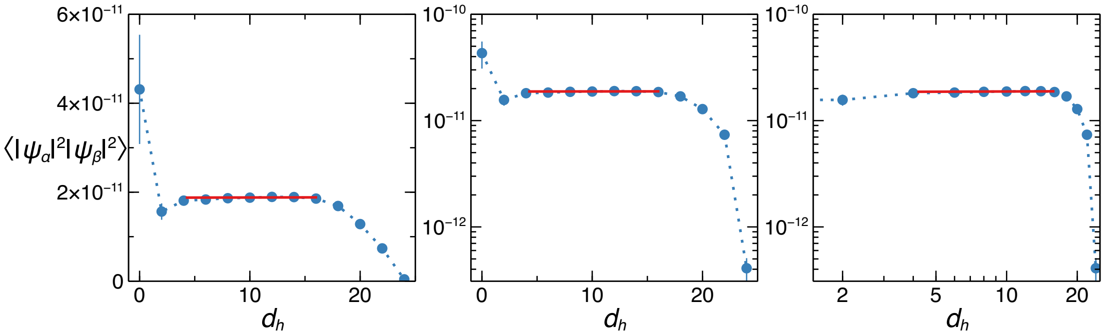

Figure B.4: Same as Figure B.3, for the Hamming distance d_h [Equation (B.11)] instead of the tunneling distance d_t. The fits are done in the range $4 \leq d_h \leq 16$.

According to the linear and the semi-logarithmic graph (left and center panels of Figure B.3), the intensity correlations for intermediate tunneling distances seem compatible with both a linear decay,

$$\left\langle |\psi_\alpha|^2 \, |\psi_\beta|^2 \right\rangle \sim 1 - b\, d_t, \tag{B.18}$$

and with an exponential decay,

$$\left\langle |\psi_\alpha|^2 \, |\psi_\beta|^2 \right\rangle \sim e^{-b\, d_t}, \tag{B.19}$$

while a polynomial decay,

$$\left\langle |\psi_\alpha|^2 \, |\psi_\beta|^2 \right\rangle \sim d_t^{-b}, \tag{B.20}$$

can be ruled out from the log-log graph (right panel of Figure B.3). This finding is clearly different from the results for multifractal states at the Anderson transition, where a polynomial decay is observed [Equation (B.8)].

As a function of the Hamming distance, the intensity correlation becomes almost constant for intermediate distances d_h. Such a behaviour would be compatible with the polynomial decay of Equation (B.8), with $\Delta_2 = 0$ and hence $D_2 = 1$. This value of D_2 is consistent with the finding that the Bose-Hubbard eigenstates become ergodic in the chaotic region for $\mathcal{N} \to \infty$, as discussed in Chapter 4. However, distance-independent correlations can be equally well described by a linear or an exponential “decay”, with decay constants $b = 0$ in Equations (B.18) and (B.19), respectively. Further research on the intensity correlations for eigenstates in the non-chaotic domain, where $D_q < 1$, would be needed to clarify whether or not $\left\langle |\psi_\alpha|^2 \, |\psi_\beta|^2 \right\rangle$ as a function of the Hamming distance shows a polynomial decay like in Equation (B.8).

Note that the distance dependence of the eigenvector correlations clearly distinguishes the Bose-Hubbard model from GOE, since for the latter, the joint probability distribution of two vector components is the same for any pair of basis states $|\alpha\rangle$, $|\beta\rangle$ [see

Equation (2.48), page 21]. For GOE, correlations such as $\langle\psi_\alpha\psi_\beta\rangle$ hence depend only on whether $|\alpha\rangle$ and $|\beta\rangle$ are equal or different, i.e., whether their (Hamming or tunneling) distance vanishes or not. Since the Hamiltonian of the embedded ensemble provides all-to-all connectivity of the single-particle modes [see the definition in Section 2.2.5], we expect that the correlations of embedded-ensemble eigenstates does depend on the Hamming distance but not on other tunneling distances.

Appendix C.

Numerical Methods

In the following, we give a short overview of the numerical methods used to diagonalize the Bose-Hubbard Hamiltonian (2.74). Our numerical programs are written in Fortran95 and are run on the high performance computing clusters “bwUniCluster”, “bwUniCluster 2.0”, “Justus” and “Justus 2” provided by the bwHPC consortium (`www.bwhpc.de`).

C.1. Exact Diagonalization

The term “exact diagonalization” describes algorithms which directly compute the diagonalization of a square matrix H (in our case the Hamiltonian) with a finite number of operations and would hence in theory be capable of finding the (numerically) exact eigenvalues and eigenvectors. A simple, yet numerically impractical, example of such a method is the following: First calculate the characteristic polynomial $\det(H - E\mathbb{1})$, e.g., by transforming $H - E\mathbb{1}$ to a triangular matrix via Gaussian elimination, and determine its roots. Once the eigenvalues E_i are known, the eigenvectors $\boldsymbol{v}_i$ can be computed exactly, solving $(H - E_i\mathbb{1})\boldsymbol{v}_i = 0$ via Gauss’s elimination method.

We use the function `syevr` of the Intel MKL library [205] to obtain the full set of eigenvalues and eigenvectors of our Hamiltonian via exact diagonalization. This routine first transforms the symmetric matrix H into a tridiagonal matrix T similar to H and then uses the dqds algorithm [206] to compute eigenvalues and eigenvectors of T. Since this procedure requires operations on dense matrices, it is necessary to store the full Hamiltonian in memory, which limits the usage of this function on the computing clusters to Hilbert space dimensions $\mathcal{N} \lesssim 10^5$. Due to the exponential increase of the Hilbert space dimension with particle number N and lattice length L [see Equation (2.78) on page 28], this limit is reached already for rather small system sizes. The largest system that we were able to treat with this function is the subspace of quasimomentum $Q = 0$ and both parities $\Pi = \pm 1$ for $N = 12$ bosons on $L = 12$ sites with PBCs, corresponding to the Hilbert space dimension $\mathcal{N} = 112\,720$ and to approximately 101.6 GB of memory to store the Hamiltonian in double precision (8 bytes per real number).

C.2. Iterative Solvers and Shift-Invert Technique

Since the Bose-Hubbard Hamiltonian is a sparse matrix (see Figure 2.7), the memory limitations of the exact-diagonalization methods can be overcome if one uses diagonalization algorithms that operate on sparse matrices. This is possible with Krylov subspace methods, e.g., the Lanczos or Arnoldi algorithms [207]. These are iterative solvers, which in each step yield a better approximation to the eigenvalues and eigenvectors. Since for m eigenvalues, at least m iteration steps are necessary [207], these methods are unfeasible for the calculation of the full spectrum.

One issue of a naive implementation of these algorithms is that eigenvalues in the center of the spectrum are typically exponentially close to each other and are therefore very hard to resolve. In the Bose-Hubbard Hamiltonian, for example, the width $\Delta_E = E_{\max} - E_{\min}$ of the spectrum scales maximally with N^2 (see for instance the classical limit discussed in Section 2.4.3, page 33) while the dimension $\mathcal{N}$ grows exponentially [see Equation (2.78) on page 28], such that the average distance $\Delta_E/\mathcal{N}$ between levels decays exponentially with N. As can be seen from the density of states in Figure 3.2 on page 37, the energy levels of the Bose-Hubbard Hamiltonian are typically much closer to each other in the center of the spectrum than at its edges. One way to circumvent this problem and to be able to calculate eigenvalues efficiently also deep within the bulk of the spectrum is to consider

$$G := (H - \varepsilon)^{-1} \tag{C.1}$$

instead of the Hamiltonian H, where ε is a target energy far from the edges of the spectrum (*shift-invert technique*) [208]. The eigenvalues of H slightly larger (smaller) than ε correspond to eigenvalues of G close to the upper (lower) edge of its spectrum, and small distances between eigenvalues of H are transformed into large distances between the corresponding eigenvalues of G. Since matrix inversion is numerically unstable [209] and since Krylov subspace methods require only the calculation of matrix-vector products $G\boldsymbol{x}$, $G^2\boldsymbol{x}$ etc. with specific vectors $\boldsymbol{x}$ [207], solving the system of linear equations

$$(H - \varepsilon)\boldsymbol{y} = \boldsymbol{x}, \tag{C.2}$$

e.g., by Gaussian elimination or by iterative solvers, is more feasible than directly calculating G and applying it to $\boldsymbol{x}$.

We implement these iterative solvers and the shift-invert technique using the libraries PETSc [210] and SLEPc [211]. With this implementation, the largest Hilbert space dimension that can be reached for the Bose-Hubbard Hamiltonian in the interaction basis is $\mathcal{N} \approx 2.6 \times 10^6$, corresponding to the subspace of a single parity for $N = L = 13$ with HWBCs and for $N = L = 15$ with PBCs and quasimomentum $Q = 0$, respectively (compare Table D.1). Due to the reduced sparsity, the largest system sizes that can be reached for the Bose-Hubbard Hamiltonian in the tunneling basis (one parity, $N = L = 12$ with HWBCs, $N = L = 14$ with PBCs and $Q = 0$) and for the embedded ensemble (one parity, $N = L = 11$) are slightly smaller. Table C.1 gives an overview of the necessary resources for exemplary computations.

system	cluster	nodes	MPI	OMP	memory per node	time
$N = L \leq 11$, HWBCs, int	Justus 2	1	1	48	192 GB	$<$ 10 minutes
$N = L = 12$, HWBCs, int	Justus 2	4	1	48	192 GB	$\approx$ 5 to $\approx$ 15 minutes
$N = L = 13$, HWBCs, int	Justus 2	30	1	48	192 GB	$\approx$ 35 to $\approx$ 50 minutes
$N = L = 13$, HWBCs, int	bwUniCluster 2.0	1 (fat)	1	160	$\approx$ 900 GB	$\approx$ 5 hours
$N = L \leq 13$, PBCs($Q = 0$), int	Justus 2	1	1	48	192 GB	$<$ 10 minutes
$N = L = 14$, PBCs($Q = 0$), int	Justus 2	4	1	48	192 GB	$\approx$ 15 to $\approx$ 30 minutes
$N = L = 15$, PBCs($Q = 0$), int	bwUniCluster 2.0	1 (fat)	1	160	$\approx$ 2.2 TB	$\approx$ 13 to $\approx$ 14 hours
$N = L \leq 10$, HWBCs, tun	Justus 2	1	1	48	192 GB	$<$ 10 minutes
$N = L = 11$, HWBCs, tun	Justus 2	1	1	48	192 GB	$\approx$ 20 to $\approx$ 30 minutes
$N = L = 12$, HWBCs, tun	bwUniCluster 2.0	1 (fat)	1	160	$\approx$ 1.5 TB	$\approx$ 7 to $\approx$ 9:30 hours
$N = L \leq 12$, PBCs($Q = 0$), tun	Justus 2	1	1	48	192 GB	$<$ 10 minutes
$N = L = 13$, PBCs($Q = 0$), tun	Justus 2	1	1	48	192 GB	$\approx$ 20 to $\approx$ 30 minutes
$N = L = 14$, PBCs($Q = 0$), tun	bwUniCluster 2.0	1 (fat)	1	160	$\approx$ 1.5 TB	$\approx$ 8 to $\approx$ 9 hours
EGOE, $N = L = 10$	Justus 2	1	1	48	192 GB	$\approx$ 2 minutes
EGOE, $N = L = 11$	Justus 2	1	1	48	192 GB	$\approx$ 20 minutes

Table C.1: Typical resources for the computation of 100 eigenstates closest to the energy target $\varepsilon \in \{0.2, 0.4, 0.5, 0.6, 0.8\}$, for one parity $\Pi = \pm 1$. Exact times may vary depending on ε, J and U. Entries in columns "MPI" and "OMP" denote, per compute node, the number of MPI tasks (i.e., separate processes running in parallel and communicating with each other by sending messages; each process accesses its own memory) and Open MP threads (i.e., parallel processes which all share their memory and hence need to run on the same node), respectively. EGOE is an abbreviation for the bosonic embedded ensemble, and "int" and "tun" denote the interaction and the tunneling basis, respectively. The keyword "fat" in the column "nodes" denotes a fat compute node of bwUniCluster2.0, which contains 80 cores with a total memory of 3 TB, as compared to 40 nodes and a total memory of 96 GB on normal nodes.

Appendix D.

Hilbert Space Dimensions of the Bose-Hubbard Model for Different Particle Numbers and Lattice Lengths

	HWBCs			PBCs, $Q = 0$		
N, L	both Π	$\Pi = -1$	$\Pi = +1$	both Π	$\Pi = -1$	$\Pi = +1$
$N = L = 7$	1716	848	868	246	113	133
$N = L = 8$	6435	3200	3235	810	370	440
$N = L = 9$	24 310	12 120	12 190	2704	1317	1387
$N = L = 10$	92 378	46 126	46 252	9252	4500	4752
$N = L = 11$	352 716	176 232	176 484	32 066	15 907	16 159
$N = L = 12$	1 352 078	675 808	676 270	112 720	55 898	56 822
$N = L = 13$	5 200 300	2 599 688	2 600 612	400 024	199 550	200 474
$N = L = 14$	20 058 300	10 028 292	10 030 008	1 432 860	714 714	718 146
$N = L = 15$	77 558 760	38 777 664	38 781 096	5 170 604	2 583 586	2 587 018

Table D.1: Hilbert space dimensions $\mathcal{N}$ of the Bose-Hubbard model for the particle numbers N, lattice lengths L (at unit filling), and symmetry subblocks considered throughout this thesis. Entries in red correspond to data out of numerical reach, while dimensions in blue are out of numerical reach only for the tunneling basis and can still be reached for the interaction basis.

Table D.1 gives an overview of the Hilbert space dimensions of the Bose-Hubbard model for the various boundary conditions (PBCs or HWBCs), symmetry blocks (parity $\Pi = \pm 1$, total quasimomentum Q for PBCs), particle numbers N, and lattice lengths L investigated at unit filling, $N = L$. Note that the parity-symmetric subspace is always larger than the parity-antisymmetric one, for all N and L, since certain interaction basis states such as $|1, \ldots, 1\rangle$ are already symmetric and hence contribute only to the symmetric subspace.

Bibliography

[1] H. Poincaré, *Mécanique céleste et astronomie: Masses fluides en rotation. Principes de Mécanique analytique. Problème des trois corps*, edited by J. Lévy (Gauthier-Villars, Paris, 1916).

[2] V. I. Arnold, *Mathematical Methods of Classical Mechanics* (Springer, New York, 1978).

[3] A. J. Lichtenberg and M. A. Lieberman, *Regular and Stochastic Motion* (Springer, New York, 1983).

[4] A. M. Ozorio de Almeida, *Hamiltonian Systems: Chaos and Quantization* (Cambridge University Press, Cambridge, 1989).

[5] M. J. Giannoni, A. Voros, and J. Zinn-Justin, eds., *Les Houches Session LII: Chaos and Quantum Physics* (North-Holland, Amsterdam, 1989).

[6] M. C. Gutzwiller, *Chaos in Classical and Quantum Mechanics* (Springer, New York, 1990).

[7] E. Ott, *Chaos in Dynamical Systems* (Cambridge University Press, Cambridge, 2002).

[8] P. Gaspard, "Dynamical Theory of Relaxation", in *Dynamics of Dissipation*, edited by P. Garbaczewski and R. Olkiewicz (Springer, Berlin, Heidelberg, 2002), pp. 111–163.

[9] N. Bohr, "Neutron Capture and Nuclear Constitution", Nature **137**, 344 (1936).

[10] "News and Views: Neutron Capture and Nuclear Constitution", Nature **137**, 351 (1936).

[11] F. M. Izrailev, "Simple models of quantum chaos: Spectrum and eigenfunctions", Phys. Rep. **196**, 299 (1990).

[12] H.-J. Stöckmann, *Quantum Chaos: An Introduction* (Cambridge University Press, Cambridge, 1999).

[13] F. Haake, *Quantum Signatures of Chaos*, 3rd ed. (Springer, Berlin, Heidelberg, 2010).

[14] F. Borgonovi, F. M. Izrailev, L. F. Santos, and V. G. Zelevinsky, "Quantum chaos and thermalization in isolated systems of interacting particles", Phys. Rep. **626**, 1 (2016).

[15] E. P. Wigner, "Characteristic Vectors of Bordered Matrices With Infinite Dimensions", Ann. Math. **62**, 548 (1955).

[16] E. P. Wigner, "Characteristic Vectors of Bordered Matrices with Infinite Dimensions II", Ann. Math. **65**, 203 (1957).

[17] E. P. Wigner, “Statistical Properties of Real Symmetric Matrices with Many Dimensions”, in Canadian Mathematical Congress Proceedings (1957), pp. 174–184.

[18] O. Bohigas, R. U. Haq, and A. Pandey, “Fluctuation Properties of Nuclear Energy Levels and Widths : Comparison of Theory with Experiment”, in *Nuclear Data for Science and Technology*, edited by K. H. Böckhoff (Springer Netherlands, Dordrecht, 1983), pp. 809–813.

[19] V. V. Flambaum, A. A. Gribakina, G. F. Gribakin, and M. G. Kozlov, “Structure of compound states in the chaotic spectrum of the Ce atom: Localization properties, matrix elements, and enhancement of weak perturbations”, Phys. Rev. A **50**, 267 (1994).

[20] D. Delande and J. C. Gay, “Quantum Chaos and Statistical Properties of Energy Levels: Numerical Study of the Hydrogen Atom in a Magnetic Field”, Phys. Rev. Lett. **57**, 2006 (1986).

[21] A. Holle, J. Main, G. Wiebusch, H. Rottke, and K. H. Welge, “Quasi-Landau Spectrum of the Chaotic Diamagnetic Hydrogen Atom”, Phys. Rev. Lett. **61**, 161 (1988).

[22] H.-J. Stöckmann and J. Stein, “‘Quantum’ chaos in billiards studied by microwave absorption”, Phys. Rev. Lett. **64**, 2215 (1990).

[23] Y. G. Sinai, “Dynamical systems with elastic reflections”, Russ. Math. Surv. **25**, 137 (1970).

[24] L. A. Bunimovich, “On the ergodic properties of nowhere dispersing billiards”, Commun. Math. Phys. **65**, 295 (1979).

[25] S. W. McDonald and A. N. Kaufman, “Wave chaos in the stadium: Statistical properties of short-wave solutions of the Helmholtz equation”, Phys. Rev. A **37**, 3067 (1988).

[26] J. Stein, H.-J. Stöckmann, and U. Stoffregen, “Microwave Studies of Billiard Green Functions and Propagators”, Phys. Rev. Lett. **75**, 53 (1995).

[27] S. Tomsovic and E. J. Heller, “Semiclassical construction of chaotic eigenstates”, Phys. Rev. Lett. **70**, 1405 (1993).

[28] P. J. Forrester, N. C. Snaith, and J. J. Verbaarschot, “Developments in random matrix theory”, J. Phys. A **36**, R1 (2003).

[29] M. L. Mehta, *Random Matrices*, 3rd ed. (Elsevier, Amsterdam, 1991).

[30] C. P. Hughes, “Random matrix theory and discrete moments of the Riemann zeta function”, J. Phys. A **36**, 2907 (2003).

[31] J. P. Keating and N. C. Snaith, “Random matrices and L -functions”, J. Phys. A **36**, 2859 (2003).

[32] M. Coram and P. Diaconis, “New tests of the correspondence between unitary eigenvalues and the zeros of Riemann’s zeta function”, J. Phys. A **36**, 2883 (2003).

[33] R. N. Mantegna and H. E. Stanley, *Introduction to Econophysics* (Cambridge University Press, Cambridge, 1999).

[34] T. Guhr and B. Kälber, “A new method to estimate the noise in financial correlation matrices”, J. Phys. A **36**, 3009 (2003).

[35] A. D. Mirlin, “Statistics of energy levels and eigenfunctions in disordered systems”, Phys. Rep. **326**, 259 (2000).

[36] G. Casati, F. Valz-Gris, and I. Guarnieri, “On the connection between quantization of nonintegrable systems and statistical theory of spectra”, Lett. al Nuovo Cim. **28**, 279 (1980).

[37] O. Bohigas, M. J. Giannoni, and C. Schmit, “Characterization of Chaotic Quantum Spectra and Universality of Level Fluctuation Laws”, Phys. Rev. Lett. **52**, 1 (1984).

[38] O. Bohigas, “Random Matrix Theories and Chaotic Dynamics”, in *Les Houches Session LII: Chaos and Quantum Physics*, edited by M. J. Giannoni, A. Voros, and J. Zinn-Justin (North-Holland, Amsterdam, 1989), pp. 87–199.

[39] S. Müller, S. Heusler, P. Braun, F. Haake, and A. Altland, “Semiclassical foundation of universality in quantum chaos”, Phys. Rev. Lett. **93**, 014103 (2004).

[40] M. V. Berry and M. Tabor, “Level clustering in the regular spectrum”, Proc. R. Soc. A **356**, 375 (1977).

[41] G. Zaslavskiĭ, “Statistics of energy levels when the integrals of motion are violated”, Sov. J. Exp. Theor. Phys. **46**, 1094 (1977).

[42] C. Cohen-Tannoudji, B. Diu, and F. Laloë, *Quantum Mechanics* (John Wiley and Sons, Hoboken, 2005).

[43] J. M. Deutsch, “Quantum statistical mechanics in a closed system”, Phys. Rev. A **43**, 2046 (1991).

[44] M. Srednicki, “Chaos and quantum thermalization”, Phys. Rev. E **50**, 888 (1994).

[45] J. M. Deutsch, “Thermodynamic entropy of a many-body energy eigenstate”, New J. Phys. **12**, 075021 (2010).

[46] F. Borgonovi, F. Mattiotti, and F. M. Izrailev, “Temperature of a single chaotic eigenstate”, Phys. Rev. E **95**, 042135 (2017).

[47] C. Murthy and M. Srednicki, “Structure of chaotic eigenstates and their entanglement entropy”, Phys. Rev. E **100**, 022131 (2019).

[48] T.-C. Lu and T. Grover, “Renyi entropy of chaotic eigenstates”, Phys. Rev. E **99**, 032111 (2019).

[49] G. De Tomasi and I. M. Khaymovich, “Multifractality Meets Entanglement: Relation for Nonergodic Extended States”, Phys. Rev. Lett. **124**, 200602 (2020).

[50] Y. V. Fyodorov and A. D. Mirlin, “Statistical Properties of eigenfunctions in a disordered metallic sample”, JETP Lett. **60**, 790 (1994).

[51] Y. V. Fyodorov and A. D. Mirlin, “Mesoscopic fluctuations of eigenfunctions and level-velocity distribution in disordered metals”, Phys. Rev. B **51**, 13403 (1995).

[52] D. Cohen and T. Kottos, “Parametric dependent Hamiltonians, wave functions, random matrix theory, and quantal-classical correspondence”, Phys. Rev. E **63**, 036203 (2001).

[53] D. V. Savin, H.-J. Sommers, and Y. V. Fyodorov, “Universal Statistics of the Local Green’s Function in Wave Chaotic Systems with Absorption”, JETP Lett. **82**, 544 (2005).

[54] H. Olofsson, S. Åberg, O. Bohigas, and P. Leboeuf, “Correlations and chaotic motion in nuclear masses”, Phys. Scr. **T125**, 162 (2006).

[55] C. Poli, D. V. Savin, O. Legrand, and F. Mortessagne, “Statistics of resonance states in open chaotic systems: A perturbative approach”, Phys. Rev. E **80**, 046203 (2009).

[56] W. Beugeling, A. Bäcker, R. Moessner, and M. Haque, “Statistical properties of eigenstate amplitudes in complex quantum systems”, Phys. Rev. E **98**, 022204 (2018).

[57] B. Mandelbrot, *The Fractal Geometry of Nature* (W. H. Freeman and Co., New York, 1982).

[58] T. C. Halsey, M. H. Jensen, L. P. Kadanoff, I. Procaccia, and B. I. Shraiman, “Fractal measures and their singularities: The characterization of strange sets”, Phys. Rev. A **33**, 1141 (1986).

[59] H. E. Stanley and P. Meakin, “Multifractal phenomena in physics and chemistry”, Nature **335**, 405 (1988).

[60] T. Nakayama and K. Yakubo, *Fractal Concepts in Condensed Matter Physics* (Springer, Berlin, Heidelberg, 2003).

[61] Y. Y. Atas and E. Bogomolny, “Multifractality of eigenfunctions in spin chains”, Phys. Rev. E **86**, 021104 (2012).

[62] Y. Y. Atas and E. Bogomolny, “Calculation of multi-fractal dimensions in spin chains”, Philos. Trans. R. Soc. A **372**, 20120520 (2014).

[63] N. Macé, F. Alet, and N. Laflorencie, “Multifractal Scalings Across the Many-Body Localization Transition”, Phys. Rev. Lett. **123**, 180601 (2019).

[64] M. Tarzia, “Many-body localization transition in Hilbert space”, Phys. Rev. B **102**, 014208 (2020).

[65] T. Orito and K.-I. Imura, “Multifractality and Fock-space localization in many-body localized states: One-particle density matrix perspective”, Phys. Rev. B **103**, 214206 (2021).

[66] I. V. Gornyi, A. D. Mirlin, and D. G. Polyakov, “Interacting Electrons in Disordered Wires: Anderson Localization and Low-T Transport”, Phys. Rev. Lett. **95**, 206603 (2005).

[67] D. Basko, I. Aleiner, and B. Altshuler, “Metal–insulator transition in a weakly interacting many-electron system with localized single-particle states”, Ann. Phys. (N. Y). **321**, 1126 (2006).

[68] E. Altman and R. Vosk, “Universal Dynamics and Renormalization in Many-Body-Localized Systems”, Annu. Rev. Condens. Matter Phys. **6**, 383 (2015).

[69] R. Nandkishore and D. A. Huse, “Many-Body Localization and Thermalization in Quantum Statistical Mechanics”, Annu. Rev. Condens. Matter Phys. **6**, 15 (2015).

[70] F. Alet and N. Laflorencie, “Many-body localization: An introduction and selected topics”, Comptes Rendus Phys. **19**, 498 (2018).

[71] D. A. Abanin, E. Altman, I. Bloch, and M. Serbyn, “Colloquium : Many-body localization, thermalization, and entanglement”, Rev. Mod. Phys. **91**, 021001 (2019).

[72] P. W. Anderson, “Absence of Diffusion in Certain Random Lattices”, Phys. Rev. **109**, 1492 (1958).

[73] F. Evers and A. D. Mirlin, “Anderson transitions”, Rev. Mod. Phys. **80**, 1355 (2008).

[74] H. Aoki, “Critical behaviour of extended states in disordered systems”, J. Phys. C **16**, L205 (1983).

[75] H. Aoki, “Fractal dimensionality of wave functions at the mobility edge: Quantum fractal in the Landau levels”, Phys. Rev. B **33**, 7310(R) (1986).

[76] A. Rodríguez, L. J. Vasquez, K. Slevin, and R. A. Römer, “Critical Parameters from a Generalized Multifractal Analysis at the Anderson Transition”, Phys. Rev. Lett. **105**, 046403 (2010).

[77] A. Rodríguez, L. J. Vasquez, K. Slevin, and R. A. Römer, “Multifractal finite-size scaling and universality at the Anderson transition”, Phys. Rev. B **84**, 134209 (2011).

[78] J. Lindinger and A. Rodríguez, “Multifractal finite-size scaling at the Anderson transition in the unitary symmetry class”, Phys. Rev. B **96**, 134202 (2017).

[79] D. J. Luitz, F. Alet, and N. Laflorencie, “Universal Behavior beyond Multifractality in Quantum Many-Body Systems”, Phys. Rev. Lett. **112**, 057203 (2014).

[80] J. Lindinger, “Multifractal properties of the ground state of the Bose-Hubbard model”, Master Thesis (Albert-Ludwigs-Universität Freiburg, 2017).

[81] J. Lindinger, A. Buchleitner, and A. Rodríguez, “Many-Body Multifractality throughout Bosonic Superfluid and Mott Insulator Phases”, Phys. Rev. Lett. **122**, 106603 (2019).

[82] M. Schneider, “Fock Space Localization of Many-Body States in the Tilted Bose-Hubbard Model”, Bachelor Thesis (Albert-Ludwigs-Universität Freiburg, 2019).

[83] M. Schneider, A. Rodríguez, and A. Buchleitner, “Fock Space Localization of Many-Body States in the Tilted Bose-Hubbard Model”, Acta Phys. Pol. A **136**, 834 (2019).

[84] A. Bäcker, M. Haque, and I. M. Khaymovich, “Multifractal dimensions for random matrices, chaotic quantum maps, and many-body systems”, Phys. Rev. E **100**, 032117 (2019).

[85] A. Pandey, “Statistical properties of many-particle spectra: III. Ergodic behaviour in random-matrix ensembles”, Ann. Phys. (N. Y). **119**, 170 (1979).

[86] L. Markus and K. R. Meyer, “Generic Hamiltonian dynamical systems are neither integrable nor ergodic”, Mem. Am. Math. Soc., No. 144 (1974).

[87] T. Geisel, G. Radons, and J. Rubner, “Kolmogorov-Arnol’d-Moser Barriers in the Quantum Dynamics of Chaotic Systems”, Phys. Rev. Lett. **57**, 2883 (1986).

[88] O. Bohigas, S. Tomsovic, and D. Ullmo, “Manifestations of classical phase space structures in quantum mechanics”, Phys. Rep. **223**, 43 (1993).

[89] A. Buchleitner, D. Delande, J. Zakrzewski, R. N. Mantegna, M. Arndt, and H. Walther, “Multiple Time Scales in the Microwave Ionization of Rydberg Atoms”, Phys. Rev. Lett. **75**, 3818 (1995).

[90] A. A. Michailidis, C. J. Turner, Z. Papić, D. A. Abanin, and M. Serbyn, “Slow Quantum Thermalization and Many-Body Revivals from Mixed Phase Space”, Phys. Rev. X **10**, 011055 (2020).

[91] R. Ketzmerick, L. Hufnagel, F. Steinbach, and M. Weiss, “New Class of Eigenstates in Generic Hamiltonian Systems”, Phys. Rev. Lett. **85**, 1214 (2000).

[92] M. Hiller, T. Kottos, and T. Geisel, “Complexity in parametric Bose-Hubbard Hamiltonians and structural analysis of eigenstates”, Phys. Rev. A **73**, 061604(R) (2006).

[93] O. Bohigas and J. Flores, “Two-body random Hamiltonian and level density”, Phys. Lett. B **34**, 261 (1971).

[94] O. Bohigas and J. Flores, “Spacing and individual eigenvalue distributions of two-body random Hamiltonians”, Phys. Lett. B **35**, 383 (1971).

[95] K. Mon and J. French, “Statistical properties of many-particle spectra”, Ann. Phys. (N. Y). **95**, 90 (1975).

[96] V. K. B. Kota and R. Sahu, “Structure of wave functions in (1+2)-body random matrix ensembles”, Phys. Rev. E **64**, 016219 (2001).

[97] L. Benet and H. A. Weidenmüller, “Review of the k-body embedded ensembles of Gaussian random matrices”, J. Phys. A **36**, 3569 (2003).

[98] V. K. B. Kota, *Embedded Random Matrix Ensembles in Quantum Physics* (Springer, Cham, 2014).

[99] C. K. Hong, Z. Y. Ou, and L. Mandel, “Measurement of subpicosecond time intervals between two photons by interference”, Phys. Rev. Lett. **59**, 2044 (1987).

[100] T. Brünner, G. Dufour, A. Rodríguez, and A. Buchleitner, “Signatures of Indistinguishability in Bosonic Many-Body Dynamics”, Phys. Rev. Lett. **120**, 210401 (2018).

[101] C. Dittel, G. Dufour, M. Walschaers, G. Weihs, A. Buchleitner, and R. Keil, “Totally Destructive Many-Particle Interference”, Phys. Rev. Lett. **120**, 240404 (2018).

[102] C. Dittel, G. Dufour, M. Walschaers, G. Weihs, A. Buchleitner, and R. Keil, “Totally destructive interference for permutation-symmetric many-particle states”, Phys. Rev. A **97**, 062116 (2018).

[103] T. Giordani, F. Flamini, M. Pompili, N. Viggianiello, N. Spagnolo, A. Crespi, R. Osellame, N. Wiebe, M. Walschaers, A. Buchleitner, and F. Sciarrino, “Experimental statistical signature of many-body quantum interference”, Nat. Photonics **12**, 173 (2018).

[104] G. Dufour, T. Brünner, C. Dittel, G. Weihs, R. Keil, and A. Buchleitner, “Many-particle interference in a two-component bosonic Josephson junction: An all-optical simulation”, New J. Phys. **19**, 125015 (2017).

[105] T. Brünner, “Signatures of partial distinguishability in the dynamics of interacting bosons”, Dissertation (Albert-Ludwigs-Universität Freiburg, 2018).

[106] G. Dufour, T. Brünner, A. Rodríguez, and A. Buchleitner, “Many-body interference in bosonic dynamics”, New J. Phys. **22**, 103006 (2020).

[107] L. F. Santos, F. Borgonovi, and F. M. Izrailev, “Onset of chaos and relaxation in isolated systems of interacting spins: Energy shell approach”, Phys. Rev. E **85**, 036209 (2012).

[108] E. J. Torres-Herrera and L. F. Santos, “Local quenches with global effects in interacting quantum systems”, Phys. Rev. E **89**, 062110 (2014).

[109] D. J. Luitz, N. Laflorencie, and F. Alet, “Many-body localization edge in the random-field Heisenberg chain”, Phys. Rev. B **91**, 081103 (2015).

[110] D. J. Luitz and Y. Bar Lev, “The ergodic side of the many-body localization transition”, Ann. Phys. (Berlin) **529**, 1600350 (2017).

[111] L. F. Santos and M. Rigol, “Localization and the effects of symmetries in the thermalization properties of one-dimensional quantum systems”, Phys. Rev. E **82**, 031130 (2010).

[112] L. F. Santos and M. Rigol, “Onset of quantum chaos in one-dimensional bosonic and fermionic systems and its relation to thermalization”, Phys. Rev. E **81**, 036206 (2010).

[113] C. Neuenhahn and F. Marquardt, “Thermalization of interacting fermions and delocalization in Fock space”, Phys. Rev. E **85**, 060101(R) (2012).

[114] M. Greiner, O. Mandel, T. Esslinger, T. W. Hänsch, and I. Bloch, “Quantum phase transition from a superfluid to a Mott insulator in a gas of ultracold atoms”, Nature **415**, 39 (2002).

[115] I. Bloch, J. Dalibard, and W. Zwerger, “Many-body physics with ultracold gases”, Rev. Mod. Phys. **80**, 885 (2008).

[116] J. P. Ronzheimer, M. Schreiber, S. Braun, S. S. Hodgman, S. Langer, I. P. McCulloch, F. Heidrich-Meisner, I. Bloch, and U. Schneider, “Expansion Dynamics of Interacting Bosons in Homogeneous Lattices in One and Two Dimensions”, Phys. Rev. Lett. **110**, 205301 (2013).

[117] F. Meinert, M. J. Mark, E. Kirilov, K. Lauber, P. Weinmann, M. Gröbner, and H.-C. Nägerl, “Interaction-Induced Quantum Phase Revivals and Evidence for the Transition to the Quantum Chaotic Regime in 1D Atomic Bloch Oscillations”, Phys. Rev. Lett. **112**, 193003 (2014).

[118] R. Islam, R. Ma, P. M. Preiss, M. E. Tai, A. Lukin, M. Rispoli, and M. Greiner, “Measuring entanglement entropy in a quantum many-body system”, Nature **528**, 77 (2015).

[119] S. S. Kondov, W. R. McGehee, W. Xu, and B. DeMarco, “Disorder-Induced Localization in a Strongly Correlated Atomic Hubbard Gas”, Phys. Rev. Lett. **114**, 083002 (2015).

[120] P. M. Preiss, R. Ma, M. E. Tai, A. Lukin, M. Rispoli, P. Zupancic, Y. Lahini, R. Islam, and M. Greiner, “Strongly correlated quantum walks in optical lattices”, Science **347**, 1229 (2015).

[121] M. Schreiber, S. S. Hodgman, P. Bordia, H. P. Lüschen, M. H. Fischer, R. Vosk, E. Altman, U. Schneider, and I. Bloch, "Observation of many-body localization of interacting fermions in a quasirandom optical lattice", Science **349**, 842 (2015).

[122] P. Bordia, H. P. Lüschen, S. S. Hodgman, M. Schreiber, I. Bloch, and U. Schneider, "Coupling Identical one-dimensional Many-Body Localized Systems", Phys. Rev. Lett. **116**, 140401 (2016).

[123] J.-Y. Choi, S. Hild, J. Zeiher, P. Schauß, A. Rubio-Abadal, T. Yefsah, V. Khemani, D. A. Huse, I. Bloch, and C. Gross, "Exploring the many-body localization transition in two dimensions", Science **352**, 1547 (2016).

[124] A. M. Kaufman, M. E. Tai, A. Lukin, M. Rispoli, R. Schittko, P. M. Preiss, and M. Greiner, "Quantum thermalization through entanglement in an isolated many-body system", Science **353**, 794 (2016).

[125] F. Meinert, M. J. Mark, K. Lauber, A. J. Daley, and H.-C. Nägerl, "Floquet Engineering of Correlated Tunneling in the Bose-Hubbard Model with Ultracold Atoms", Phys. Rev. Lett. **116**, 205301 (2016).

[126] P. Bordia, H. Lüschen, S. Scherg, S. Gopalakrishnan, M. Knap, U. Schneider, and I. Bloch, "Probing Slow Relaxation and Many-Body Localization in Two-Dimensional Quasiperiodic Systems", Phys. Rev. X **7**, 041047 (2017).

[127] M. Rispoli, A. Lukin, R. Schittko, S. Kim, M. E. Tai, J. Léonard, and M. Greiner, "Quantum critical behaviour at the many-body localization transition", Nature **573**, 385 (2019).

[128] T. Kohlert, S. Scherg, X. Li, H. P. Lüschen, S. Das Sarma, I. Bloch, and M. Aidelsburger, "Observation of Many-Body Localization in a One-Dimensional System with a Single-Particle Mobility Edge", Phys. Rev. Lett. **122**, 170403 (2019).

[129] A. Lukin, M. Rispoli, R. Schittko, M. E. Tai, A. M. Kaufman, S. Choi, V. Khemani, J. Léonard, and M. Greiner, "Probing entanglement in a many-body-localized system", Science **364**, 256 (2019).

[130] A. Buchleitner and A. R. Kolovsky, "Interaction-Induced Decoherence of Atomic Bloch Oscillations", Phys. Rev. Lett. **91**, 253002 (2003).

[131] A. R. Kolovsky and A. Buchleitner, "Quantum chaos in the Bose-Hubbard model", Europhys. Lett. **68**, 632 (2004).

[132] C. Kollath, A. M. Läuchli, and E. Altman, "Quench Dynamics and Nonequilibrium Phase Diagram of the Bose-Hubbard Model", Phys. Rev. Lett. **98**, 180601 (2007).

[133] G. Roux, "Quenches in quantum many-body systems: One-dimensional Bose-Hubbard model reexamined", Phys. Rev. A **79**, 021608 (2009).

[134] G. Biroli, C. Kollath, and A. M. Läuchli, "Effect of Rare Fluctuations on the Thermalization of Isolated Quantum Systems", Phys. Rev. Lett. **105**, 250401 (2010).

[135] C. Kollath, G. Roux, G. Biroli, and A. M. Läuchli, "Statistical properties of the spectrum of the extended Bose-Hubbard model", J. Stat. Mech. **2010**, P08011 (2010).

[136] G. Roux, "Finite-size effects in global quantum quenches: Examples from free bosons in an harmonic trap and the one-dimensional Bose-Hubbard model", Phys. Rev. A **81**, 053604 (2010).

[137] W. Beugeling, R. Moessner, and M. Haque, "Finite-size scaling of eigenstate thermalization", Phys. Rev. E **89**, 042112 (2014).

[138] S. Sorg, L. Vidmar, L. Pollet, and F. Heidrich-Meisner, "Relaxation and thermalization in the one-dimensional Bose-Hubbard model: A case study for the interaction quantum quench from the atomic limit", Phys. Rev. A **90**, 033606 (2014).

[139] W. Beugeling, R. Moessner, and M. Haque, "Off-diagonal matrix elements of local operators in many-body quantum systems.", Phys. Rev. E **91**, 012144 (2015).

[140] W. Beugeling, A. Andreanov, and M. Haque, "Global characteristics of all eigenstates of local many-body Hamiltonians: participation ratio and entanglement entropy", J. Stat. Mech. **2015**, P02002 (2015).

[141] R. Dubertrand and S. Müller, "Spectral statistics of chaotic many-body systems", New J. Phys. **18**, 033009 (2016).

[142] D. Fischer, D. Hoffmann, and S. Wimberger, "Spectral analysis of two-dimensional Bose-Hubbard models", Phys. Rev. A **93**, 043620 (2016).

[143] J. de la Cruz, S. Lerma-Hernández, and J. G. Hirsch, "Quantum chaos in a system with high degree of symmetries", Phys. Rev. E **102**, 032208 (2020).

[144] Y. Y. Atas, E. Bogomolny, O. Giraud, and G. Roux, "Distribution of the Ratio of Consecutive Level Spacings in Random Matrix Ensembles", Phys. Rev. Lett. **110**, 084101 (2013).

[145] L. Pausch, E. G. Carnio, A. Rodríguez, and A. Buchleitner, "Chaos and Ergodicity across the Energy Spectrum of Interacting Bosons", Phys. Rev. Lett. **126**, 150601 (2021).

[146] L. Pausch, E. G. Carnio, A. Buchleitner, and A. Rodríguez, "Chaos in the Bose–Hubbard model and random two-body Hamiltonians", New J. Phys. **23**, 123036 (2021).

[147] I. C. Percival, "Recent Developments in Classical Mechanics", in *Les Houches Session LII: Chaos and Quantum Physics*, edited by M. J. Giannoni, A. Voros, and J. Zinn-Justin (North-Holland, Amsterdam, 1989), pp. 11–86.

[148] M. V. Berry, "Some quantum-to-classical asymptotics", in *Les Houches Session LII: Chaos and Quantum Physics*, edited by M. J. Giannoni, A. Voros, and J. Zinn-Justin (North-Holland, Amsterdam, 1989), pp. 251–303.

[149] U. Klein, "What is the limit $\hbar \to 0$ of quantum theory?", Am. J. Phys. **80**, 1009 (2012).

[150] T. A. Brody, J. Flores, J. B. French, P. A. Mello, A. Pandey, and S. S. M. Wong, "Random-matrix physics: spectrum and strength fluctuations", Rev. Mod. Phys. **53**, 385 (1981).

[151] T. Guhr, A. Müller–Groeling, and H. A. Weidenmüller, "Random-matrix theories in quantum physics: common concepts", Phys. Rep. **299**, 189 (1998).

[152] G. Casati, B. V. Chirikov, and I. Guarneri, “Energy-Level Statistics of Integrable Quantum Systems”, Phys. Rev. Lett. **54**, 1350 (1985).

[153] B. Dietz and K. Życzkowski, “Level-spacing distributions beyond the Wigner surmise”, Z. Physik B **84**, 157 (1991).

[154] J. M. G. Gómez, R. A. Molina, A. Relaño, and J. Retamosa, “Misleading signatures of quantum chaos”, Phys. Rev. E **66**, 036209 (2002).

[155] Á. L. Corps and A. Relaño, “Long-range level correlations in quantum systems with finite Hilbert space dimension”, Phys. Rev. E **103**, 012208 (2021).

[156] Á. L. Corps, A. Relaño, and R. A. Molina, private communication, 2022.

[157] V. Oganesyan and D. A. Huse, “Localization of interacting fermions at high temperature”, Phys. Rev. B **75**, 155111 (2007).

[158] O. Giraud, N. Macé, É. Vernier, and F. Alet, “Probing Symmetries of Quantum Many-Body Systems through Gap Ratio Statistics”, Phys. Rev. X **12**, 011006 (2022).

[159] M. E. Muller, “A note on a method for generating points uniformly on n-dimensional spheres”, Commun. ACM **2**, 19 (1959).

[160] N. D. Chavda, V. Potbhare, and V. K. B. Kota, “Statistical properties of dense interacting boson systems with one- plus two-body random matrix ensembles”, Phys. Lett. A **311**, 331 (2003).

[161] A. Rényi, “On measures of entropy and information”, in Proceedings of the fourth Berkeley Symposium on Mathematics, Statistics and Probability (1961), pp. 547–561.

[162] J. T. Edwards and D. J. Thouless, “Numerical studies of localization in disordered systems”, J. Phys. C **5**, 807 (1972).

[163] V. E. Kravtsov, I. M. Khaymovich, E. Cuevas, and M. Amini, “A random matrix model with localization and ergodic transitions”, New J. Phys. **17**, 122002 (2015).

[164] M. P. A. Fisher, P. B. Weichman, G. Grinstein, and D. S. Fisher, “Boson localization and the superfluid-insulator transition”, Phys. Rev. B **40**, 546 (1989).

[165] M. Lewenstein, A. Sanpera, V. Ahufinger, B. Damski, A. Sen(De), and U. Sen, “Ultracold atomic gases in optical lattices: mimicking condensed matter physics and beyond”, Adv. Phys. **56**, 243 (2007).

[166] M. A. Cazalilla, R. Citro, T. Giamarchi, E. Orignac, and M. Rigol, “One dimensional bosons: From condensed matter systems to ultracold gases”, Rev. Mod. Phys. **83**, 1405 (2011).

[167] K. V. Krutitsky, “Ultracold bosons with short-range interaction in regular optical lattices”, Phys. Rep. **607**, 1 (2016).

[168] T. Orell, A. A. Michailidis, M. Serbyn, and M. Silveri, “Probing the many-body localization phase transition with superconducting circuits”, Phys. Rev. B **100**, 134504 (2019).

[169] C. Berke, E. Varvelis, S. Trebst, A. Altland, and D. P. DiVincenzo, “Transmon platform for quantum computing challenged by chaotic fluctuations”, arXiv:2012.05923 (2020).

[170] W. Fulton and J. Harris, *Representation Theory* (Springer, New York, 2004).

[171] Y. Kosmann-Schwarzbach, *Groups and Symmetries* (Springer, New York, 2010).

[172] M. Hiller, “Parametric Bose-Hubbard Hamiltonians: Quantum Dissipation, Irreversibility, and Pumping”, Dissertation (Georg-August-Universität Göttingen, 2007).

[173] M. Hiller, T. Kottos, and T. Geisel, “Wave-packet dynamics in energy space of a chaotic trimeric Bose-Hubbard system”, Phys. Rev. A **79**, 023621 (2009).

[174] B.-G. Englert, *Lectures on Classical Mechanics* (World Scientific, Singapore, 2015).

[175] T. Engl, J. D. Urbina, and K. Richter, “Periodic mean-field solutions and the spectra of discrete bosonic fields: Trace formula for Bose-Hubbard models”, Phys. Rev. E **92**, 062907 (2015).

[176] W. S. Bakr, A. Peng, M. E. Tai, R. Ma, J. Simon, J. I. Gillen, S. Folling, L. Pollet, and M. Greiner, “Probing the Superfluid-to-Mott Insulator Transition at the Single-Atom Level”, Science **329**, 547 (2010).

[177] S. Rachel, N. Laflorencie, H. F. Song, and K. Le Hur, “Detecting Quantum Critical Points Using Bipartite Fluctuations”, Phys. Rev. Lett. **108**, 116401 (2012).

[178] M. Gerster, M. Rizzi, F. Tschirsich, P. Silvi, R. Fazio, and S. Montangero, “Superfluid density and quasi-long-range order in the one-dimensional disordered Bose–Hubbard model”, New J. Phys. **18**, 015015 (2016).

[179] G. E. Astrakharchik, K. V. Krutitsky, M. Lewenstein, and F. Mazzanti, “One-dimensional Bose gas in optical lattices of arbitrary strength”, Phys. Rev. A **93**, 021605(R) (2016).

[180] G. Boéris, L. Gori, M. D. Hoogerland, A. Kumar, E. Lucioni, L. Tanzi, M. Inguscio, T. Giamarchi, C. D’Errico, G. Carleo, G. Modugno, and L. Sanchez-Palencia, “Mott transition for strongly interacting one-dimensional bosons in a shallow periodic potential”, Phys. Rev. A **93**, 011601(R) (2016).

[181] H. Hasegawa, S. Adachi, and H. Harada, “On the scaling properties of the energy spectrum of hydrogen in a uniform magnetic field”, J. Phys. A **16**, L503 (1983).

[182] A. C. Davison, *Statistical Models* (Cambridge University Press, Cambridge, 2003).

[183] E. Cho, M. J. Cho, and J. Eltinge, “The Variance of Sample Variance From a Finite Population”, Int. J. Pure Appl. Math. **21**, 387 (2005).

[184] C. E. Sandifer, *How Euler Did It* (Mathematical Association of America, 2007).

[185] F. W. J. Olver, A. B. Olde Daalhuis, D. W. Lozier, B. I. Schneider, R. F. Boisvert, C. W. Clark, B. R. Miller, B. V. Saunders, H. S. Cohl, and M. A. McClain, eds., *NIST Digital Library of Mathematical Functions*, `http://dlmf.nist.gov/`, Release 1.1.2 of 2021-06-15.

[186] I. Gertsbakh, *Measurement Theory for Engineers* (Springer, Berlin, Heidelberg, 2003).

[187] A. Lakshminarayan, S. Tomsovic, O. Bohigas, and S. N. Majumdar, “Extreme Statistics of Complex Random and Quantum Chaotic States”, Phys. Rev. Lett. **100**, 044103 (2008).

[188] D. L. Wallace, “Asymptotic Approximations to Distributions”, Ann. Math. Stat. **29**, 635 (1958).

[189] S. Kullback and R. A. Leibler, “On Information and Sufficiency”, Ann. Math. Stat. **22**, 79 (1951).

[190] T. M. Cover and J. A. Thomas, *Elements of Information Theory* (John Wiley and Sons, Hoboken, 2006).

[191] M. Walschaers, “Efficient quantum transport”, Dissertation (Albert-Ludwigs-Universität Freiburg, 2016).

[192] C. Dittel, G. Dufour, G. Weihs, and A. Buchleitner, “Wave-Particle Duality of Many-Body Quantum States”, Phys. Rev. X **11**, 031041 (2021).

[193] E. Brunner, “Many-Body Interference , Partial Distinguishability and Entanglement”, Master Thesis (Albert-Ludwigs-Universität Freiburg, 2019).

[194] C. Haen, “Distinguishability-induced quantum-to-classical transitions in many-body interference”, Master Thesis (Albert-Ludwigs-Universität Freiburg, 2020).

[195] A. Rubio-Abadal, J.-Y. Choi, J. Zeiher, S. Hollerith, J. Rui, I. Bloch, and C. Gross, “Many-Body Delocalization in the Presence of a Quantum Bath”, Phys. Rev. X **9**, 041014 (2019).

[196] E. Brunner, private communication, 2021.

[197] M. C. Tichy, M. Tiersch, F. de Melo, F. Mintert, and A. Buchleitner, “Zero-Transmission Law for Multiport Beam Splitters”, Phys. Rev. Lett. **104**, 220405 (2010).

[198] L. Aolita, C. Gogolin, M. Kliesch, and J. Eisert, “Reliable quantum certification of photonic state preparations”, Nat. Commun. **6**, 8498 (2015).

[199] T. V. Zache, T. Schweigler, S. Erne, J. Schmiedmayer, and J. Berges, “Extracting the Field Theory Description of a Quantum Many-Body System from Experimental Data”, Phys. Rev. X **10**, 011020 (2020).

[200] M. Kliesch and I. Roth, “Theory of Quantum System Certification”, PRX Quantum **2**, 010201 (2021).

[201] M. V. Berry, “Regular and irregular semiclassical wavefunctions”, J. Phys. A **10**, 2083 (1977).

[202] M. V. Berry, “Semi-classical mechanics in phase space: A study of Wigner’s function”, Philos. Trans. R. Soc. A **287**, 237 (1977).

[203] J. D. Urbina and K. Richter, “Random wave functions with boundary and normalization constraints”, Eur. Phys. J. Spec. Top. **145**, 255 (2007).

[204] R. W. Hamming, “Error Detecting and Error Correcting Codes”, Bell Syst. Tech. J. **29**, 147 (1950).

[205] *Developer Reference for Intel Math Kernel Library: ?syevr*, `https://software.intel.com/content/www/us/en/develop/documentation/onemkl-developer-reference-fortran/top/lapack-routines/lapack-least-squares-and-eigenvalue-problem/lapack-least-squares-eigenvalue-problem-driver/symmetric-eigenvalue-problems-lapack-driver/syevr.html`, Version 2021.4 of 2021-09-27.

[206] B. N. Parlett and O. A. Marques, “An implementation of the dqds algorithm (positive case)”, Linear Algebra Appl. **309**, 217 (2000).

[207] G. H. Golub and C. F. Van Loan, *Matrix Computations*, 4th ed. (Johns Hopkins University Press, Baltimore, Maryland, 2013).

[208] F. Pietracaprina, N. Macé, D. J. Luitz, and F. Alet, “Shift-invert diagonalization of large many-body localizing spin chains”, SciPost Phys. **5**, 045 (2018).

[209] W. H. Press, S. A. Teukolsky, W. T. Vetterling, and B. P. Flannery, *Numerical Recipes: The Art of Scientific Computing*, 3rd ed. (Cambridge University Press, Cambridge, 2007).

[210] S. Balay, S. Abhyankar, M. F. Adams, S. Benson, J. Brown, P. Brune, K. Buschelman, E. M. Constantinescu, L. Dalcin, A. Dener, V. Eijkhout, W. D. Gropp, V. Hapla, T. Isaac, P. Jolivet, D. Karpeev, D. Kaushik, M. G. Knepley, F. Kong, S. Kruger, D. A. May, L. Curfman McInnes, R. Tran Mills, L. Mitchell, T. Munson, J. E. Roman, K. Rupp, P. Sanan, J. Sarich, B. F. Smith, S. Zampini, H. Zhang, H. Zhang, and J. Zhang, *PETSc Users Manual*, tech. rep. ANL-21/39 - Revision 3.16 (Argonne National Laboratory, 2021).

[211] V. Hernandez, J. E. Roman, and V. Vidal, “SLEPc: A scalable and flexible toolkit for the solution of eigenvalue problems”, ACM Trans. Math. Softw. **31**, 351 (2005).